# Impact of 3D non axisymmetrical magnetic perturbations on the transport and turbulence in the edge plasma of tokamaks

Benjamin Luce

Aix*Marseille université
Initiative d'excellence

NNT/NL: 2020AIXM0001/001ED000

# PHD THESIS

# Impact of 3D non axisymmetrical magnetic perturbations on the transport and turbulence in the edge plasma of tokamaks

Presented by:
Benjamin LUCE

**Discipline**
Sciences pour l'ingénieur

**Spécialité**
Fusion magnétique

**École doctorale**
ED 353 Sciences pour l'ingénieur: Mécanique, Physique, Micro et Nanoélectronique

**Laboratoire/Partenaires de recherche**
M2P2, CNRS, Centrale Marseille-AMU, France
IRFM, CEA Cadarache, France

**Composition du jury**

| | |
|---|---|
| PR. Alexander KENDL<br>IAP, Innsbruck Universität | Rapporteur |
| DR. Hinrich LÜTJENS<br>CPhT, École Polytechnique | Rapporteur |
| PR. Peter BEYER<br>PIIM, AMU | Examinateur |
| CR. Laure VERMARE<br>LPP, École Polytechnique | Examinatrice |
| CR. Patrick TAMAIN<br>IRFM, CEA | Co-encadrant de thèse |
| DR. Eric SERRE<br>M2P2, AMU | Directeur de thèse |

M2P2 UMR 7340 CNRS - Aix-Marseille Université - Centrale Marseille

DE LA RECHERCHE À L'INDUSTRIE cea

IRFM

I, undersigned, Benjamin LUCE, hereby declare that the work presented in this manuscript is my own work, carried out under the scientific direction of Eric SERRE and Patrick TAMAIN, in accordance with the principles of honesty, integrity and responsibility inherent to the research mission. The research work and the writing of this manuscript have been carried out in compliance with both the french national charter for Research Integrity and the Aix-Marseille University charter on the fight against plagiarism.

This work has not been submitted previously either in this country or in aother country in the same or in a similar version to any other examination body.

Marseille, October 31, 2020

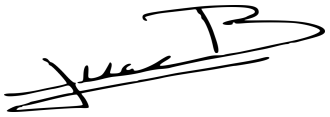

# Résumé

Pour un mix énergétique, la maîtrise de la fusion nucléaire offre l'opportunité d'une source d'énergie abondante et renouvelable. Les tokamaks ont montré les meilleurs performances pour confiner un plasma de fusion grâce à des champs magnétiques et ont été choisis comme la prochaine génération de machines pour la recherche en fusion (ITER). L'évacuation des flux de chaleur et l'augmentation du temps de confinement sont les deux principaux défis pour les tokamaks. Ils sont directement en lien avec le transport perpendiculaire, essentiellement turbulent, vers le mur. Pour améliorer le confinement, le mode H est recherché. Il crée un piedestal sur la pression dans le plasma de bord, réduisant le transport perpendiculaire mais est associé à des relaxations, les ELMs, responsables d'un afflux de chaleur transitoire sur les murs au-delà des limites tolérables. Pour supprimer ou mitiger les ELMs, des pertubations magnétiques 3D (MPs) ont été ajoutées grâce à des bobines externes. Les impacts des MPs sur les ELMs, la transition L-H, leur écrantage ou leur résonance sur le champ magnétique ont été étudiés. Peu de données existent sur leur impact sur la turbulence dû à la difficulté de mesures expérimentales et à la complexité sur les outils numériques nécessaires.

Dans cette thèse, nous abordons la question par la modélisation du plasma de bord, de l'extérieur du coeur à la SOL. 2 codes complémentaires sont utilisés : un code fluide 3D électrostatique turbulent, TOKAM3X et un à champs moyens, SOLEDGE3X_HDG.

Avec TOKAM3X, un effort conjoint de l'IRFM (CEA), du M2P2 et du PIIM, nous observons l'impact de MPs 3D sur la turbulence de bord. La capacité de traiter des perturbations 3D a été ajoutée durant cette thèse. Une approche par étape a suivi, d'abord par des simulations isothermes electrostatiques avec une MP mode simple dans une géométrie circulaire avec limiteur. Des observations expérimentales ont été reproduites comme la perte de densité par les MPs, ansi que les variations du champ électrique radial, associées à une redistribution poloïdale et toroïdale des flux. Les MPs impactent modérément la turbulence, réduisant l'intermittence dans la SOL et les fluctuations de densité. Une complexification du modèle a été faite sur des simulations non isothermes. Nous montrons l'importance du découplage entre particule et énergie. Différents résultats sont observés lorsqu'un flux simpliste de particules en provenance du coeur est comparé à un flux recyclé, plus réaliste, en provenance du limiteur. Des tendances expérimentales sont retrouvées dans le cas avec recyclage mais seulement partiellement dans le cas sans. L'impact sur la turbulence est à nouveau modéré mais différent suivant les cas, particulièrement lorsque l'on distingue la turbulence associée à l'énergie ou aux particules.

Une analyse des conséquences de ces observations sur les simulations à champs

moyens est proposée par à une comparaison directe. Des différences significatives sont observées par rapport aux simulations turbulentes qui ont des perturbations toroïdales non-axisymétriques d'amplitudes bien plus importantes. Leur localisation spatiale est également différentes. Ces résultats démontrent certaines limites de l'approche à champs moyens sur la modélisation des MPs et appellent à poursuivre l'effort sur des simulations turbulentes auto-consistantes. Enfin, les premiers résultats sur des simulations à champs moyens TOKAM3X avec des MPs plus réalistes sont présentés. L'impact est plus faible (en amplitude) et plus localisé. Une extension de ce travail a été implémentée sur SOLEDGE3X_HDG, utilisant pour la première fois son modèle 3D, pour explorer des géométries et MPs plus complexes (jusqu'à un ripple en géométrie WEST). Les MPs réalistes ont un comportement similaire aux observations faites avec TOKAM3X champs moyens mais avec des différences notables. Le ripple modifie l'équilibre global du plasma mais, en accord avec la théorie, impacte faiblement sa symétrie toroïdale.

Mots clés : fusion, plasma de bord, SOL, turbulence, transport, RMP, ripple

# Abstract

For the energetic mix, the mastery of fusion offers the possibility of an abundant and sustainable source of energy. Tokamaks have demonstrated the best performance to confine a burning plasma with magnetic fields and are the concept chosen for the next generation fusion research device (ITER). The power exhaust and the increase of the confinement time are two major challenges for tokamaks. These are linked to the perpendicular, mostly turbulent transport toward the wall. To improve the confinement, high confinement regimes (H-mode) are sought. The H-mode creates a pressure pedestal at the edge plasma, decreasing the perpendicular transport but is associated with deleterious relaxation events, the Edge Localized Modes (ELMs), which lead to transient heat fluxes to the wall beyond tolerable limits. In order to mitigate or suppress the ELMs. 3D magnetic perturbations (MP) have been added through external coils. If the impact of MPs on ELMs, on the L-H transition, their screening by the plasma or their resonance on the magnetic field have been studied, few data exist on their impact on the turbulent transport owing to the difficulty of measuring relevant quantities in experiments and to the complexity of the required numerical tools on the modelling side.

In this thesis, we tackle this question through the modeling of the edge plasma, from the outside core to the Scrape-Off Layer (SOL). 2 codes are used to address 2 complementary aspects: a 3D electrostatic fluid turbulent code, TOKAM3X and a mean-field one, SOLEDGE3X_HDG.

With the TOKAM3X code, a joint effort of IRFM (CEA), M2P2 and PIIM, this thesis aims at observing the impact of 3D MPs on edge turbulence. The capability to treat 3D perturbations has been added to the code. A step-by-step approach has been followed, starting with an electrostatic isothermal model with single mode MP in a limiter circular geometry. This first study reproduces some experimental observations, such as the loss of density due to MPs (density pump-out) as well as the variation of the radial electric field, associated with a redistribution of poloidal and parallel flows. In this model, the MPs only moderately impact turbulence properties, mainly decreasing its intermittency in the SOL as well as the density fluctuations. A complexification of the model is then done, going into non isothermal simulations. We show that the decoupling of particles and energy is important, as different results are observed when a simplistic incoming particle flux from the core is used compared with a more realistic recycling source around the limiter. Experimental trends are recovered for the recycling cases but only partially for the non recycling ones. The impact on

turbulence is still moderated but quite different between the two sets, especially when one distinguishes between particles and energy associated turbulence. An analysis of the consequences of such findings for mean-field simulations is then proposed through a direct comparison. It shows a significant difference with turbulent simulations having higher amplitudes of non-axisymmetric density perturbations. Their spatial localization are also distinct. These results demonstrate some of the limits of the constant transport ansatz used in mean-field codes for modeling of MPs and call for further studies with self-consistent turbulent transport. Finally, first results in the direction of more realistic MPs spectra are presented, using TOKAM3X mean-field cases as a start. Their impact is smaller and more localized on the Low Field Side (LFS). An extension of this work is done on SOLEDGE3X_HDG, testing its 3D ability for the first time, in more complex geometries and even simulating a realistic ripple in WEST geometry. Realistic MPs shows comparable behaviour with the mean-field version of TOKAM3X with notable differences. Ripple shows a modification of the global equilibrium but, as predicted by theory, little impact on toroidal non-axisymmetric events.

Keywords: fusion, edge plasma, SOL, turbulence, transport, RMP, ripple

# Aknowledgements

I would like to thank Aix-Marseille Université and the CEA to give me the opportunity to do the thesis. These thanks, beyond institutions, go particularly toward Eric Serre, my PhD director, and Patrick Tamain, mu PhD supervisor. Both have been extremely helpeful from the organisational point of view from Eric to the scientific one from Patrick.
A big thanks goes to Frederic Schwander from who, as a lost Centralien, I ask for a PhD. He was the one to send me to Eric and Patrick, and so was at the starting point of three years of excruciating . . . challenging, I mean challenging, time! He helped me a few time around particularly nasty mathematic problem.
I wish to thank Giorgio for his welcome help to implement the 3D magnetic perturbation inside HDG, which was a time trial that began in January, 2020 to be abruptly stopped by the COVID but still had to go on (and his insight was the best I could have had).
Special thanks must go to Mathieu Perret, Elias Laribi, Raffaele Tattali and Manuel Scotto, fellow PhD students in fusion, whose discussions help me to understand plasma physics better. Their insight being somewhat not to far away from mine, it was easier for me to improve than having a discussion with a specialist with years of experience and well above my modest abilities!
I wish to thank Jérémie (L.), Jean-Baptiste, Jérémie (J.), Isabelle, Eléonore, Camille, Sylvia and so many others PhD students and Post-Docs I interact with, to bear with me, my constant chatter and my mood swing, especially at the end during the redaction of this manuscript.
Finally, I absolutly must thank my family. Merci Auriane pour, dès tes 8 ans, avoir tenté de comprendre ce que ton grand frère faisait. Merci Grand-mère pour avoir montré le même interêt alors que les sciences ne sont pas ton domaine de prédilection. Enfin, merci maman d'avoir cru en moi et d'y croire encore! Cette thèse est aussi la tienne.

# Contents

# Acronyms

CFR Closed Field lines Region. 63, 64, 67–72, 76–78, 81–87, 95–101, 103–108, 110, 111, 113–116, 119, 121, 122, 124, 125, 128, 129, 131, 132, 136, 143, 144, 161, 162

D-T Deuterium-Tritium. 8, 14, 15, 30

ELM Edge Localized Mode. 8, 14, 32, 33

ETB Edge Transport Barrier. 32

HFS High Field Side, inner side of a tokamak. 69, 71, 72, 75, 77–79, 81–87, 90, 100, 101, 109, 115, 119, 121, 122, 131, 136, 138, 145, 155

ITER International Thermonuclear Experimental Reactor. 18, 28, 30–32, 163

LFS Low Field Side, outer side of a tokamak. 66–79, 81–90, 100, 101, 108–117, 119, 121, 122, 124, 126–128, 131, 136, 138, 145, 148, 149, 155, 162

MHD MagnetoHydroDynamics. 33

MP Magnetic Perturbation. 9, 10, 33, 37, 61–91, 93–119, 121, 123–136, 138, 140, 142–149, 155–162

PFC Plasma Facing Component. 28, 46

RMP Resonant Magnetic Perturbation. 8–10, 14, 32–34, 36, 37, 64, 86, 133, 134, 140–146, 148–150, 159, 162

SOL Scrape-Off Layer. 8, 9, 14, 28–30, 46, 47, 61, 63, 64, 67–73, 75, 77–87, 89, 90, 96, 97, 99–101, 103–108, 111–121, 124, 125, 127–129, 131, 135, 136, 143, 145, 149, 161, 162

# Nomenclature

| | |
|---|---|
| $\eta_{\parallel/\perp}$ | Parallel/Perpendicular Spitzer resitivity, scalar. 43 |
| $\lambda_N$ | SOL width, scalar. 80, 117–120 |
| $\lambda_q$ | Power SOL width, scalar. 29, 117, 119, 120 |
| $\nu_c$ | Collision frequency, scalar. 23, 24, 41, 42 |
| $\nu^\star$ | Collisionality, scalar. 43, 53, 64, 92 |
| $\omega_c$ | Cyclotron frequency, scalar. 42, 44, 50 |
| $\rho_L$ | Larmor radius, scalar. 23, 44, 50, 80, 119, 145 |
| $\tau_{e/i}$ | Electron/Ion collision time, scalar. 42 |
| $c_s$ | Sound speed, scalar. 29 |
| | |
| $k_B$ | Boltzmann constant, scalar, $1.3806505 \times 10^{-23} \mathrm{J \cdot K^{-1}}$. 15 |

# 1. Introduction

## Table of Content

This chapter aims at a general presentation of controlled nuclear fusion. The tokamak, a magnetic confinement device, is the focus on this part with the introduction of some important parameters necessary for the understanding of this thesis.

## 1.1. Controlled nuclear fusion: a general introduction

The control of the thermonuclear reaction, or fusion reaction, occuring in the stars, aims at adding a new energy source for producing electricity. This section explains the choice of the deuterium tritium reaction as well as a quick view of the different ways to create controlled fusion reactions.

### 1.1.1. Fusion reactions: the choice of D-T fusion

Fusion reactions occur naturally in the stars. The reaction is quite complex and evolves the inconspicuous weak interaction. Through the high pressures and temperatures, matter is submitted to, hydrogen atoms are separated into electrons and protons (nuclei for hydrogen), forming a ionized state of matter: a plasma. Chain reactions done in several complex steps transform the hydrogen into hydrogen isotopes ${}^{2}_{1}\mathrm{H}$, called deuterium ${}^{2}_{1}\mathrm{D}$, that then fuses with hydrogen to form helium 3, ${}^{3}_{2}\mathrm{He}$ and two helium 3 fuse to form 2 protons (hydrogen ion) and a helium nucleus (noted $\alpha$), ${}^{4}_{2}\mathrm{He}$. This process involving the smallest nuclei of the matter, produces great amount of energy due to the mass difference between the products and the reactants, following the famous law: $E = m \cdot c^2$.

On Earth, helium 3 is almost inexistant but deuterium can be found in ocean water (0.03% of the total hydrogen mass). To achieve a fusion reaction, the Coulomb repulsion must be vanquished. In the stars, the enormous mass exerts a massive pressure and, coupled with a high temperature, it allows to bypass the Coulomb potential and to ensure an efficent probabality for the two particles to fuse (mostly by tunnel effect, even at such temperature). This probability is called the cross-section and depends on the temperature and the particles considered. Figure 1.1 gives an idea for different pair of particles as a function of the temperature, expressed in keV, at normal pressure. The electron-Volt (eV) is an energy unit and can be easily convert into Kelvin with the Boltzmann constant $k_B$. Thus 1 eV $\rightarrow 1.16 \cdot 10^4$ K. We can immediately see that the most favorable reaction at the lowest temperature (still of the order of a hundred millions Kelvin) is Deuterium-Tritium (D-T).

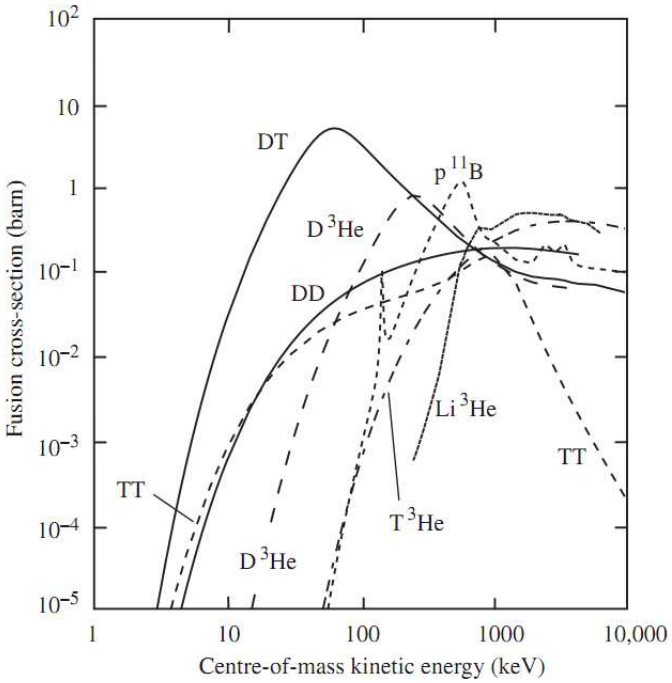


Figure 1.1.: Cross-section of main fusion reactions as a function of thermal energy [123, Chap. 1]

Due to the rarity of helium 3 and the unfavorable behaviour of the D-D reaction at low temperature[1], the fusion reaction of interest on the Earth is:

$$ {}^{2}_{1}\mathrm{D} + {}^{3}_{1}\mathrm{T} = {}^{2}_{2}\mathrm{He}\ (3.5\ \mathrm{MeV}) + {}^{1}_{0}\mathrm{n}\ (14.1\ \mathrm{MeV}) \tag{1.1} $$

To give an order of comparison, for the same mass of matter, the amount of resulting energy (in Joule) of such fusion reaction is a million times larger compare to a typical combustion reaction with oil and 5 to 10 times higher than a fission reaction with uranium. The energy given in parenthesis is the one transported by each particle. The alpha particles He contained 1/5 of the energy, whereas 4/5 are in the neutron $n$. This neutron can be used to artificially produced tritium (a non-existent element in the universe as its half-life is only 12 years) from ${}^{6}_{3}\mathrm{Li}$, an isotope of lithium. The neutron is also the particles that shall heat the wall and allows to extract the energy (the $\alpha$ particles shall remains confined by the magnetic field in a tokamak).

### 1.1.2. Energetic approach: the Lawson's criterion

To achieve an efficient fusion reaction on the Earth, the matter must be heated to hundreds of millions of Kelvin. This temperature forces the matter to a state of plasma, where nuclei (ions) and electrons are mostly (even completely) decoupled, resulting

[1] Low from a certain point of view...

in a mixture of free electrons and ions. To outline the yield of a fusion reactor, the amplification factor $Q$ is defined as:

$$Q = \frac{P_{\text{fus}}}{P_{\text{inj}}} \tag{1.2}$$

where $P_{\text{inj}}$ is the injected power through heating. The methods of heating from external sources, in a non exhaustive list, range from ohming heating, high velocity particule injection, waves heating and laser heating. Internal source of heating is mainly the collisional process with the $\alpha$ particules. Performing an energetic balance with the sink mechanisms, such as the radiative process or the conductive and convective losses, the Lawson's criterium can be written as [65]:

$$nT_i\tau_E = f(Q) \tag{1.3}$$

where $n$ is the plasma density, $T_i$ is the ion temperature and $\tau_E$ is the confinement time of the energy. This time translates the exponential decay of the energy when all external sources are shut down. The conditions to have a viable fusion machine to produce electricity state:

$$Q \geq 1 \quad \text{or} \quad nT_i\tau_E \geq 2.7 \cdot 10^{21}\ \text{m}^{-3} \cdot \text{keV} \cdot \text{s}^{-1} \tag{1.4}$$

The maximisation of $Q$ can thus be roughly reduced with the maximisation of the plasma density, the temperature and the energy confinement time. Depending of the maximization criteria, different fusion devices had been considered through history. In practice $Q = 1$ is not sustainable from an economic point of view and the goal is actually more $Q \geq 40$ (only 1/3 of the heating power can be transform into electricity, according to Carnot's theorem).

### 1.1.3. Different ways to see fusion: inertial or magnetic fusion

The number of proposed devices since the beginning of the world wilde research (1951) for mastering fusion energy is vast. Considering D-T fusion, the ion temperature is more or less imposed to be $T_i \sim 20$ keV, which in itself constitute an upper limit due to the technical challenge to achieve such a temperature on a large cluster of particles (a particule accelerator can go a lot higher but on a really small number of particles). The two other free parameters are thus the density and the energy confinement time. Increasing both at the same time is not realistic and this constraint gave birth to two different ways to see controlled fusion devices:

- the inertial confinement devices at high density ($n \geq 10^{31}\ \text{m}^{-3}$) but low confinement time ($\tau_E \leq 10^{-11}$ s).
- the magnetic confinement devices at low density ($n \leq 10^{20}\ \text{m}^{-3}$) but high confinement time ($\tau_E \geq 1$ s).

The inertial confinement method uses high power LASER to compress a micro pellet of solid D-T. The research is more military oriented and few devices exist through the world. The most well-known are the NIF (National Ignition Facility) in the USA and the LMJ (Laser MegaJoule) in France.

The magnetic confinement method uses powerful electromagnetic fields to confine low density plasmas. The research is mainly oriented toward civilian applications (electricity production). The most advanced concept is the tokamak and recent developments in computer technology (through Computer Aided Design) have allowed the return of another device called stellarator (Wendelstein-7X being the most recent one, in Germany [28]).

In this thesis, we study the tokamak configuration. A large number of machines exist in the world. DIII-D [92] and NSTX-U [75] are US machines, WEST [14] a french one, TCV [21] is in Switzerland, ASDEX-U [76] in Germany, MAST-U [56] and JET [72] in the UK, EAST [130] in China, K-STAR [89] in Korea, JT-60SA [2] in Japan, etc. Recent developments have resulted in the International Thermonuclear Experimental Reactor (ITER) project, the largest tokamak to date, currently build in France with the conjoint effort of the EU and associates (Switzerland, UK), the USA, China, India, Korea, Russia and Japan.

## 1.2. Tokamak configuration

This section discusses the basic principles of the tokamak configuration. It goes from the basic principle of the machine to the complex geometry of current tokamaks.

### 1.2.1. Basic principles

With a temperature of more than a hundred millions degrees, the containement of the matter in the state of a burning plasma is of immediate concern. A plasma being a charged state of the matter, the use of magnetic fields is the first answer to avoid direct contact with a solid wall. The history of the tokamak was probably born from the observation of the earth natural magnetic field. At the Poles, the magnetic field is stronger and when solar winds strike the Earth, the particles follow the magnetic field lines and bounce at the Poles. A part of the particles can bypass the magnetic field and create the famous aurora borealis. The specific configuration of a weak magnetic field at the center and a stronger one at the ends is the basic principle of the mirror configuration [94], one of the first kind of magnetic devices. To avoid the leak at the extremities (where the magnetic field is stronger), the device can be closed in a torus, which is closed to a tokamak form.

To create a toroidal magnetic toroidal field $\boldsymbol{B}_{\text{tor}}$, toroidal coils are set evenly around the torus (in red on Fig. 1.2). In theory, the charged particles follow the toroidal field

lines (circles) in a helical pattern. The gyration radius of a particles around a field line is called the Larmor radius $\rho_L$:

$$\rho_L = \frac{m_s v_\perp}{q_s B} \tag{1.5}$$

where $m_s$ is the mass of the particle, $q_s$ its charge and $v_\perp$ the cross-field velocity, which is of the order of the thermal velocity $v_{T_s} = \sqrt{T_s/m_s}$. For a deuterium ion $D^+$, at a temperature of around 10keV, in a magnetic field of 3T (Tesla), typical of magnetic confinement machines, the Larmor radius is of the order of $\rho_L \approx 5 \cdot 10^{-3}$m. With the toroidal magnetic field, the particles are thus theoritically confined in the transverse direction, but still free in the parallel one. This freedom is not a problem due to the periodicity of the magnetic field. Nevertheless, a toroidal field creates inhomogeneities between the High Field Side (HFS) and Low Field Side (LFS). By application of the Ampère Law, it can be shown that $B_{\text{tor}} \propto 1/R$, with $R$ the major radius (see Fig. 1.3). The magnetic field is stronger at the HFS, resulting in different kind of drifts for the particles (see Subsection 2.1.1 about the drift ordering). One of the drifts, due to the magnetic gradient, is vertical by nature. It creates a top-bottom polarization of the plasma, as the ions and electrons drift in opposite direction, generating a vertical electric field. This electric field then drives the $E \times B$ drift, directed to the outer side of the tokamak, and main responsible of the loss of confinement. To counter these drifts, a second magnetic field has been added (by russian researchers in the 1950s), the poloidal magnetic field $\boldsymbol{B}_{\text{pol}}$. It is created by a toroidal current generated through the plasma by induction. The induction coil is situated at the center of the torus and called the central solenoid (in yellow on Fig 1.2).

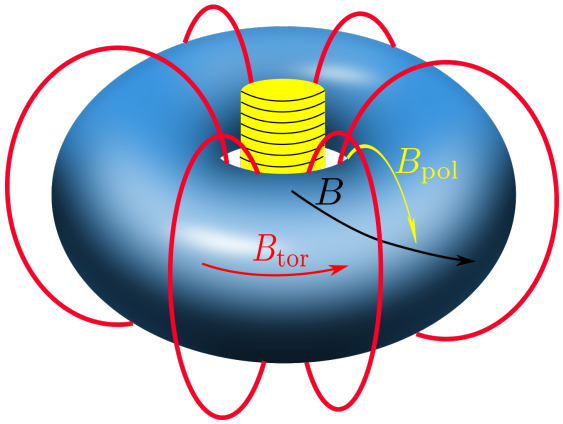


Figure 1.2.: Basic sketch of a tokamak. In red are the poloidal coils that create the toroidal magnetic field $\boldsymbol{B}_{\text{tor}}$. In yellow is the central solenoid that drives (by induction) the plasma current and thus the poloidal magnetic field $\boldsymbol{B}_{\text{pol}}$. The resulting magnetic field $\boldsymbol{B}$ is in black

The resulting magnetic field $\boldsymbol{B} = \boldsymbol{B}_{\text{tor}} + \boldsymbol{B}_{\text{pol}}$ create a helicoidal field with magnetic field lines turning around the torus. The ratio between the two fields is, in most

tokamaks, around 1:10, with the strongest being the toroidal field. The complete magnetic field forms an infinite set of magnetic surfaces from where field lines lie upon (see Fig. 1.3). The internal forces in the plasma are expressed through the plasma pressure $p$ and to maintain the plasma equilibrium, the magnetic field directly opposes this pressure. The basic condition for equilibrium in the MHD approximation writes (see [132, Sec. 3.2]):

$$\boldsymbol{j} \times \boldsymbol{B} = \boldsymbol{\nabla} p \tag{1.6}$$

where $\boldsymbol{j}$ is the current density. We can immediately see ($\boldsymbol{B} \cdot \boldsymbol{\nabla} p = 0$) that magnetic surfaces are also surfaces of constant pressure and that the current lie in the magnetic surfaces. To better study the plasma equilibrium, the poloidal magnetic flux function $\psi$ is introduced, which is a representation of the poloidal flux lying within each magnetic surface and thus a constant for each surface. It is then natural to labelled $\psi$ each flux surface (see Fig. 1.3). $\psi$ can then define a radial coordinate different from the minor radius $r$, as flux surfaces are not necessarily circle nor centered in the torus. In an axisymmetrical equilibrium (independant of the toroidal angle $\varphi$), we have thus $\boldsymbol{B} \cdot \boldsymbol{\nabla} \psi = 0$ and the poloidal magnetic field is directly related to $\psi$, defined as the poloidal flux per radian in $\varphi$.

To characterize the number of poloidal turn per toroidal one of a field line on a toroidal flux surface, we define the rotational transform $\iota$ [13]:

$$\iota = 2\pi \frac{\mathrm{d}\Psi_p}{\mathrm{d}\Psi_t} \tag{1.7}$$

where $\Psi_p$ is the poloidal magnetic flux and $\Psi_t$ the toroidal one. In tokamak, the term safety factor $q = 2\pi/\iota$ is preferred. Rational values of $q = m/n$ play an important role in stability, with $m$ the poloidal mode number (integer) and $n$ the toroidal one (integer). In simple term, $q$ translates the number of toroidal turns $m$ by number of poloidal turns $n$ done by the field lines[2]. A higher value of $q$ is, in general, a condition for a better stability. To calculate the safety factor, one would need to follow a field line, whose equation can be written:

$$\frac{\mathrm{d}l_\theta}{B_{\mathrm{pol}}} = \frac{\mathrm{d}l_\varphi}{B_{\mathrm{tor}}} \tag{1.8}$$

where $\mathrm{d}l_X$ are distance in the toroidal ($X = \varphi$), resp. poloidal ($X = \theta$) direction while moving in the poloidal, resp. toroidal, direction. In an axisymmetrical configuration, $\mathrm{d}l_\varphi \approx R\mathrm{d}\varphi$, then the safety factor can be written as (see [132, Sec. 3.4]) $q = \oint \mathrm{d}l_\varphi/(2\pi)$, which simply is another description of the field line winding. It follows:

$$q(\psi) = \frac{1}{2\pi} \oint \frac{B_{\mathrm{tor}}}{R B_{\mathrm{pol}}} \mathrm{d}l_\theta \tag{1.9}$$

This expression is correct only in axisymmetrical system. A more general expression would necessitate the use of curvilinear coordinates $(\psi, \theta^*, \zeta)$, which is beyond a

[2] Yes, $n$ is the toroidal mode number but symbolizes the number of poloidal turns of the field line

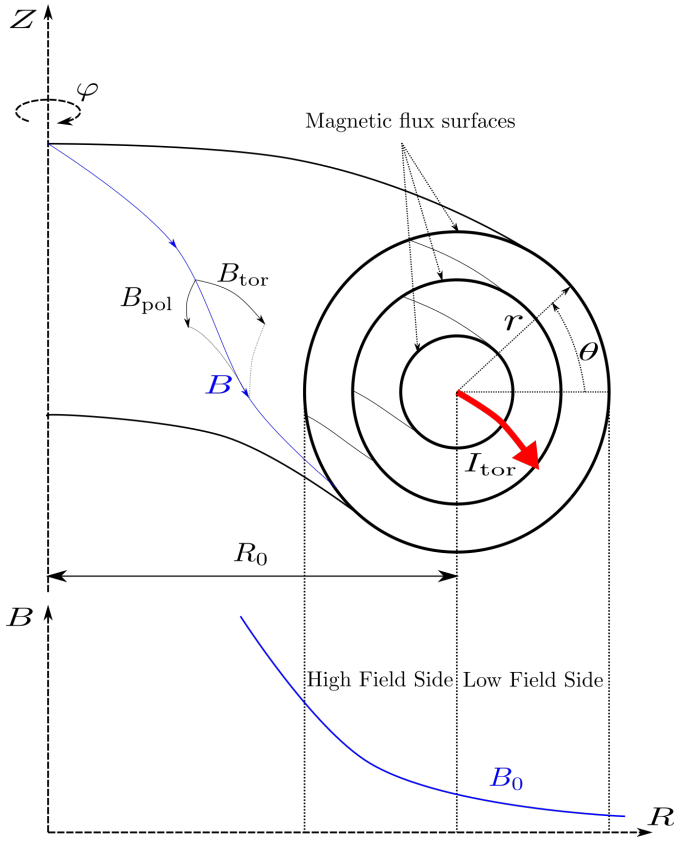


Figure 1.3.: Schematic of flux surfaces in a tokamak. A field line is drawn in blue on the external flux surface. The radial dependency of the magnetic field is plotted highlighing the difference between the inner side (HFS) and the outer side (LFS) (adapted from [47]).

simple introduction and thus are discussed in Chap. 2.

### 1.2.2. Magnetic configuration: from limiter to divertor

The plasma is confined on closed flux surfaces but but the confinement is not perfect (due to various mechanims among which turbulence introduced further) and there is always a point where the plasma encounters the wall. The flux surfaces hitting a wall are called opened and the name Scrape-Off Layer (SOL) is given to this specific region. In contrast, flux surfaces which do not interact with the wall are said closed. The outermost closed flux surface, by definition tangential to the wall of the reactor at one point at least, is refered to as the Last Closed Flux Surface (LCFS). Owing to its shape in divertor geometry (introduced below), it is also often called separatrix. The SOL is where the plasma-wall interactions happen and the study of this specific region of the plasma is generally gathered around the term edge plasma (as opposed to the core region).

On Fig. 1.4, we show two typical configurations for a tokamak. The left one is a limiter configuration on a circular geometry. The plasma encounters a target (often described along the generic term of Plasma Facing Component, PFC) that directly lays on the path of the plasma, before the wall of the machine itself. On the right is a divertor configuration (X-point geometry) where the targets are situated further away from the core, which use a tertiary magnetic field to divert the plasma toward the PFC (target).

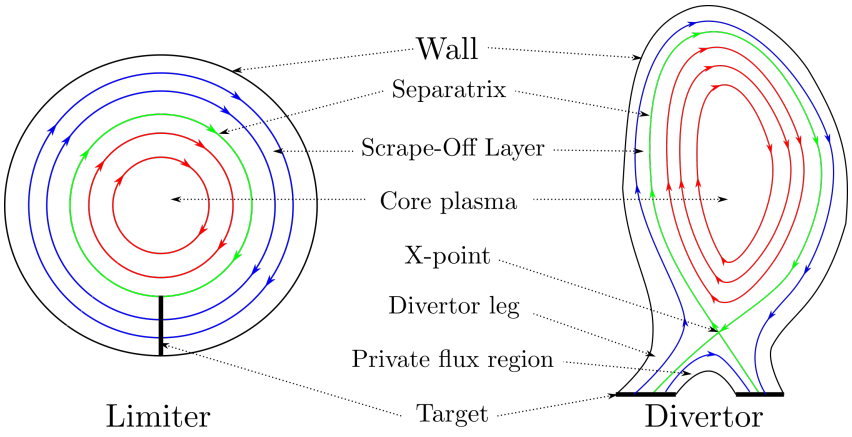


Figure 1.4.: Limiter (left) and divertor (right) configuration. The plain thick black lines are the target, the green line marks the separatrix. The blue lines are the open flux surfaces and the red ones the closed flux surfaces (adapted from [3]).

The targets are often made in extremely thermal resistant material such as tungsten or carbon. The advantage of the limiter configuration is the absence of supplementary coil to create a X-point and the inherently vertically stable configuration, as the plasma just lay uppon the PFC. Its disavantage is the sputtering of particles from the target that pollutes the core and thus considerably hinders the fusion reaction, by radiating, thus cooling the reaction and by diluting the available D-T fuel. It is especially true for tungsten particles whose Z number are largely bigger than deuterium or tritium ions, creating partially ionized heavy impurities, resulting in a lot of cooling by radiation (electrons permanently energize and de-energize themselves).
The divertor configuration is an answer to this problem as well as a way to provide plasma volume to cool the plasma by radiation before arriving at the target. Finally the divertor configuration has shown a capability to access higher mode of confinement, so called H-mode (see [128] for a review of H-mode or Section 1.3.3 for a quick introduction). For these reasons, most present machines and all expected ones (to date) are designed in divertor configuration.

The largest challenge of the edge plasma is on the ideal properties wished for said plasma. Where the core must be as clean and hot as possible, the edge plasma must be as cold as possible, which can be ashieved by a polluted plasma. The temperature

gradient in this region are thus considerable, as well as the number of species that could interact inside this region, rendering the physics quite complex.

## 1.3. Transverse transport in tokamak

A tokamak plasma, and especially the edge of the plasma, is fundamentally in a state outside of thermodynamic equilibrium, due to the temperature gradient between the core and the wall. The tokamak allows for a fast transport process in the parallel direction but in closed field line region (such as the core plasma), the critical part of the transport is the transverse one, responsible of the loss of confinement. In open field line region (the SOL), a complex equilibrium exists between parallel and perpendicular transport, so that both become relevant, and thus critical, to improve the plasma confinement.

### 1.3.1. Classical and neoclassical transport

The first mechanism for tranverse transport process is related to the Coulombian interaction. This random walk can be described by a diffusion coefficient and is called classical transport. The flux of particles is directly proportional to the opposite of the density gradient, translating a transport process directed radially outward:

$$\mathbf{\Gamma}_\perp = -D_\perp \mathbf{\nabla}_\perp n \tag{1.10}$$

With $n$ the density of particles and $\mathbf{\nabla}_\perp$ the gradient perpendicular to the equilibrium magnetic field. This diffusion coefficient $D_\perp$ depends on the collision frequency $\nu_c$, which varies as $nT^{-3/2}$ [19, Sec. 5.6], and the Larmor radius $\rho_L$, which varies as $T^{1/2}$. The coefficient writes:

$$D_\perp = \nu_c \rho_L^2 \tag{1.11}$$

This classical description results in a typical transport coefficient estimated around $10^{-2}$ $\mathrm{m}^2 \cdot \mathrm{s}^{-1}$, several order of magnitude lower than what is observed in experimental tokamaks.

The second description, called neoclassical transport, takes into account the inhomogeneities of the magnetic field in a torus. The estimation of new transport coefficient is higher by one or two order of magnitude but still below the observed transport in experiments. The Fig. 1.5 offers a comparison between the two models, showing that the neoclassical transport takes into account different regimes [59].

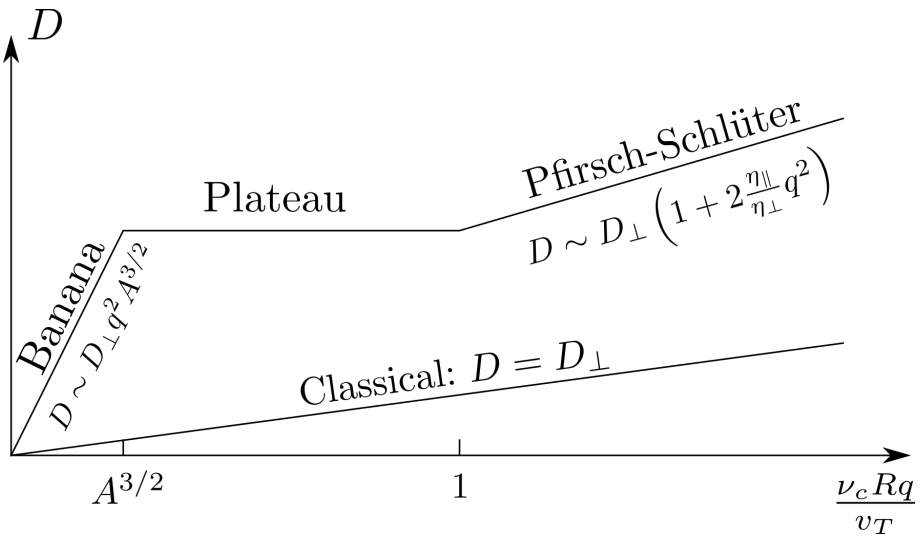


Figure 1.5.: Variation of the diffusion coefficient for the classical and neoclassical theories as a function of the collision frequency $\nu_c$ (adpated from [132, Sec. 4.7]). $A = r/R_0 \ll 1$ is the aspect ratio and $v_T$ is the thermal velocity. $\eta_{\parallel/\perp}$ is the parallel/perpendicular resistivity (see [132, Sec. 2.16] for a definition)

### 1.3.2. Anomalous (turbulent) transport

The collision theory is not enough to explain the larger transport seen in the experiments. This anomalous transport has been proven to be of turbulent nature [71, 133]. This turbulence has been observed experimentally and is the object of 2D [42, 49, 103] and 3D [1, 87, 99, 120] edge plasma simulations to better understand its behaviour (from the most simple turbulent structure to the full edge plasma), resulting in a complex approach to correctly take into account all relevant scales [108]. This anomalous transport in the edge plasma takes the form of intermittent filaments, aligned on the magnetic field lines, sometimes called blobs [134]. This transport is partly due to the electric drift, noted $\boldsymbol{u}_E$, associated to the fluctuations of the electric potential. These fluctuations of the electric potential $\tilde{U}$ coupled with those of the density $\tilde{n}$ can explain the anomalous transport, resulting in a average radial transport experimentally observed to be around 1 $\mathrm{m}^2 \cdot \mathrm{s}^{-1}$. The temporal average of this radial transport writes:

$$\Gamma^r \propto \langle \tilde{n}\tilde{U} \rangle_t \tag{1.12}$$

Where the superscript $r$ denotes the radial (also noted $\psi$ in curvilinear coordinates) direction. This transport results thus from the dephasing between electric potential and density structures, being minimal when these structures are in phase, maximal when in quadrature. In the electrostatic turbulence studied in this thesis, two types of micro-instabilities, at the origin of the turbulence, are considered [79, 80, 107]:

- the drift-waves mechanism (see Fig. 1.6): this instability appears with the in-

teraction between a homogenous magnetic field and a density gradient. In the poloidal direction, electron density and electric potential fluctuations appear. The apparition of an electric field leads to the existence of a radial $\boldsymbol{E} \times \boldsymbol{B}$ drift. If the electrons are considered adiabatic, any potential fluctuation will be in phase with the electon density one. It results in a poloidal phase velocity without radial transport. As the resistivity $\eta_{\parallel}$ in a plasma is not zero, the electrons are not adiabatic and, consequently, a phase shift exists between the two fluctuations, leading to the growth of the drift wave instability, the so-called resitive drift wave.

- the interchange mechanism (see Fig. 1.7): the edge instability appears due to the interaction between a magnetic field, its gradient and the pressure gradient. Starting with a density (or pressure) fluctuation (on the scheme, it could be drawn in-between each equipotential, with a positive fluctuation where the arrows are larger and a negative one where they are thinner), the $\nabla B$-drift polarizes the fluctuation (vertical arrows, separating electrons and ions), creating a vertical electric field (black thin arrows). This electrical field generates an $\boldsymbol{E} \times \boldsymbol{B}$-drift. If the density/pressure and magnetic field gradients are in the same direction, the $\boldsymbol{E} \times \boldsymbol{B}$-drift goes toward the outer side. It thus amplifies the initial fluctuation at the LFS, resulting in a ballooning structure there.

The numerical modeling of the anomalous transport requires the resolution of all spatial and temporal scales of the turbulence that vary over several orders. That leads to costly 3D fluid simulations with codes called turbulence codes [104, 108, 119]. These accurate but costly models target predictive capabilities for the behaviour of future devices. For engineering purpose, with short restitution times and large parameter ranges variations, 3D [45], or even 2D [18], reduced models are preferred, filtering high-frequencies fluctuations by averaging. In this case, the so-called transport (or mean-field) codes do not resolve explicitly the small spatial scales and high-frequencies time oscillations which are modeled through a diffusive transport transverse to the magnetic field-lines using a gradient-like diffusion assumption. Perpendicular diffusion coefficients are thus free parameters in the model, that need manual tuning to reproduce some experiments. To better understand the complex physics of anomalous transport, a turbulent approach must be used. It is for example mandatory to adress topics such as the transition transition between L to H-mode (see following section), correctly analyze the asymmetry of the turbulent transport in the poloidal plane (between the inner and outer midplane) or simply to evaluate transport coefficients and their evolution with plasma parameters/geometry and reach predictive capabilities for the behaviour of future devices.

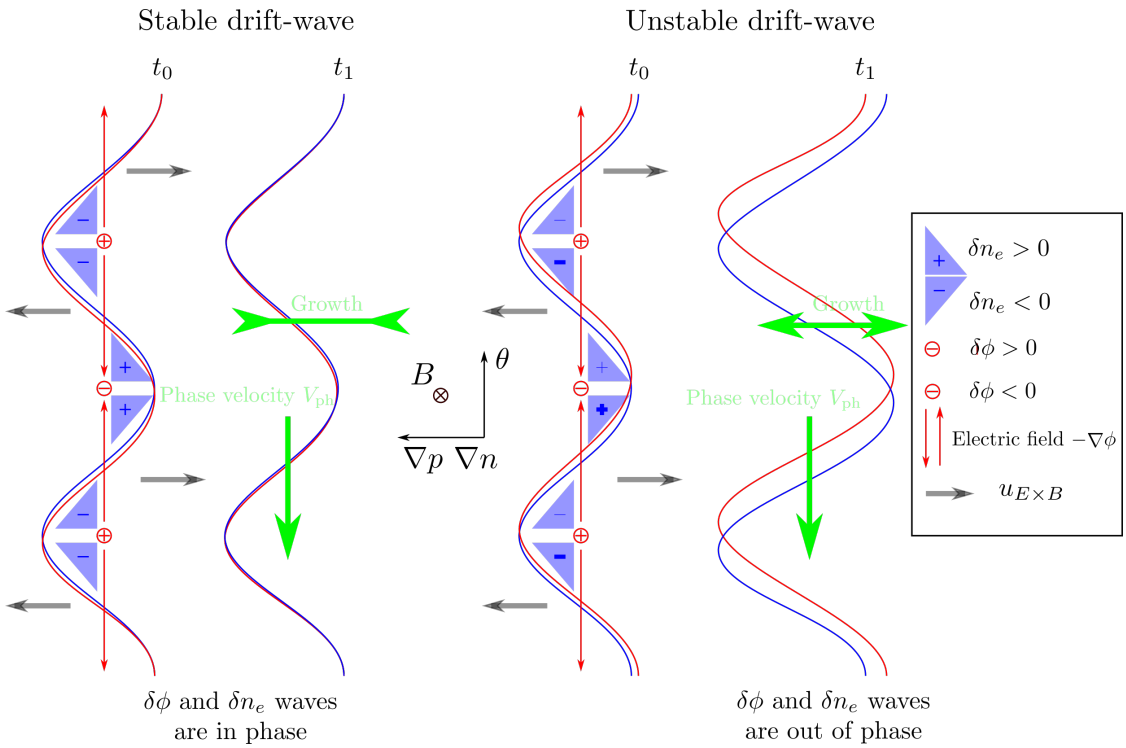


Figure 1.6.: Scheme of the drift wave instability (adpated from [82]).

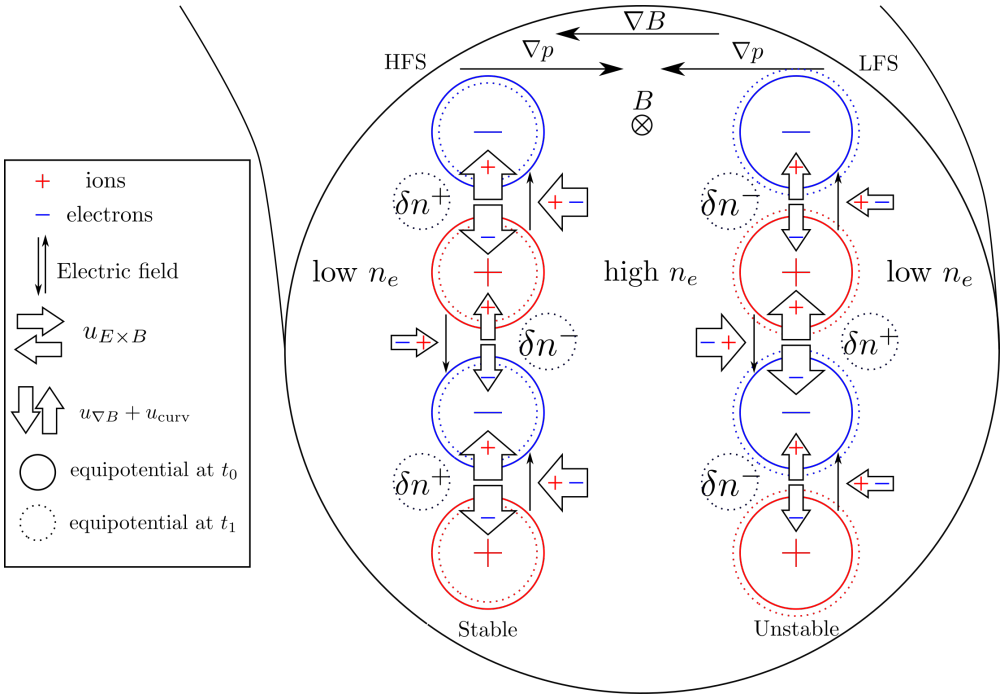


Figure 1.7.: Scheme of the interchange instability (adpated from [82]).

### 1.3.3. Transport barriers, H-mode and Edge Localized Modes

In the last sections, we have spoken about advanced confinement modes. We have seen that turbulence is responsible of the cross-field transport. When fully developped, it sets the so called L-mode, with low confinement time. In 1982, in ASDEX, a divertor tokamak, a high confinement mode (H-mode) was discovered [129]. The H-mode can be described as a sharp increase of the pressure gradient at the edge plasma. It is generated by a transport barrier and this pressure increase is usually called a pedestal, due to the fact that it globally increases the pressure in the whole plasma (allowing an increase of the density and the temperature in the core). See Fig. 1.8 for a typical pressure profile as a function of the radius between L and H-mode regime. The transport barrier appears near the separatrix in the closed field lines region and, if the mechanism is not totally understood, several observations point out the role poloidal shear flows, driven by various effects such as neoclassical effects [20], magnetic shear [43] or particles orbit losses [111] resulting in the creation of this barrier [128]. It allows a reduction of the turbulence and thus of the transverse transport, increasing the confinement time $\tau_E$.

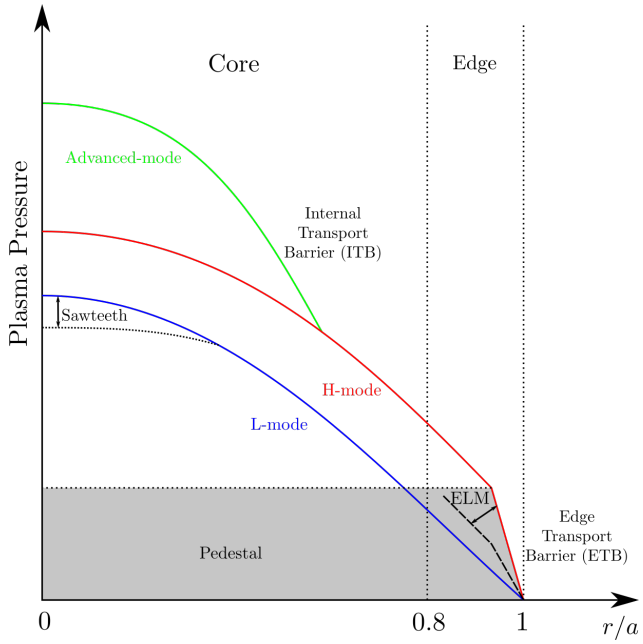


Figure 1.8.: Typical pressure profiles as a function of the radius for different confinement regimes (adapted from [83]). The effect of main MHD instabilities, especially ELMs, in terms of fluctuation on the profile is also indicated.

If the improvement of the plasma confinement in H-mode is desirable, a drawback is its quasi-systematic association with the existence of Edge Localized Modes (ELMs) [57]. The ELMs are edge MHD instabilities in the form of sudden bursts of energy at the frequency of 10 to 1000 Hz. It is a relaxation mechanism that brutally

releases the acumulated energy, resulting to an increase of the particles and heat fluxes [69] on the targets, up to ten times the amount during a quiescent H-mode (without ELMs). It can potentially critically damage the machine, even if ELMs can also provide density control and limit plasma core impurities. Recent researches are thus two-fold on the topic of H-mode:

- understanding the L-H transition and mechanisms behind the formation of the transport barrier.
- understanding and controlling the resulting ELMs in H-mode operating regimes.

The L-H transition has already been approached through the identification of scalling law from existing experiments, resulting in the scaling used to guide the design of ITER (the International Thermonuclear Experimental Reactor, presently built in France with the collaboration of the EU, USA, Russia, China, India, Japan and Korea) [74]. To understand the mechanism behind the formation of the barrier, a study of turbulence itself is nevertheless still a present topic in research.
The understanding and control of the ELM has been the object of several experiments and numerical simulations. It is the subject of the next subsection.

## 1.4. Plasma-wall interaction

The open magnetic field lines and the tokamak wall lead to different physical properties for the plasma at the edge than in the core [112]. In particular, in the SOL due to plasma wall interactions at the targets conceived to sustain the high amount of energy flowing from the core but also at any other Plasma Facing Component (PFC) such as antennas.

### 1.4.1. The role of the SOL in the plasma particles, momentum and energy balances

The particles coming in the SOL encounter a wall (limiter or divertor) which can result in several phenomena:

- The recycling: charged particles strike the wall and are immediately neutralized by recombination. They are thus not influenced by the magnetic field and move freely. A large proportion of them get reflected back towards the plasma where they get re-ionized.
- the retention: the particles react with the wall and stay there. This can erode the wall when the particles combine with the wall, resulting in chemical erosion.

With these two processes, the SOL acts as a sink for plasma particles, energy and momentum. During the recycling, most particules are re-ionized, which contributes

to the loss of energy in the edge plasma. The SOL, even with re-ionization, still acts as a particles sink, as there is still more particles going out than in. However, by fixing the particles loss, the recycling (and so, in most tokamaks the SOL) becomes the major source of particles for the plasma.

### 1.4.2. The SOL width, a key parameter for the SOL equilibrium

In the simplest picture, we have seen that particles come in the SOL, strike the wall and recombine into neutral atoms. The wall hence appears as a perfect particles sink for the plasma. We will see in Sec. 2.1.2 that the related physics imposes very specific boundary conditions for the edge plasma. One of the key consequences is that particles flow towards the wall at a velocity equal to the accoustic velocity of the plasma, $c_s = \sqrt{k_B(\gamma_e T_e + \gamma_i T_i)/m_i}$, with $\gamma_s$ the polytropic indexes. For a simple isothermal model $\gamma_e = \gamma_i = 1$, which we consider there. This way, the particles balance of open flux surfaces can be represented by a simple radial transport equation:

$$\frac{\partial}{\partial r}\Gamma_r \approx -\frac{nc_s}{L_c} \tag{1.13}$$

where $r$ is the perpendicular (radial) direction, $\Gamma_r = nv_r$ is the radial flux going into the SOL and $nc_s/L_c$ translates the parallel flux going into the target. $L_c$ is the length of the field lines between the two targets. We can now assume a diffusive radial transport so that:

$$\Gamma_r = -D_\perp \frac{\partial n}{\partial r} \tag{1.14}$$

which evolves to solve a second order partial differential equation, with $n$ as an unknown, resulting in:

$$n = n_0 \exp\left(-\frac{r - r_0}{\lambda_n}\right) \tag{1.15}$$

with $\lambda_n$ the density decay length or density SOL width. For the diffusive hypothesis, it writes $\lambda_n^{\text{diff}} = \sqrt{D_\perp L_c/c_s}$. It translates a typical length of loss of particles according to a vanishing exponential. In experiments, the profiles are rarely perfectly exponential due to various effects, including the fact that a diffusive description of anomalous transport with constant and homogeneous transport coefficients is an oversimplication compared with the dynamics at play. Nevertheless, the ideal picture presented here gives a reference frame of interpretation for plasma profiles in the SOL.

### 1.4.3. The issue of power-exhaust

The deposit of particles on the target is not so much a problem as the energy they carry. The reasoning done with the density decay width can be reproduce for the heat flux too. To sustain the integrity of the target, a sufficient spreading of the heat flux is necessary. The width of this spreading is noted $\lambda_q$.

To illustrate the issue of power-exhaust, we take the example of ITER. 500 MW of power is produced through the fusion process, while 50 MW come from heating sources. According to the D-T fusion, 4/5 of the fusion power are taken away by the neutrons, that are not subjected to the magnetic field. Around 50 MW are dispersed by bremstrahlung and impurity radiation. It lets 100 MW going directly into the SOL through convective and diffusive processes, noted $P_{\mathrm{SOL}}$. Similarly to the particles profile, energy balance imposes that the peak heat flux $q_{\mathrm{peak}}$ is inversely proportional to the wetted surface of contact $S_{\mathrm{wet}}$ of received power:

$$q_{\mathrm{peak}} \propto \frac{P_{\mathrm{SOL}}}{S_{\mathrm{wet}}} \tag{1.16}$$

where $S_{\mathrm{wet}} = 2\pi R_0 \lambda_q / \alpha_{\mathrm{geo}}$, with $\alpha_{\mathrm{geo}}$ a geometrical factor related to the magnetic flux expansion between the mid-plane and the targets. Taking the ITER major radius $R_0 = 6\mathrm{m}$ and $\lambda_q = 1\mathrm{mm}$ according to the reference scaling law in [34], then with $\alpha_{\mathrm{geo}} = 0.1$, we obtain $q_{\mathrm{peak}} \approx 265\mathrm{MW}\cdot\mathrm{m}^{-2}$. This is above the engineering limit of $10\mathrm{MW}\cdot\mathrm{m}^{-2}$. To spread the heat flux as much as possible, $\lambda_q$ needs to be as big as possible (the other variables being fixed by the machine itself). Past studies have demonstrated that the heat decay length is sensitive to various parameters, e.g. the poloidal position of the plasma-wall contact point, which a simple 1D model cannot capture [23]. In any case, the orders of magnitude given above, demonstrate the need for a strategy to mitigate heat fluxes coming out of the plasma before they reach the targets. The currently foreseen solution relies on a specific aspect of edge plasma physics, namely detachment, introduced in the next section.

### 1.4.4. The necessity for detachement regime

Current technological limits make it mandatory to keep steady state heat fluxes to solid surfaces below $10\mathrm{MW.m}^{-2}$. In ITER burning plasmas, this limit will be largely exceeded in the absence of specific measures to reduce these fluxes before they impact the wall. The use of Tungsten as armour material in the divertor (for various reasons exposed in [33]) also imposes another limit on the energy of ions impacting the wall which should stay below 10eV to avoid physical sputtering. The foreseen strategy to cope with such conditions was the main drive for the design of the ITER divertor. It relies on 2 key physical phenomena:

1. the interaction between the plasma and neutral particles naturally present in the volume of the divertor due to particle recycling: a significant part of the energy required to re-ionize neutral particles is dissipated under the form of photon radiation which isotropically redistribute the associated energy flux on a large surface of the wall. Moreover, particle recycling strongly increases the density in the divertor region (it can, in some regimes, locally go up to a factor of 10 to 100 higher than the mid-plane values), hence decreasing the amount of energy carried by each particle. It is possible to control the weight of these dissipation

mechanisms simply by controlling the density level of the plasma.

2. the interaction between the plasma and impurities: the plasma-wall interaction in the divertor produces various types of impurities due to chemical or physical sputtering mechanisms. Due to their high Z number, these impurities do not get entirely ionized in the edge plasma and radiate a large amount of energy. Additional impurities (usually noble gases to avoid any spurious chemical interaction with the rest of the plasma/wall components) can also be injected voluntarily, thus giving an additional control knob on the dynamics of the divertor.

Combining neutral recycling (through density control) and impurity seeding, it is possible to reach a point where most of the power incoming in the divertor is converted into radiation before reaching the target and the plasma temperature drops below the 10eV range at the targets. If the plasma temperature goes low enough, the plasma can even partly recombine into neutrals in front of the target. One ends up with a plasma separated from the wall by a "cushion" of neutral particles, refered to as a detached plasma. This regime has been demonstrated in experiments in current meidum sized machines[68]. Reaching and controlling this regime in ITER will be mandatory for high power pulses.

The understanding of the interaction of the plasma with impurities and neutral particles is thus a central aspect of edge plasma modelling in sight of ITER and reactors beyond. On the modeling side, including such physics in codes requires a significant complexification of models because neutral particles need specific kinetic treatment in foreseen plasma conditions and due to the large number of atomic and mollecular reactions between ionized and neutral species that need to be taken into account. This explains why, up-to-date, such modeling has been carried out only in mean-field plasma codes. The inclusions of such physics in turbulence codes is one of the on-going challenges of edge plasma modeling for tokamaks. The topic becomes all the more complex when considering 3D perturbed fields as the plasma dynamics is dependent on the 3D field structure while the neutrals dynamics is insensitive to it

## 1.5. 3D magnetic perturbations

We have considered the tokamak to have a toroidally axisymmetrical magnetic field. Actually, this is not the case. First, by conception, magnetic perturbations exist in the toroidal direction such as, for example, magnetic error field, caused by unavoidable failings in the design or alignment of the coils, or the ripple. The ripple is a magnetic perturbation due to the discretization of the main poloidal coils generating the toroidal field. The field is stronger at the level of the coils than in between two coils. This effect is starker at the LFS. The transport process created by ripple is considered mainly diffusive and neglectable in present machines [24, 109, 115]. At the end of this thesis, a few mean-field simulations with ripple with the SOLEDGE3X-HDG code are done, but the main study of this thesis concerns another kind of magnetic perturbations,

one voluntarily added for controlled purpose: the Resonant Magnetic Perturbation (RMP). The main goal of the RMPs is the suppression or mitigation of the ELMs and is the subject of the following section. A review on the different kind of 3D magnetic perturbations, with a focus on RMPs can be found in [38].

### 1.5.1. ELM control methods

ITER has been designed to run in H-mode. It will achieve its target of a $Q = 10$ amplification factor only if a stable H-mode regime can be sustained. Due to the energy contained in an ITER plasma, the ELMs resulting during the relaxation process are predicted [35] to deposit an amount of energy beyond the sustainability of current engineering capabilities [33, 110]. It becomes thus necessary to mitigate the ELMs in ITER. An active control method has been chosen, considering that, if the Edge Transport Barrier (ETB) is the origin of the ELMs, it could be possible to degrade the ETB enough to mitigate or suppress the ELMs but still preserving the H-mode to achieve a good confinement. Several approaches have been considered [7], among which are vertical kicks [25] (shacking the plasma to artificially increase the ELMs frequency and reduce their amplitudes), pellet pacing (injecting pellet near the pedestal at high frequency to trigger artificial ELMs of lower amplitudes) and external magnetic perturbations (often called resonant magnetic perturbations, RMPs, created by several sets of additional coils around the tokamak).

The RMPs increase the radial transport by degrading the ETB and will be deployed on ITER to control the ELMs [64, 125]. RMPs tear nested flux surfaces, creating magnetic islands (see Fig 1.9 and Refs. [127, 132]). A magnetic island creates a short-cut for the radial transport across the island width, due to the parallel transport being allowed to transit in the perpendicular direction. The island offers almost no resistance to the radial transport, which is usually avoided in the core plasma but can serve an important purpose for ELM suppression. Experimental evidences show the success of RMPs to suppress ELMs during H-mode operations [39, 63], sustained by numerical modeling [85, 88].

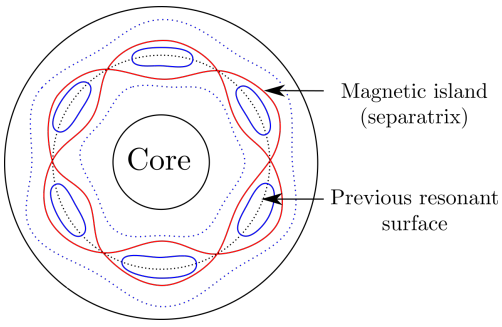


Figure 1.9.: Shematic poloidal slice of a circular plasma with a resonant flux surface forming magnetic islands (adapted from [83])

The magnetic perturbations (MPs) are decomposed into poloidal $m$ and toroidal $n$ mode numbers and the islands are formed on flux surfaces of rational security factor $q = m/n$. For example, a magnetic perturbation with a mode $(m = 6, n = 2)$ creates a chain of 6 islands on the flux surface $q = 6/2 = 3$. If the amplitude of the perturbation increases, or the perturbation is composed of several dominant modes, the islands may overlap with higher order ones and even create a chaotic zone, called stochastic region, where the flux surfaces are completly broken and no island is visible. These changes in the magnetic manifold can have, at least, two influences on the plasma transport:

- A perturbation of the perpendicular transport, from the mean-field one to the turbulent one, in the edge plasma.
- A perturbation of the detachment due to the additional non-aisymmetrical component on the magnetic field, which should impact the plasma but not neutrals.

At the current time, no numerical code is able to take into account the two effect in a coupled and self-consistent way. The second point is thus specifically looked at thanks to the EMC3-EIRENE 3D mean-field transport code [46]. The first point is the object of this thesis and could have an impact on the work done in the second point.

In the following sections, we make a quick state of the Art review, focusing first on the experimental observations before then discussing about the modelisation effort on the topic of RMP-like magnetic perturbations.

### 1.5.2. Experimental evidences of turbulent transport modifications with RMP

A large number of experiments with RMP deals with the ELM control in H-mode. It has been shown that RMP can effectively mitigate or suppress the ELM on several tokamaks (see Review [38]) such as DIII-D [36], JET [70], ASDEX [116], KSTAR [61], etc. These studies have been coupled with numerical simulations [6, 84], ranging from the study of the ELMs themselves [88] to the screening of RMP by the plasma [5]. On a side note, to the present date, no numerical code ever manages to create a self-consistent H-mode and subsequently ELMs, although the modeling of a single ELM crash has been done with edge MHD codes such as JOREK [88], BOUT++ [30] and NIMROD [16] or simplified ELMs with gyrofluid code [62]

Concerning the particles transport, the universally observed effect of RMP is the density pump-out, which translates as a loss of particles at the edge plasma, whereas the ion temperature profile increases [37] but a decrease of the electronic pressure [105]. The pump-out suggests the existence of $\boldsymbol{E} \times \boldsymbol{B}$ convective transport mechanism, that seems linked to the dominant island chain. It has been noted that the toroidal velocity

is highly impacted by the RMP [77, 118], suggesting the importance of a self-consistent radial electric field in futur simulations. Finally, concerning the heat flux, it has been shown on MAST [124] and DIII-D [81] that the RMPs split the heat flux pattern on the target. All those observations have been done in both H-mode and L-mode regimes.

The study of turbulence itself with RMPs is rare due to the difficulties of measuring turbulence itself. The impacts seen in experiments are mainly on the density fluctuations (standart deviation). For L-mode studies, on MAST [118], the fluctuations increase before the separatrix but decrease in the SOL. On DIII-D [77], the density fluctuations does not increase and the changes are attributed to a transition from ion temperature gradient to trapped electron mode regime in the edge plasma. We should nevertheless note that no measurement has been done in the SOL in this study. A comparison has been made between MAST L-mode and DIII-D H-mode in [78], stating that density fluctuations increase in the plasma edge in L-mode, suggesting a role of turbulence in the density pump-out, but they decrease in H-mode, suggesting a different mechanism for the increased particles transport in H-mode.

Overall there is strong evidence that RMPs perturbate the equilibrium and turbulence properties in the edge plasma. Nevertheless, the experimental database for turbulence is particularly sparse due to the difficulty to measure edge turbulence properties. The support from numerical simulations then becomes a precious tool to progress in the understanding of physical mechanisms at play.

### 1.5.3. Numerical studies of 3D magnetic perturbations: from mean-field to turbulent simulations

To study RMP effect on transport, mean-field codes have been used recently such as EMC3-EIRENE [44]. It allows to compute realistic 3D geometries (such as NSTX, DIII-D, ITER) and with the use of ad-hoc transport coefficients, better understand the impact of RMP on the transport. In [45], a study is done on an NSTX-U configuration. The splitting feature of the heat flux, observed in experiments as seen in the section above, is recovered when the RMP is activated. The interesting part is the observation that the splitting occurs only at the outer target (LFS) and not at the inner one (HFS). It underlines the importance of having a 3D codes to simulate the behaviour of plasma subjected to non-axisymmetric magnetic perturbations.

However, the mean-field approach used in EMC3 imposes to make assumptions concerning the nature and the amplitude of transverse transport, as well as concerning the impact of RMPs on these. In the absence of better information, the strategy applied is to assume that transport (collisional and anomalous) can be described by homogeneous diffusion coefficients which do not change when applying RMPs. In other words, when considering input parameters to such simulations, RMPs are assumed to impact solely the magnetic equilibrium. This assumption can be questionned based

on the experimental evidence given above showing an impact of RMPs on turbulence properties. Addressing this question requires the use of turbulent codes able to deal with the 3D aspect of RMPs. The first kind of approach was done during the years of ergodic divertor studies [102]. Instead of having magnetic island chains like for RMP, the magnetic perturbations creates stochastic field lines. This researches have an interest for the turbulent aspect of the transport as, sometimes, part of the RMPs can create small stochastic zones. An interesting study can be found in [8, 9]. These early 3D electrostatic resistive ballooning turbulent simulations manage to recover key feature, such as the decrease of pressure fluctuations due to the suppression of large scale structures. A suppression of the sheared poloidal flow, associated to zonal flows, is also noted, which is confirmed in [67], where RMPs decrease the energy of zonal flows. The decrease of pressure fluctuations can be directly linked to a decrease of density fluctuations, observed in experiments. An increase of the $\boldsymbol{E} \times \boldsymbol{B}$ fluctuations has been noted, leading to an increase of the turbulent heat diffusivity. Some features are not observed due to the lack of a self-consistent radial electric field, not implemented in the model. The following studies have been on barrier relaxations through RMPs [10, 66] and thus more on the topic of ELMs control simulation, showing the RMPs ability to stabilize barrier relaxations in single mode whereas multiple harmonics result in an energy degradation. It is shown that the conductive (turbulent) part of the energy flux in the radial direction is the main component when RMP are applied.

A gyrofluid model was used in [95, 97], with RMP. In that case the amplitude of the magnetic perturbations has been tuned to have either magnetic islands or to be strong enough to create a stochastic zone. Reiser notes a reduction of the local amplitude of density fluctuations with a destruction of blob (filament) structures in the SOL, attributed to a reduction of the turbulent part of the $\boldsymbol{E} \times \boldsymbol{B}$ transport. An early study in [96] with the same code states of the influence of collisionality, density and velocity fluctuations being higher at low collisionality, whereas only velocity fluctuations increase at higher one. A more recent study using the same code [91], in a non-isothermal version, shows magnetic islands in the simulation domain and manages to reproduce a density pump-out but a decrease of the temperature profiles too (wich is contradictory to some experiments discussed before). The study underlines the dominant static influence of the RMP (and the islands), compensating the loss of the temporally fluctuating part for the density fluctuations.

To date, few in-depth study of the impact of RMP and islands on edge plasma turbulence in a full 3D framework have been done.

## 1.6. Context and objectives of the thesis

Studying 3D edge plasma dynamic is a necessary part for understanding and predict the plasma-wall interactions in fusion machines. 2D mean-field codes use a toroidal axisymmetrical hypothesis and 2D turbulent codes use the so-called flute assumption

by averaging the parallel dynamic and focusing mainly on perpendicular dynamics. The last assumption is based on the peculiar dynamic of tokamak plasma, where the parallel one is much faster than the perpendicular one. Without even considering the limit of 2D codes for 3D magnetic perturbations, one can argue this approach by considering typical time scale of both directions. Let us note the perpendicular velocity $v_\perp \sim 10^2$ m$\cdot$s$^{-1}$ and a typical perpendicular length scale, the SOL width $\lambda_N \sim 10^{-2}$ m, then the typical perpendicular time scale would be $\tau_\perp \sim 10^{-4}$ s. The same reasoning in the parallel direction gives $\tau_\parallel \sim L_\parallel / c_s \sim 10/10^5 \sim 10^{-4}$ s. The order can be thus quite near for both directions, justifying the interest to 3D codes.

This thesis focuses on the impact of 3D magnetic perturbations on transport and turbulence at the plasma edge of a circular tokamak with a limiter.

### 1.6.1. Mean-field versus turbulent modeling

Mean-field codes often play a key role in the design of new machines due to their capability to solve extremely realistic geometries such as ITER. The equation models allow for a fast computational solution, even in 3D geometries. Their main weakness is actually their predictive abilities due to the lack of self-consistent turbulence, and thus self-consistent perpendicular transport, which is often approximated by diffusive terms.

The turbulent codes are, on the contrary, self-consitent in the perpendicular transport, but at an important computational cost. The following sections discuss on the use of one mean-field code and one turbulent code for this thesis.

### 1.6.2. Turbulent modeling of RMPs: the choice of TOKAM3X

Turbulent codes able to study the edge (with SOL) plasma, with realistic geometry, are numerous with for example BOUT++ [31, 32], GBS [90, 100], GRILLIX [113, 114] and TOKAM3X [121, 122]. In this thesis, we use TOKAM3X. The code is field aligned on the magnetic grid and handles divertor configurations. An isothermal [48] and a non-isothermal [4] versions exist as well as a coupling with EIRENE, a neutral kinetic code used to handle self-consistent recycling in TOKAM3X.

The state-of-the-art turbulence code TOKAM3X based on a drift-reduced Braginskii's fluid model is thus used. Both isothermal (see Chap. 3) and non isothermal plasmas are considered (see Chap. 4). During this thesis, we have implemented small 3D magnetic perturbations in TOKAM3X, which until now required a toroidally axisymmetric magnetic equilibrium. We focus essentially on single mode magnetic perturbation as a first step towards higher complexity. A careful analysis of the behaviour of the fluxes, especially the $E \times B$ ones is done, as well as the observation of the mean-fields such as the radial profile of the density, the temperatures, the pressure or the electric potential (and thus the radial electric field). This is to draw a coherent

and self-consistent picture of the edge plasma when MPs are switch on. The turbulent behaviour through the standart deviation, the skewness and the probability density functions is studied as well as the effect of MPs on the turbulent structures themselves through the correlation length.

#### 1.6.2.1. Mean-field modeling of RMPs: TOKAM3X (mean-field) and SOLEDGE3X-HDG

Concerning transport codes, one of the most recent and advanced code for edge plasma modeling with fluid approach is EMC3-EIRENE. Benchmark with SOLPS [12], a 2D transport code, EMC3 [44]is a fieldline aligned 3D grid transport code, with purely classical parallel transport and coupled with the EIRENE [98] code, a kinetic code for the physics of impurities. In this thesis, we use a newcomer, SOLEDGE3X-HDG [52–54], benchmarked with the 2D code SOLEDGE2D [17, 18] (a similar code to SOLPS). SOLEDGE3X-HDG is a 2D-3D transport code using a non-aligned grid approach with a hybrid Discontinuous Galerkin method. This code is especially interesting for solving edge plasma in complex and realistic geometries.

After the study of turbulent transport with single mode MP in turbulent models of increasing complexity, we switch first toward mean-field isothermal simulations with TOKAM3X. We indeed compare the behaviour of turbulent isothermal and mean-field isothermal TOKAM3X simulations in Chap. 5. Then we analyse the behaviour of the plasma from single mode MPs and to more complex and realistic RMPs. In the following part of this last chapter, we add the realistic MP model to the SOLEDGE3X-HDG code, a 2D-3D transport code, based on Braginskii's fluid model and able to run on realistic geometries through a Hybrid Discontinuous Galerkin non field aligned scheme. We thus test for the first time the 3D capability of SOLEDGE3X-HDG with the isothermal model during this thesis. The realistic RMP approach allows us to show an historical case of the ripple perturbation on a WEST geometry.

# 2. 3D fluid codes for edge plasma simulations

## Table of Content

This chapter describes the physical, mathematical and numerical models implemented in the two codes used in this thesis to study 3D magnetic effects.

TOKAM3X [122] is a state-of-the-art 3D turbulence code developped by the team for more than 10 years. The code solves the 3D drift-reduced Braginskii fluid equations at the edge of the plasma, in a region encompassing close and open magnetic field lines and till now for a magnetic equilibrium assumed to be toroidally invariant. Note that at the time of writting this thesis, TOKAM3X is merging with the SOLEDGE2D mean-field code [18] into SOLEDGE3X that includes self-consistently turbulence and/or mean-field models, neutrals physics, impurities, with realistic magnetic and wall geometries.

SOLEDG3X-HDG[54] is the most recent release of SOLEDGE3X. It solves 2D-3D mean flow fluid equations (transport code) on unstructured meshes using a hybrid discontinuous Galerkin method. Such an approach allowing meshes non aligned on the magnetic geometry, is original in the magnetic fusion community. This allows us to address simulations for tokamak walls and magnetic equilibria of any complexity, these latter being able to be unsteady without requiring any remeshing.

The physical, mathematical and numerical models are introduced in the following for each code.

## 2.1. The drift-fluid model of the plasma edge

We introduce the physical concepts of interest to derive the models treated by the two codes TOKAM3X and SOLEDG3X-HDG.

### 2.1.1. The fluid model

To understand the movement of ordinary matter, the simplest way is to apply the fundamental principle of dynamics for each particles. In the field of magnetica fusion plasm, the particles are charged and submitted to electromagnetic fields. Other forces, such as gravity, can be shown to be negligible. This is called the particule description. For a particle $j$ of mass $m_j$, of charge $q_j$, the equation of motion writes:

$$m_j \mathrm{d}_t \boldsymbol{v}_j = q_j(\boldsymbol{E} + \boldsymbol{v}_j \times \boldsymbol{B}) \tag{2.1}$$

where $\boldsymbol{E}$ and $\boldsymbol{B}$ are the electric and magnetic fields, and $\boldsymbol{v}$ the particle velocity. In this description, the electromagnetic field is described by the Maxwell equations in a local way that merges the global electromagnetic fields from the tokamak coils and the local electromagnetic fields due to the interaction between the other particles. Assuming $N_j$ particles, with $6+1$ degrees of freedom (3 in position and 3 in velocity, in a phase space, 1 in time), the number of unknowns at each time is is $6N_j$. With a density

of $10^{20}$ particles per cubic meter[1] in a burning plasma of tokamak, the calculation is a computationally futile attempt at the present time. Thus, a reduced system is a necessity felt for practically achievable calculations.

#### 2.1.1.1. From kinetic to fluid approach

Rather than from a particule point of view, the plasma can then be described using distribution functions $f_s(t, \boldsymbol{x}, \boldsymbol{v})$, where $t$ is the time, $\boldsymbol{x}$ the position and $\boldsymbol{v}$ the velocity. The distribution function represents the probability density to find a particle in an elementary volume $\mathrm{d}^3\boldsymbol{x}\mathrm{d}^3\boldsymbol{v}$ around the considered position $(\boldsymbol{x}, \boldsymbol{v})$ The mathematical background to go from a particular to a kinetic description is provided in the work of Kilmontovitch, Vlasov and Boltzmann (list not exhaustive). A quick overview can be found in [82, Chap. 2] (see also Appendix A.1). The time and space evolution of the distribution function is described by the Boltzman equation:

$$\partial_t f_s + \boldsymbol{v}\cdot\boldsymbol{\nabla}_{\boldsymbol{x}} f_s + \boldsymbol{a}\cdot\boldsymbol{\nabla}_{\boldsymbol{v}} f_s = C_s \tag{2.2}$$

where $C_s$ is a collision operator due to intra and inter-species collisions ($C_s = 0$ in the Vlasov equation). Note that the subscript $s$ stands for species not on a particular level anymore but on a statistical one. $\boldsymbol{a}$ is the acceleration and can be developped into: $\boldsymbol{a} = \dfrac{q_s}{m_s}(\boldsymbol{E} + \boldsymbol{v}\times\boldsymbol{B})$.

The last few years of research have seen the development of full 6D (or more often 5D) (gyro)-kinetic codes. This allows for a fine description (within some limits related to the approximation made in the gyro-average) of plasma turbulence but with the trade-off of the need of enormous computational times and memory storage. The GYSELA code [55] is one example of a 5D gyrokinetic code.

To futher reduce the computational cost (at the price of a simpler description), the fluid approach consists in averaging the distribution function in the velocity space $\Omega$. A number of moments are thus obtained and the first few are used to solve a fluid model of plasma. The $n^{\text{th}}$ moment $\mathscr{M}_s^{(n)}$ writes:

$$\mathscr{M}_s^{(n)} = \int_\Omega \boldsymbol{v}^{\otimes n} f_s(t,\boldsymbol{x},\boldsymbol{v})\mathrm{d}\boldsymbol{v} \quad \text{with} \quad \boldsymbol{v}^{\otimes n} \equiv \underbrace{\boldsymbol{v}\otimes\cdots\otimes\boldsymbol{v}}_{n \text{ times}} \quad \text{and} \quad \boldsymbol{v}^{\otimes 0} \equiv 1 \tag{2.3}$$

The integration on the velocity space of equation 2.2 reduces the problem dimension from 6D to 3D with multiple fluid equations. The resulting infinite set of fluid equations is thus strictly equivalent to the equation 2.2. The integrated Boltzmann equation gives in its general form $\forall n \in \mathbb{N}$:

$$\int_\Omega \boldsymbol{v}^{\otimes n}\partial_t f_s \mathrm{d}^3\boldsymbol{v} + \int_\Omega \boldsymbol{v}^{\otimes n}\boldsymbol{\nabla}_{\boldsymbol{x}}\cdot(\boldsymbol{v} f_s)\mathrm{d}^3\boldsymbol{v} + \int_\Omega \boldsymbol{v}^{\otimes n}\boldsymbol{\nabla}_{\boldsymbol{v}}\cdot\left(\frac{q_s}{m_s}(\boldsymbol{E}+\boldsymbol{v}\times\boldsymbol{B})f_s\right)\mathrm{d}^3\boldsymbol{v} = \int_\Omega \boldsymbol{v}^{\otimes n} C_s \mathrm{d}^3\boldsymbol{v} \tag{2.4}$$

[1] 10 000 times less than the air at sea level

Density, velocity (momentum) and temperature (energy) corresponds to the three first equations of the infinite set 2.4. The particularity of the set 2.4 is the dependancy of the $n^{\text{th}}$ momentum to the $(n+1)^{\text{th}}$ one. The system must then be closed by expressing the last $(n+1)^{\text{th}}$ momentum using lower order moments. Different kinds of closure exists, but one of the most simple and at the same time keeping a certain amount of self-consistent physics, is based on the assumption of strong collisionality in the plasma. According to the $H$-theorem, the distribution function will thus tend toward a Maxwellian if the distribution function changes are only due to collisional processes. Thus, we assume that:

$$f_s \approx n_s \left(\frac{m_s}{2\pi k_B T_s}\right) \exp\left(\frac{-|\boldsymbol{v}-\boldsymbol{u}_s|^2}{v_T^2}\right) \tag{2.5}$$

where $T$ is the temperature, $n$ is the density, $v_T$ is the termal velocity and $\boldsymbol{u}_s$ is the fluid velocity. The Braginskii closure [15] is one proposal for fluid plasma in tokamaks. The validity criterium is $\nu_c \gg \omega$, which means that the collision frequency is larger than the frequency of the modelled physical phenomena. For a 1D model, we can take $\omega \sim v_T/L_\parallel$. Typical collision times can be found in [132, Sec. 2.15]. For a plasma at $T = 100eV$, it is equal to about $1\mu$s. More the plasma will be cold more the fluid approach will be rigorously justified. It is why such approach is largely used in the plasma edge and especially into the SOL which is much colder than in the core region.

#### 2.1.1.2. Derivation of fluid equations

Assuming the distribution function 2.5 exponentially vanishes, we have:

$$\forall n \in \mathbb{N},\ \lim_{\boldsymbol{v}\to+\infty} \boldsymbol{v}^{\otimes n} f_s = 0 \tag{2.6}$$

We can then derive the continuity, momentum and energy equations from the three first equations of moments in Eq. 2.4. The following notations are used:

$$n_s(t,\boldsymbol{x}) = \mathscr{M}_s^{(0)} \tag{2.7}$$

$$n_s \boldsymbol{u}_s = \mathscr{M}_s^{(1)} \tag{2.8}$$

$$S_s = \int_\Omega C_s f_s \mathrm{d}^3\boldsymbol{v} \tag{2.9}$$

where $\boldsymbol{u}_s$ is the fluid velocity already introduced above (and now properly defined). $S_s$ is the collisonal particle source. The particle balance equation ($n=0$) follows as (see Appendix A.2.1):

$$\partial_t n_s + \boldsymbol{\nabla}\cdot(n_s\boldsymbol{u}_s) = S_s \tag{2.10}$$

The momentum balance equation calls for more calculation. We set $\boldsymbol{w}_s = \boldsymbol{v} - \boldsymbol{u}_s$ as the fluctuating part of the fluid velocity, such that $\int_\Omega \boldsymbol{w}_s f_s \mathrm{d}^3\boldsymbol{v} = 0$. The following

definitions are used:

$$\overline{\overline{\mathbf{\Pi}}}_s^{\text{tot}} = m_s \int_\Omega \boldsymbol{w}_s \otimes \boldsymbol{w}_s f_s \mathrm{d}^3\boldsymbol{v} = p_s \mathbb{1} + \overline{\overline{\mathbf{\Pi}}}_s^{\text{clos}} \tag{2.11}$$

is the total pressure tensor. It can be decomposed into a scalar isotropic pressure $p_s$ and a residual anisotropic tensor, $\overline{\overline{\mathbf{\Pi}}}_s^{\text{clos}}$, where Brag stands for Braginskii, as it will be explained in the following part. We note $p_s = \mathrm{Tr}(\overline{\overline{\mathbf{\Pi}}}_s^{\text{tot}})/3$, and we define the temperature $T_s = p_s/n_s$ (in eV).

$$\boldsymbol{R}_s = m_s \int_\Omega \boldsymbol{v}_s C_s \mathrm{d}^3\boldsymbol{v} \tag{2.12}$$

is the collisional momentum source. It leads to (see Appendix A.2.2):

$$\partial_t(m_s n_s \boldsymbol{u}_s) + \boldsymbol{\nabla}\cdot\left(m_s n_s \boldsymbol{u}_s \otimes \boldsymbol{u}_s + \overline{\overline{\mathbf{\Pi}}}_s^{\text{tot}}\right) = q_s n_s(\boldsymbol{E} + \boldsymbol{u}_s \times \boldsymbol{B}) + \boldsymbol{R}_s \tag{2.13}$$

Isothermal models stop the momentum hierarchy at this level with a closure on the pressure tensor. Anisothermal models add the next momentum. As a remark, the momentum equation is a vector equation, with thus 3 scalar equations (in 3D). The energy equation is a second order tensor equation (9 scalar equations in 3D). This level of details is redundant for most applications where the pressure is considered as quasi isotropic and the trace of the tensor equation for energy only is retained. This writes (see Appendix A.2.3):

$$\partial_t E_s^{\text{tot}} + \boldsymbol{\nabla}\cdot(E_s^{\text{tot}}\boldsymbol{u}_s + \boldsymbol{u}_s \cdot \overline{\overline{\mathbf{\Pi}}}_s^{\text{tot}} + \boldsymbol{q}_s) = n_s q_s \boldsymbol{E}\cdot\boldsymbol{u}_s + Q_{C_s} + \boldsymbol{R}_s \cdot \boldsymbol{u}_s \tag{2.14}$$

with $\boldsymbol{q}_s$ the heat flux and $Q_{C_s}$ the collisional energy source. $E_s^{\text{tot}} = \frac{1}{2} m_s n_s |\boldsymbol{u}_s|^2 + \frac{3}{2} p_s$, with the scalar pressure $p_s = \frac{1}{3}\mathrm{Tr}\left(\overline{\overline{\mathbf{\Pi}}}_s^{\text{tot}}\right)$.

#### 2.1.1.3. Braginskii closures

In the framework of fluid equations truncated at second order (Eqs. 2.10,2.13,2.14), some moments at high order remain unknowns. These are $S_s$, $\overline{\overline{\mathbf{\Pi}}}_s^{\text{clos}}$, $\boldsymbol{R}_s$, $Q_{C_s}$ and $\boldsymbol{q}_s$. The Braginskii's closure [15] was developped to express these unknowns from lower order moments with two main hypothesis. First is the hypothesis of a strongly magnetized plasma, meaning that the Larmor frequency is higher than all the other frequencies (the Lorentz force is dominant): $\omega_c \tau_{e/i} \gg 1$. Second is the hypothesis of a highly collisional plasma near thermodynamic equilibrium, meaning that the collision frequency is higher than all the other frequencies (except, according to Braginskii's work, the cyclotronic one $\omega_c$): $\nu_c \tau_{e/i} \gg 1$, where $\nu_c$ is the collisional frequency. The

collisionality is defined as:

$$\nu^\star = \frac{L_\parallel}{\lambda_c} \tag{2.15}$$

where $L_\parallel$ is a typical parallel length (along magnetic field lines) and $\lambda_c$ is the collisional mean free path. At the edge of the plasma, $\nu^\star \approx 10^3$ while in the core $\nu^\star \approx 10$. For turbulent models, turbulent fluctuation frequencies must be controlled to be lower than the collision frequencies. This allows to perform a closure relying on the assumption of small deviation of distribution functions from the Maxwellians (see Chapman-Enskog theory).

In the following, the main results of the Braginskii's closure are recalled. First is the collisional particle source $S_s$. As particles can only be created by ionisations, dissociations or fusion reactions (neglected in first approximation for the latter) $S_s = 0$. Nevertheless, for numerical flux driven models, a constant source of particles is added, which can be seen as ionization processes or particles coming from the core.

For the others terms, we consider a two species plasma of electrons and protons (hydrogen isotope). We proceed with the collisional momentum source $\boldsymbol{R}_s = \boldsymbol{R}_s^u + \boldsymbol{R}_s^T$, with $\boldsymbol{R}_s^u$ a friction force and $\boldsymbol{R}_s^T$ a thermal force. For electrons, it becomes:

$$\boldsymbol{R}_e = \boldsymbol{R}_s^u + \boldsymbol{R}_e^T = e n_e (\eta_\parallel j_\parallel \boldsymbol{b} + \eta_\perp \boldsymbol{j}_\perp) - 0.71 n_e \boldsymbol{\nabla} T_e - \frac{3}{2} \frac{n_e}{\omega_{C_e} \tau_e} \boldsymbol{b} \times \boldsymbol{\nabla}_\perp T_e \tag{2.16}$$

where $\boldsymbol{j} = j_\parallel \boldsymbol{b} + \boldsymbol{j}_\perp = -e n_e (\boldsymbol{u}_e - \boldsymbol{u}_i)$ is the current density and $\eta_{\parallel/\perp}$ are the parallel / perpendicular Spitzer resitivities defined as:

$$\eta_\perp = \frac{m_e}{e^2 n_e \tau_e} = \frac{\eta_\parallel}{0.51} \propto T_e^{-3/2} \tag{2.17}$$

Note that $\boldsymbol{R}_i = -\boldsymbol{R}_e$

The collisonal energy source $Q_{C_s}$ is:

$$Q_{C_i} = 3 \frac{m_e}{m_i} \frac{n_e (T_e - T_i)}{\tau_e} \text{ for ions and} \tag{2.18}$$

$$Q_{C_e} = \eta_\parallel j_\parallel^2 + \eta_\perp j_\perp^2 + \frac{1}{e n_e} \boldsymbol{j} \cdot \boldsymbol{R}_e^T - 3 \frac{m_e}{m_i} \frac{n_e (T_e - T_i)}{\tau_e} \text{ for electrons} \tag{2.19}$$

The Braginskii's tensor $\overline{\overline{\boldsymbol{\Pi}}}_s^{\text{clos}}$ can be subdivided in a viscous tensor, a Finite Larmor Radius (FLR) tensor and a residual one. The viscous one is of the highest amplitude and the FLR one compensates at highest order with the difference of the diamagnetic advection and the $\boldsymbol{\nabla} B$-drift when only their divergence are taken into account (which is the case in equation 2.13). This is the so called diamagnetic cancellation (see section below on drift ordering for a definition of the drift velocities). The expression of each term in equation 2.20 can be found in [3, 15, 47, 82, 117] as well as the calculation for

the diamagnetic cancellation.

$$\overline{\overline{\mathbf{\Pi}}}_s^{\text{clos}} = \overline{\overline{\mathbf{\Pi}}}_s^{\text{vis}} + \overline{\overline{\mathbf{\Pi}}}_s^{\text{FLR}} + \overline{\overline{\mathbf{\Pi}}}_s^{\text{res}} \tag{2.20}$$

Finally, the closure on heat flux $\boldsymbol{q}_s$ can once more be split into a friction and a termal part:

$$\begin{aligned}\boldsymbol{q}_e = \boldsymbol{q}_e^u + \boldsymbol{q}_e^T = 0.71 p_e (u_{e,\parallel} - u_{i,\parallel})\boldsymbol{b} + \frac{2}{3}\frac{p_e}{\omega_{c_e}\tau_e}\boldsymbol{b}\times(\boldsymbol{u}_{e,\perp} - \boldsymbol{u}_{i,\perp}) \\ - \chi_{e,\parallel}\boldsymbol{\nabla}_\parallel T_e - \chi_{e,\perp}\boldsymbol{\nabla}_\perp T_e - \frac{5}{2}\frac{p_e}{m_e\omega_{c_e}}\boldsymbol{b}\times\boldsymbol{\nabla}_\perp T_e\end{aligned} \tag{2.21}$$

$$\boldsymbol{q}_i = -\chi_{i,\parallel}\boldsymbol{\nabla}_\parallel T_i - \chi_{i,\perp}\boldsymbol{\nabla}_\perp T_i - \frac{5}{2}\frac{p_i}{m_e\omega_{c_e}}\boldsymbol{b}\times\boldsymbol{\nabla}_\perp T_i \tag{2.22}$$

with $\chi_s$ is the thermal conductivity of species $s$.

#### 2.1.1.4. Drift ordering

The drift ordering is based on the assumption that the characteristic plasma frequency $\omega$ is slow compared to the ion cyclotronic frequency $\omega_c$: $\epsilon_\omega = \frac{\omega}{\omega_c} \ll 1$. This leads to a strong scale separation between the Larmor radius $\rho_L$ and a characteristic length of turbulence structure $l_\perp$, such that: $\epsilon_l = \frac{\rho_L}{l_\perp} \ll 1$. Within the drift ordering, it is useful to split the analysis of the dynamics into the parallel and perpendicular directions to the magnetic field, by decomposing the velocity for the ions and the electrons:

$$\boldsymbol{u}_s = u_{\parallel,s}\boldsymbol{b} + \boldsymbol{u}_{\perp,s} \tag{2.23}$$

where the perpendicular components of the velocity are described in terms of drifts. In the present models, two first-order drift velocities are defined such that:

$$\boldsymbol{u}_{\perp,s}^{(1)} = \frac{\boldsymbol{E}\times\boldsymbol{B}}{B^2} + \frac{\boldsymbol{B}\times\boldsymbol{\nabla}p_s}{q_s n_s B^2} = \boldsymbol{u}_E + \boldsymbol{u}_\star \tag{2.24}$$

with $\boldsymbol{u}_E$ the electric drift velocity and $\boldsymbol{u}_\star$ the diamagnetic drift velocity.

The mechanism related to the electrical drift velocity is illustrated on Fig. 2.1a. Charged particles in a magnetized environement follow the magnetic field lines with a gyration motion. If a perpendicular (to the magnetic field) electric field exists, the gyration motion is deformed as the particle is accelerated during one half of the circulatory motion and decelerated during the other half. Depending of the sign of the charge of the particle, the effect is reversed. But, as the gyration motion is reversed depending on the sign, the global drift motion for both ions and electrons occurs in the same direction. Thus the electric drift does not create a current, but does create a global fluid-like motion by the local variation of the electric potential, a motion that is a transport of plasma, perpendicular to the magnetic field lines.

The diamagnetic drift velocity (see Fig. 2.1b), a purely fluid veloicty, is created through a collective motion of particles but actually with little transport of matter involved. A pressure gradient induces a spatial inhomogeneity of the number of particle gyrating in one direction compared with the other one (density gradient) or of their velocity (temperature gradient). The isobar at a lower pressure has less and/or slower particles in gyration compared to the one at higher pressure. This results in a difference of motion, even if the guiding centers themselves have a little drift. This property has a major consequence on the nature of transport due to the diamagnetic drift velocity. This can be seen with the divergence of the particle flux carried by the diamagnetic drift:

$$\boldsymbol{\nabla}\cdot(n_s\boldsymbol{u}_\star) = \frac{1}{q_s}\left(\boldsymbol{\nabla}p_s\times\boldsymbol{\nabla}\left(\frac{1}{B^2}\right)\right)\cdot\boldsymbol{B} \tag{2.25}$$

This way, the divergence of the diamagnetic particle flux reduces to a curvature term, i.e. a term that is non-zero only when the magnetic field is not homogeneous. Since the gradient length of the magnetic field (the major radius $R_0$) is large compared with that of other fields (the minor radius $a$ at most), the resulting transport is actually much smaller than what could be naively infered from the amplitude of the diamagnetic velocity. This effect reflects the fact that guiding centers actually drift much slower than the diamagnetic velocity. One can easily demonstrate that the diamagnetic particle flux actually reduces to the one carried by the curvature drift velocity $\boldsymbol{u}_{\nabla B} = \pm 2T_s\frac{\boldsymbol{B}\times\boldsymbol{\nabla}B}{B^3}$. The demonstration is given in Appendix A.3:

$$\boldsymbol{\nabla}\cdot(n_s\boldsymbol{u}_\star) = \boldsymbol{\nabla}\cdot(n_s\boldsymbol{u}_{\nabla B}) \tag{2.26}$$

The latter result can be shown to be valid for other fluid balance equations, although in a more subtle way. For momentum and energy balances, it is contributions from the Braginskii tensor that counterbalance most of the diamagnetic drift flux, leading to a remainder equivalent to an advection by the curvature drift velocity. This effect is often refered to as the diamagnetic drift cancellation [58, 126]. In the models used in this thesis, it is practically used by replacing the diamagnetic velocity by the $\nabla B$-drift velocity whenever it appears in the equations. As a final remark, we have actually neglected an advection term of the parallel momentum due to the parallel velocity. If taken into account, a third velocity can be expressed. The full calculation is given in [18]. This is the curvature drift velocity $\boldsymbol{u}_{\text{curv}}$. Its impact is really small and is sometimes account for as a second order drift (see [82]). This drift comes from the spatial variation of $\boldsymbol{B}$ a particle can experience in its parallel trajectory and can be ignored in the hypothesis of small Mach numbers but should be taken into account in case of large amplitude flows. In this thesis, we have used in each simulation this third drift velocity.

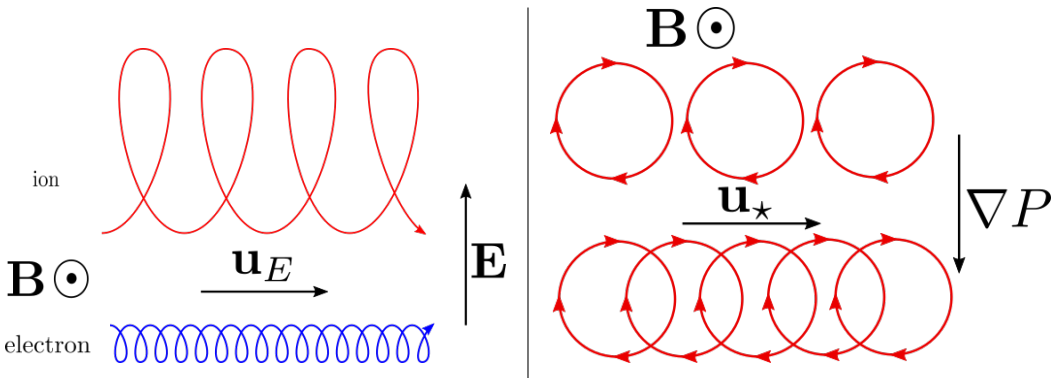


(a) Electrical drift (b) Diamagnetic drift

Figure 2.1.: Physical sketch of the first order drift velocities

### 2.1.2. Physics of open field lines

In the Scrape-Off Layer (SOL), the magnetic field lines encounter the Plasma Facing Component (PFC). The interaction between a plasma and a solid wall induces different phenomena. The charged particles hit the wall, creating first a recombination of the ions and the electrons into neutral species. The wall is thus an energy and particle sink for the plasma, even if, in steady-state, through recycling, the wall can then become a source of particles (with losses, so the particle sink boundary condition is still valid). The particle fluxes are thus extremely different in the SOL than in a close field lines region (CFL). The heat fluxes, in contrario, always see the wall as a sink.

In this section, we quickly describe some physical impacts of the wall on the particles. A more detailled work can be found in [112]. We assume an isothermal case with equal ion and electron temperatures $T_i = T_e$, such that the thermal velocity ratio $v_{T_e}/v_{T_i} = \sqrt{m_i/m_e} \ll 1$. This shows that, at the same temperature, ions are slower than electrons. Physically, this translates intially into a larger flux for electrons than for ions at the wall. Due the larger electrons flux, an electrical field arises at the proximity of the wall, resulting in a natural sheath that accelerates ions but descelerates electrons. The electrical sheath region builds up until the fluxes of ions and electrons reach an equilibrium. A simple scheme of a 1D SOL is given on Fig. 2.2, with the $z$-axis along the parallel direction. If we write the normalized electric potential $\Phi = eU/T_e$, with $U$ the electric potential, $e$ the elementary charge, the Maxwell-Gauss equation gives:

$$\frac{\mathrm{d}^2\Phi}{\mathrm{d}z^2} = \frac{e^2 n_0}{\epsilon_0 T_e}\frac{n_e - n_i}{n_0} \tag{2.27}$$

with $n_0$ the average plasma density, $n_i$ the ion density and $n_e$ the electron density. The physical expansion of the sheath is directly given by the characteristic length appearing in the equation: the Debye's length $\lambda_D = \sqrt{e^2 n_0/(\epsilon_0 T_e)}$. For a tokamak plasma with a temperature $T_e = 50$ eV and a density $n_0 = 10^{19}$ m$^{-3}$, the Debye's length is of the order of $10^{-5}$ m, which is to be compared to the parallel length $L_\parallel = 2\pi qR \sim 100$ m. As a

consequence, the sheath is not modelled explicitly in the fluid codes but its effects are taken into account through specific boundary conditions called Bohm boundary conditions.

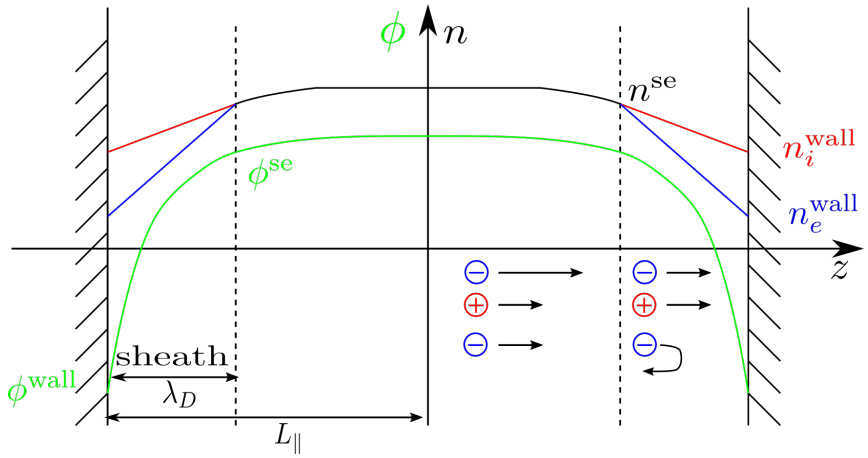


Figure 2.2.: Sketch of a 1D SOL. Profiles of potential and density along the parallel direction (scaling not respected)

#### 2.1.2.1. The Bohm boundary conditions

To study the dynamics of the sheath, we take a reference electric potential far from it and set it to zero. The region when the potential starts to drop and the ions to be accelerated is called the pre-sheath. For simplicity, values at the entrance of the sheath are noted $(\cdot)^{se}$ for the sheath entrance. We assume an isothermal plasma, so that $T_i = 0$ (a more general case is given in [112, Sec. 2.4]), a ion electrical charge $q_i = 1$ and equal sources of ions and electrons (which is generally the case). We assume adiabatic ions, meaning that as $m_i \gg m_e$, and neglect the electron inertial terms in front of the ion one. This allows us to assume that the electrons follow the Boltzmann's distribution:

$$n_e = n_e^{se} \exp\left(\frac{e(\phi - \phi^{se})}{k_B T_e}\right) \tag{2.28}$$

Now, to solve the Poisson's equation 2.27, we need to express $n_i$ as a function of $\phi$. As the Debye's length is much smaller than the mean free path, we can assume that the sheath is collisionless (no ionization or recombination inside the sheath) and so the flux of ions is conserved $n_i u_i = n_i^{se} u_i^{se}$. Thanks to the energy conservation and assuming the electron temperature to be much larger than the ion one, we know that:

$$\frac{1}{2} m_i u_i^2 = -e\phi \tag{2.29}$$

Then, with the quasi-neutrality hypothesis at the sheath entrance (and only there) $n_e^{se} = n_i^{se} = n^{se}$, we can write:

$$n_i = n^{se}\sqrt{\frac{\phi^{se}}{\phi}} \tag{2.30}$$

So that the Poisson's equation becomes (dimensional one):

$$\frac{\mathrm{d}^2\phi}{\mathrm{d}z^2} = -\frac{n^{se}e}{\epsilon_0}\left[\sqrt{\frac{\phi^{se}}{\phi}} - \exp\left(\frac{e(\phi-\phi^{se})}{k_B T_e}\right)\right] \tag{2.31}$$

By defining $\delta\phi = \phi^{se} - \phi$, we can make a Taylor expansion which leads at first order to:

$$\frac{\mathrm{d}^2\delta\phi}{\mathrm{d}z^2} = -\frac{e^2 n^{se}\delta\phi}{\epsilon_0 k_B T_e}\left(1 - \frac{k_B T_e}{2e|\phi^{se}|}\right) \tag{2.32}$$

An exponentially vanishing solution is possible if:

$$e|\phi^{se}| \geq \frac{k_B T_e}{2} \tag{2.33}$$

With the energy conservation equation from above, it becomes the Bohm's criteria:

$$u^{se} \geq \sqrt{\frac{k_B T_e}{m_i}} \equiv c_s \tag{2.34}$$

If we define the Mach number as $M \equiv u_\parallel / c_s$, the Bohm's criteria writes as $M^{se} \geq 1$ that means that the plasma should achieved a supersonic velocity before the sheath entrance. Let's note that the sound speed $c_s$ in a plasma is still different from the sound speed in fluid as the latter propagates through mechanical collisions whereas the former propagates through electrostatic interactions. A more detailed study of the supersonic transition in the edge plasma can be found in [51].

The expression of the sound speed can be generalized for hot ions plasma according to [112] into:

$$c_s = \sqrt{\frac{k_B(\gamma_e T_e + \gamma_i T_i)}{m_i}} \tag{2.35}$$

where $\gamma_{e/i}$ is the polytropic index (for ion and electron respectively), equal to 1 for an isothermal plasma and 5/3 for an adiabatic plasma with isotropic pressure.

#### 2.1.2.2. The Bohm-Chodura boundary conditions

We have assumed so far field lines normal to the solid surface, which is generally not the case in tokamaks. The Bohm conditions must thus take into account an incidence angle $\alpha$. This angle is actually made as small as possible to reduce the heat flux on the targets such that $q_{\mathrm{peak}} = q_\parallel \sin(\alpha)$. In this situation, the perpendicular drifts have to

be taken into account leading to the Bohm-Chodura's boundary condition [93]:

$$|(u_\parallel \boldsymbol{b} + \boldsymbol{u}_\perp) \cdot \boldsymbol{n}_{\text{wall}}| \geq c_s |\boldsymbol{b} \cdot \boldsymbol{n}_{\text{wall}}| \tag{2.36}$$

where $\boldsymbol{n}_{\text{wall}}$ is the normal to the wall, flux directed toward the wall.

#### 2.1.2.3. Bohm conditions for the current

Following the Bohm conditions in the normal incidence case, we can expressed the plasma flux at the sheath entrance as:

$$\Gamma^{se} = n^{se} v^{se} = n^{se} c_s \tag{2.37}$$

As already mentioned, we can assume the ions flux to be constant in the sheath and consequently the flux at the wall to be the same at the sheath entrance: $\Gamma_i^w = \Gamma^{se}$. Finally, assuming the electron density at the wall to follow a Boltzmann distribution similar to Eq. 2.28, the current in the parallel direction at the wall writes:

$$j_\parallel^w = e(\Gamma_i^w - \Gamma_e^w) = e n^{se} c_s \left(1 - \exp\left(\Lambda + \frac{e(\phi^w - \phi^{se})}{k_B T_e}\right)\right) \tag{2.38}$$

where $\exp(\Lambda) = v_e^w / c_s$. The condition to having $j_\parallel^w = 0$ at the wall gives:

$$\Lambda = \frac{e(\phi^{se} - \phi^w)}{k_B T_e} \tag{2.39}$$

defining the potential drop in the sheath for a wall at floating potential. Its expression can be found in [112, Sec. 2.6].

#### 2.1.2.4. Bohm conditions for the energy balance

According to [112, Sec 2.8], in a collisionless sheath, the heat flux is convective and writes:

$$q_{e/i}^{se} = \gamma_{e/i} k_B T_{e/i} \Gamma^{se} \tag{2.40}$$

with $\gamma_{e/i}$ the sheath heat transmission coefficients.

## 2.2. TOKAM3X: 3D fluid turbulence code

TOKAM3X is a first principle 3D turbulent code for edge plasma modeling. The code solves the equations based on a Braginskii's closure and drift-reduced model as seen in the upper sections, in an electrostatic framework. Two general models can be solved, the isothermal one and the anisothermal one. Both are described and used in this thesis. The isothermal model assumes constant temperatures in time and space. The anisothermal model uses self-consistant temperature dynamics.

### 2.2.1. Normalization

As in most numerical codes, every quantity is normalized by a reference one. The use of normalized quantities has 2 advantages:

- it often allows one to reduce the size of the parameter space of the model by reducing the number of free parameters to their minimum (eliminating possible redundancies).
- it allows the code to run with quantities of the order of 1 which can be of precious help when debugging or analysing the output of the code.

In the model solved by TOKAM3X, a typical reference density $n_0$ is chosen according to its value at the separatrix of typical tokamaks. The same goes for the reference temperature $T_0$ and $B_0$, the reference magnetic field, is taken on the machine magnetic axis. Lengths (meter) are normalized by the ion Larmor radius $\rho_L = \sqrt{m_i T_0}/(eB_0)$, the time scale is set by the ion cyclotronic frequency $\omega_c = eB_0/m_i$. Actually, only 3 reference quantities are needed, the others can then be expressed according to said quantities and some physical constants (such as the ion mass $m_i$ or the electronic charge $e$): $T_0$, $B_0$, and $n_0$.

### 2.2.2. TOKAM3X equations

The continuity equation is set under the hypothesis of quasi-neutrality, so that $n_i/n_0 \sim n_e/n_0 \equiv N$. TOKAM3X makes an approximation for the continuity equation by taking the ion continuity equation but neglecting the polarization drift, due to its complexity and numerical difficulties associated with its treatment. It leads to:

$$\partial_t N + \boldsymbol{\nabla}\cdot(\Gamma_i \boldsymbol{b} + N\boldsymbol{u}_{\perp,i}) = \boldsymbol{\nabla}\cdot(D_{\perp N}\boldsymbol{\nabla} N) + S_N \tag{2.41}$$

with $\Gamma_i = n_i u_{\parallel,i}/(n_0 c_s)$, $\boldsymbol{u}_{\perp,i} \approx \boldsymbol{u}_E + \boldsymbol{u}_{\nabla B,i} + \boldsymbol{u}_{\text{curv}}$. We have potentially another equation on the electrons for the particule conservation, but due to the quasi-neutrality assumption $n_e = n_i$, TOKAM3X uses the ions one, the electrons one is used for the charge conservation. In TOKAM3X, the assumption $\Gamma_e \sim \Gamma_i$ is also done. The term $\boldsymbol{\nabla}\cdot(D_{\perp N}\boldsymbol{\nabla} N)$ is a diffusive term modeling transport at scales smaller than the grid cells or due to collisions. $S_N$ is is a volumetric particle source whose distribution can be chosen arbitrarily. It is often applied in the vicinity of the inner boundary of the simulation domain to model a particle flux coming from the core region. Its position can change with the anisothermal model, coming from the wall or the target (the so-called recycling).

The parallel momentum equation is the results of the parallel projection of the balance momentum equation for ions and electrons. Due to the small mass of the electrons compare to ions, the inertial terms for the electron balance are neglected. The divergence of the Braginskii's tensor is neglected too. For electrons, it leads to:

$$0 = -n_e e E_\parallel - \nabla_\parallel p_e + R_\parallel \tag{2.42}$$

where $\nabla_\parallel = \boldsymbol{b}\cdot\boldsymbol{\nabla}$. For the ions:

$$m_i\left(\partial_t\Gamma_i + \boldsymbol{\nabla}\cdot(\Gamma_i(u_{\parallel,i}\boldsymbol{b}+\boldsymbol{u}_{\perp,i}))\right) = +n_i eE_\parallel - \nabla_\parallel p_i - R_\parallel \tag{2.43}$$

Once summing the 2 equations, using the continuity equation and the normalization process, we obtain:

$$\partial_t\Gamma_i + \boldsymbol{\nabla}\cdot\left(\Gamma_i\left(\frac{\Gamma_i}{N}\boldsymbol{b}+\boldsymbol{u}_{\perp,i}\right)\right) = -\nabla_\parallel(P_e+P_i) + \boldsymbol{\nabla}\cdot\left(D_{\perp\Gamma}N\boldsymbol{\nabla}(\frac{\Gamma_i}{N}) + D_{\perp N}\frac{\Gamma_i}{N}\boldsymbol{\nabla}N\right) + S_\Gamma \tag{2.44}$$

where $\boldsymbol{\nabla}\cdot\left(D_{\perp\Gamma}N\boldsymbol{\nabla}(\frac{\Gamma_i}{N}) + D_{\perp N}\frac{\Gamma_i}{N}\boldsymbol{\nabla}N\right)$ is a diffusive term modeling scales smaller than the grid scale and $S_\Gamma$ is a momentum source from the core region. $\Gamma_i = Nu_{\parallel,i}$ so that in this equation, only $N$, $\Gamma_i$, $P_e$ and $P_i$ are unknown. The pressure can be expressed as $P_{e/i} = NT_{e/i}$ so that one needs 2 additional equations on the electron and ion temperatures respectively are needed ($T_e = T_i = 1$ for an isothermal model or two equations for an anisothermal model).

Expressing the electrostatic assumption as $E_\parallel = -\nabla_\parallel\Phi$ and the parallel component of the friction term $R_\parallel = -0.71N\nabla_\parallel T_e + \eta_\parallel NJ_\parallel$ according to the Braginskii's closure in Eq. 2.42 leads to the parallel conservation law or Ohm's law:

$$\eta_\parallel NJ_\parallel = \nabla_\parallel P_e - N\nabla_\parallel\Phi + 0.71N\nabla_\parallel T_e \tag{2.45}$$

The next equation is the charge equation whose calculation can be found in [47, 117]. This equation simply translates the conservation of the charge:

$$\boldsymbol{\nabla}\cdot\boldsymbol{j} = 0 = \boldsymbol{\nabla}\cdot(j_\parallel\boldsymbol{b}) + \boldsymbol{\nabla}\cdot\boldsymbol{j}_p + \boldsymbol{\nabla}\cdot\boldsymbol{j}^* \tag{2.46}$$

where $\boldsymbol{j}_p$ is the polarisation current and $\boldsymbol{j}^*$ is the diamagnetic current. The latter is easily expressible as the current resulting from the flux difference from the $\nabla B$-drift of ions and electrons (where we use the equality between the divergence of the diamagnetic drift and $\nabla B$-drift). The former is more complex and is often simplified through a so-called Boussinesq approximation [11]. This allows to write the charge conservation as a function of vorticity noted $W$, which is actually the equation for the potential obtaining $\Phi$:

$$W = \boldsymbol{\nabla}\cdot\left(\frac{1}{B^2}\boldsymbol{\nabla}_\perp\Phi + \frac{1}{NB^2}\boldsymbol{\nabla}_\perp P_i\right) \tag{2.47}$$

The charge conservation ends up as the vorticity equation:

$$\partial_t W + \boldsymbol{\nabla}\cdot\left(W\left(\frac{\Gamma_i}{N}\boldsymbol{b}+\boldsymbol{u}_{\perp,i}\right)\right) = \boldsymbol{\nabla}\cdot(N(\boldsymbol{u}_{\nabla B,i}-\boldsymbol{u}_{\nabla B,e})) + \boldsymbol{\nabla}\cdot(J_\parallel\boldsymbol{b}) + \boldsymbol{\nabla}\cdot(D_{\perp,W}\boldsymbol{\nabla}W) \tag{2.48}$$

with $\boldsymbol{\nabla}\cdot\boldsymbol{J}^* = \boldsymbol{\nabla}\cdot(N(\boldsymbol{u}_{\nabla B,i}-\boldsymbol{u}_{\nabla B,e}))$. $\boldsymbol{\nabla}\cdot(D_{\perp,W}\boldsymbol{\nabla}W)$ is a modeling term for small scale structures.

The isothermal model of TOKAM3X assumes $T_e = T_i = 1$ and the pressures become simply $P_e = P_i = NT_e = NT_i = N$. For the anisothermal model, two set of equations

are added. The energy balance of both ions and electrons are written with a number of simplifications too. First, we neglect the contributions of the perpendicular velocities on the total energy, so that all associated terms in the energy conservation vanish (e.g. $\boldsymbol{E}\cdot\boldsymbol{u}_s$ and $\boldsymbol{R}_s\cdot\boldsymbol{u}_s$ where only the parallel contribution is kept). The same assumption about the perpendicular drift as in the density balance is also done. The ion drift replaces the electron one. The anisotropic part of the pressure tensor (the Braginskii's tensor) is once again neglected. To close the equation, the heat fluxes $\boldsymbol{q}_{e/i}$ and the friction sources $Q_{C,i/e}$ are futher are further simplified, keeping only the dominant terms of the Braginskii closure, leading to:

$$\boldsymbol{q}_{e/i} = -K_{0,e/i}\, T_{e,i}^{5/2} \nabla_\parallel T_{e,i} \boldsymbol{b} \tag{2.49}$$

where $K_{0,e/i}$ is a constante chosen as a parameter in the code.

$$Q_{C,i} = -Q_{C,e} = \frac{m_e}{m_i}\nu^\star \frac{N}{\tau_e}(T_e - T_i) \tag{2.50}$$

The balance energy equation for electron writes then:

$$\begin{aligned}\partial_t\left(\frac{3}{2}P_e\right) + \boldsymbol{\nabla}\cdot\left(\frac{5}{2}P_e\frac{\Gamma_i}{N}\boldsymbol{b} + \frac{5}{2}P_e\boldsymbol{u}_{\perp,e} + \boldsymbol{q}_e\right) &= \boldsymbol{u}_{\perp,e}\cdot\boldsymbol{\nabla}P_e - \Gamma_i E_\parallel + \frac{\Gamma_i}{N}R_\parallel + Q_{C,e} \\ &+ \boldsymbol{\nabla}\cdot\left(D_{\perp,T_e}N\boldsymbol{\nabla}T_e + D_{\perp,N}\frac{3}{2}T_e\boldsymbol{\nabla}N\right) + S_{E_e}\end{aligned} \tag{2.51}$$

It is to be noted in this equation the approximations $(J_\parallel - \Gamma_i)E_\parallel \sim -\Gamma_i E_\parallel$ and $\Gamma_e/N \equiv u_{\parallel,e} \sim u_{\parallel,i} \equiv \Gamma_i/N$. Then for ions, we have:

$$\begin{aligned}\partial_t\left(\frac{3}{2}P_i + \frac{1}{2}\frac{\Gamma_i^2}{N}\right) + \boldsymbol{\nabla}\cdot\left[\left(\frac{5}{2}P_i + \frac{1}{2}\frac{\Gamma_i^2}{N}\right)\frac{\Gamma_i}{N}\boldsymbol{b} + \left(\frac{5}{2}P_i + \frac{1}{2}\frac{\Gamma_i^2}{N}\right)\boldsymbol{u}_{\perp,i} + \boldsymbol{q}_i\right] &= \boldsymbol{u}_{\perp,i}\cdot\boldsymbol{\nabla}P_i + \Gamma_i E_\parallel - \frac{\Gamma_i}{N}R_\parallel + Q_{C,i} \\ &+ \boldsymbol{\nabla}\cdot\left(D_{\perp,T_i}N\boldsymbol{\nabla}T_i + D_{\perp,N}\left(\frac{3}{2}T_i + \frac{1}{2}\frac{\Gamma_i^2}{N^2}\right)\boldsymbol{\nabla}N + \Gamma_i D_{\perp,\Gamma_i}\boldsymbol{\nabla}\left(\frac{\Gamma_i}{N}\right)\right) + S_{E_i}\end{aligned} \tag{2.52}$$

with, as a reminder $P_e = NT_e$ and $P_i = NT_i$. The $S_X$ terms are energy sources from the core and the two divergence terms with diffusion coefficient terms ($D_\perp$) are for the modeling of scales smaller than the grid.

The TOKAM3X equations are thus:

$$\partial_t N + \boldsymbol{\nabla}\cdot(\Gamma_i\boldsymbol{b} + N\boldsymbol{u}_{\perp,i}) = \boldsymbol{\nabla}\cdot(D_{\perp N}\boldsymbol{\nabla}N) + S_N \tag{2.53}$$

$$\partial_t\Gamma_i + \boldsymbol{\nabla}\cdot\left(\Gamma_i\left(\frac{\Gamma_i}{N}\boldsymbol{b} + \boldsymbol{u}_{\perp,i}\right)\right) = -\nabla_\parallel(P_e + P_i) + \boldsymbol{\nabla}\cdot\left(D_{\perp\Gamma}N\boldsymbol{\nabla}(\frac{\Gamma_i}{N}) + D_{\perp N}\frac{\Gamma_i}{N}\boldsymbol{\nabla}N\right) + S_\Gamma \tag{2.54}$$

$$\eta_\parallel N J_\parallel = \nabla_\parallel P_e - N\nabla_\parallel \Phi + 0.71 N \nabla_\parallel T_e \tag{2.55}$$

$$\partial_t W + \boldsymbol{\nabla}\cdot\left(W\left(\frac{\Gamma_i}{N}\boldsymbol{b} + \boldsymbol{u}_{\perp,i}\right)\right) = \boldsymbol{\nabla}\cdot(N(\boldsymbol{u}_{\nabla B,i} - \boldsymbol{u}_{\nabla B,e})) + \boldsymbol{\nabla}\cdot(J_\parallel \boldsymbol{b}) + \boldsymbol{\nabla}\cdot(D_{\perp,W}\boldsymbol{\nabla} W) \tag{2.56}$$

$$\begin{aligned}\partial_t\left(\frac{3}{2}P_e\right) + \boldsymbol{\nabla}\cdot\left(\frac{5}{2}P_e\frac{\Gamma_i}{N}\boldsymbol{b} + \frac{5}{2}P_e\boldsymbol{u}_{\perp,e} + \boldsymbol{q}_e\right) &= \boldsymbol{u}_{\perp,e}\cdot\boldsymbol{\nabla}P_e - \Gamma_i E_\parallel + \frac{\Gamma_i}{N}R_\parallel + Q_{C,e} \\ &+ \boldsymbol{\nabla}\cdot\left(D_{\perp,T_e}N\boldsymbol{\nabla}T_e + D_{\perp,N}\frac{3}{2}T_e\boldsymbol{\nabla}N\right) + S_{E_e}\end{aligned} \tag{2.57}$$

$$\begin{aligned}\partial_t\left(\frac{3}{2}P_i + \frac{1}{2}\frac{\Gamma_i^2}{N}\right) + \boldsymbol{\nabla}\cdot\left[\left(\frac{5}{2}P_i + \frac{1}{2}\frac{\Gamma_i^2}{N}\right)\frac{\Gamma_i}{N}\boldsymbol{b} + \left(\frac{5}{2}P_i + \frac{1}{2}\frac{\Gamma_i^2}{N}\right)\boldsymbol{u}_{\perp,i} + \boldsymbol{q}_i\right] &= \boldsymbol{u}_{\perp,i}\cdot\boldsymbol{\nabla}P_i + \Gamma_i E_\parallel - \frac{\Gamma_i}{N}R_\parallel + Q_{C,i} \\ &+ \boldsymbol{\nabla}\cdot\left(D_{\perp,T_i}N\boldsymbol{\nabla}T_i + D_{\perp,N}\left(\frac{3}{2}T_i + \frac{1}{2}\frac{\Gamma_i^2}{N^2}\right)\boldsymbol{\nabla}N + \Gamma_i D_{\perp,\Gamma_i}\boldsymbol{\nabla}\left(\frac{\Gamma_i}{N}\right)\right) + S_{E_i}\end{aligned} \tag{2.58}$$

One of the free parameters of the model is the normalized parallel Spitzer resistivity, which is proportional to the collisonality:

$$\eta_\parallel \propto 0.51\frac{m_e}{m_i}\nu^\star T_e^{-3/2} \tag{2.59}$$

In isothermal model, we can thus choose to fixe $\eta_\parallel$ to fixe $\nu^\star$, whereas a self-consitent model can be used in non-isothermal simulations. Typically, for TORE-SUPRA at the separatrix, we have $\nu^\star = 0.01$. In TOKAM3X, we used $\eta_\parallel = 10^{-5}$ in isothermal simulations (corresponding to $\nu^\star \approx 0.07$) and $\nu^\star = 0.05$ in non-isothermal ones with a self-consitent paralle resistivity.

### 2.2.3. Magnetic geometry

TOKAM3X uses a flux surface aligned coordinate approach and complex geometries can be described. Before this thesis, it was only for axisymmetrical magnetic geometries. This is done through the so-called curvilinear coordinates. A complete study of this kind of topology is beyond the scope of this thesis but can be found in [27]. We detail here only the main lines of the topic. Let us assume we have access to the magnetic field in cylindrical coord-nates $\boldsymbol{B}(R,Z,\phi)$ with $R$ the major radius, $Z$ the vertical axis and $\phi$ the toroidal curvilinear coordinate. We assume the existence of flux surfaces, which are tangent to the magnetic field lines.

To have a topology based on the magnetic topology, we need to define a 3D non-orthogonal and local basis. We define a set of three scalars $(\psi,\theta^*,\zeta)$ with $\psi$ labelling

flux surfaces, $\theta^*$ a poloidal curvilinear coordinate and $\zeta$ a toroidal curvilinear coordinate. $\psi$ is a radial coordinate and can be sometimes refer with a $r$ subscript or superscript, especially in simplified circular geometry. In TOKAM3X, $\zeta$ is actually a local curvilinear angle noted $\varphi$, as a toroidal angle, and such that $\varphi \in [0, 2\pi]$. This is due to the fact that tokamaks are considered periodic. This allows one to define a transformation operation of a position vector $\boldsymbol{r}$ as:

$$\boldsymbol{r}(R, Z, \phi) = \boldsymbol{r}(\psi, \theta^*, \varphi) \tag{2.60}$$

The notation curvilinear comes from the fact that iso-coordinate lines are not necessarily straight lines or even orthogonal to one another. At every point in space, a triptic of vectors can be defined to create a basis. The vectors tangent to the iso-coordinate curves form the covariant basis:

$$\boldsymbol{e}_\psi = \frac{\partial \boldsymbol{r}}{\partial \psi} \; ; \; \boldsymbol{e}_{\theta^*} = \frac{\partial \boldsymbol{r}}{\partial \theta^*} \; ; \; \boldsymbol{e}_\varphi = \frac{\partial \boldsymbol{r}}{\partial \varphi} \tag{2.61}$$

whereas the vectors orthogonal to the plane defined by two curves form the contravariant basis:

$$\boldsymbol{e}^\psi = \boldsymbol{\nabla}\psi \; ; \; \boldsymbol{e}^{\theta^*} = \boldsymbol{\nabla}\theta^* \; ; \; \boldsymbol{e}^\varphi = \boldsymbol{\nabla}\varphi \tag{2.62}$$

By construction, the two basis (see Fig. 2.3b for the $(\psi, \theta^*, \zeta)$ basis, the $(\psi, \theta^*, \varphi)$ one would have the covariant and contravariant $\varphi$ vectors being the same) have a certain number of properties detailled in Appendix B. Beyond the mathematical properties, the most important one is the axisymmetrical assumption in the toroidal direction. It translates into:

$$\boldsymbol{e}_\varphi \cdot \boldsymbol{e}_\psi = \boldsymbol{e}_\varphi \cdot \boldsymbol{e}_{\theta^*} = \boldsymbol{e}^\varphi \cdot \boldsymbol{e}^\psi = \boldsymbol{e}^\varphi \cdot \boldsymbol{e}^{\theta^*} = 0 \quad , \quad \boldsymbol{e}^\varphi \times \boldsymbol{e}_\varphi = \boldsymbol{0} \tag{2.63}$$

Which is the mathematical justification that, in practice, the mesh is magnetically aligned in the poloidal plan $(\psi, \theta^*)$, but in the toroidal direction, the mesh follows the toroidal angle $\varphi$ and not the magnetic field lines.

The magnetic field can be expressed as the curl of a potential vector $\boldsymbol{A}$, following [59]. It writes $\boldsymbol{A} = \Psi_p(\psi)\boldsymbol{\nabla}\varphi + \Psi_t(\psi, \theta^*)\boldsymbol{\nabla}\theta^*$. Then we have:

$$\boldsymbol{B} = \boldsymbol{\nabla}\Psi_p \times \boldsymbol{\nabla}\varphi + \boldsymbol{\nabla}\Psi_t \times \boldsymbol{\nabla}\theta^* \tag{2.64}$$

where $\Psi_t$ and $\Psi_p$ are toroidal and poloidal flux functions whose parameter depencies are chosen so that $\boldsymbol{B} \cdot \boldsymbol{\nabla}\psi = 0$. This means that the magnetic field has no radial $(\psi)$ component in the covariant basis. Furthermore, the field lines are thus ensured to lie

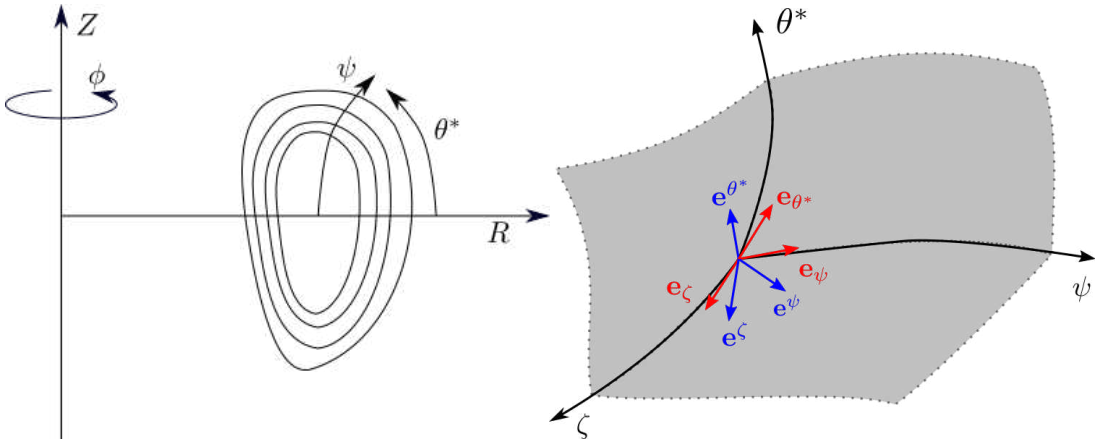


(a) Flux surfaces in $(R, Z, \phi)$

(b) Curvilinear vectors in general configuration. In TOKAM3X $\boldsymbol{e}_\zeta$ and $\boldsymbol{e}^\zeta$ have the same direction and are noted $\boldsymbol{e}_\varphi$ or $\boldsymbol{e}^\varphi$

Figure 2.3.: Scheme of the different basis

on flux surfaces. The magnetic field can be written:

$$\boldsymbol{B} = \frac{\mathrm{d}\Psi_p}{\mathrm{d}\psi}\boldsymbol{e}^\psi \times \boldsymbol{e}^\varphi + \frac{\partial \Psi_t}{\partial \psi}\boldsymbol{e}^\psi \times \boldsymbol{e}^{\theta^*} \tag{2.65}$$

$$= B^{\theta^*}\boldsymbol{e}_{\theta^*} + B^\varphi \boldsymbol{e}_\varphi, \quad \text{with} \quad B^{\theta^*} = -\frac{1}{J}\frac{\mathrm{d}\Psi_p}{\mathrm{d}\psi} \quad \text{and} \quad B^\varphi = \frac{F}{R|\boldsymbol{e}_\varphi|} \tag{2.66}$$

Where we have set:

$$\frac{\partial \Psi_t}{\partial \psi} = \frac{FJ}{R|\boldsymbol{e}_\varphi|}, \quad F = \frac{\mu_0 I_{\mathrm{tor}}}{2\pi} \tag{2.67}$$

with $J$ the Jacobian of the transformation between cylindrical and curvilinear coordinates (see Appendix B) and $I_{\mathrm{tor}}$ the toroidal current in the plasma (obtained from an application of the Ampère's law on the magnetic field). $R$ is the radius. We can note that, once normalized, the toroidal contravariant component of the magnetic field ends up as $\hat{B}^\varphi = F/R$ which shows an inversely proportional to $R$ toroidal field, an important property of tokamaks.

### 2.2.4. Numerical methods

TOKAM3X uses a conservative finite-difference discretization method. The time evolution is done by a Runge-Kutta scheme of order one to four. The advancement of each term in the equations depends on their respective dynamics. Advection terms follow an explicit scheme, a shock-capturing Roe-Marquina one [29, 101] completed with a Weighted Essentially Non Oscillatory (WENO) interpolation [73].

The perpendicular diffusive terms use an explicit advancement. The parallel heat

diffusion terms, use an implicit one to avoid breaking the CFL condition. The implicit advancement of these terms is done as a final step in the numerical scheme.

Finally, two terms are treated differently through an implicit scheme due to their dynamics: the parallel current term (more specifically its dependency in Phi) in the vorticity equation and the heat fluxes in the energy balances. Both terms have parallel dynamics much faster than the perpendicular advection terms. We describe the case for the vorticity equation as it is the most complex one. Once the advection terms are computed, the expression of the parallel current from the Ohm's law 2.45 is substituted in the vorticity equation 2.48. Then, with the potential function as unknown, the following equation is solved implicitely:

$$(\mathscr{L}^{\perp}+\mathscr{L}^{\parallel}\delta t)\Phi^{t+1} = W^{\star} - \boldsymbol{\nabla}\cdot\left(\frac{1}{N^t B^2}\boldsymbol{\nabla}_{\perp}P_i^t\right) - \delta t\boldsymbol{\nabla}\cdot\left(\frac{1}{N^t\eta_{\parallel}}\boldsymbol{b}\nabla_{\parallel}P_e^t + \frac{0.71}{\eta_{\parallel}}\boldsymbol{b}\nabla_{\parallel}T_e^t\right) \quad (2.68)$$

Where $W^{\star}$ is a field resulting from the explicit advancement. $\mathscr{L}^{\perp} = \boldsymbol{\nabla}\cdot\left(\frac{1}{B^2}\boldsymbol{\nabla}_{\perp}\right)$ and $\mathscr{L}^{\parallel} = \boldsymbol{\nabla}\cdot\left(\frac{1}{\eta_{\parallel}}\boldsymbol{b}\nabla_{\parallel}\right)$ are operators. $(\mathscr{L}^{\perp}+\mathscr{L}^{\parallel}\delta t)$ is a 3D operator inverted thanks to a direct sparse L-U solver with the support of specific libraries such as PASTIX.

### 2.2.5. Boundary conditions and flux control

In the toroidal direction, periodic conditions are set. TOKAM3X solves both closed and open flux surfaces (SOL). Periodic conditions are also applied in the poloidal direction for closed flux surface zones. The Bohm boundary conditions are set in the SOL region. With respect to Sec. 2.1.2, at the target (limiter or divertor), a Bohm-Chodura boundary condition is imposed for the momentum:

$$\Gamma^{se} = |(u_{\parallel,i}\boldsymbol{b} + \boldsymbol{u}_{\perp,i})\cdot\boldsymbol{n}_{\text{wall}}| \geq c_s|\boldsymbol{b}\cdot\boldsymbol{n}_{\text{wall}}| \quad (2.69)$$

with $c_s = \sqrt{T_e + T_i}$ here. The condition for the parallel current (and thus the electric potential) is the linearized version of Eq. 2.38:

$$j_{\parallel} \approx \pm N(\Lambda - \Phi) \quad (2.70)$$

The sign depends on the side of the target. A condition on the parallel gradient of the potential is set using the Ohm's law and the condition on the parallel current:

$$\nabla_{\parallel}\Phi = \pm\eta_{\parallel}N(\Lambda-\Phi) + \frac{\nabla_{\parallel}P_e}{N} + 0.71\nabla_{\parallel}T_e \quad (2.71)$$

We finally have a condition (still on the target) for the parallel heat flux:

$$q_{e/i} = \gamma_{e/i}NT_{e/i} \quad (2.72)$$

At the inner and outer radial boundaries, a Neumann condition $\partial_\psi X = 0$ is applied for all unknown fields $(N, \Gamma, \Phi, W, T_e, T_i)$.

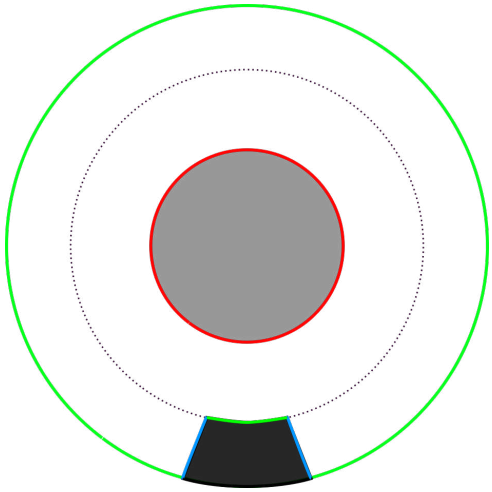

Figure 2.4.: Scheme of the boundary conditions used in TOKAM3X. In red are the inner (core) bounday, in green the outer (wall) boundary and in blue the target boundaries. The grey and black parts are in the simulation domain. The buffer zones are a few cells in the domain at every boundaries.

To fullfill the conservation properties of the code, sources and sinks have to be carefully tuned. In TOKAM3X, the particle density is driven by a volumetric source and the sinks are given by the fluxes at the boundaries. If the Bohm-Chodura condition is well-defined, the Neumann conditions in the radial direction need, on the other hand, more control. Such a simple condition must not reflect a physical border but just a limitation in the geometry. If the turbulence is not dampened near the boundaries, unphysical phenomena appear (stronger gradient, stronger turbulence, etc). Consequently, at the inner boundary, a null flux condition is imposed: $\Gamma^\psi = 0$. This prevents unwanted source losses. For numerical stability, the implementation of buffer region is done, where, near the inner boundary, the diffusive coefficient is artificially increased to homogeneise the plasma. This radial zone is limited to a few cells (one to four at most) in order to limit the computational cost.

### 2.2.6. Quick overview in the litterature

TOKAM3X is a well established code in its specialities. Its isothermal model has been used to described edge plasma turbulence in circular limiter geometry [121] and quickly in realistic X-point geometry [48]. The non-isothermal model has allowed to study turbulent behaviour in circular limiter geometry [4]. Recent developments have added the neutral physics in TOKAM3X coupling with the EIRENE code [41]. In the community of edge plasma turbulent codes (such as the already discussed BOUT++,

GBS or GRILLIX), TOKAM3X is on the same league and the 3D MPs added in this thesis should allow it to keep a good position on the market.

## 2.3. SOLEDGE3X-HDG: 3D fluid transport code

SOLEDGE3X-HDG is a 2D-3D code using Hybrid Discontinuous Galerkin method to solve a reduced 2D-3D transport equation model in realistic tokamak geometry. The model can be chosen isothermal or anisothermal [52–54]. For this thesis, we only use the 3D isothermal model. The reason is that this is the first time the 3D version of SOLEDGE3X-HDG is used, so we choose the simplest model as a starting point. The code is moreover still under development with the recent addition of neutral physics and turbulence. Nevertheless, the strength of SOLEDGE3X-HDG compare to TOKAM3X is the geometry. In SOLEDGE3X-HDG, thanks to high order finite elemnts, any magnetic and wall geometries can be given.

### 2.3.1. Transport equations

In the same way as for TOKAM3X, the drift ordering hypothesis is done, splitting parallel and perpendicular dynamics. We write $\boldsymbol{u} = u\boldsymbol{b} + \boldsymbol{u}_\perp$. In SOLEDGE3X-HDG, only the ion diamagnetic drift is taken into account, substituted by the curvature drift velocity under the diamagnetic cancellation:

$$\boldsymbol{u}_\perp = \boldsymbol{u}_{\nabla B} = \frac{2T_i}{B}\frac{\boldsymbol{B}\times\boldsymbol{\nabla}B}{B^2} \tag{2.73}$$

A minimum system of equations with the ion density and parallel momentum balances leads to:

$$\begin{cases} \partial_t N + \boldsymbol{\nabla}\cdot(N\boldsymbol{u}) - \boldsymbol{\nabla}\cdot(D\boldsymbol{\nabla}_\perp N) = S_N \\ \partial_t \Gamma_i + \boldsymbol{\nabla}\cdot(\Gamma_i \boldsymbol{u}) + \boldsymbol{b}\nabla_\parallel(2N) - \boldsymbol{\nabla}\cdot(\mu\boldsymbol{\nabla}_\perp\Gamma_i) = S_\Gamma \end{cases} \tag{2.74}$$

where $S_N$ and $S_\Gamma$ are sources of particles and momentum flux. $c_s$ is the dimensionless sound speed. $D$ and $\mu$ are diffusion coefficient that take into account both collisional transport and the turbulence in the cross-field direction, assumed to be constante. In this thesis $D = \mu$.

### 2.3.2. Boundary conditions

The boundary condition are similar to the one in TOKAM3X. The density at the wall is left free and the plasma-wall interactions are done with mainly a Bohm condition for the parallel velocity. It simply translates as:

$$\begin{cases} \Gamma_i \geq +N\sqrt{2} \text{ if } \boldsymbol{b}\cdot\boldsymbol{n} > 0 \\ \Gamma_i \leq -N\sqrt{2} \text{ if } \boldsymbol{b}\cdot\boldsymbol{n} < 0 \end{cases} \tag{2.75}$$

with $\boldsymbol{n}$ the outer normal to the wall. When the field lines are almost tangent to the wall, the Bohm theory is not true anymore so a switch has been implemented when $|\boldsymbol{b}\cdot\boldsymbol{n}| < 0.1$ so that the condition turns into a free density and momentum flux and a Neumann condition $\partial_t X = 0$.

### 2.3.3. Non-aligned grid and numerical methods

One limit of field-aligned grid code is to handle complex geometry of the wall. SOLEDGE3X-HDG can accurately discretize real geometries of tokamaks. It aims toward a computationaly efficiency as well as being flexible with magnetic geometry. This flexibilty stems from the use of a finitie elements method on unstructured meshes (see Figs 2.5).

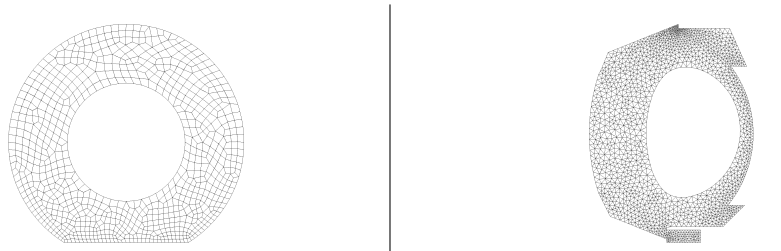

(a) Mesh horizontal limiter

(b) Mesh WEST geometry

Figure 2.5.: Non-aligned grid for SOLEDGE3X-HDG

A high-order Hybrid Discontinuous Galerkin (HDG) algorithm is used. The mathematical background of this scheme is beyond the scope of this thesis but details can be found in [53]. We just recapitulate the step of the HDG method.

To solve the system 2.74, a local problem is solved in each element of the finite-element discretization, then a global problem allows to solve the system in the whole mesh skeleton (corresponding to the boundaries between elements). The local problem is a weak formulation of the system, written in conservative form, expressed as a conservative variable $\boldsymbol{U} = N, N\Gamma_i$ in each nodes (nodes are constitutive parts of an element of the mesh). Thanks to the weak formulation, $\boldsymbol{U}$ is expressed into another approximation, the trace solution, defined on the element borders $\hat{\boldsymbol{U}}$. The global problem comes from the conservation of the fluxes in weak form applied on this element borders. From the global problem solved for $\hat{\boldsymbol{U}}$, $\boldsymbol{U}$ can be recovered in each element. The advantage of the HDG method are:

- The problem is decomposed in a combination of local problems in each elements and a local problem corresponding to the flux between elements.
- Each local problem is independant from the others and thus making the scheme highly parallel.

- The global problem has less degrees of freedom than the total number of degrees of freedom of the problem, which decreases its computational cost.

The time discretization is fully implicit with a Backward Euler scheme (first order) or Geiler scheme (second order). Non-linear terms are linearized with a Newton-Raphson method.

### 2.3.4. Quick overview in the litterature

The first benchmark of SOLEDGE3X-HDG with SOLEDGE2D in [53] has been done with a WEST geometry in an isothermal model. It has been able to reach a steady-state solution in a few minutes compare to the hours necessary for SOLEDGE2D. The results between the two codes are extremely similar. Furthermore, SOLEDGE3X-HDG is able to solve the equations in the core plasma, allowing to avoid to set boundary conditions on the inner boundaries. It is an advantage as numerical codes can be extremely sensible to arbitrarily set boundary conditions. In [52], SOLEDGE3X-HDG solve with an isothermal model a transient magnetic equilibrium on a WEST geometry, from a limiter to divertor transition, a completely new feature in the current codes for plasma transport simulations.

# 3. Self-consistent study of isothermal turbulent transport in circular geometry with 3D magnetic perturbations

## Table of Content

In this chapter, we analyze the impact of single mode magnetic perturbations (MPs) on turbulence and transport in the edge of a circular limited and isothermal plasma. The TOKAM3X code introduced in Chap. 2 is used for that purpose. We first describe the changes made in the code to deal with 3D magnetic perturbations, before reporting simulation results.

## 3.1. Implementation of 3D magnetic perturbations in TOKAM3X

As introduced in Section 2.2.3, the magnetic field $\boldsymbol{B}_0$ in TOKAM3X derives from a potential vector of the form:

$$\boldsymbol{A}_0 = \Psi_p^0(\psi)\boldsymbol{\nabla}\varphi + \Psi_t^0(\psi,\theta^*)\boldsymbol{\nabla}\theta^* \tag{3.1}$$

The code was thus originally only able to deal with toroidally axisymmetric magnetic equilibria, with however arbitrary geometries in the poloidal cross-section. The first task of this PhD consisted thus in modifying the magnetic equilibrium implementation to allow a perturbative approach (small amplitude perturbations) for 3D magnetic perturbations. The potential vector is thus rewritten as:

$$\boldsymbol{A} = \Psi_p^0(1+\epsilon_p)\boldsymbol{\nabla}\varphi + \Psi_t^0\boldsymbol{\nabla}\theta^* \tag{3.2}$$

with $|\epsilon_p(\psi,\theta^*,\varphi)| \ll 1$. The small amplitudes assumption allows us to keep a mesh aligned on the flux surfaces along the magnetic field lines. This leads (see Appendix B.2 for more) to the following expression for the magnetic field $\boldsymbol{B}$:

$$\begin{aligned}
\boldsymbol{B} &= B^{\varphi}\boldsymbol{e}_{\varphi} + B^{\theta^*}\boldsymbol{e}_{\theta^*} + B^{\psi}\boldsymbol{e}_{\psi} \\
&= B^{\varphi}||\boldsymbol{e}_{\varphi}||\frac{\boldsymbol{e}_{\varphi}}{||\boldsymbol{e}_{\varphi}||} + B^{\theta^*}||\boldsymbol{e}_{\theta^*}||\frac{\boldsymbol{e}_{\theta^*}}{||\boldsymbol{e}_{\theta^*}||} + B^{\psi}||\boldsymbol{e}_{\psi}||\frac{\boldsymbol{e}_{\psi}}{||\boldsymbol{e}_{\psi}||} \\
&= B^{\varphi}\sqrt{g_{\varphi\varphi}}\hat{\boldsymbol{e}}_{\varphi} + B^{\theta^*}\sqrt{g_{\theta^*\theta^*}}\hat{\boldsymbol{e}}_{\theta^*} + B^{\psi}\sqrt{g_{\psi\psi}}\hat{\boldsymbol{e}}_{\psi} \\
&= B^{\mathrm{tor}}\hat{\boldsymbol{e}}_{\varphi} + B^{\mathrm{pol}}\hat{\boldsymbol{e}}_{\theta^*} + B^{\mathrm{psi}}\hat{\boldsymbol{e}}_{\psi}
\end{aligned} \tag{3.3}$$

where $(B^{\mathrm{tor}}, B^{\mathrm{pol}}, B^{\mathrm{psi}})$ are the toroidal, poloidal and radial covariant components of the magnetic field. The magnetic perturbations mainly introduce a new radial term, otherwise equal to zero in the former version of TOKAM3X.

This new component of the magnetic field leads to the many additional components that must have been implemented in the TOKAM3X model. A special attention has been given to the perpendicular velocity drifts. Let a scalar quantity $f$, then the related drift velocity can be written as:

$$\boldsymbol{u}_{\mathrm{drift}} = \alpha\frac{\boldsymbol{B}\times\boldsymbol{\nabla}f}{B^2} \tag{3.4}$$

where $\alpha$ is a term depending on which drift velocity is considered. For example the electric drift sets $\alpha = 1$ and $f = \Phi$, whereas the $\nabla B$, for ions sets $\alpha = 2T_i/B$ and $f = B$. The curvature drift sets $\alpha = \Gamma_i^2/(N_i^2 B)$ and $f = B$. The complete calculation of the drift velocities is done in Appendix B.3. We summarize here by saying that each vector component gains a new term from the radial component of the magnetic field. As already mentionned, in this approach the mesh can remain aligned along the magnetic fiels lines and only the equations are changed.

All these new terms are treated explicitly is the numerical scheme assuming that they remain small that does not impact too much the stability condition of the numerical scheme. It is especially important for the vorticity equation 2.48, from whom the potential evolution is done implicitely.

## 3.2. Simulations set-up for this chapter

The poloidal cross-section is circular with an infinitely thin limiter located at the bottom. The computational domain emcompasses both open (SOL) and closed field lines (CFR). Only half a torus is computed, assuming a $\pi$-periodic solution in the toroidal direction. The mesh resolution sets as $\psi \times \theta^* \times \varphi = 64 \times 512 \times 64$ (see Figs. 3.1). Each simulation runs for a longer time than the confinement time. The steady state is assumed to be reached when the slidding average of integral quantities, such as the total particle content, on a time scale longer than the fluctuation correlation time does not vary of more than $2-3\%$.

| Simulation | $a$ | $m$ | $n$ |
|---|---|---|---|
| Reference | 0 | 0 | 0 |
| MP no island | 1 | 6 | 4 |
| | 2 | 6 | 4 |
| | 3 | 6 | 4 |
| | 1 | 10 | 6 |
| MP islands | 1 | 6 | 2 |
| | 1 | 15 | 4 |
| | 1 | 18 | 4 |
| | 1 | 22 | 6 |

Table 3.1.: Parameters $(a, m, n)$ for the MPs used in the simulations. $a$ is the amplitude, $m$ the poloidal mode number and $n$ the toroidal one. $n$ is given for a full torus.

**Geometrical parameters and magnetic field** - The aspect ratio is set as $\mathscr{A} = \frac{R_0}{a} = 3.4$. The minor radius is equal to $256\rho_L$ (in Larmor radius unit). The simulated domain is defined such that $r/a \in [0.8, 1.2]$, with $r/a = 1$ being the separatrix. The reference value $B_0$ for the magnetic field is chosen by convention as the amplitude of the toroidal field on the magnetic axis, so that $F = 1$ and the safety factor $q$ in the simulation box follows a parabolic profile with values bounded in $[3, 6]$, 6 being the value at the wall. The magnetic field is oriented such that the $\nabla B_i$ velocity drift is going toward the bottom of the machine.

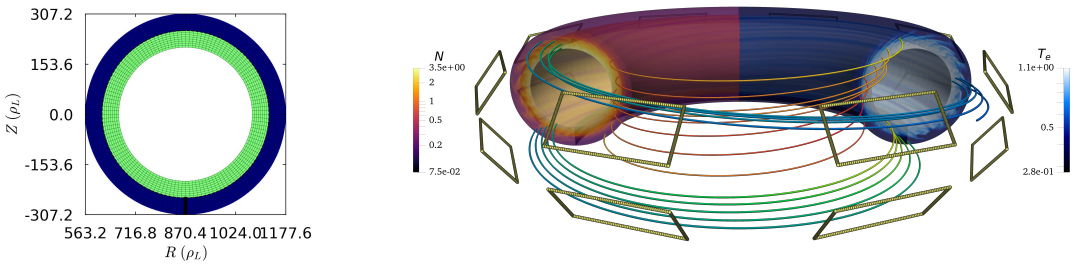


(a) Mesh (b) 3D view

Figure 3.1.: (3.1a) Poloidal cut of the 3D mesh. The limiter is the thick black line at the bottom. The mesh is coarsened two times in each direction for readability. The green part is the Closed Field lines Region (CFR), the blue part the Scrape-Off Layer (SOL). (3.1b) 3D view of a TOKAM3X simulation (here non isothermal model, see Chap. 4). The RMP coils are represented in yellow (see Chap 5, in this chapter a simplified model is used). Magnetic field lines are drawn. A density snapshot can be seen on the left and an electron temperature snapshot on the right.

**Plasma parameters** - The normalized parallel resistivity $\eta_\parallel$, which is directly dependent on the collisionality in isothermal simulation, is set as:

$$\eta_\parallel = 10^{-5} \tag{3.5}$$

that corresponds to $\nu^\star \approx 0.07$. The effective diffusion is equal to:

$$D_{\perp,X} = 10^{-2}\rho_L^2\omega_c \tag{3.6}$$

It is a trade-off to be small enough to ensure dominant turbulent transport while preserving the numerical stability with respect to the mesh resolution.

**Sources** - The simulations are flux-driven so we set a particle source at the inner boundary (in this model without neutrals, the particles are assumed coming from the core). The form of the source is a radially decaying function (vanishing exponential) after a few cells, to ensure a constant particle source with no effect on the solutions away from the boundary.

**Magnetic perturbations (MPs)** - A first simulation of reference without MP is run. Then, the 3D perturbation is fixed equal:

$$\epsilon_p = a \cdot 10^{-3} \sin\left(m\theta^* - n\varphi\right) \tag{3.7}$$

with the triptic $(a, m, n)$ a set of constants whose different values are given in table 3.1. The toroidal mode $n$ is given for a full torus. In the following, the legend for each simulation in the plots is $(a, m, n)$. The reference simulation is noted $(0,0,0)$. The expression of the perturbation is correct in circular geometry only as we have $\theta^* = \theta$, the poloidal angle.

## 3.3. Direct observation on the magnetic field

In agreement with theory on magnetic perturbations, depending on the mode number, magnetic islands can naturally form on flux surfaces of rational $q = m/n$ (remind that the parabolic safety factor profile varies between $3 \leq q \leq 6$). In this case, the corresponding solution is called solution with magnetic island, as opposed to the case without magnetic island. The solutions without magnetic islands are actually due to the fact that the amplitude of the perturbation is to weak to break the magnetic surfaces. We thus expected to observe islands for example for MP $(1,6,2)$ at $q = 3$ but not MP $(1,6,4)$ as $q = 3/2$ is outside of the computational domain.
To observe magnetic islands, Poincaré plots are drawn. Poincaré plots are obtained by following a set of magnetic field lines (if possible uniformly distributed on flux surfaces) and marking a point each time they intersect a given poloidal plane. This is done by solving the following system of equations:

$$\begin{cases} \dfrac{\mathrm{d}l_\psi}{\mathrm{d}l_\varphi} &= \dfrac{B^\psi}{B^\varphi} \\ \dfrac{\mathrm{d}l_{\theta^*}}{\mathrm{d}l_\varphi} &= \dfrac{B^{\theta^*}}{B^\varphi} \end{cases} \tag{3.8}$$

This system corresponds to follow a magnetic field line $s$, as by definition, an infinitesimal element of the field line $\mathrm{d}s$ can be defined as $\mathrm{d}\boldsymbol{s} \times \boldsymbol{B} = \boldsymbol{0}$, where $\boldsymbol{s}$ is the curvilinear abscissa along a field line. By noting $\mathrm{d}\boldsymbol{s} = \mathrm{d}l_\psi \boldsymbol{e}_\psi + \mathrm{d}l_{\theta^*} \boldsymbol{e}_{\theta^*} + \mathrm{d}l_\varphi \boldsymbol{e}_\varphi$ and expressing $\boldsymbol{B}$ the same way in the covariant basis, it is easy to retrieve the system above. Poincaré plots reduce to 2D maps of the particle movement by taking a poloidal slice.

The Figs. 3.2 shows two Poincaré sections for MP $(1,6,4)$ (Fig. 3.2a) and MP $(1,6,2)$ (Fig. 3.2b). For the case $(1,6,4)$, we observe no island, as expected, since the flux surface $q = 6/4 = 1.5$ is outside of the domain. For the case $(1,6,2)$ the $m = 6$ islands are as expected on the flux surfaces $q = 6/2 = 3$. Nevertheless, we can note the existence of islands of smaller amplitudes for other flux surfaces. This phenomenon is a resonance due to the way the perturbation is implemented on an equilibrium magnetic field that takes into account the helicity of said field. The poloidal magnetic field can actually be expressed as $B_p = \boldsymbol{\nabla}\Psi_p \times \boldsymbol{\nabla}\varphi \propto \frac{|\Psi_p|}{R_0(1+\mathscr{A}\cos(\theta^*))}$. The dependency in $1/R$ leads to a Taylor serie expansion in $\theta^*$ (due to the $\epsilon_p$ perturbation), involving successives modes and not only the mode excited by the perturbation of $\Psi_p$. As a direct consequence, subsequent modes with decreasing amplitude are found, as in

this case, modes $m = 7 \ldots 11$. For the case $(1,6,4)$, the amplitude of the subsequent modes are too small to be able to break the flux surfaces into islands, explaining the absence of them.

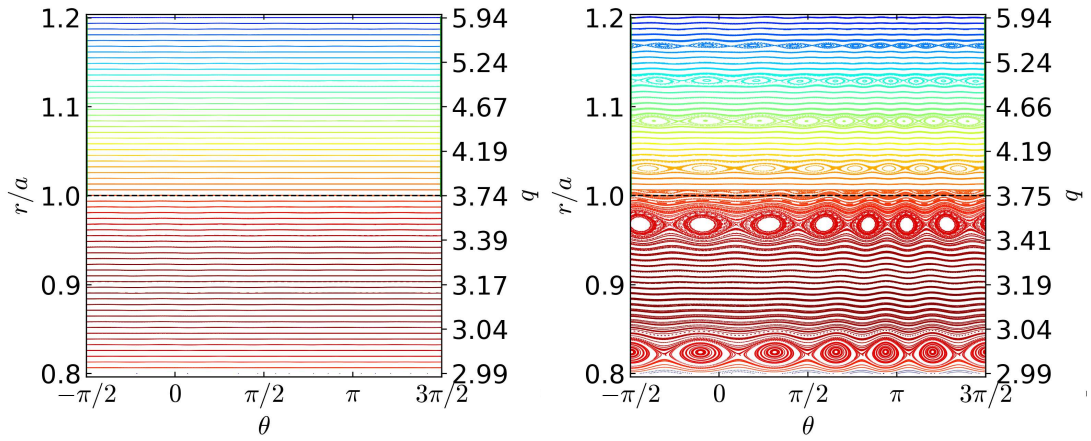


(a) $(a,m,n) = (1,6,4)$ (b) $(a,m,n) = (1,6,2)$

Figure 3.2.: Poincaré sections for different MPs. The value of the safety factor $q$ has been plotted on the vertical axis on the right side. As a convention $\theta^* = 0$ is the Low Field Side (LFS or outer) midplane. Increasing $\theta^*$ is in the electron diamagnetic direction. No magnetic island (3.2a) and magnetic islands at $q = 6/2$ (3.2b)

In the poloidal and toroidal directions, the response of the magnetic field to any MP is as expected. The Fourier transforms of the norm of the total magnetic field $|\boldsymbol{B}|$ is shown on Fig. 3.3. The plots are drawn at $r/a = 0.9$ and $\varphi = \pi/8$. It shows that peak values correspond to the poloidal $m$ mode of the perturbation, with a secondary peak of smaller amplitude corresponding to a harmonic at $2m$. The peaks become more visible for high $m$, typically $m \geq 10$, specially when magnetic islands appear in the simulation box, Fig. 3.3b. Results in the toroidal direction are not shown, the spectra being simply composed of two peaks, one at $n = 0$ corresponding to the toroidal component of the magnetic field and the other one to the wavenumber of the perturbation.

## 3.4. Impact of three-dimensional single MP on the mean fields

In this section, we describe the effects of single mode MPs on the mean fields (time averaged), distinguishing between the cases with or without magnetic islands. A coherent picture is drawn upon each field and basic trends are given if possible.

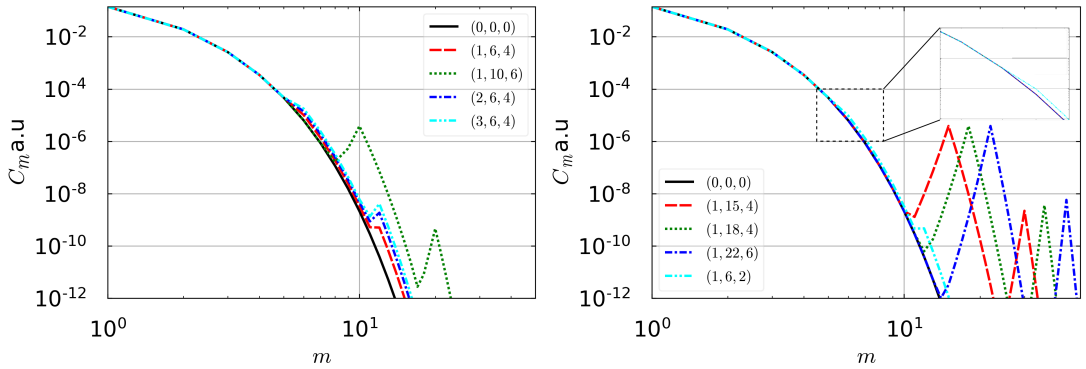


(a) Case MP no island

(b) Case MP islands

Figure 3.3.: Fourier transforms in the poloidal direction of the norm of the total magnetic field $|\boldsymbol{B}|$ for different MPs without (3.3a) or with (3.3b) magnetic islands inside the computational domain. $r/a = 0.9$ and $\varphi = \pi/8$. $C_m$ is the energy for each mode $m$.

### 3.4.1. Density pump-out

Experiments in DIII-D [40], JET [70] or MAST [118] have shown that the presence of MPs leads to a degradation of the particle confinement marked by a decrease of the plasma density. It is commonly called density pump-out and is often seen through the time trace of the density in experiments. In the same way, the time trace of the particle content in the simulation is plotted on Figs 3.4. We can clearly see that as soon as the MP is activated, the particle content drops by a few percent (5 to 10% at most), which is a clear reminiscent of the experimental density pump-out. We observe a pump-out for all perturbated cases for the simulations without magnetic island (see Fig. 3.4a) with a greater amplitude for the cases $(2,6,4)$ and $(1,10,6)$. It seems that a threshold exists with respect to the amplitude of the MP for the pump-out, as the case $(3,6,4)$ is similar to $(1,6,4)$. For the cases with magnetic islands (see Fig. 3.4b), the maximal pump-out is for the cases $(1,15,4)$ and $(1,6,2)$ whereas the case $(1,22,6)$ could almost be seen as a pump-in. No visible trends can be isolated concerning the pump-out effect with respect to the mode numbers or the amplitude of the perturbation.

### 3.4.2. Mean profiles

After seeing the time trace of the particle content, we take a look at the density radial profile. The Low Field Side (LFS) midplane shows the strongest impact and to better see the impact in the SOL, we plot such profiles on a log scale on Fig. 3.5. The corresponding density gradient, $-\nabla_\psi N/N$ is plotted too. The radial density profiles at the Low Field Side, outer side of a tokamak (LFS) midplane in the far Closed Field lines Region (CFR), shows that whatever the MP, the radial gradient remains almost unchanged while the density is reduced. Then, just before the separatrix, the gradient

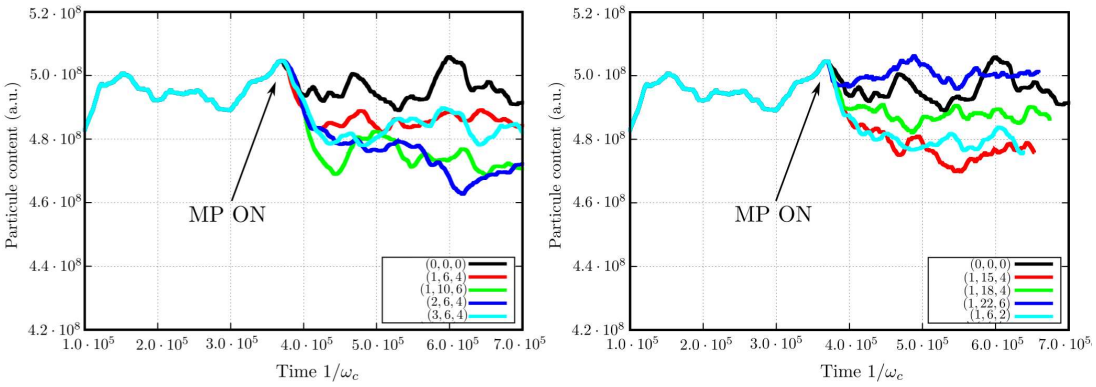


Figure 3.4.: Time traces of the particle content in the simulation box for the case without (3.4a) and with (3.4b) magnetic islands.

decreases compared to the reference, resulting in an increase of the density profiles. The gradient, then, peaks at the separatrix, with a lower peak for most MPs. The density profiles show globally a higher density around the separatrix and in the near SOL, when MP are on. The gradient decreases after the separatrix, in the same way, with or without MPs. Deeper into the SOL, the density profiles flatten, with a mostly higher gradient.

For the cases without magnetic island, (Fig. 3.5a), the density deviation from the reference solution increases with the MP amplitude (see solutions $(1,6,4)$, $(2,6,4)$) but seems to have a saturation as $(3,6,4)$ is really similar to $(2,6,4)$. The solution $(1,10,6)$ behaves almost similarly to the solution $(2,6,2)$, with changes starker than the case of similar amplitude $(1,6,4)$. Thus, even without magnetic islands, the response of the density profile can be impacted in similar way with either a higher amplitude with lower mode number or a lower amplitude but with higher mode number of the perturbation.

For the cases with magnetic island (Fig. 3.5b), the density deviation from the reference solution changes with the MP mode number, the amplitude, here, being the same for all MPs. The changes are however more pronounced than in the solutions without magnetic island, especially around the separatrix and in the SOL. Density gradients decrease more sharply around the separatrix under the effect of the resonant MPs (see Figs. 3.5c and 3.5d). It results in a higher density around the separatrix for these MPs.

The density profile is the first visible change in experiments with MPs. We have seen that the pump-out seems to occur more in the CFR whereas the behaviour in the SOL looks more like an increase of particle. A second observable field is the radial electric field, directly impacted by the new radial component of the magnetic field. Figs. 3.6 show the radial profiles of the mean electrostatic potential $\Phi$ at the LFS midplane. Without magnetic islands (Fig. 3.6a), an increase is observed for most studied cases in the CFR as well as a global drop in the SOL, leading to a flattening of the profile. The

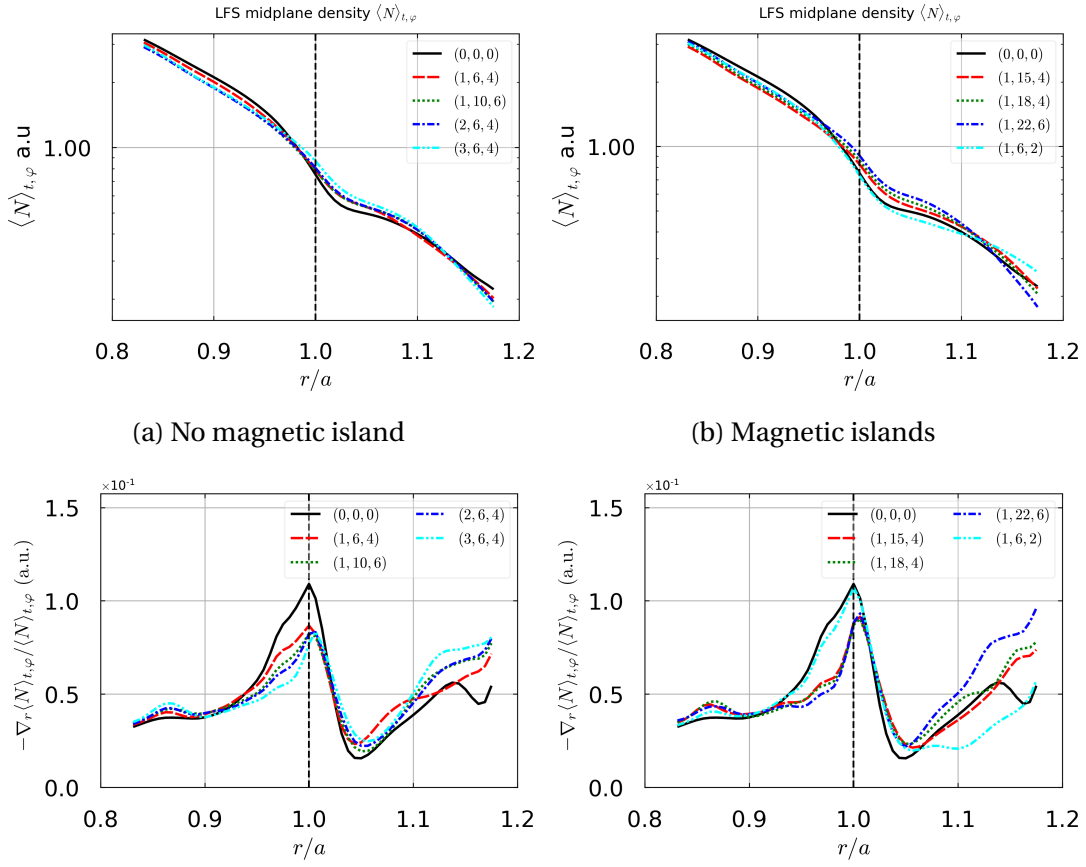


(a) No magnetic island

(b) Magnetic islands

(c) No magnetic island

(d) Magnetic islands

Figure 3.5.: Radial profiles of the mean density (3.5a,3.5b) in log scale and of the density radial gradient (3.5c,3.5d) at the LFS midplane for different MPs. MPs with no magnetic island in the simulation box (3.5a,3.5c). MPs with magnetic islands (3.5b,3.5d). Quantities are averaged on time $t$ and toroidal direction $\varphi$. The vertical dashed line is the separatrix.

direct consequence is an increase of the radial electric field $E_r = \nabla_\psi \Phi$. This trend is observed experimentally too [22, 118, 131]. With magnetic islands (Fig. 3.6b), the shift of potential is a global increase in both CFR and SOL, except in the far SOL where the potential decreases below the reference value of the non perturbated solution. We observe that the amplitude of the increase for the electric potential is dependent on both the mode and the amplitude. Higher modes $(m, n)$ or higher amplitudes $a$ seem to increase the rise of the electric potential.

Figs. 3.6c,3.6d show the radial profiles of the mean radial electric field at the LFS midplane. As a side note, the HFS midplane profile follows the same trend. For the cases without magnetic island (Fig. 3.6c), the flattening of $E_r$ on perturbated solutions, hints by the profile of $\Phi$, is confirmed. The mean radial electric field, negative in the CFR in the reference simulation, shifts towards positive values resulting in a

much lower amplitude. Deeper into the SOL, the mean radial electric field flattens with respect to the reference solution but the profiles become nearly independent on the MP. For the cases with magnetic islands (Fig. 3.6d), in the CFR, the mean radial electric field shifts in the same manner with the MP wavenumber. In the SOL near the separatrix, $E_r$ sharply increases, with an increasing radial gradient with the MPs amplitude, then decreases to a plateau in the far SOL. This flattening of the

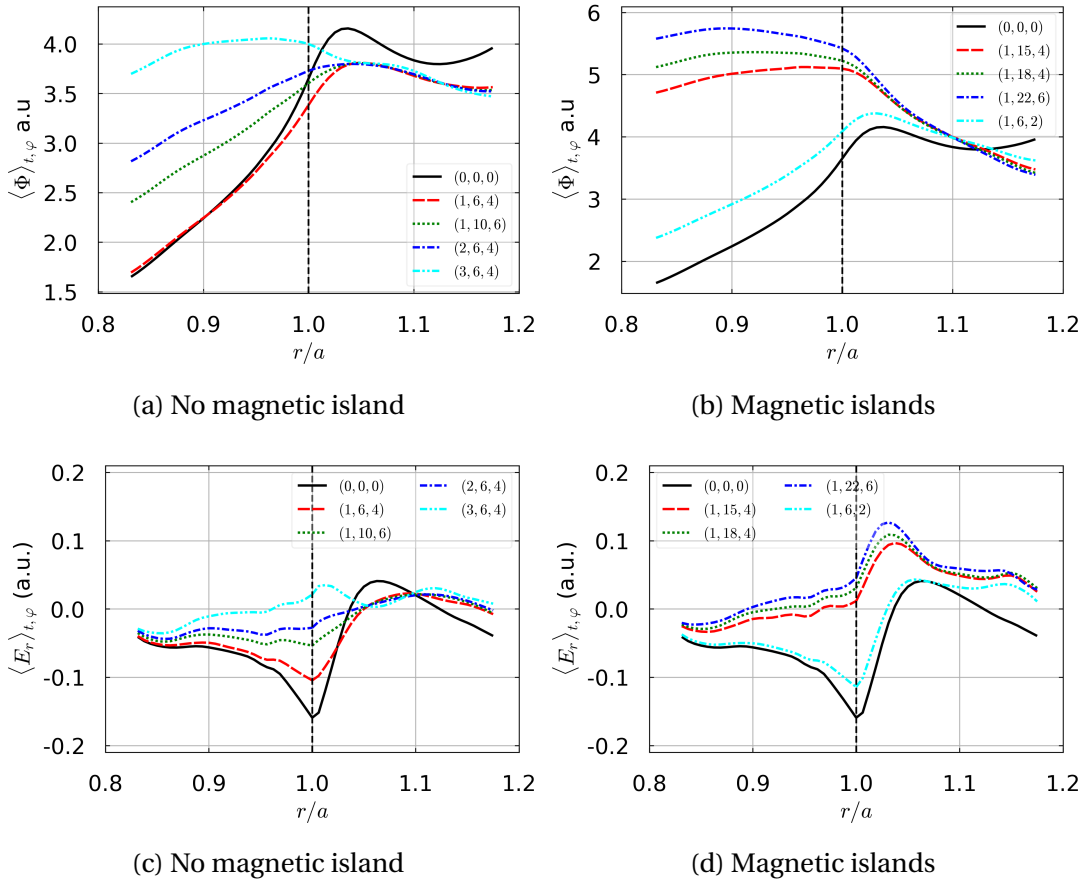


(a) No magnetic island

(b) Magnetic islands

(c) No magnetic island

(d) Magnetic islands

Figure 3.6.: Radial profiles of the mean electrostatic potential $\Phi$ (3.6a,3.6b) and of the mean radial electric field $E^r = \langle -\partial_r \Phi \rangle_{t,\varphi}$ (3.6c,3.6d) at the LFS midplane for different magnetic perturbations (MPs). MPs with no magnetic island (3.6a,3.6c) in the simulation box. MPs with magnetic islands (3.6b,3.6d). Quantities are averaged on time $t$ and in the toroidal direction $\varphi$. The vertical dashed line is the separatrix.

electric potential and the corresponding drop of the radial electric field can have direct consequences on the parallel flows, and this is the object of the following section.

### 3.4.3. Impact on flows and rotation

The change of the radial electric field leads to a reorganization of the plasma rotation and flows which is illustrated by a change of the parallel velocity. It has been experimentally measured in [118] and can be a point of qualitative comparison with the simulations. Fig. 3.7 shows the radial profiles of the mean parallel Mach number ($M_\parallel = \Gamma/(N\sqrt{2})$) averaged on time and on the toroidal direction at the LFS (Figs 3.7c and 3.7d) and HFS (Figs 3.7a and 3.7b) midplanes. A positive Mach number corresponds to the electron diamagnetic direction (in our case, it corresponds to a negative Mach number at the outer target, going toward the positive value at the inner target).

At the HFS midplane, in the cases without island, Fig. 3.7a shows a decrease of $M_\parallel$ for the perturbed solutions around the separatrix, with a reversal of the sign of $M_\parallel$. In the far SOL and in the far CFR, the variations with respect to the reference case are very small. In the cases with magnetic islands in the simulation box, Fig. 3.7b shows similar trends around the separatrix but a significant increase of $M_\parallel$ in the far SOL and a more significant increase in the far CFR than in the cases without magnetic islands. We note that the decrease (or increase if relevant) is more pronounced for high amplitudes or high mode numbers.

At the LFS midplane (Figs 3.7c and 3.7d), all cases show similar trends with a global increase of $M_\parallel$ for perturbated solutions, with still a stronger increase for higher modes or amplitudes. On Fig. 3.7d, the presence of magnetic islands lead to a larger rise of the profiles. For low amplitude and modes MPs, such as $(1,6,2)$ and $(1,6,4)$, the increase of $M_\parallel$ is actually a decrease of the parallel flow as it tends to zero. For larger amplitudes or modes, the MPs create a positive parallel flow, so that the increase is both a change in the direction of the flow and an increase of the speed of the flow. This trend is observed in [118], at least in the SOL. In the CFR, the parallel flow is shown to increase, which we observed mostly at the HFS midplane.

### 3.4.4. Impact on radial transport

In order to better understand the changes in the radial profiles of the density $N$ and the potential $\Phi$ on the global plasma behaviour, the different components of the radial flux are analyzed. As the simulation is flux-driven, and the forcing value of the flux is constant through all simulations, the radial particle flux is constant. The radial particle flux can be decomposed into 5 components:

$$\Gamma^\psi = \Gamma^\psi_{E\times B} + \Gamma^\psi_{\nabla B_i} + \Gamma^\psi_{\text{curv}} + \Gamma^\psi_{\text{diff}} + \Gamma^\psi_\parallel \tag{3.9}$$

The terms successively denote the $E\times B$ velocity driven flux (comprising a mean-field and a turbulent component), responsible of the turbulent transport, two contributions of the 2 curvature driven drifts i.e. the $\nabla B_i$ flux and the curvature one, the diffusive flux and the last one the radial component of parallel flux. The latter is non zero only when MP are turned on.

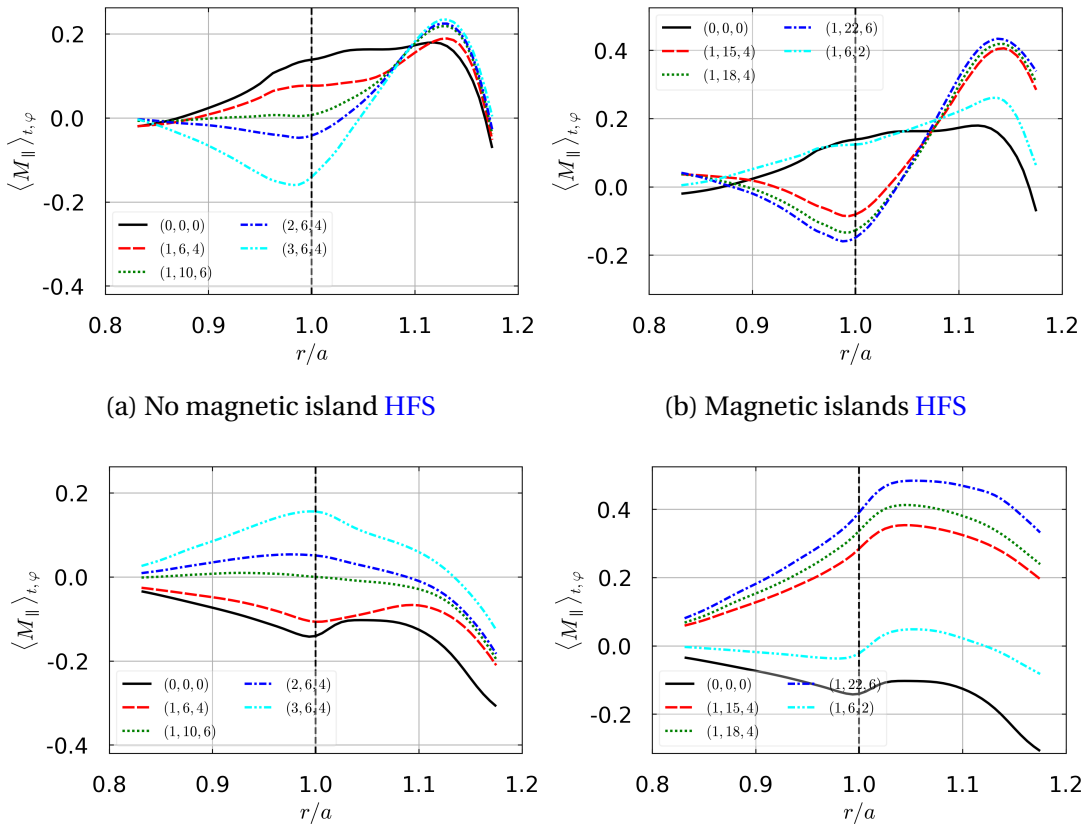


(a) No magnetic island HFS

(b) Magnetic islands HFS

(c) No magnetic island LFS

(d) Magnetic islands LFS

Figure 3.7.: Radial profiles of the mean parallel Mach number $M_\parallel = \Gamma/(N\sqrt{2})$ averaged on time and in the toroidal direction at the LFS (3.7a,3.7b) and at the HFS (3.7c,3.7d). MPs without magnetic islands in the simulation box (3.7a,3.7c) and with magnetic islands (3.7b,3.7d). The vertical dashed line is the separatrix.

#### 3.4.4.1. Flux-surface averaged fluxes

The mean flux is estimated here by integrating each component along the flux surface (in $\theta, \varphi$), then averaged on time. The $E \times B$, the $\nabla B_i$ and the curvature components are shown on Fig. 3.9 at LFS. The diffusive component is shown on Figs. 3.8. The last component is neglectable even with MP, and will thus not be discussed here. To give an idea, the contribution of the $\Gamma_\parallel^\psi$ flux is systematically lower than 1% of the total flux.

In the CFR, both the $E \times B$ and $\nabla B_i$ fluxes slightly increase near the separatrix, that is compensated by an equivalent decrease of the diffusive flux, in both cases with or without magnetic islands. The changes are more complex in the middle and far SOL. For the cases without magnetic island, the $E \times B$ flux (Fig. 3.9a) decreases

in the far SOL, which is partially compensated by an increase of the diffusive flux (Fig. 3.8a). For the cases with magnetic islands, the trend is a growth of the $E \times B$ flux in the middle SOL (Fig. 3.9b) but a decrease in the far SOL. The diffusive flux increases comparably to the decrease of the $E \times B$ flux (Fig. 3.8b). As a note, the $\nabla B_i$ flux is negative (Figs. 3.9c and 3.9d), that explains why the sum of the $E \times B$ and the diffusive fluxes is above 100%. Finally the curvature drift shows an interesting behaviour as the case without magnetic island (Fig. 3.9e) is not impacted whereas the case with magnetic island (Fig. 3.9f) shows a decrease in the SOL accoringly to the mode number. These observations demonstrate a direct impact of the MPs on radial transport mechanisms, explaining the changes in density profiles and the density pump-out. The fact that the radial projection of the parallel flux remains negligible in all our simulations also demonstrates that the perturbation of the profiles cannot be attributed to a direct contribution of parallel mechanims to radial transport in spite of the presence of magnetic islands. A more detailed analysis of the impact on turbulence properties is proposed in Section 3.5.

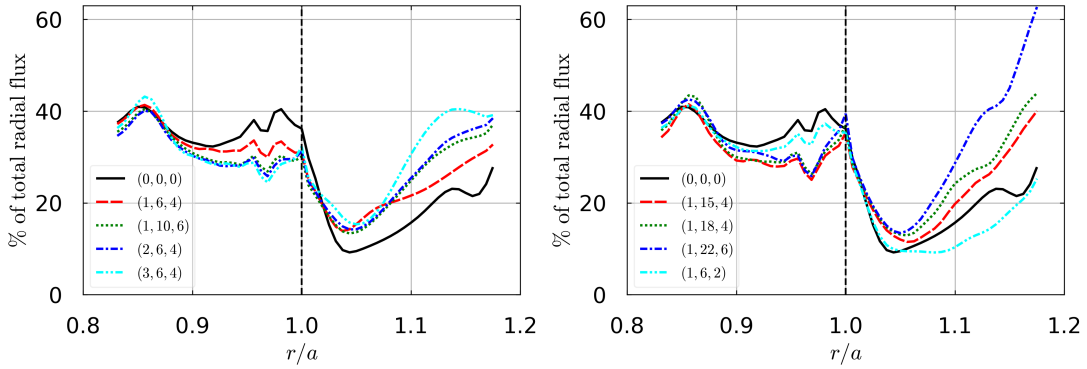


(a) No magnetic island

(b) Magnetic islands

Figure 3.8.: Radial profiles of the mean diffusive flux $\Gamma^{\psi}_{\text{diff}}$ (3.8a,3.8b) at LFS. Cases without magnetic islands (3.8a) in the simulation box. Cases with magnetic islands (3.8b) in the simulation box. The quantities are averaged both in time $t$ and in the poloidal and toroidal directions $(\theta, \varphi)$. The vertical dashed line denotes the separatrix

### 3.4.4.2. Poloidal distribution of $\langle \Gamma^{\psi} \rangle_{t,\varphi}$

In order to explain the changes in the parallel flow velocity, we now investigate the poloidal distribution of radial fluxes. Indeed, the time averaged parallel flow in the edge plasma is driven by two mecanisms: the sheath boundary conditions and the necessity to balance the local divergence of the radial flux ($\boldsymbol{\nabla} \cdot \boldsymbol{\Gamma} = 0$). The poloidal distribution and asymetries of radial fluxes hence are key in the understanding of the

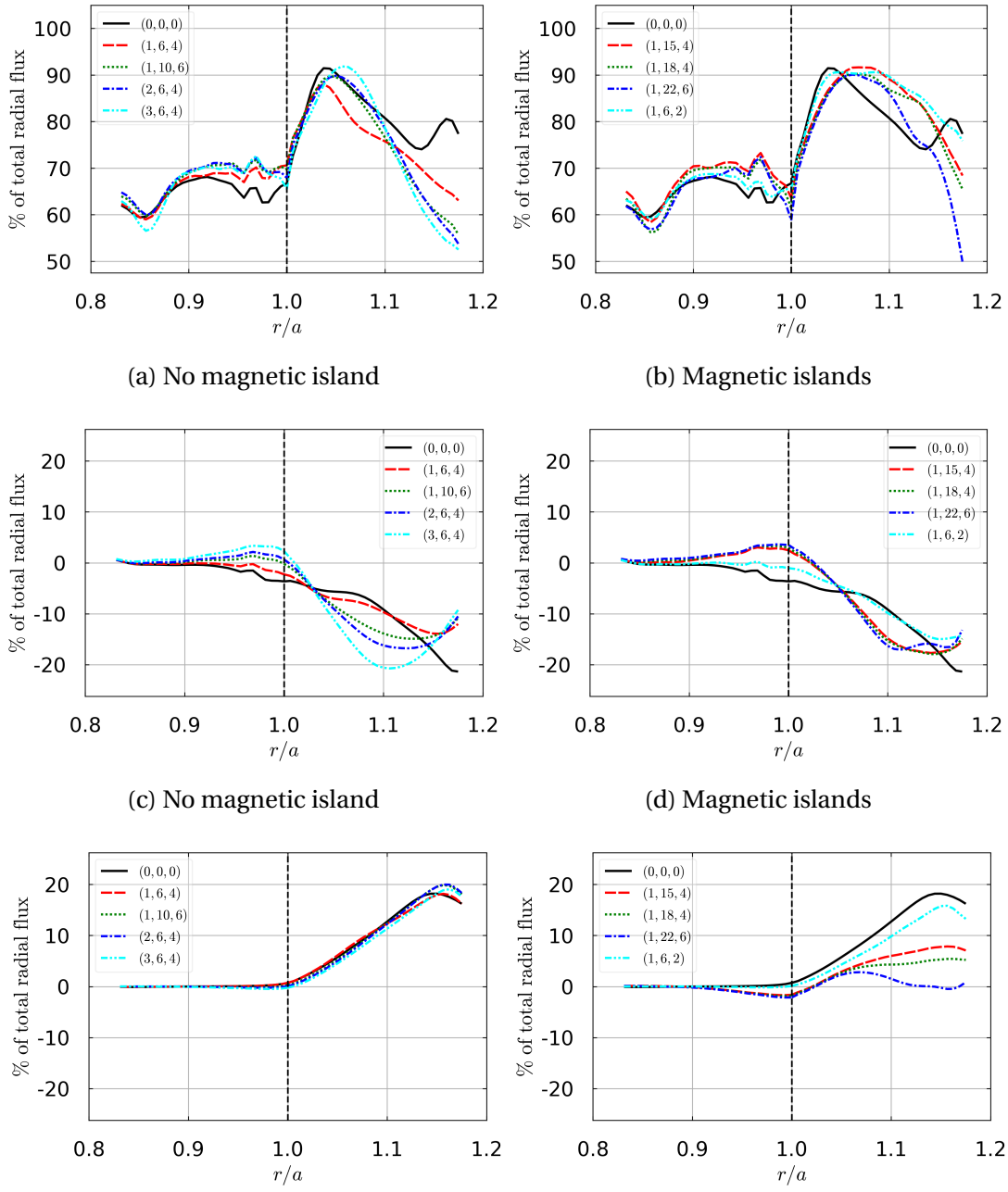


(a) No magnetic island

(b) Magnetic islands

(c) No magnetic island

(d) Magnetic islands

(e) No magnetic island

(f) Magnetic islands

Figure 3.9.: Radial profiles of the mean $E \times B$ flux $\Gamma^{\psi}_{E\times B}$ (3.9a,3.9b), $\nabla B_i$ flux (3.9c,3.9d) and curvature flux $\Gamma^{\psi}_{\text{curv}}$ (3.9e,3.9f) at LFS. Cases without magnetic island (3.9a,3.9c,3.9e) in the simulation box. Cases with magnetic islands (3.9b,3.9d,3.9f) in the simulation box. The quantities are averaged both in time $t$ and in the poloidal and toroidal directions $(\theta^*, \varphi)$. The vertical dashed line denotes the separatrix

changes on parallel flows $M_\parallel$. For each quantity we note:

$$f(t,\psi,\theta^*,\varphi) = \bar{f}(\psi,\theta^*,\varphi) + \tilde{f}(t,\psi,\theta^*,\varphi) \tag{3.10}$$

where $\bar{f} = \langle f \rangle_t$ is averaged over time and $\langle \tilde{f} \rangle_t = 0$ per construction. We are interested here in the time averaged fluctuating parts, so that only the product of two (or more) fluctuating parts remains. We apply this decomposition to $\langle \Gamma^\psi_{E\times B} \rangle_{t,\varphi} = \langle N u^\psi_{E\times B} \rangle_{t,\varphi}$.

$$\langle N u^\psi_{E\times B} \rangle_t \equiv \bar{\Gamma}^\psi_{E\times B} = \bar{N}\bar{u}^\psi_{E\times B} + \tilde{N}\tilde{u}^\psi_{E\times B} \equiv \bar{\Gamma}^\psi_{\bar{E}\times B} + \bar{\Gamma}^\psi_{\tilde{E}\times B} \tag{3.11}$$

Where we note, by simplicity, the time averaged $E\times B$ radial flux as $\bar{\Gamma}^\psi_{E\times B}$, the part, corresponding to the mean-field flux solved by transport code without turbulence, is noted $\bar{\Gamma}^\psi_{\bar{E}\times B}$ and the part, corresponding to the averaged flux driven by turbulence, is noted $\bar{\Gamma}^\psi_{\tilde{E}\times B}$.

Fig. 3.10 shows the poloidal mean profiles related to the decomposition of $\bar{\Gamma}^\psi_{E\times B}$, averaged in the toroidal direction at the flux surface $r/a = 0.9$. The Fig. 3.10a clearly shows a shift to the LFS midplane ($\theta = 0$) of the ballooning of the total $\bar{\Gamma}^\psi_{E\times B}$ mean flux when the solution is perturbated by MP. This shift is larger when magnetic islands are in the simulation box as shown on Fig. 3.10b. This change in the poloidal asymmetry is directly related to the change of $M_\parallel$. This is underlined by the complex role plays by the mean and fluctuating part of the flux.

If the fluctuating part is the major contribution of the flux (see on Fig. 3.10e and 3.10f) with an increase of the ballooning in the upper LFS midplane, the mean-field part varies the most. The mean contribution shows a complete reversal (see on Figs. 3.10c and 3.10d) around the LFS midplane.
The others mean-field contributions, $\bar{\Gamma}^\psi_{\nabla B_i}$ and $\bar{\Gamma}^\psi_{\text{curv}}$, are not shown here as their variations are at least one order of magnitude lower than the $E\times B$ mean-field variations. Furthermore, the most varying part, the $\bar{\Gamma}^\psi_{\text{curv}}$ for the case with magnetic islands, shows a similar profile as the mean-field $E\times B$ with an increase at the bottom of the machine and a decrease at the top, the reference case being completely flat.

The main conclusion of this part is that the MPs create a poloidal redistribution of the radial fluxes, especially the mean-field part and particularly the $E\times B$ flux. This is linked to the poloidal reorganization of the density and is in agreement with the parallel flow changes.

#### 3.4.4.3. On the role of the $E\times B$ transport

To explore the ballooning, we continue by studying the radial profiles of the mean-field and turbulent part of the $E\times B$ flux at both HFS and LFS midplanes on Figs. 3.11. One can clearly have a more detail view for the HFS midplane. The Figs 3.11a and 3.11b confirm the lack of change of the static part $\bar{\Gamma}^\psi_{\bar{E}\times B}$ in the SOL both without and with islands. Nevertheless, near the separatrix, a decrease can be seen. We note for the case

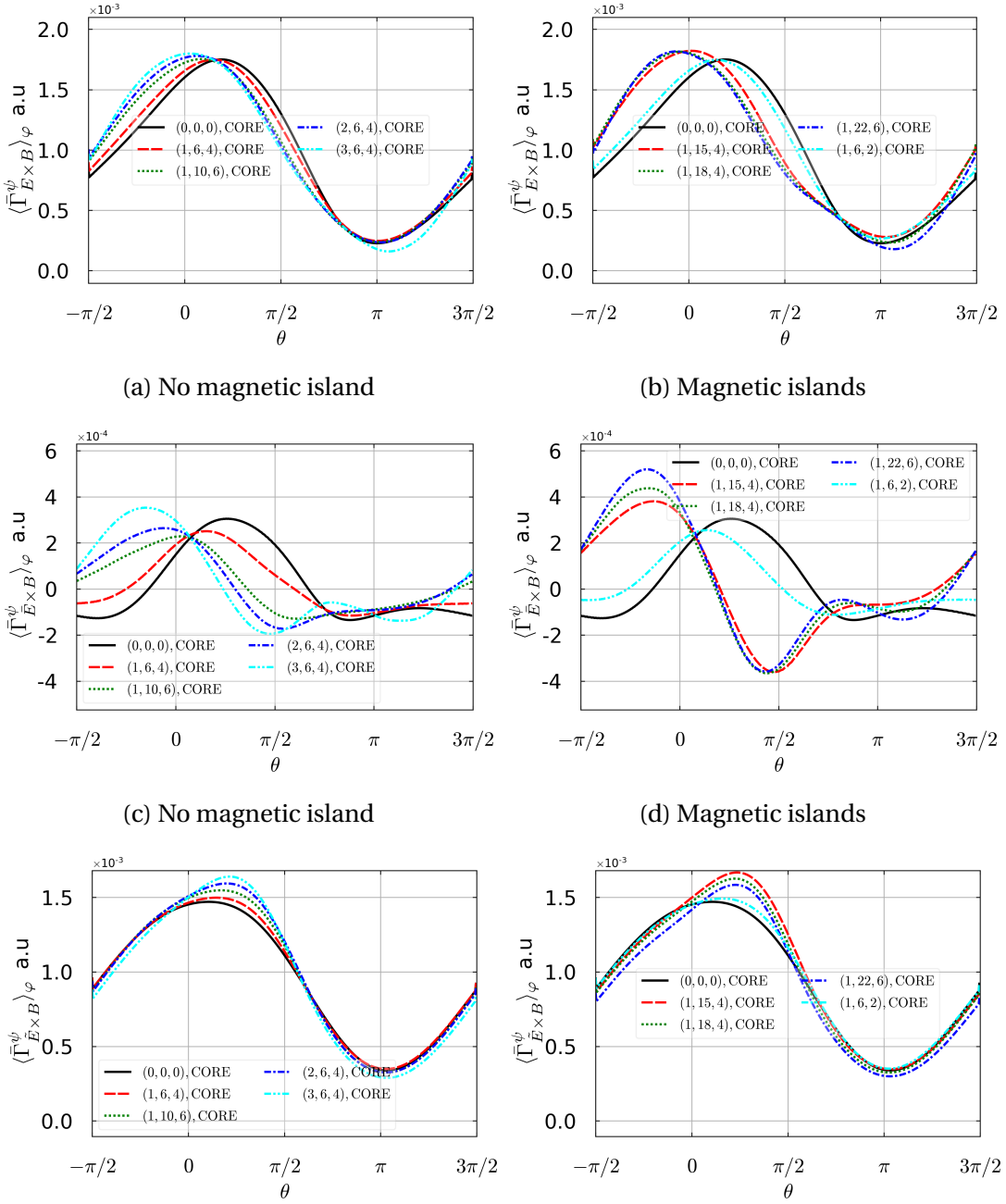


(a) No magnetic island

(b) Magnetic islands

(c) No magnetic island

(d) Magnetic islands

(e) No magnetic island

(f) Magnetic islands

Figure 3.10.: Poloidal profiles of the $E \times B$ total flux $\bar{\Gamma}^{\psi}_{E\times B}$ (3.10a,3.10b), the mean-field part $\bar{\Gamma}^{\psi}_{\bar{E}\times B}$ (3.10c,3.10d) and the fluctuating part $\tilde{\Gamma}^{\psi}_{\tilde{E}\times B}$ (3.10e,3.10f) parts at $r/a = 0.9$ (CFR). Quantities are $(t,\varphi)$-averaged. (3.10a,3.10c,3.10e) cases without magnetic islands in the simulation box. (3.10b,3.10d,3.10f) cases with magnetic islands in the simulation box. $\theta = 0$ corresponds to the LFS midplane.

without magnetic island that the decrease is deeper for higher amplitude or higher mode numbers. With magnetic islands, the decrease reaches a threshold for all high mode numbers.
At LFS midplane (Fig.3.11c and 3.11d), the static part of the tranport increases with the MP at the CFR, which is what has been observed in the poloidal profiles. The increase seems linked to the amplitude and the mode numbers. For the case without magnetic island (Fig.3.11c), the increase goes up with the amplitude and the mode numbers and reverse just after the separatrix, fluctuating then around zero value of the static transport when the MP are on. For the case with magnetic islands (Fig.3.11d), the increase is stronger and goes up with the mode numbers in the CFR. Then, in the SOL, we see a progressive decrease toward zero, except for the low mode number where the value stays constant in the SOL.

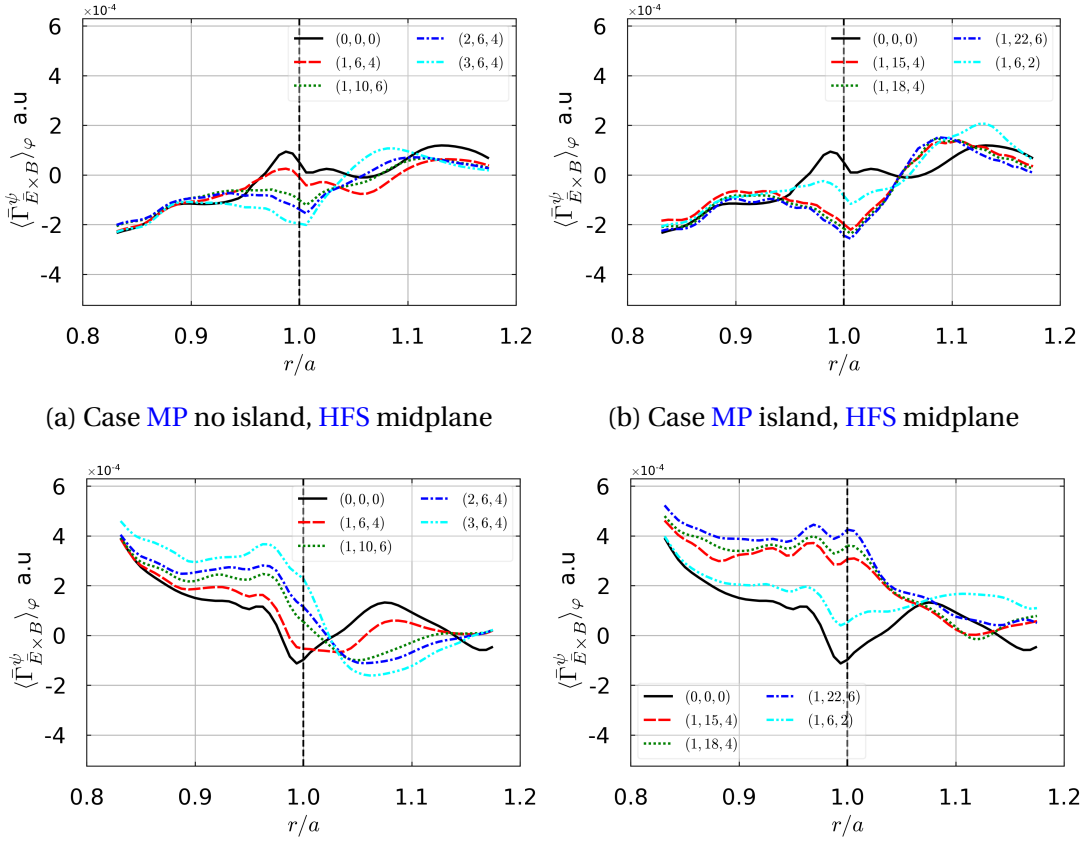


(a) Case MP no island, HFS midplane

(b) Case MP island, HFS midplane

(c) Case MP no island, LFS midplane

(d) Case MP island, LFS midplane

Figure 3.11.: Radial profile of $(t,\varphi)$-averaged of $\bar{\Gamma}^{\psi}_{\tilde{E}\times B}$, the static (mean-field) part of the $E\times B$ radial transport

Concerning the turbulent part, shown in Figs. 3.12, the changes are not in the same regions. At HFS midplane, we notice no change at the CFR, neither without magnetic island (Fig. 3.12a), nor with (Fig. 3.12b). A decrease is noted in the SOL, independant

of the MP for the case without island but more important for higher mode numbers for the case with. At LFS midplane, the turbulent part is quasi not impacted by the MP. For the case without magnetic island (Fig. 3.12c), a small increase can be observed in the CFR just before the separatrix, whereas with magnetic islands (Fig. 3.12d), a decrease is seen at the separatrix only. For both, the change happens in a similar fashion not dependant of the MP.

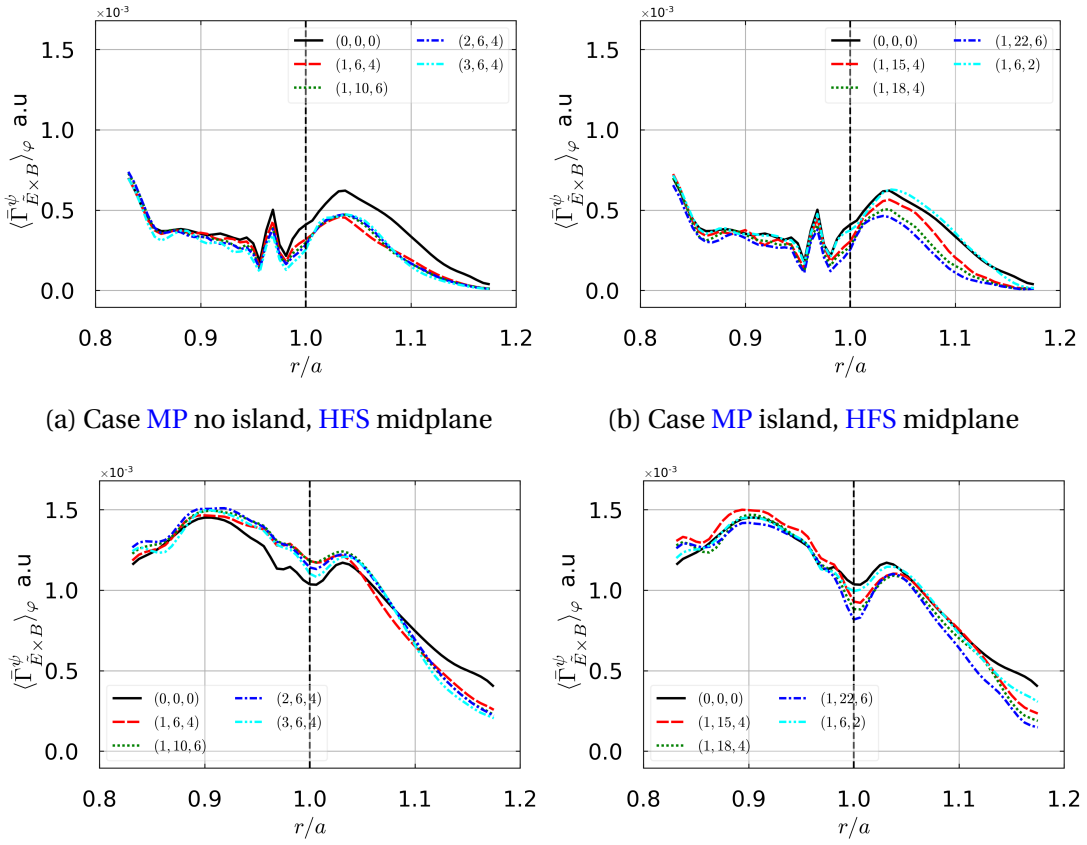


(a) Case MP no island, HFS midplane

(b) Case MP island, HFS midplane

(c) Case MP no island, LFS midplane

(d) Case MP island, LFS midplane

Figure 3.12.: Radial profiles of $(t,\varphi)$-averaged of $\tilde{\Gamma}^{\psi}_{\tilde{E}\times B}$, the fluctuating part of the $E\times B$ radial transport

The $E\times B$ transport hints of a clear change of ballooning. The picture we have is that MPs tend to shift the ballooning from the top LFS to bottom LFS (while still being around the LFS midplane). The radial $E\times B$ transport increases in the SOL in the lower part of the outer midplane but mostly due to the static component of the transport. Whereas the turbulent part increases the ballooning at the upper outer midplane, it is compensated by the static part that decreases in this region. This is the case in the CFR. The global balloning in the SOL is then shifted toward the top of the machine. Finally, we note that the turbulent part is dominant but the fluctuations created by the MP are of similar order for the turbulent and static parts.

### 3.4.5. On the role of the $E \times B$ shear

An explanation of the changes observed on the mean flow could have been the decrease of the shearing flow into the SOL, mainly the $E \times B$ shear $s_{E\times B}$, due to MPs. Even if effectively the impact of MPs is a global reduction of the shear as shown on Fig. 3.13, the reduction is much stronger for the non resonant modes than for the resonant ones, while the impact on the ballooning is stronger for resonant modes. It seems so that the shearing reduction due to MPs is not the main mechanism related to this mean flow modification.

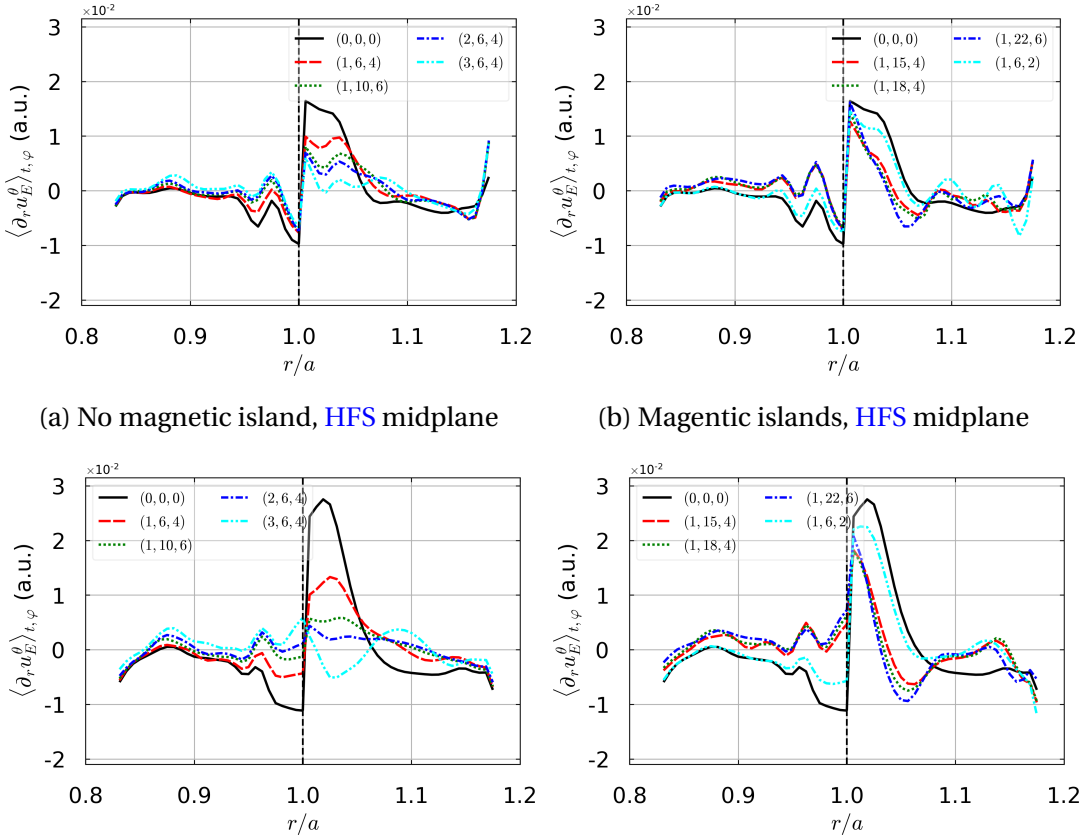


(a) No magnetic island, HFS midplane

(b) Magentic islands, HFS midplane

(c) No magnetic island, LFS midplane

(d) Magnetic islands, LFS midplane

Figure 3.13.: Radial profiles of the $E \times B$ shear averaged over $(t, \varphi)$ at the HFS midplane 3.13a,3.13b and at the LFS midplane 3.13c,3.13d, $\langle s_{E\times B} \rangle_{t,\varphi} = \langle \partial_r u^{\theta^*}_{E\times B} \rangle_{t,\varphi}$. $\langle s_{E\times B} \rangle_{t,\varphi} = \langle \partial_r u^{\theta^*}_{E\times B} \rangle_{t,\varphi}$. MPs corresponding to magnetic islands into the computational domain 3.13b,3.13d or not 3.13a,3.13c.

### 3.4.6. SOL width

The flux reorganization incites us to analyze the impact of the MPs on the SOL width. The decrease of the density in the SOL can be approximated into an exponential de-

| Density decay length (in $\rho_L$) | | | | | |
|---|---|---|---|---|---|
| | MP | $\langle\lambda_N\rangle$ | Trend | $\langle\lambda_{N,\text{near}}\rangle$ | Trend |
| | (0,0,0) | 36 | – | 11 | – |
| MP no island | (1,6,4) | 30 | ↘ | 14 | ↗ |
| | (2,6,4) | 30 | ↘ | 15 | ↗ |
| | (3,6,4) | 28 | ↘ | 16 | ↗ |
| | (1,10,6) | 30 | ↘ | 15 | ↗ |
| MP islands | (1,6,2) | 41 | ↗ | 11 | – |
| | (1,15,4) | 33 | ↘ | 13 | ↗ |
| | (1,18,4) | 31 | ↘ | 13 | ↗ |
| | (1,22,6) | 29 | ↘ | 13 | ↗ |

Table 3.2.: SOL density decay length $\lambda_N$ (in Larmor radius $\rho_L$) averaged in poloidal and toroidal direction. $\lambda_{N,\text{near}}$ is taken in the near SOL near the separatrix.

cay such that $\partial_\psi \langle N\rangle_t = \langle N\rangle_t / \lambda_N$ where $\lambda_N$ is the density gradient length, sometimes called the density decay length. The impact of MP on $\lambda_N$ is shown in Tab. 3.2. The values are obtained through an exponential fit of the density in the SOL. Except for the perturbation (1,6,2) with an increase of around 10%, the density decay length decreases when the solution is perturbated. This decrease is of the order of 20%, and curiously of similar order for every MP. The mechanism of the drop of $\lambda_N$ can be seen as a consequence of the flow reorganization discussed before. This is what has been seen in Fig. 3.5 except for the perturbation (1,6,2). The solutions also show an increase of the radial density gradient in the SOL, which is also a reason for the decrease in $\lambda_N$. The particularity of (1,6,2) can not be explained but we underline, that it is an extremum in the scan in mode numbers with larger islands than the others.

As a remark, we could argue on the behaviour of $\lambda_N$, as the density gradient in the SOL, near the separatrix, decreases, especially for the cases without magnetic islands (see Figs. 3.5). This means that just after the separatrix, $\lambda_N$ actually increases due to the MP, as shown as $\lambda_{N,\text{near}}$ in Tab. 3.2 (which is directly calculated as a local $\lambda_N$). This is one of the limits of reducing the SOL width to a single averaged value with a simple exponential curve fit. A double exponential for the near and far SOL could have been more accurate but it raises the question of the choice of what can be considered near and far SOL. Thus, for a simple isothermal model, we should conclude that the SOL width, on average, decreases due to MP but increases locally just after the separatrix.

## 3.5. Impact of MP on turbulence properties

We have seen in the previous section that MPs impact the plasma equilibrium via a reorganization of particles fluxes, including the radial flux driven by turbulence. Changes in the properties of fluctuations have also been reported experimentally as a signature of the impact of MP on the edge plasma [103, 118]. Here, the impact of the MPs on turbulent fluctuations is analyzed.

Quantities are decomposed into a mean and a fluctuating part as presented in Eq 3.10. The fluctuations properties are analyzed from Probability Density Functions (PDFs). The skewness for any variable $X$ is defined here as:

$$\gamma_1(X) = E\left[\left(\frac{X-\mu_X}{\sigma_X}\right)^3\right] \tag{3.12}$$

where $\mu_X$ is the mean and $\sigma_X$ the standart deviation of $X$. The Pearson's moment coefficient of excess kurtosis is defined as:

$$\gamma_2(X) = E\left[\left(\frac{X-\mu}{\sigma}\right)^4\right] - 3 \tag{3.13}$$

where the minus 3 stands for having a kurtosis of 0 for a normal distribution.

### 3.5.1. Impact on the fluctuations levels

The evolution of the fluctuations level for density events in the radial direction, characterized here by the toroidal averaged of $\sigma_N/N$, is shown on Fig. 3.14. To compare both the difference with or without magnetic island and the poloidal asymmetry of the turbulence, the standard deviation is plotted at the HFS and the LFS midplane.

At the HFS midplane on Figs. 3.14a and 3.14b the fluctuations level in the CFR is low (of the order of 5%) and rather constant in the radial direction up to the vicinity of the separatrix. This trend remains unsensitive to MPs, whether magnetic islands are present or not. On the contrary, MPs have a clear impact on the density fluctuations level in the SOL. In this region, MPs reduce the fluctuations level from around 25% down to 15 to 20% depending on cases. In the cases with no magnetic island, the lowering of fluctuation level is nearly independent of the MP, whereas it becomes very sensitive to the perturbations wavenumber in the cases with magnetic islands. In these cases, the difference in the fluctuations levels with respect to the unperturbated case increases with $r/a$, and with the poloidal wavenumber $m$ of the perturbations.

At the LFS midplane on Figs. 3.14c and 3.14d, the fluctuations level in the CFR rapidly and continuously increases with $r$, independently of the MP, from 10% at the core boundary to 25% at the separatrix. The difference of amplitude with the HFS illustrates the ballooned character of turbulent transport already mentionned in Section 3.4. In the near SOL, the fluctuations level decreases with respect to the unperturbated case. The differences are larger in the cases with magnetic islands (up

to 5% absolute increase) than without islands (at most 1%). The trend is opposite with an increase of the fluctuations level when perturbations are added (at the notable exception of the (1,6,2) case). The amplitude of the increase does not seem to depend on the presence or not of magnetic islands, and no clear trend emerges with the mode number. However, the transition from lower fluctuations level in the near SOL to higher fluctuations level in the far SOL is systematically located further from the separatrix, when magnetic islands are present.

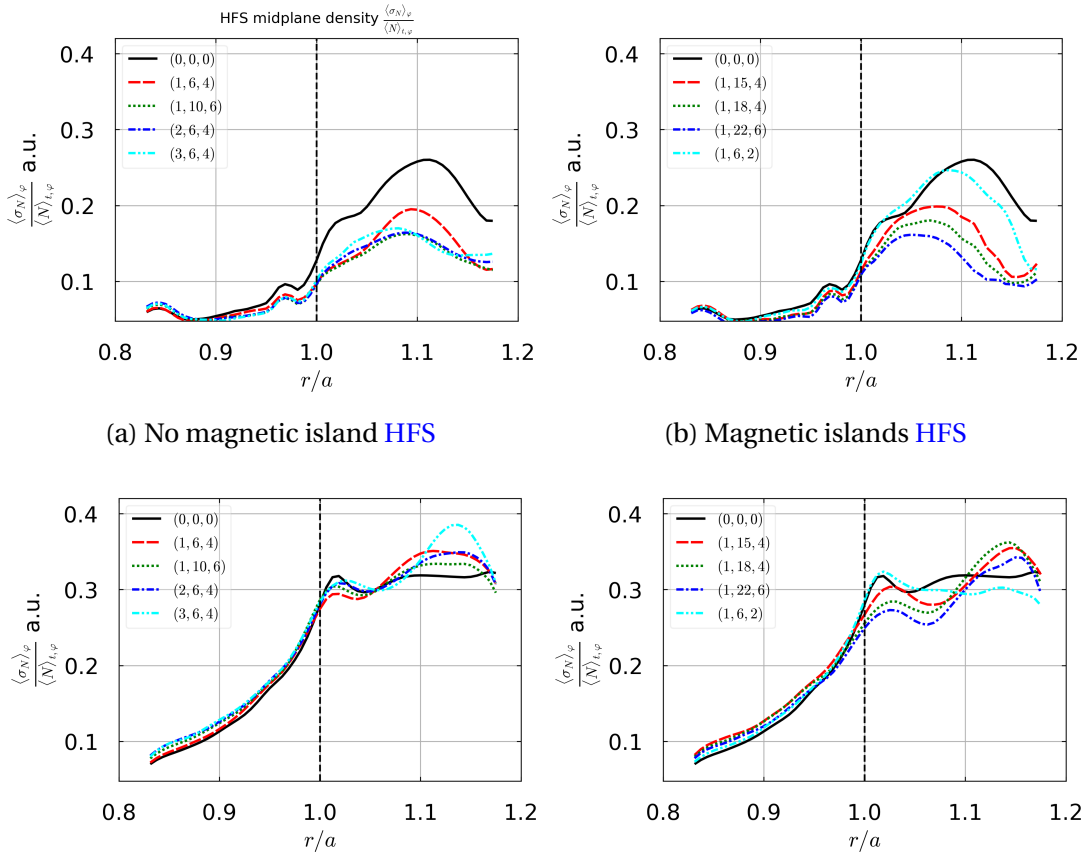


(a) No magnetic island HFS

(b) Magnetic islands HFS

(c) No magnetic island LFS

(d) Magnetic islands LFS

Figure 3.14.: Radial profiles of the standart deviation over time of the density averaged in the toroidal direction $\varphi$ and normalized by the $(t,\varphi)$-averaged density at the HFS (3.14a,3.14b) and at the LFS (3.14c,3.14d). Cases with no magnetic island (3.14a,3.14c) in the simulation box. Cases with magnetic islands (3.14b,3.14d). The dashed line is the separatrix.

### 3.5.2. Impact on the turbulence intermittency

The PDFs of the density are plotted on Fig. 3.15 at two radial locations in the CFR and into the SOL at LFS midplane, i.e. $r/a = 0.98$ and $r/a = 1.02$, respectively. Both

locations correspond to a region with magnetic islands (if relevant). The color zones correspond to the direct histogram of the events and the curves are obtained through a kernel density estimation[1]. In the CFR, the PDFs of the perturbated solutions are nearly Gaussian for the case without magnetic island (see Fig. 3.15a). The cases with magnetic islands (see Fig. 3.15b) show a positive skewness (skewed to the right), which seems stronger for higher mode number. This is a visible effect of the islands on thef turbulence itself.

In the SOL, the PDF of the reference case shows a PDF shape characterized by intermittent turbulence with a well-marked positive skewness with a large number of events concentrated on the left of the mean of the PDF (see Figs. 3.15c and 3.15d).

For the cases without magnetic island (Fig. 3.15c), the PDF skews to the right, similarly with the reference case, which is still a mark of intermittency. Nevertheless, with a higher amplitude (or mode number), the peak of the curve decreases, forcing the distribution toward a less skewed profile.
For the cases with magnetic islands (Fig. 3.15d), the peaks of the PDFs decrease immediately for all MPs with no visible trends. The PDFs are still skewed to the right but as for the cases without magnetic islands, the PDFs tends toward a gaussian shape, compared to the reference case. These results show that the MPs change the turbulence properties only a little in the CFR. The changes occur mainly near the separatrix and in the SOL with an opposite effect between the HFS and LFS midplanes. At the HFS midplane, the intermittency and bursty behaviour of the turbulence increases while the effect is opposite at the LFS midplane. The intermittency still exists but with less high density (bursty) events.

The radial profiles of the skewness of the density along the time axis are now shown on Fig. 3.16 at both HFS and LFS. It is noted $\gamma_{1,N}$ and it is averaged in the toroidal direction. In the CFR, all plots show that the impact of MPs is weak, with a nearly zero skewness in this region. We note nevertheless an increase of the skewness for the LFS midplane when we approach the separatrix. The near zero value means that, as in the reference solution, density events stay clearly well centered around the mean value with no favorable events (bursts or sinks). These plots show whatever the solution a larger skewness on the LFS midplane than on the HFS corresponding to the turbulence ballooning already mentionned.

In the SOL, the impact of perturbations is larger in all plots. At the HFS midplane and with respect to the reference solution (Figs. 3.16a and 3.16b), there is a small decrease of the skewness near the separatrix, this effect being more pronounced in the case without magnetic island, followed by a large increase in the middle of the SOL, this effect being now more pronounced in the case with magnetic islands. For non resonant modes Fig. 3.16a, there is no clear dependence of the solution on the wavenumber or the amplitude of the pertubation even if the perturbation of largest amplitude has the largest skewness all the others behave fairly similarly. For resonant modes Fig. 3.16b, MP of high wavenumbers lead to a high positive skewness. As a final

[1] It is, in simple term, a smoothing data problem, so that the PDFs look nicer than a naive histogram

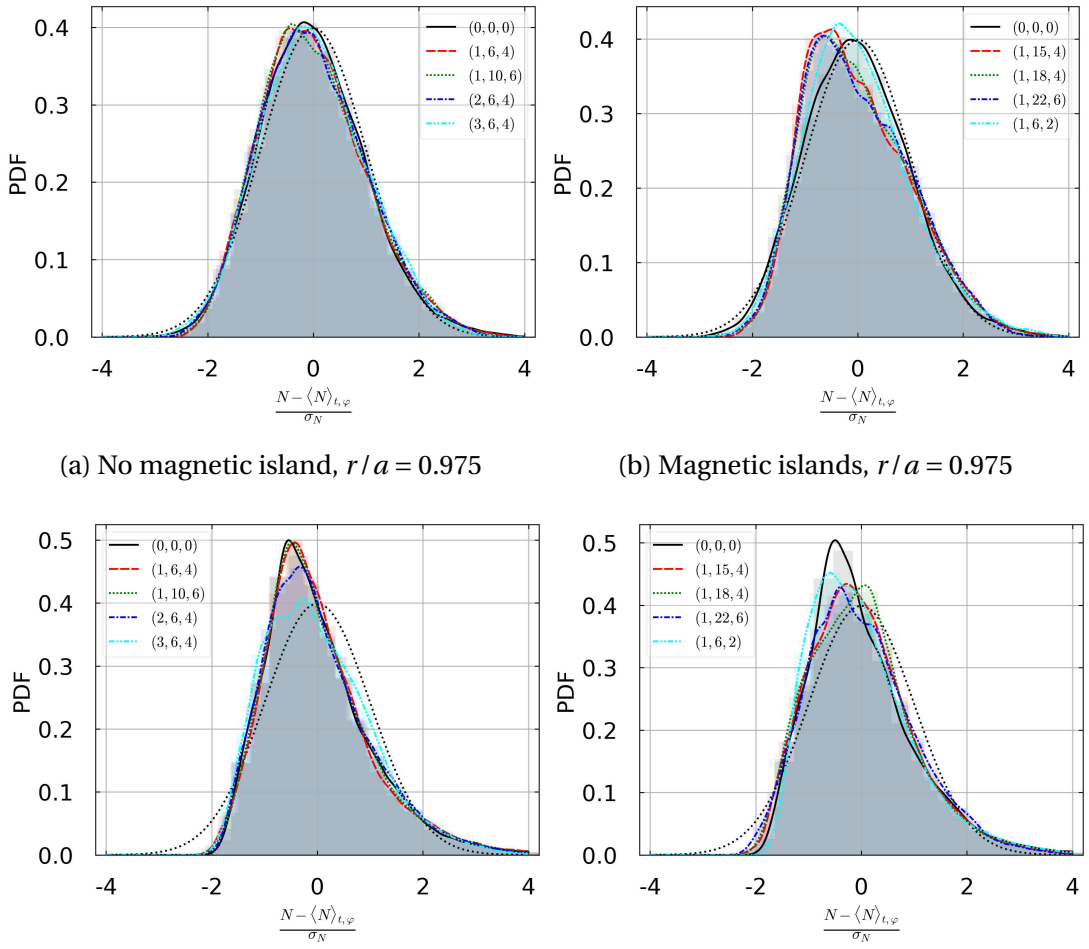


(a) No magnetic island, $r/a = 0.975$

(b) Magnetic islands, $r/a = 0.975$

(c) No magnetic island, $r/a = 1.0188$

(d) Magnetic islands, $r/a = 1.0188$

Figure 3.15.: Normalized PDFs of density events along $(t,\varphi)$-axis at the LFS midplane and at two radial positions in the CFR and in the SOL, i.e. $r/a = 0.98$ 3.15a,3.15b and $r/a = 1.02$ 3.15c,3.15d. Cases with no magnetic island 3.15a,3.15c in the simulation box. Cases with magnetic islands 3.15b,3.15d. As a reference, the dotted black line corresponds to an exact Gaussian. The color zones is the histogramm of each curve. The curves have been obtain with a kernel density estimation.

overall trend at HFS midplane, we can see that MPs seem to shift spacially to the left the behaviour into the SOL of the density events (the events arising earlier with MP).

At LFS midplane, without or with magnetic islands, the largest changes concentrate into the SOL. For non resonant modes and with respect to the reference solution, the skewnesses of the perturbed solutions are smaller in the vicinity of the separatrix and then become larger deeper into the SOL, Fig. 3.16c. These deviations become larger when the amplitude of the perturbation is increased. We note an increase of

the skewness in the far SOL. A similar trend is observed with magnetic islands, but the skewness remains smaller than the reference solution even in the far SOL (see Fig. 3.16d). The deviation becomes larger with the mode wavenumber.

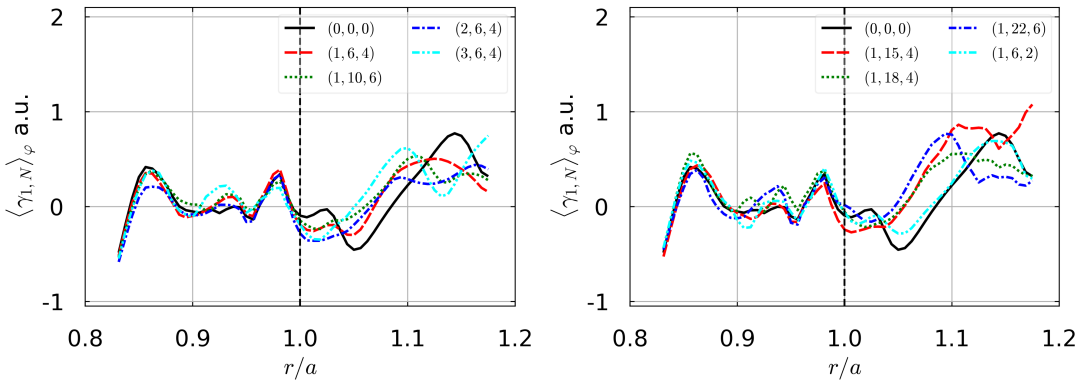


(a) No magnetic island, HFS midplane

(b) Magnetic islands, HFS midplane

(c) No magnetic island, LFS midplane

(d) Magnetic islands, LFS midplane

Figure 3.16.: Radial profiles of the skewness over time of the density, averaged over $\varphi$. HFS midplane 3.16a,3.16b. LFS midplane 3.16c,3.16d. The error bar for each curve is estimated to be smaller than 5%.

To see the repartition of extrem density events (both positive and negative), the radial profiles of the kurtosis, averaged in $\varphi$, is plotted on Figs. 3.17. Beginning at the HFS midplane with Fig. 3.17a and 3.17b, both shows little change in the CFR. We note an increase at the middle of the SOL. Without magnetic island, this increase occurs for the highest mode numbers and is pretty similar for the others mode numbers despite their varying amplitudes. When the magnetic islands are presents (Fig. 3.17b), the case with high mode numbers shows the highest effect, with the exception of MP $(1,18,4)$. This increase switch the sign of the kurtosis and can double the amplitude. The near zero kurtosis hints of a normal distribution in CFR. On the opposite, with the kurtosis near one in the SOL, the weight of extreme events in the distribution is

over-represented.

At LFS midplane, the effect is quite similar for both cases with a small decrease of the kurtosis in CFR to tend near zero and a sharp decrease in the SOL, just after the separatrix. Except for the far SOL, the MP seem to decrease the kurtosis. Without magnetic island (Fig. 3.17c), the mode numbers does not seem to change the effect but the amplitude does, with a stonger flattening for higher amplitude. With magnetic islands (Fig. 3.17d), the higher the mode numbers, the stronger the flattening is. This caracterizes a strong effect on turbulent events, with a loss of extrem events after the separatrix. The bursty behaviour of the turbulence with the change between a closed then opened fieldline region looks to be dampened by the MP.

To conclude, the MP have a small impact on the CFR, both at LFS and HFS midplane. At HFS midplane, in the middle SOL, extrem events seems to be amplified by MPs. At LFS midplane, the extrem events are considerably dampened by MP just after the separatrix but remain in high number in the far SOL.

### 3.5.3. Shape of turbulent structures

The MPs modify the magnetic equilibrium, creating islands of various sizes. It raises the question of the modification of the turbulent structures themselves.
We thus plot on Figs. 3.18 the auto-correlation length of density fluctuation in the poloidal direction, taken at $r/a = 1.05$ and averaged it along the time and toroidal axis. In practice we compute the correlation on the quantity $(N - \langle N \rangle_{\theta^*})/\sigma_N^{\theta^*}$ by mean of Fourier transform (with enough padding zero as the turbulent signal is far from periodic in the SOL). We clearly see that no variation are observed on the central peak, meaning that the length of typical structures in the poloidal direction is not influenced by MP. The variations occur mainly on the neighbour peaks, which show an increase when MP are applied. The impact of MP seems, in our cases, to add a few poloidal harmonics on turbulence.

## 3.6. Implications for mean field modeling

So far, the numerical analysis of the impact of RMPs on the edge equilibrium plasma including neutrals recycling have only been performed using mean-field codes [45]. In the absence of better indications, these studies are conducted assuming that perpendicular diffusion coefficients characterizing anomalous radial transport remain unchanged when RMPs are switched on. Our simulations allow us to cast some light on this assumption. An effective transport coefficient has been computed from turbulence simulations. It has been defined as:

$$D_\perp = -\frac{\Gamma^\psi}{\nabla_\psi N} = -\frac{\Gamma^\psi_{E\times B} + \Gamma^\psi_{\nabla B_i} + \Gamma^\psi_{\text{curv}} + \Gamma^\psi_{\text{diff}} + \Gamma^\psi_{\parallel}}{\nabla_\psi N} \tag{3.14}$$

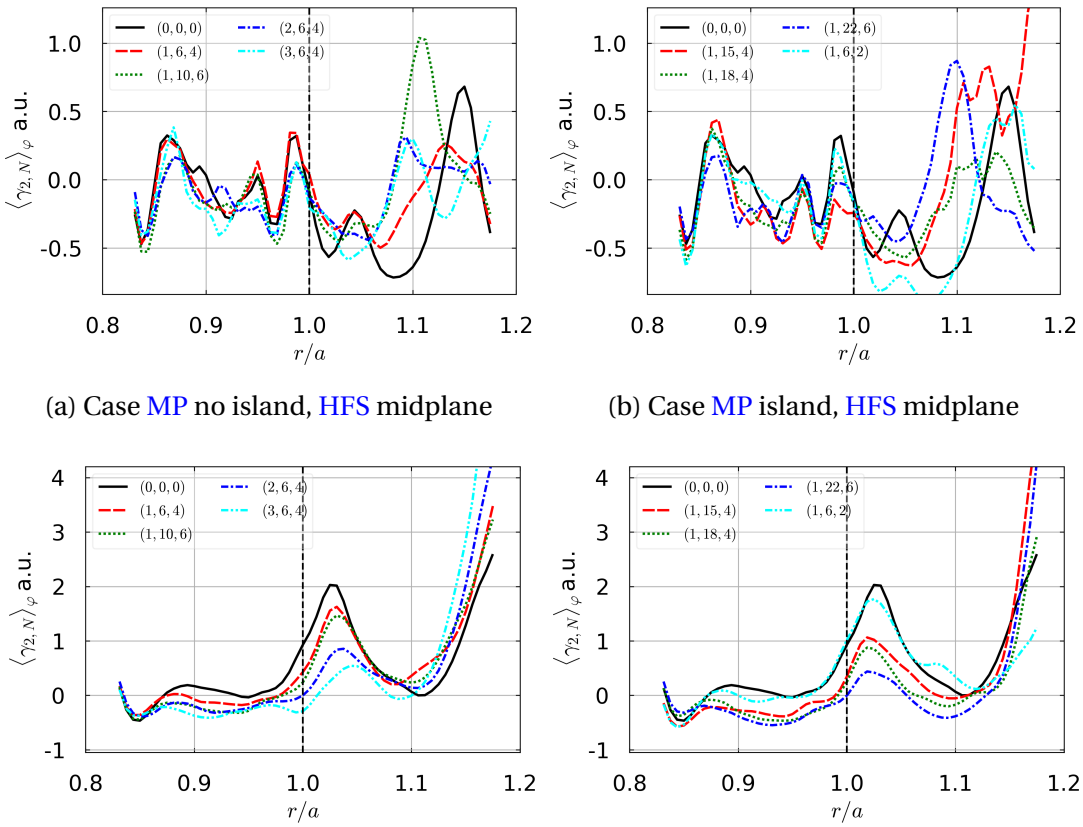


(a) Case MP no island, HFS midplane

(b) Case MP island, HFS midplane

(c) Case MP no island, LFS midplane

(d) Case MP island, LFS midplane

Figure 3.17.: Radial profile of the kurtosis over time of the density, averaged over $\varphi$. A positive kurtosis (leptokurtic) means fatter tails, 0 is a gaussian and a negative kurtosis means thinner tails. The dashed line is the separatrix, the SOL is on the left side.

We show the variations of $D_\perp$ at the LFS midplane in the SOL in table 3.3, where we can clearly see the loss of perpendicular transport for most MP (except (1,6,2)). The decrease can go beyond 20% for the case (1,22,6). The decrease of $D_\perp$ is actually consistent with the observations of the increase of the density gradient in the SOL. Nevertheless, an average over the radial direction hides a lot about the true behaviour of the diffusion coefficient, that varies significantly depending on the localization. The Figs. 3.19 illustrate the radial variations at the LFS midplane of $D_\perp$. We can see the small increases when MPs are on near the separatrix in the CFR, consistent with the decrease of the density gradient (see Figs. 3.5) and the small increase of the radial flux. The decrease, noted with the radial average, is still present but occurs mainly after the separatrix and in the mid SOL.

The Figs. 3.20 illustrate two examples of 2D maps in the poloidal plane of the time and toroidal averaged $D_\perp$, to better show the poloidal variations of the diffusion

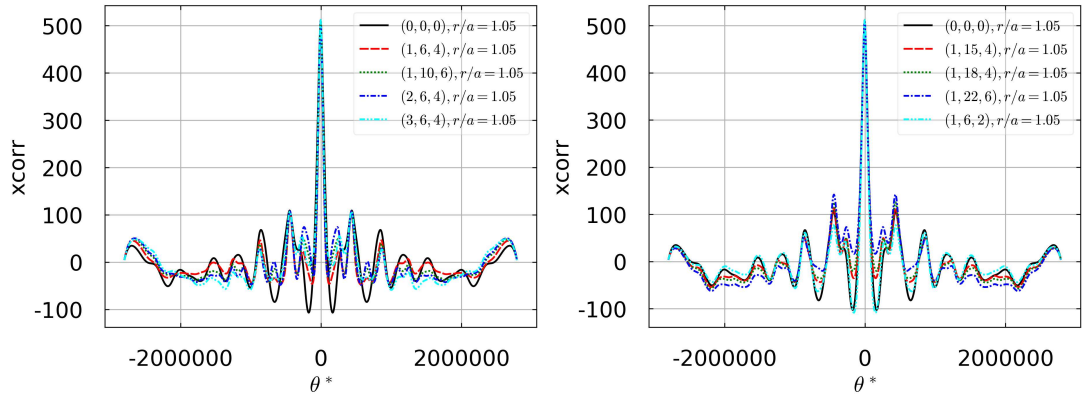


(a) Case MP no island, $r/a = 1.05$ (b) Case MP island, $r/a = 1.05$

Figure 3.18.: Autocorrelation function in the poloidal direction of density fluctuation, averaged in time and $\varphi$ at $r/a = 1.05$

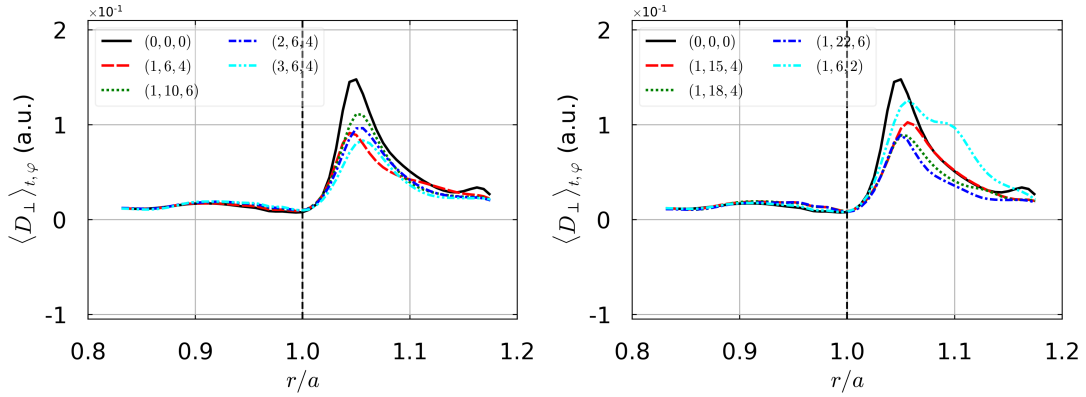


(a) No magnetic islands (b) Magnetic islands

Figure 3.19.: Radial profil at the LFS midplane of $D_\perp$, averaged in time and $\varphi$.

coefficient. Results show a rather weak variations in the poloidal direction of this coefficient, with as expected highest values on the LFS (appart from the immediate vicinity of the limiter where even negative effective transport coefficients are found). A complete study we have performed, shows a global lowering of the averaged $D_\perp$ (in the same way as $\lambda_N$) when MPs are applied: $D_\perp = 3.3 \cdot 10^{-2} (\rho_L^2 \omega_c)$ for the reference solution $(0,0,0)$, and $D_\perp$ oscillates between $2.3 \cdot 10^{-2}$ and $2.8 \cdot 10^{-2}$ depending on the perturbation, excepted for an unexplained reason for the MP $(1,6,2)$ for which $D_\perp = 3.8 \cdot 10^{-2}$.

The comparison between turbulent and mean-field simulations is continued in the Chapter 5. The observations done during this chapter hint to possible diverging behaviours between the two approaches.

| $D_\perp$ (in $\rho_L^2\omega_c$) | | | |
|---|---|---|---|
| | MP | $\langle D_\perp \rangle$ | Trend |
| | (0,0,0) | 0.066 | – |
| MP no island | (1,6,4) | 0.049 | ↘ |
| | (2,6,4) | 0.050 | ↘ |
| | (3,6,4) | 0.044 | ↘ |
| | (1,10,6) | 0.053 | ↘ |
| MP islands | (1,6,2) | 0.076 | ↗ |
| | (1,15,4) | 0.053 | ↘ |
| | (1,18,4) | 0.047 | ↘ |
| | (1,22,6) | 0.042 | ↘ |

Table 3.3.: SOL $D_\perp$ at LFS midplane, averaged on time and in the toroidal direction

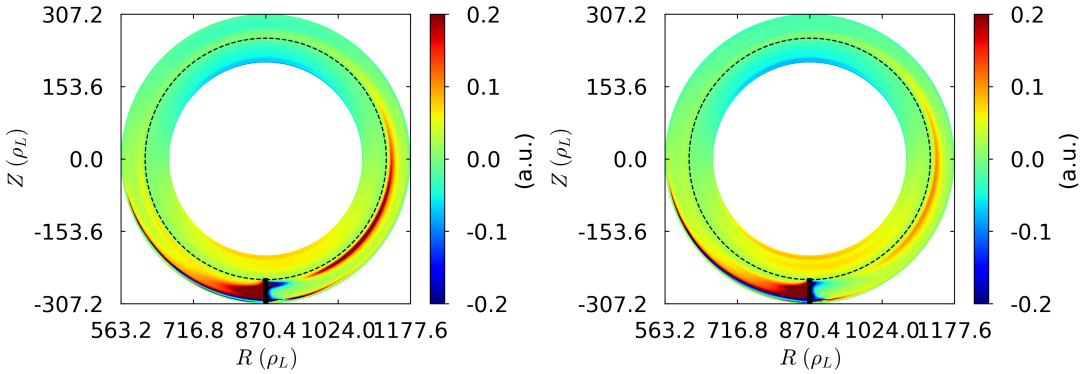


(a) Reference solution (0,0,0)

(b) Magnetic perturbation (1,15,4)

Figure 3.20.: 2D map in the poloidal plane of the effective diffusion coefficient for the radial transport $D_\perp = \Gamma^\psi / \nabla_\psi N$, averaged in time and $\varphi$.

## 3.7. Conclusion

This work is a first step toward a better understanding of the impact of 3D magnetic perturbations (MPs) on electrostatic and isothermal fluid turbulence at the edge of a limiter plasma in circular geometry. Single mode 3D MPs of small amplitude have been considered eventually leading to magnetic islands in the computational domain or not depending on the wavenumbers combination in the poloidal and toroidal direction (resonant modes or not). Results show an impact of MPs on the plasma equilibrium, and on a lesser extent, on the turbulence properties, with a magnitude which depends on bothe the MPs amplitude and wavenumbers.

Concerning the plasma equilibrium, numerical results show an impact on profiles and flow. They recover some key features seen in experiments, such as the loss of density in the edge of the closed field lines region and the decrease of the radial electric field, coupled with a change of the plasma rotation. These changes of profiles are associated with a reorganisation of both mean and turbulent fluxes in the edge plasma, leading to strong changes and even local reversal of the parallel velocities (hence toroidal rotation). The latter effect had also been reported in experiments.

As far as exhaust issues are concerned, numerical results have shown that the MPs impact the SOL width, with a decrease of the SOL width, on average, consistent with the increase of the radial density gradient in the SOL. This is most probably related to the overall decrease of the radial turbulent transport in the SOL, driven by a drop of the fluctuations level in the presence of a MPs. We note, nevertheless, that just after the separatrix, MPs locally increase the SOL width.

Concerning the fluctuation properties, MPs do not change the fundamental nature of edge turbulence which remains dominated by intermittent large amplitude events associated with radially filamentary structures. Nevertheless, quantitative properties are impacted, especially in their spatial distribution (LFS/HFS asymmetries and radial profiles). MPs trigger a drop of the relative density fluctuations level in the near SOL. In the far SOL, the fluctuations level is found to decrease on the HFS but increase on the LFS. Intermittency, measured here as the skewness of the PDF of density fluctuations is also impacted, with a reduction in the vicinity of the separatrix in open field lines. On the opposite, an increase of the skewness of density fluctuations is observed in the outermost part of the close field lines when magnetic islands are present. The latter effect is more marked when magnetic islands are present in the vicinity of the separatrix. We have noted a difference between LFS and HFS midplane, with a more important decrease of the skewness in the SOL, near the separtrix at LFS midplane compare to the HFS midplane. The skewness increases then at the HFS in the mid SOL whereas this increase is observed on the far SOL at the LFS only. Finally, the shape of the turbulent structures show more poloidal harmonics with MPs.

Finally, the study of the behaviour of an equivalent diffusion coefficient (taking into account turbulent transport) hints to a complex influence of the MPs both (at least) in the radial and poloidal directions. This calls for a comparison between mean-field and turbulent simulations that will be the topic of Chap. 5.

# 4. Turbulent heat transport in circular geometry with 3D magnetic perturbations

## Table of Content

This chapter extends the analysis of Chap. 3 to a non-isothermal model.

# 4.1. Settings for non-isothermal simulations

## 4.1.1. Implementation of magnetic perturbation in non isothermal simulations

The same magnetic perturbation described in Section 3.1 is considered. In particular, modified drift terms have been explicitely added in the resolution of the energy equations 2.51 and 2.52. This is especially important for the heat fluxes define as:

$$\boldsymbol{q}_{e/i} = K_{0,e/i} T_{e,i}^{5/2} \nabla_{\parallel} T_{e,i} \boldsymbol{b} \tag{4.1}$$

This term is treated implicitely in a similar way as for the vorticity equation. As for the vorticity, the perturbated terms added due to MPs are treated in an explicit way, assuming them to be small enough to not impact numerical stability of the code.

## 4.1.2. Simulation settings

The simulations set-up is similar to the one defined in Chap. 3, with however two key differences related to the definition of the parallel resistivity $\eta_{\parallel}$ and the introduction of the parallel heat conductivity.

| Simulation | $a$ | $m$ | $n$ |
|---|---|---|---|
| Reference | 0 | 0 | 0 |
| MP | 1 | 6 | 2 |
| | 0.35 | 15 | 4 |

Table 4.1.: Parameters $(a, m, n)$ for the MPs used in the non isothermal simulations. $a$ is the amplitude, $m$ the poloidal mode number and $n$ the toroidal one. $n$ is given for a full torus.

The parallel resistivity $\eta_{\parallel}$ is now dependent on both $\nu^{\star}$ and the local dimensionless electron temperature $T_e$ according to the following expression:

$$\eta_{\parallel} \propto \nu^{\star} T_e^{-3/2} \tag{4.2}$$

with $\nu^{\star} = 0.05$ at the separatrix. Thus $\eta_{\parallel}$ is now a function of time and space.
The collisionality also determines the collisional parallel heat conductivity derived from the Braginskii model such that:

$$K_{\parallel,e/i} \propto T_e^{5/2} / \nu^{\star} \tag{4.3}$$

**Sources -** In non isothermal simulations, particle and energy sources are set independently and can eventually be decoupled as will be done later on in this manuscript. For a start, we set both at the inner boundary (assuming the particles and energy come from the core). The form of the source is a radially decaying function (vanishing exponential) after a few cells, to ensure a constant particle source and to have no effect

on the simulation away from the boundary.

In a second set of simulations, the position of the particles source has been changed assuming that 10% come from the core and 90% come from the top of the limiter (located at the bottom) in the form of a vanishing exponential in $\psi$ and $\theta^*$ directions. The sources of particle have been set so that the integral of the two sources (from the core and from the limiter) is equal to the integral of the source of particles coming only from the core. This models a simplified recycling phenomenon, the particles in experiments, mainly coming from the target through the recycling process. A scheme of the particles and energy sources is illustrated on Fig. 4.1. A 2D map of a full recycling source of particles is given on Fig. 4.2b. The standard case with particles coming from the core is plotted on Fig. 4.2a.

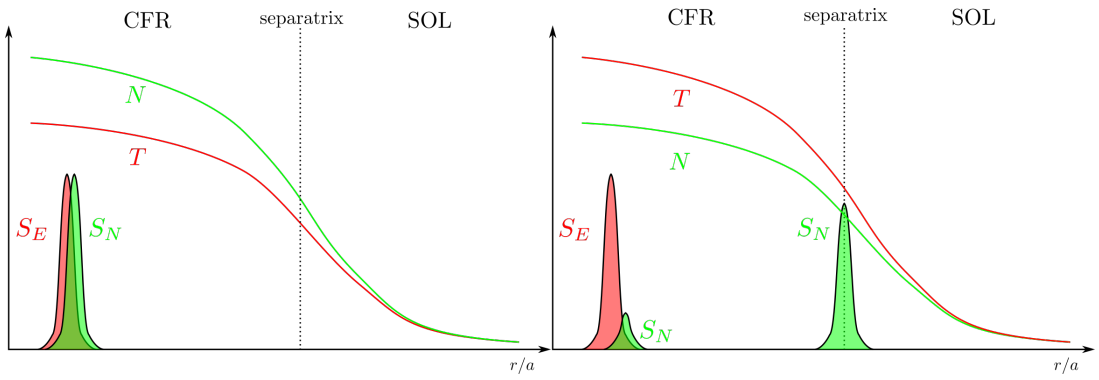


(a) Core (b) Recycling

Figure 4.1.: Sources repartitions of density and energy for the standart cases (4.1a) and recycling cases (4.1b). The Gaussian-like functions are not to scale.

In the following we distinguish cases without recycling (particles coming from the core) and cases with recycling (particles coming mainly from the limiter). A time shot of the density fluctuations levels on Figs. 4.3 illustrates the large differences in the turbulence patterns between the solutions without (Fig. 4.3a) and with (Fig. 4.3b) recycling.

**Magnetic perturbations (MPs)** - Let's consider small magnetic perturbations under the form:

$$\epsilon_p = a \cdot 10^{-3} \sin\left(m\theta^* - n\varphi\right) \tag{4.4}$$

where $(a, m, n)$ define the amplitude, the poloidal and toroidal modes, respectively, given in Table 4.1. The toroidal mode $n$ is given for a full torus. The reference simulation corresponds to $(a, m, n) = (0, 0, 0)$.

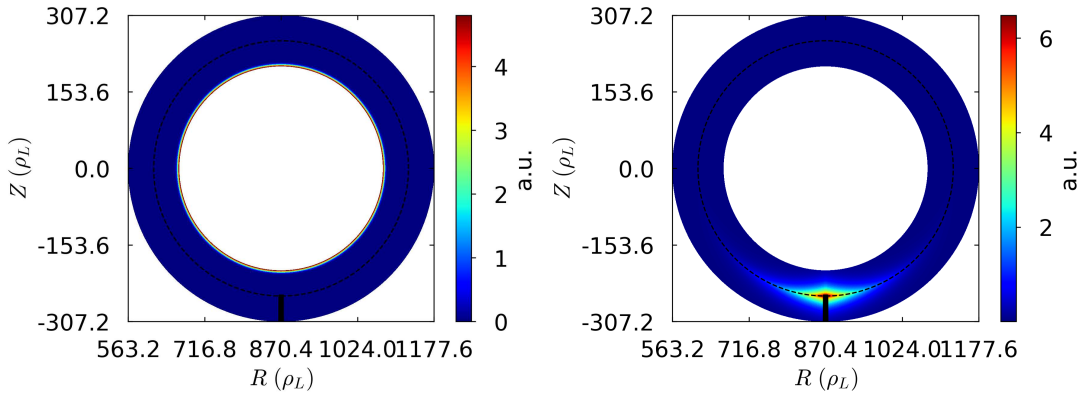


(a) 100% from the core

(b) 100% from the target

Figure 4.2.: Distribution of the source of particles. Case 4.2a: 100% of the particles coming from the core. Case 4.2b: 100% of the particles produced by the recycling and coming from the target

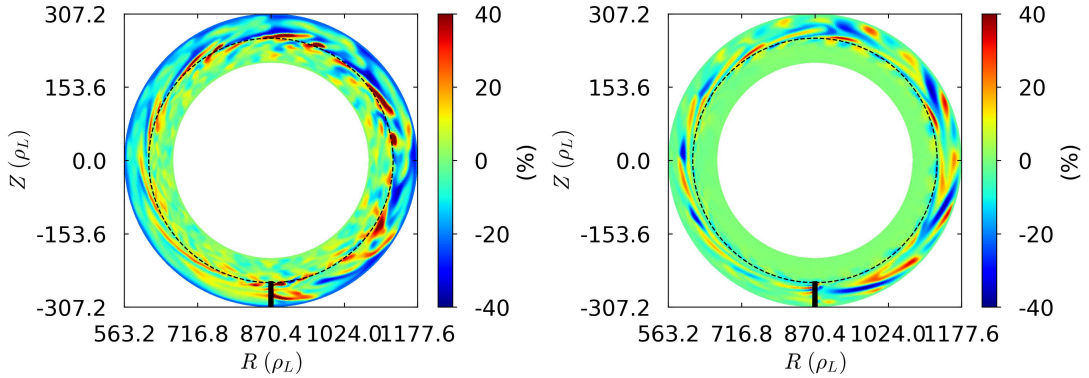


(a) No recycling

(b) Recycling

Figure 4.3.: Instantaneous 2D map of density fluctuations ($N - \bar{N}$) at $\varphi = \pi/2$ (mid of the half-torus). Left (4.3a) is the reference without recycling. Right 4.3b is the reference with recycling.

### 4.1.3. Density pump-in or pump-out: the importance of recycling

Fig. 4.4 shows the time traces of the particles content for different configurations. Without recycling, a density pump-in (around 20%) is observed when the MPs are switched on. This is not observed in experiments. However, former results comparing solutions with recycling and without recycling suggest that relocating the particle source in the vicinity of the limiter leads to a major reorganization of fluxes in the edge plasma. We have then decided to run simulations in similar conditions but with

a particle source mimicking recycling as described above.

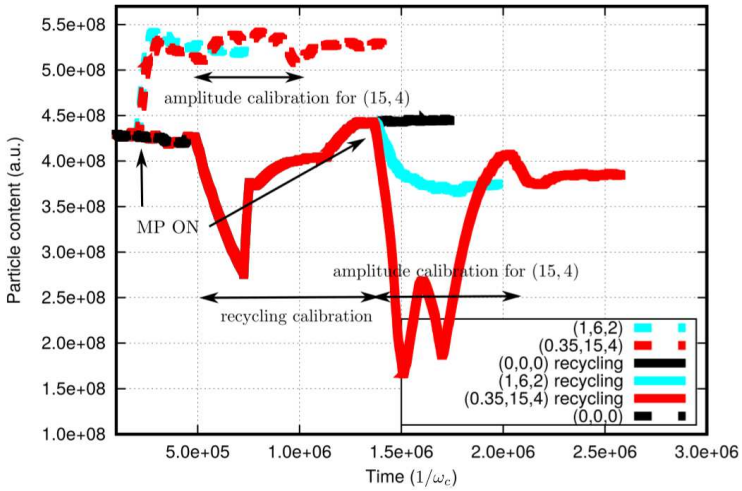


Figure 4.4.: Time trace of the particle content for the sources of particles and energy comming from the core (dashed lines) and with recycling (full lines).

With recycling and MPs, the pump-in becomes a pump-out (around 20%) as shown on Fig. 4.4. This change underlines the sensitivity of the solution to the position of the particles source and hints on a complex interaction between particles and energy fluxes that the isothermal model could not take into account.

## 4.2. Impact of 3D MPs on the mean fields

The time traces of the particles content have shown different behaviour between simulations with or without recycling. In the following, we analyze the impact of MPs in each case in order to highlight the role played by the source position in the observed phenomenology. The comparison is made first between the two reference simulations then between the different MP cases.

### 4.2.1. Mean profiles

Toroidal and poloidal averaged radial profiles of the density are shown on Fig. 4.5b and Fig. 4.5a with and without recycling, respectively. The corresponding density gradient defined as $-\nabla_\psi N/N$ is plotted below (see Figs. 4.5d and 4.5c respectively). There is a difference on the density radial profiles between the two reference cases. The density is clearly lower in the CFR for the recycling cases. It is linked to a decrease of the density gradient, with a flattening of the density profile. This is an expected behaviour as the relocation of the source from the inner boundary to the limiter leads to the disappearance of particles fluxes in the CFR (there is no source of particles at

the inner boundary anymore so no flux to evacuate). The fluxes being mainly driven by the radial gradient, the system does not require anymore the build up of steep density profiles to evacuate the incoming particles flux.

Without recycling, the density profiles with MPs show a clear pump-in on the whole profiles, with a stronger one in the CFR compare to the SOL. The pump-in is around 15% at most in the CFR and lower than 5% in the SOL.
With recycling, we clearly see a pump-out in the CFR which is at most around 30% in the CFR, then it shifts to a small pump-in after the separatrix of the same order of magnitude as the ones in the SOL for the cases without recycling. It is coherent with the 20% pump-out observed in the time trace of the particle content.
The last comment about the density profiles can be done uppon the MPs themselves. The two are vastly different in modes number and amplitude. We can nevertheless see a similar behaviour between the high amplitude/low mode numbers $(1,6,2)$ and low amplitude/high mode numbers $(0.35,15,4)$.

Regarding the density gradients, we observe a similar trend for the two reference cases in the CFR, then a peak value near the separatrix, stronger for the solution with recycling. The peaking of the density gradient in the recycling case is enhanced by the localization of the source near the separatrix, which calls for a progressive build-up of the radial flux/gradient when moving out radially in this region. Without recycling, the MPs do not change the gradient much in the CFR but this latter decreases in the far SOL. With recycling however, the gradient clearly decreases in the CFR and at the separatrix whereas its value with MPs are almost the same as the reference with recycling in the SOL.

Figs. 4.6 show now the electron $T_e$ and ion $T_i$ temperatures radial profiles, averaged on time, toroidal and poloidal directions. Between the reference cases, the change in the particle source location impacts the temperatures profiles in an opposite way with respect to the density profiles. When the source is located at the inner boundary (no recycling), temperature profiles are relatively flat in the CFR. In contrast, when the particles source is located at the limiter (recycling) the profiles are steeper and the temperatures larger. This can be again related to the change in the radial distribution of the radial fluxes, as it will be discussed later in more details. When the source of particles and energy are located both at the inner boundary, both outwards particle and energy fluxes are driven in the CFR. In that case, most of the energy flux is driven convectively by the particle flux. When the sources are decorrelated (different locations), only an outwards energy flux is present in the CFR. The energy flux then needs to be conductive, and can only be driven by a temperature gradient.

With MPs, for the non recycling cases, both the electron (see Fig. 4.6a) and the ion (see Fig. 4.6c) temperatures decrease. For each temperature, the decrease is the same for the two MPs. For $T_e$, the decrease is around 30% in the CFR, then the disturbed profiles come close to the reference one in the SOL. For $T_i$, the decrease is similar in the CFR, but then a constant decrease of around 10% is maintained in the SOL between

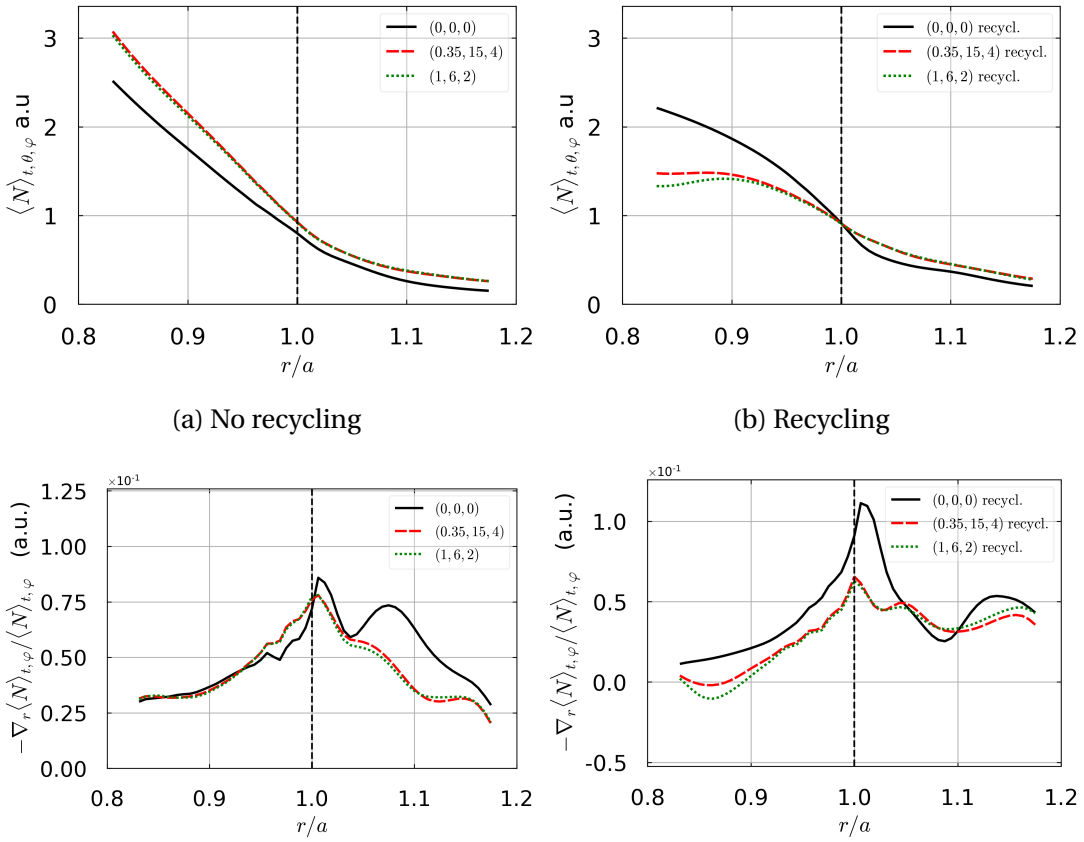


(a) No recycling (b) Recycling

(c) No recycling (d) Recycling

Figure 4.5.: Radial profiles of the time, toroidal and poloidal averaged density (4.5a,4.5b) and of the corresponding density radial gradient (4.5c,4.5d) for different magnetic perturbations. Cases without recycling (4.5a,4.5c). Cases with recycling (4.5b,4.5d). The vertical dashed line is the separatrix.

the disturbed profiles and the reference one. The electron (Fig. 4.6b) and ion (Fig. 4.6d) temperatures for the recycling cases with MPs have different behaviours. For $T_e$, the temperature is higher with MPs than the reference one near the core (far CFR), then it decreases below the reference at the mid CFR until just after the separatrix. In the SOL, MPs lead to flatter temperature gradients, so that the electron and ion temperatures which are lower than in the no-MP reference in the near SOL progressively become larger than the reference in the far SOL. The trend is almost identical for both MPs. For $T_i$, the decrease compared to the reference occurs in the whole CFR and just after the separatrix and amounts to around 5%. Both MPs solutions provide similar profiles, with the case $(0.35, 15, 4)$ decreasing a bit more in the CFR (less than 1% more).

We have stated that the density pump-out observed in experiments and retrieved in the isothermal simulations cannot be found in the non isothermal ones without recycling. In isothermal models, the density gradient is the only drive for turbulence

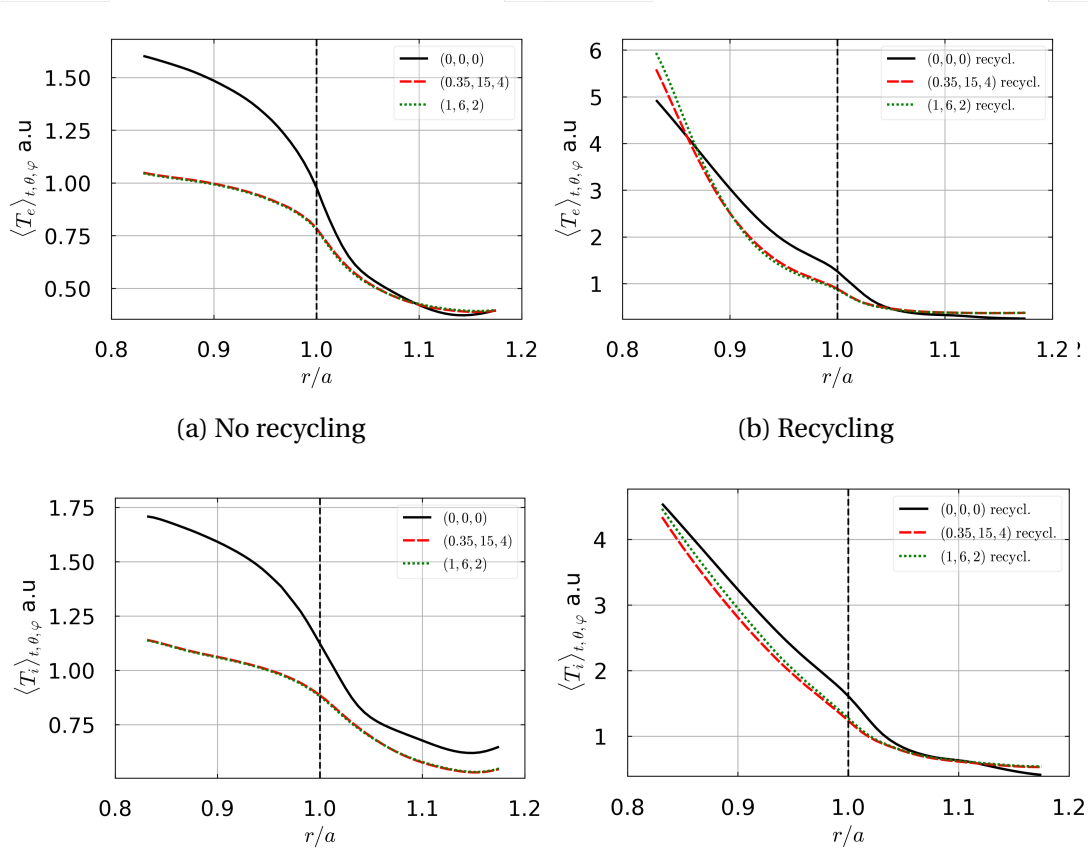


(a) No recycling

(b) Recycling

(c) No recycling

(d) Recycling

Figure 4.6.: Radial profiles of the time, toroidal and poloidal averaged electron (4.6a,4.6b) and ion (4.6c,4.6d) temperatures for different magnetic perturbations. Cases without recycling (4.6a,4.6c). Cases with recycling (4.6b,4.6d). The vertical dashed line is the separatrix.

while in non-isothermal models it is the pressure gradient (thus a combination of the density and temperature gradients) that plays this role. The averaged radial profiles of both pressures for the two kind of simulations (recycling or not) are shown on Figs. 4.7. The reference simulations show scale difference for both pressures with or without recycling. With respect to the solution without recycling, $P_e$ is multiplied by a factor 2 or 3 at the same radial position in the CFR (Figs. 4.7a and 4.7b). $P_i$ follows the same trend (Figs 4.7c and 4.7d). In spite of having the same energy source (hence pressure) in both cases, the difference most likely lies in the difference of temperature profiles. As explained above, the solutions with recycling exhibit hotter temperatures in the CFR, leading to significantly lower local collisionalities (i.e., lower parallel resistivity and larger parallel heat conduction in the present model). It has been shown in recent TOKAM3X simulations (R. Tatali, submitted to Nuclear Fusion) that the collisionality strongly impacts the turbulent transport in the CFR with a reduction of

anomalous transport when the collisionality decreases. This way, the relocation of the particle source drives a better energy confinement that explains the steepening of the pressure gradients. Furthermore, with or without recyling, the MPs always induce a loss of electron or ion pressures in the CFR. It is of around 20% for the non recycling cases (Figs. 4.7a and 4.7c) and 30% for the recycling ones (Figs. 4.7b and 4.7d).

The pressure profiles in disturbed solutions are quite similar. In the SOL, the impact of MPs is much milder, with mainly a flattening/decrease in the near SOL, driven by continuity, to a flattening in the CFR.

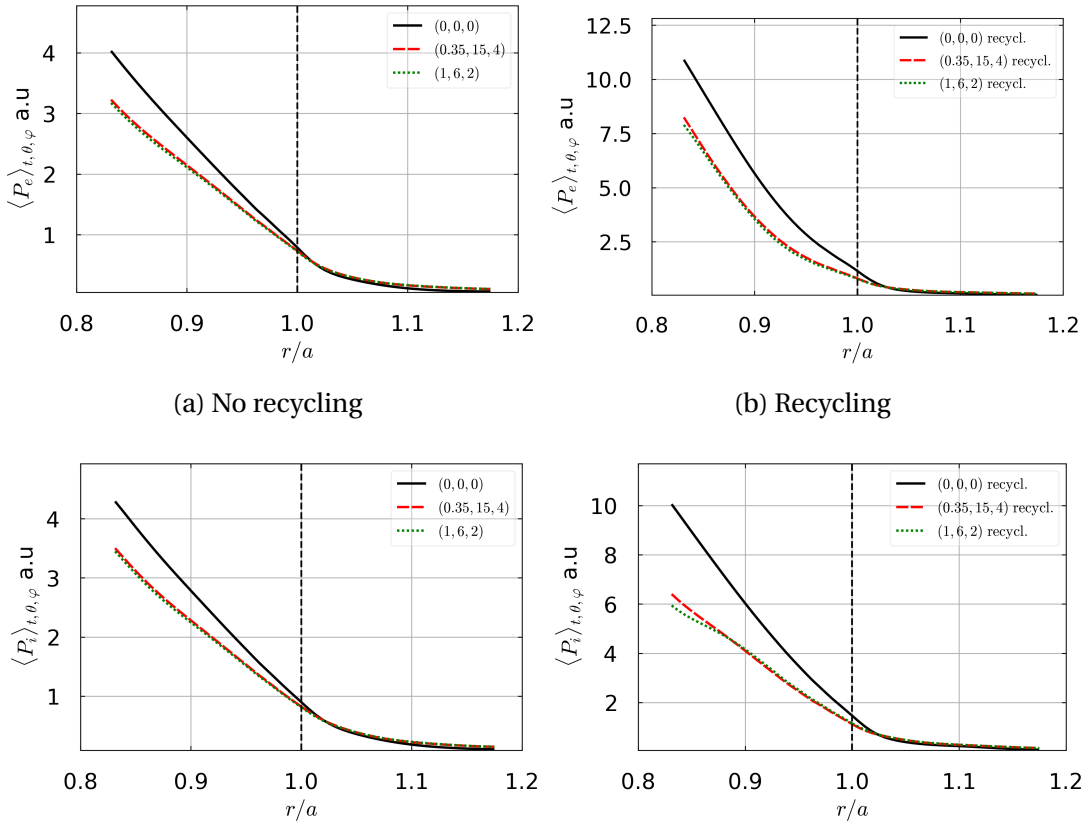


(a) No recycling

(b) Recycling

(c) No recycling

(d) Recycling

Figure 4.7.: Radial profiles of the time, toroidal and poloidal averaged electron (4.7a,4.7b) and ion (4.7c,4.7d) pressures for different magnetic perturbations (MPs). Cases without recycling (4.7a,4.7c). Cases with recycling (4.7b,4.7d). The vertical dashed line is the separatrix.

We have seen in isothermal simulations (and it was observed in experiments too), that MPs create a change of electric potential leading to a modification of the parallel transport. The averaged radial profiles of the electric potential and the corresponding radial electric field are plotted at the LFS midplane in Figs. 4.8. The electric potential

$\Phi$ profiles (Figs. 4.8a and 4.8b), show that the reference simulation with recycling has far lower value in the CFR at the same radial position. This effect can be explained by the change in the ion pressure gradient. Indeed, force balance in the CFR makes us expect that the radial electric field has to compensate the radial gradient of the ion pressure: $E_r \sim -\partial_r P_i$. The steepening of $P_i$ hence leads to a steepening of the potential profiles. Conjugated with an approximately fixed point in the SOL due to Bohm boundary conditions ($\Phi \sim 3T_e$), one ends up with a decrease of the electrostatic potential.

The disturbed solutions with MPs show a similar behaviour as the one already observed for isothermal simulations: the electric potential increases in the CFR but does not vary much in the SOL. For the non recycling cases, the MPs increase similarly the potential in the CFR. For the recycling cases, the MPs increase comparatively more the potential in the CFR with a stronger increase for the (1,6,2) MP.

Concerning the radial electric field profiles (Figs 4.8c and 4.8d), the trend is similar between the two solutions of reference, except that the amplitude of the variations are two times larger for the case with recycling in the CFR than without. For the cases without recycling, the radial electric field is negative in the CFR and tends to higher values when MPs are switched on, but remains negative. The plots for the two MPs solutions are almost the same. For the reference solution with recycling, the electric field is negative in the CFR but goes into positive value at some points when the MPs are switched on. The increase is the most important for the perturbation (1,6,2). For both cases with/without recycling the trend is the flattening of $E_r$ and a reduction of its amplitude due to MPs.

### 4.2.2. Impact on flows

The variation of the radial electric field lets presume of a reorganization of the flows which should be sensed also on the parallel flows. Figs; 4.9 show the average poloidal profile of the parallel Mach number $M_\parallel = \Gamma/(N\sqrt{T_e + T_i})$ at two radial positions, in the CFR at $r/a = 0.9$ (Figs. 4.9a and 4.9b) and in the SOL at $r/a = 1.1$ (Figs. 4.9c and 4.9d). The poloidal angle $\theta = 0$ is the LFS midplane and $\pi/2$ is the top of the machine. A positive Mach number corresponds to the electron diamagnetic direction. Without recycling (Figs. 4.9a and 4.9c), the poloidal distribution of the parallel Mach number in the reference case is quite similar to the isothermal case. The main difference is the weak impact of the MPs. At $r/a = 0.9$, the reversal of $M_\parallel$ due to MPs in isothermal cases does not occur there, and the same can be said at $r/a = 1.1$. Still, in the SOL, we note an increase of $M_\parallel$ at the HFS of the machine with the MPs. Both MPs for the non recycling cases have similar behaviour.
The solutions with recycling are largely different (Figs. 4.9b and 4.9d). First, the reference solution shows little change in $M_\parallel$ in the CFR ($r/a = 0.9$) but we still note greater oscillations around the LFS midplane. These oscillations in the SOL ($r/a = 1.1$)

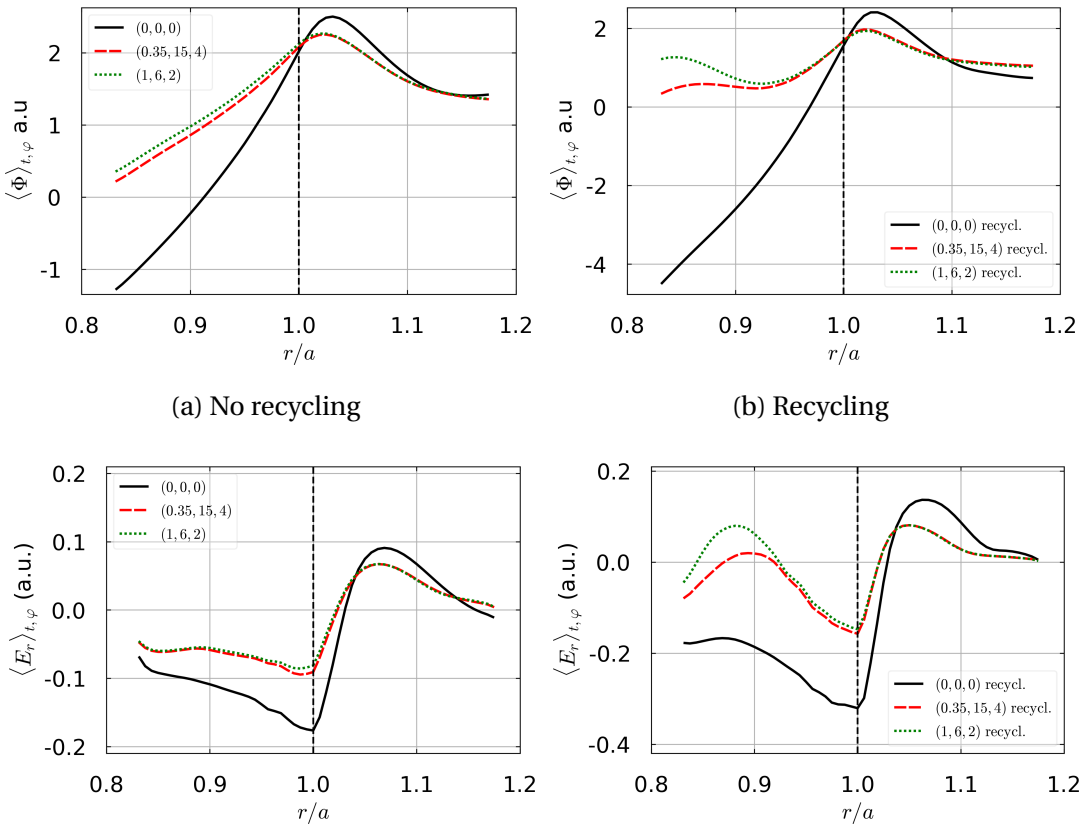


(a) No recycling

(b) Recycling

(c) No recycling

(d) Recycling

Figure 4.8.: Radial profiles of the time and toroidal averaged electrostatic potential $\Phi$ (4.8a,4.8b) and of the mean radial electric field $E_r = \langle -\partial_r \Phi \rangle_{t,\varphi}$ (4.8c,4.8d) at the LFS midplane with or without recycling, for different MPs. Cases without recycling (4.8a,4.8c). Cases with recycling (4.8b,4.8d). The vertical dashed line is the separatrix.

are considerably amplified compare to the solution without recycling. They can be interpreted as the presence of Pfirsch-Schlütter flows of large amplitude. The $M_\parallel$ in the solution of reference in the SOL is three times higher at the LFS midplane, and negative at the HFS. The presence of MPs increases the oscillations in the CFR, particularly at the LFS midplane (positive $M_\parallel$) and HFS midplane (negative $M_\parallel$). The effect is the strongest for the case (1,6,2). In the SOL, still with recycling, the MPs decrease the poloidal oscillations of $M_\parallel$ in a similar fashion for both MPs. $M_\parallel$ is thus lower at the LFS (but still positive) and higher at the HFS (passing from a negative reference one to barely positive, showing a decrease of the plasma velocity in absolute value).

Considering these observations, the solutions with recycling seem more in agreement with the experimental measurements mentioned in Chapter 3.

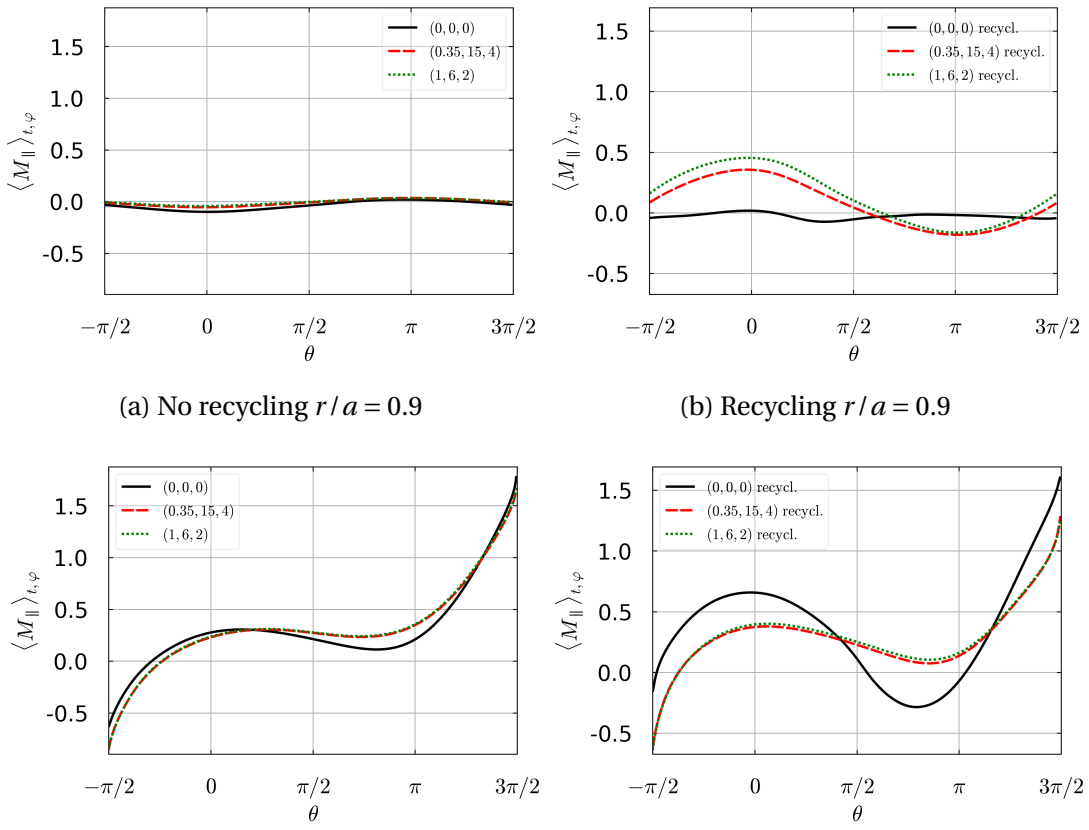


(a) No recycling $r/a = 0.9$

(b) Recycling $r/a = 0.9$

(c) No Recycling $r/a = 1.1$

(d) Recycling $r/a = 1.1$

Figure 4.9.: Poloidal profiles of the time and toroidal averaged parallel Mach number $M_\parallel = \Gamma/(N\sqrt{T_e + T_i})$ at $r/a = 0.9$ (4.9a,4.9b) and at $r/a = 1.1$ (4.9c,4.9d). Cases without recycling (4.9a,4.9c) and with recycling (4.9b,4.9d). The vertical dashed line is the separatrix.

### 4.2.3. Impact on particles and energy radial transport

The electric potential variations as well as the parallel velocity ones hint at a change in the radial transport for the particles and the energy. We concentrate on the electron energy and particles transport in this section. The radial energy flux can be decomposed into:

$$\Gamma^{\psi}_{e,E_{e/i}} = \Gamma^{\psi}_{E\times B,E_{e/i}} + \Gamma^{\psi}_{\nabla B_e,E_{e/i}} + \Gamma^{\psi}_{\text{diff},E_{e/i}} + \Gamma^{\psi}_{\parallel,E_{e/i}} \tag{4.5}$$

The radial particle flux can be decomposed into:

$$\Gamma^{\psi}_{e,N} = \Gamma^{\psi}_{E\times B,N} + \Gamma^{\psi}_{\nabla B_i,N} + \Gamma^{\psi}_{\text{diff},N} + \Gamma^{\psi}_{\parallel,N} \tag{4.6}$$

The parallel component, due to TOKAM3X approximations is considered to be the same for both ions and electrons. A notable difference between the energy and

particles fluxes is the $\nabla B$ drift, which comes from the ion in the particles fluxes. In the following, we note the particles fluxes as:

$$\Gamma^{\psi}_{X,N} = N u^{\psi}_{X} \tag{4.7}$$

with $X$ being the corresponding drift. The energy fluxes are noted:

$$\Gamma^{\psi}_{X,E_{e/i}} = N T_{e/i} u^{\psi}_{X} \tag{4.8}$$

#### 4.2.3.1. Flux-surface averaged fluxes

We estimate the radial fluxes for both particles and energy by integrating the full (then each component) flux along the flux surfaces (poloidal and toroidal directions). The profiles are then averaged in time. The total particles and electron energy balances are plotted on Figs. 4.10. The first difference between solutions with recycling and without is visible on the particle fluxes (Figs. 4.10a, and 4.10b). Without recycling, the particle flux builds up close to the inner boundary of the simulation domain where is located the source, and it remains constant (no losses) radially up to the separatrix. With recycling, the particle flux is much lower in the CFR, and progressively builds up moving out radially and encountering the source. Contrary to the isothermal simulations, the MPs increase the total particles flux in the SOL. The electron energy flux balance is similar for the solutions with or without recycling (Figs. 4.10c and 4.10d) in the sense that both have energy fluxes in the CFR. The solutions with recycling exhibit energy fluxes without particle fluxes, which suggests a change from a convective to a conductive regime. There are nevertheless notable differences.

We first note that contrary to the particle fluxes, the electron energy fluxes are never exactly constant in the CFR. They tend to increase regularly with the radius, the increase being more marked in the solution with recycling. Such behaviour can be explained by the fact that the electron energy is not a conserved quantity in our model. Neither is the sum of the electron and ion energies. The sum of the electron and ion energy balances exhibits additional flux terms, in particular carried by currents, that can lead to energy exchanges between the components of the flux. In the CFR, MPs have opposite effects depending on the location of the source between the solutions with recycling and without. Indeed, without recycling, MPs perturbations lead to an increase of the electron energy flux by around 10%, while they lead to a decrease by around 15% in the solutions with recycling. On the contrary in the SOL the effects are in the same direction for both particles source locations. The decay of the flux is slower with MPs, leading to a larger electron energy flux through out the SOL.

We then decompose the global fluxes into their different terms according to Eq. 4.6. The first decomposition is on the particle fluxes. The main components are, as for the isothermal model, the $E \times B$ and diffusive fluxes, and they are plotted in Figs. 4.11, in percentage of the global particule flux. The $\nabla B_i$ particle flux numbers for less than 20% of the total flux in non recycling case (but is not negligible in the recycling case,

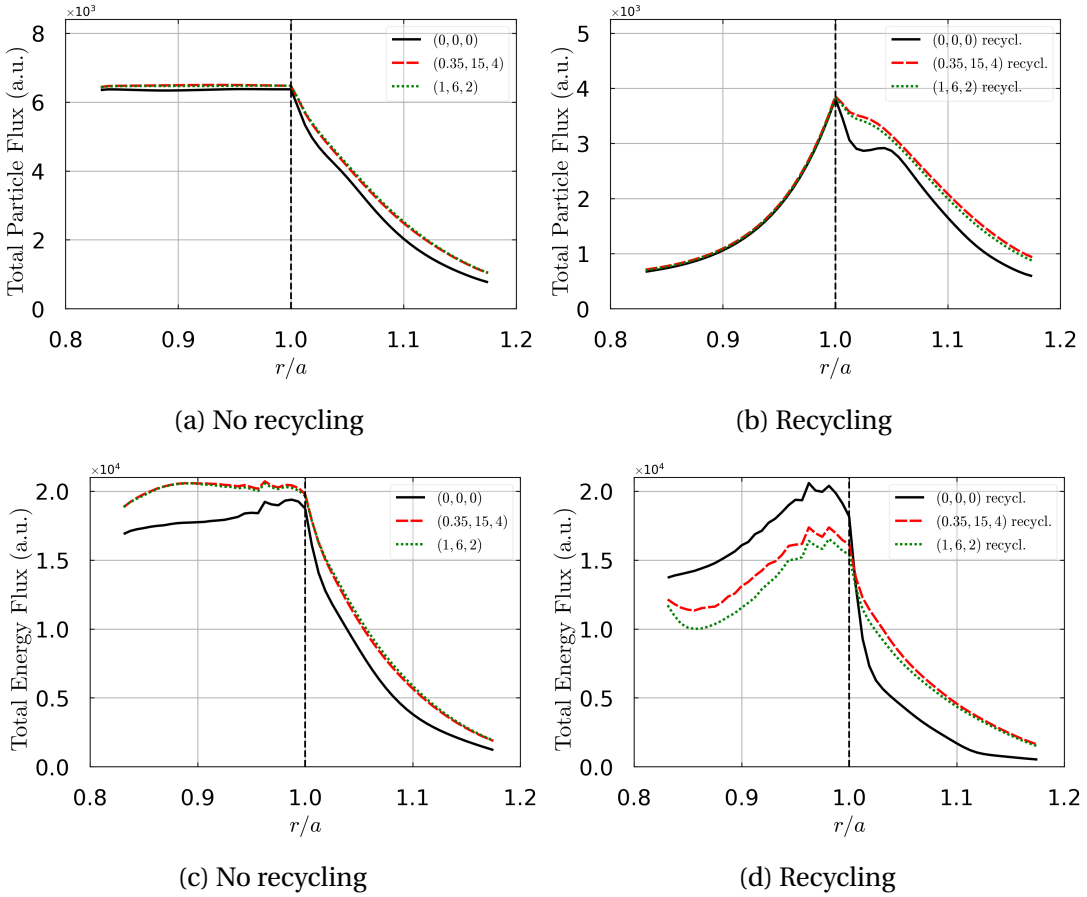


(a) No recycling

(b) Recycling

(c) No recycling

(d) Recycling

Figure 4.10.: Radial profiles of the total radial flux-surface averaged flux of particles (4.10a,4.10b) and electron energy (4.10c,4.10c). The dashed line denotes the separatrix. Cases without recycling (4.10a,4.10c). Cases with recycling (4.10b,4.10d)

wighting more than 50% in the CFR) and the parallel flux below 1% is thus absolutely negligible. Concerning the solutions without recycling, the $E \times B$ flux (Fig. 4.11a) constitutes 70 to 80% of the fluxes. The MPs decrease by 5% the flux in the CFR just before the separatrix but increase them by up to 15% in the mid SOL. This behaviour is completely opposite to the isothermal simulations. The diffusive flux (Fig. 4.11c) clearly adapts itself to the variations of the $E \times B$ flux, having opposite behaviour.

For the solutions with recycling, the $E \times B$ flux (Fig. 4.11b) decreases considerably in the CFR to a negative value (around -40%). This negative value hints to a turbulent flux from the source going toward the core, i.e. going in the opposite direction to the pressure gradient. The diffusion, thus compensates with the $\nabla B_i$ flux (Figs 4.11d and 4.12b). In the SOL, the $E \times B$ component constitutes up to 60% of the total flux. MPs shift the relative weight of the $E \times B$ driven particle towards positive values. One

can then distinguish three regions: close to the inner boundary, the MPs lead to a reversal of the $E \times B$ flux; in the middle of the CFR, the contribution of the $E \times B$ driven particle flux decreases and becomes negligible; in the outer part of the CFR and in the SOL, the $E \times B$ contribution, which was positive, is enhanced from 50% to 90% of the global flux. The diffusive flux (Fig 4.11d), as said before, compensates the loss of the $E \times B$ flux in the CFR (or its increase for the MP cases). In the SOL, the diffusive flux is similar for the solutions of reference or the MPs disturbed solutions, with nevertheless a loss of flux near the separatrix and in the far SOL.

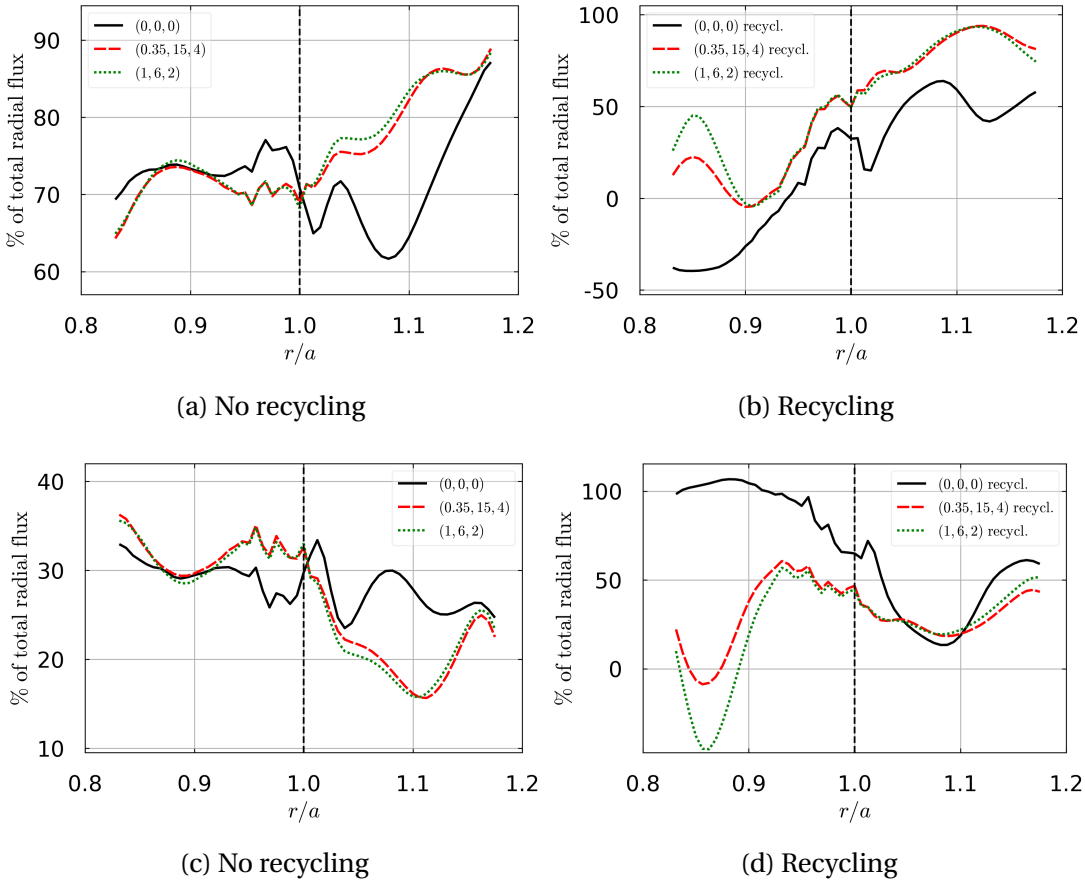


(a) No recycling

(b) Recycling

(c) No recycling

(d) Recycling

Figure 4.11.: Radial profiles of the $E \times B$ (4.11a,4.11b) and diffusive (4.11c,4.11d) radial flux-surface averaged fluxes of particles. The dashed line denotes the separatrix. Cases without recycling (4.11a,4.11c). Cases with recycling (4.11b,4.11d)

Figs 4.12 show the two last components of the particle fluxes: the $\nabla B_i$ and the parallel one. As for the isothermal simulations, the parallel component is completely negligible for the cases without (Fig 4.12c) and with (Fig 4.12d) recycling, with a maximum value barely above 0.1% of the total flux. The role of the $\nabla B_i$ flux is more interesting. For the solutions without recycling (Fig 4.12a), it constitutes only a small

part of the fluxes, around 20% at most (staying mostly below 10%) and can be positive or negative depending on the exact location. The MPs tend to decrease it in the SOL.

For the solutions with recycling (Fig 4.12b), it plays a more significant role, compensating the loss of the $E \times B$ flux in the CFR. The solution of reference shows that up to 40% of the flux comes from the $\nabla B_i$ flux in the far CFR. It decreases to small values (below 10%) near the separatrix, passing even negative, but increases then in the SOL, passing positive once again (still below 25%) before decreasing. The MPs increase the trend in the CFR, to compensate the $E \times B$ flux. In the SOL, the MPs seem to decrease the $\nabla B_i$ flux.

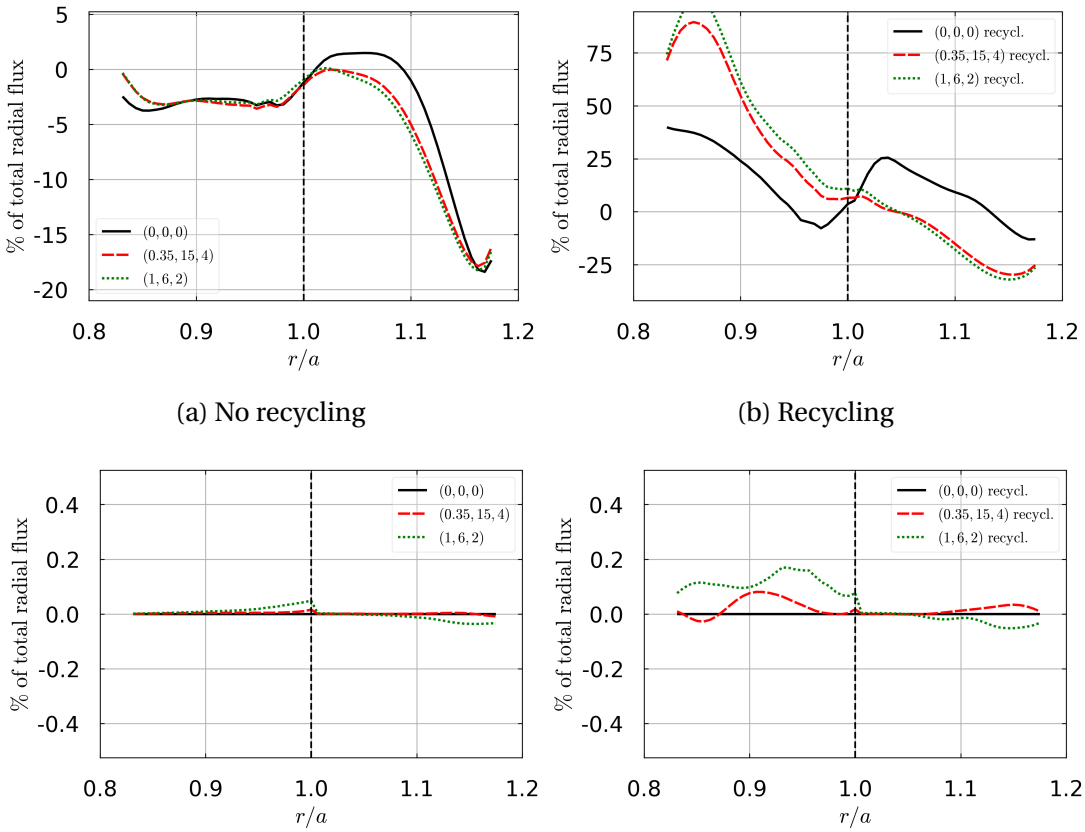


(a) No recycling

(b) Recycling

(c) No recycling

(d) Recycling

Figure 4.12.: Radial profiles of the $\nabla B_i$ (4.12a,4.12b) and parallel (4.12c,4.12d) radial flux-surface averaged fluxes of particles. The dashed line denotes the separatrix. Cases without recycling (4.12a,4.12c). Cases with recycling (4.12b,4.12d)

We now look at the energy flux decomposition. We begin with the two major components in percentage of the total electron energy flux, the $E \times B$ and the diffusive fluxes shown on Figs. 4.13. For the solutions without recycling, the $E \times B$ (Fig. 4.13a)

flux is above 70% in the CFR and near SOL, and above 80% of the total flux in the rest of the SOL. The MPs increase the flux by 10% in the CFR, but do not impact it in the SOL. The diffusive flux (Fig. 4.13c) is below 30% in the CFR and below 20% in the SOL. It complements the $E \times B$ flux.

For the solutions with recycling, the $E \times B$ energy flux (Fig. 4.13b) has a similar trend with the particles, with an increase from negative values at the inner boundary (-20%) up to positive values of the order of 65% at the separatrix. It goes to 90% at most in the mid SOL but with low values, below 50%, just after the separatrix and in the far SOL. The MPs tend to increase the proportion of the flux driven by the $E \times B$ drift both in the CFR (from 20% at the mid CFR and up to 80% just before the separatrix), leading to a flat profile in the SOL at 80% of the total flux. The diffusive flux (Fig 4.13d) compensates clearly the loss of the $E \times B$ energy flux, in the same way as for the particles profiles. The only difference with the MPs is in the far CFR where the diffusive flux, contrary to the $E \times B$ one, does not show a peak value. This is nevertheless seen in the $\nabla B_i$ profiles, as explained in the following description.

We plot the contribution of the $\nabla B_e$ and parallel fluxes in percentage of the total radial flux on Figs 4.14. As expected, the parallel component is completely negligible without (Fig. 4.14c) or with (Fig. 4.14d) recycling. The energy $\nabla B_e$ flux also has a small contribution for the solutions without recycling (Fig 4.14a) and a bigger one for the solutions with recycling (Fig. 4.14b). In these simulations, the reference in the CFR peaks at almost 30% at the inner boundary before decreasing to 0% at the separatrix and having small oscillations (around 5 to 10%) in the SOL. The MPs trigger a reversal in the far at the center of the simulation domain, in a mirror image of what happens to the energy $E \times B$ flux. Then in the SOL, MPs seem to flatten the $\nabla B_e$ profile into positive values (around 5 to 10% of the total flux).

#### 4.2.3.2. Poloidal distribution of $\langle \Gamma^{\psi}_{X,N} \rangle_{t,\varphi}$

To better understand the change in the radial flows, their poloidal distributions are now investigated. We know that the time averaged parallel flow is driven by both the sheath boundary conditions and the poloidal distribution of the divergence of the radial flux. To give a thorough overview, we study the poloidal distribution of both particles and energy fluxes at $r/a = 0.9$ and $r/a = 1.1$, in the CFR and in SOL, respectively. For particles, we study the $E \times B$ and the $\nabla B_i$ mean and fluctuating parts of the fluxes following the decomposition:

$$f(t,\psi,\theta^*,\varphi) = \bar{f}(\psi,\theta^*,\varphi) + \tilde{f}(t,\psi,\theta^*,\varphi) \tag{4.9}$$

where $\bar{f} = \langle f \rangle_t$ is averaged over time and $\langle \tilde{f} \rangle_t = 0$ per construction. For the particles flux, the decomposition can be written:

$$\langle N u^{\psi}_X \rangle_t \equiv \bar{\Gamma}^{\psi}_{X,N} = \bar{N}\bar{u}^{\psi}_X + \overline{\tilde{N}\tilde{u}^{\psi}_X} \equiv \bar{\Gamma}^{\psi}_{X,\bar{N}} + \bar{\Gamma}^{\psi}_{X,\tilde{N}} \tag{4.10}$$

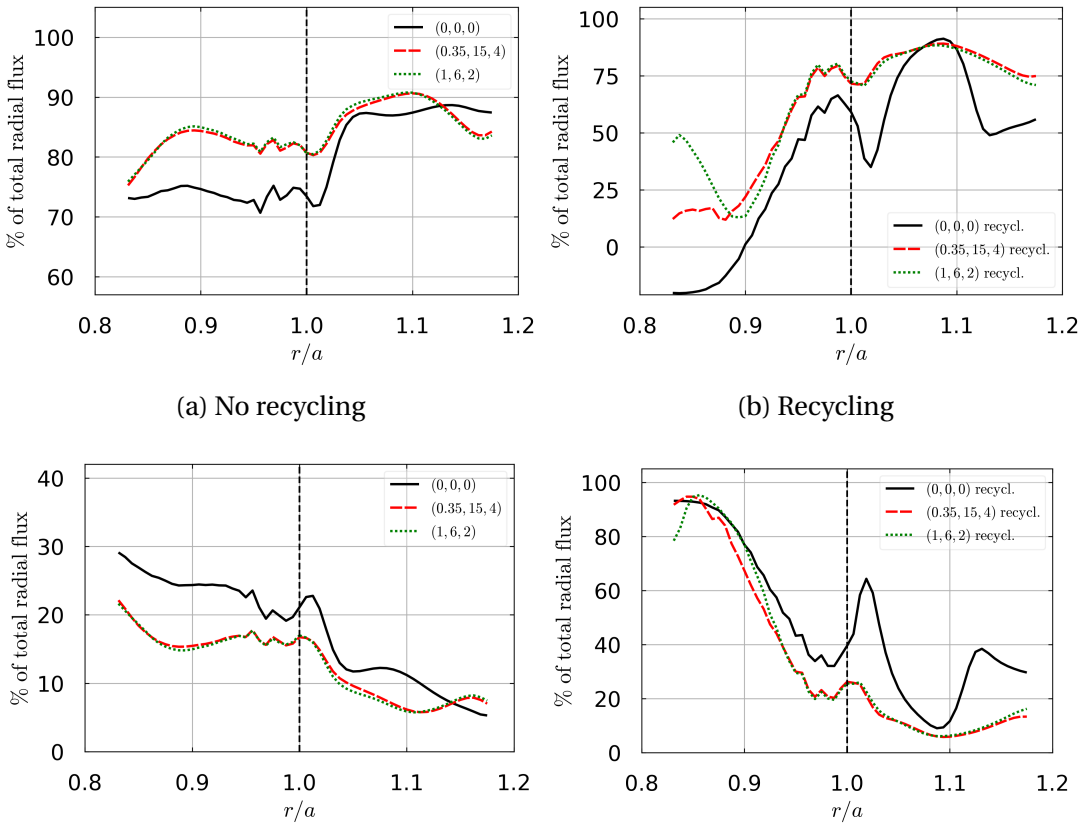


(a) No recycling

(b) Recycling

(c) No recycling

(d) Recycling

Figure 4.13.: Radial profiles of the $E \times B$ (4.13a,4.13b) and diffusive (4.13c,4.13d) radial flux-surface averaged energy fluxes of electrons. The dashed line denotes the separatrix. Cases without recycling (4.13a,4.13c). Cases with recycling (4.13b,4.13d)

The time averaged flux decomposed thus into two terms, the product of mean fields components plus the product of fluctuating components. We call the total mean flux the time averaged flux, the mean-field mean flux the product of the mean fields, and the fluctuating-field mean flux the product of the fluctuating fields.

Starting with the poloidal distribution of the particles fluxes, the poloidal profiles of $\Gamma^{\psi}_{E\times B,N}$, the $E \times B$ radial particule flux, time and $\varphi$ averaged is plotted for $r/a = 0.9$ (in the CFR) on Figs. 4.15 and for $r/a = 1.1$ (in the SOL) on Figs. 4.16.

In the CFR, the solutions without recycling for the total mean flux are shown on Fig. 4.15a. The solution of reference exhibits a ballooning at the LFS, which is amplified by the MPs on the disturbed solutions. The mean-field mean flux (Fig. 4.15c) and the fluctuating-field mean flux (Fig. 4.15e) profiles show that most of the flux comes from the fluctuating-field mean part. Regarding now the solutions with recycling, the total mean flux (Fig. 4.15b) exhibits a more complex structure. While the flux is positive

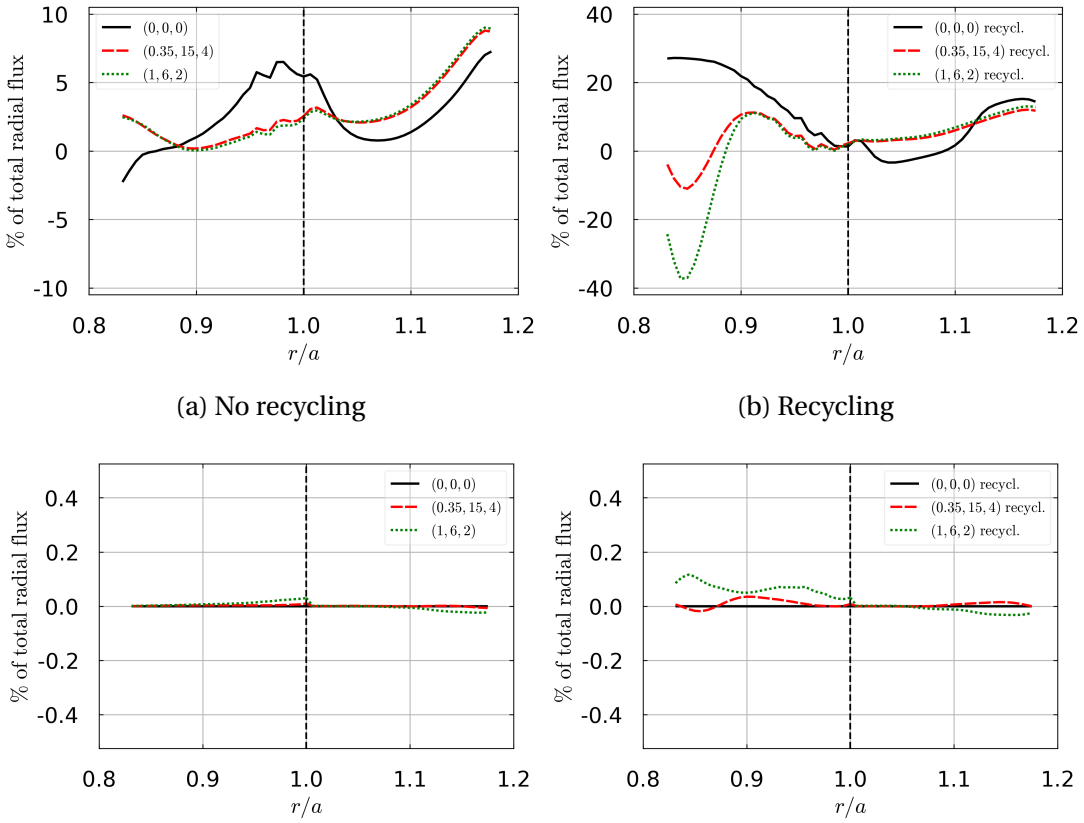


(a) No recycling

(b) Recycling

(c) No recycling

(d) Recycling

Figure 4.14.: Radial profiles of the $\nabla B_e$ (4.14a,4.14b) and parallel (4.14c,4.14d) radial flux-surface averaged energy fluxes of electron. The dashed line denotes the separatrix. Cases without recycling (4.14a,4.14c). Cases with recycling (4.14b,4.14d)

between the limiter and the LFS mid-plane, a large amplitude inwards flux is present just above the LFS midplane. This negative peak is localized at $\theta in[0,\pi/3]$, and the flux rapidely decreases to almost zero in the whole HFS core region. We thus have the reverse of the usual ballooning picture. The mean-field mean (Fig. 4.15d) and fluctuating-field mean (Fig. 4.15f) decompositions show that most of the flux comes from the mean-field mean part even if a turbulent part still exists at the LFS of the machine. As the particles source is not symmetric in the solutions with recycling, it is likely that the poloidal distribution of the density is inhomogeneous, resulting in an outward $\nabla B_i$ flux (more ions at the bottom of the machine results in an outward flux, as the ions drift toward the bottom). The particle flux from the core is only 10%, leading to a necessary flux reorganization to compensate the outward flux. This could explain the behaviour of the total mean (and mainly mean-field mean part) $E \times B$ flux, which shows a reverse picture of the usual pattern.

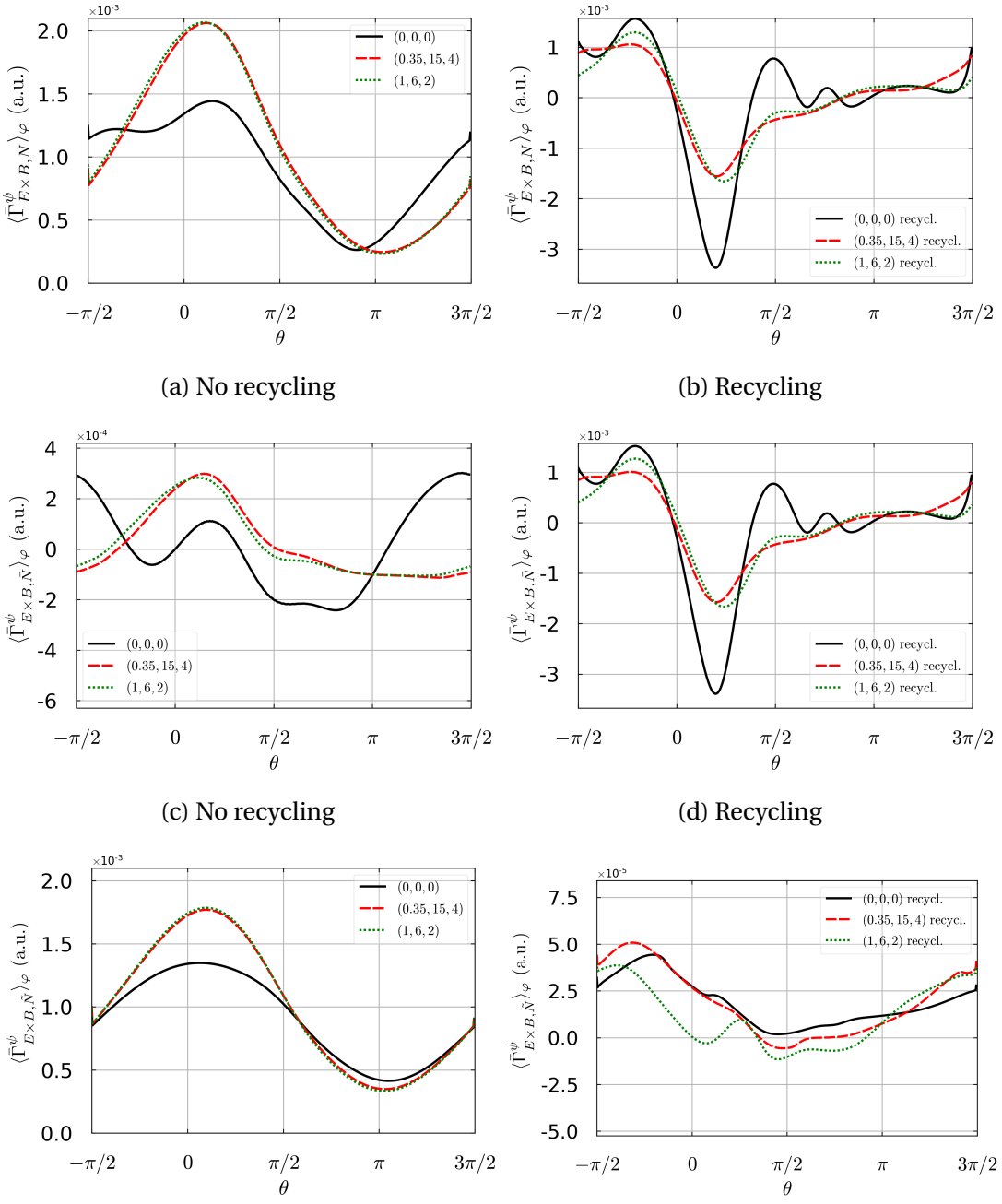


(a) No recycling

(b) Recycling

(c) No recycling

(d) Recycling

(e) No recycling

(f) Recycling

Figure 4.15.: Poloidal profiles of the $E \times B$ total mean flux $\bar{\Gamma}^{\psi}_{E\times B,N}$ (4.15a,4.15b), the mean-field mean $\bar{\Gamma}^{\psi}_{E\times B,\tilde{N}}$ (4.15c,4.15d) and the fluctuating-field mean $\bar{\Gamma}^{\psi}_{E\times B,\tilde{N}}$ (4.15e,4.15f) parts at $r/a = 0.9$ (CFR). Quantities are $(t,\varphi)$-averaged. (4.15a,4.15c,4.15e) cases without recycling. (4.15b,4.15d,4.15f) cases with recycling. $\theta = 0$ corresponds to the LFS midplane.

In the SOL, the solutions without recycling for the total mean $E \times B$ flux are shown on Fig. 4.16a. The solution of reference (without perturtbation) still shows a ballooning at the LFS, which is amplified by 100% by the MPs. The decomposition into the mean-field (Fig. 4.16c) and the fluctuating-field mean parts (Fig. 4.16e) shows that almost all the $E \times B$ flux comes from the fluctuating-field mean part. For the solutions with recycling now, the total mean flux (Fig. 4.16b) shows no ballooning but an almost constant positive flux, which doubles with the MPs. The mean-field (Fig. 4.15d) and fluctuating-field (Fig. 4.15f) mean decompositions show that most of the flux comes from the turbulent part, even if a mean-field mean part still exists. The fluctuating-field mean part shows a strong ballooning at the LFS, which almost doubles with the MPs.

Regarding now the poloidal distribution of the $\nabla B_i$ flux, the time and $\varphi$ averaged poloidal profiles of the $\Gamma^{\psi}_{\nabla B_e,N}$, the $\nabla B_e$ radial particule flux is plotted in the CFR ($r/a = 0.9$) and in the SOL ($r/a = 1.1$) on Figs. 4.17 with only the total mean flux. The fluctuating-field mean flux is actually always negligible (at least one order of magnitude lower than the mean-field mean flux), resulting in the $\nabla B_i$ mean flux being mainly from the mean-field mean part. Fig. 4.17a shows the profiles of the total mean flux in the CFR for the solutions without recycling. The profile of the solution of reference takes the form of a sinusoid, whose amplitude decreases in the disturbed solutions with the MPs. The sinusoid form seems consistent with the radial profile of $\nabla B_i$, plotted on Figs. 4.12, where the integrale is near zero at $r/a = 0.9$.

Fig. 4.17b shows now the profiles of the total mean flux for the solutions with recycling. The profile for the solution of reference is of similar form, with an higher amplitude (at least by a factor two), but the amplitude losses are stronger in the disturbed solutions with the MPs with respect to solutions without recycling. The fact that the $\nabla B_i$ flux integral on Figs. 4.12 lets suppose that the periodic form is actually a bit deformed, resulting in a non zero contribution of the $\nabla B_i$ particle flux. This is probably due to the non symmetrical particles source distribution, resulting in local inhomogeneities of the density and thus of the important contribution of the $\nabla B_i$ flux in the solutions with recycling cases compare to the solutions without recycling.

The total $\nabla B_i$ mean flux is shown in the SOL on Fig. 4.17c for the solutions without recycling. The profile of the solution of reference takes the form of a deformed sinusoid, whose amplitude increases in the disturbed solutions with MPs. The MPs increase the amplitude of the profiles, particularly at the top and bottom of the machine. In the solutions with recycling, the total mean flux (Fig. 4.17d) is of similar form, but the increase of the amplitude is stronger when the solution is disturbed by the MPs.

As a conclusion for the particule fluxes, the important part is the change in ballooning through $\bar{\Gamma}^{\psi}_{E\times B,N}$, in both the CFR and SOL for the non recycling cases at the LFS, mainly from the fluctuating-field mean part, amplified by MPs. The same MPs create a loss of flux at the top and bottom of the machine through $\bar{\Gamma}^{\psi}_{\nabla B_i,N}$, mainly the mean-field mean part.
For the recycling cases, an opposite trend to the expected ballooning exists in the CFR,

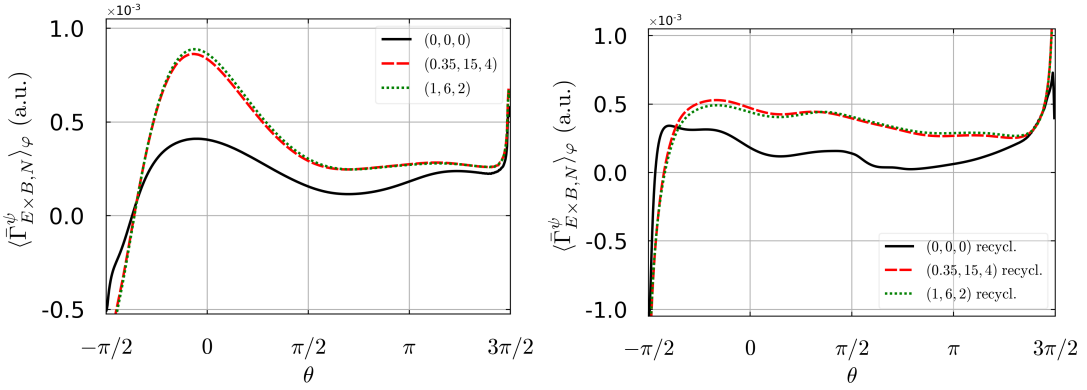


(a) No recycling

(b) Recycling

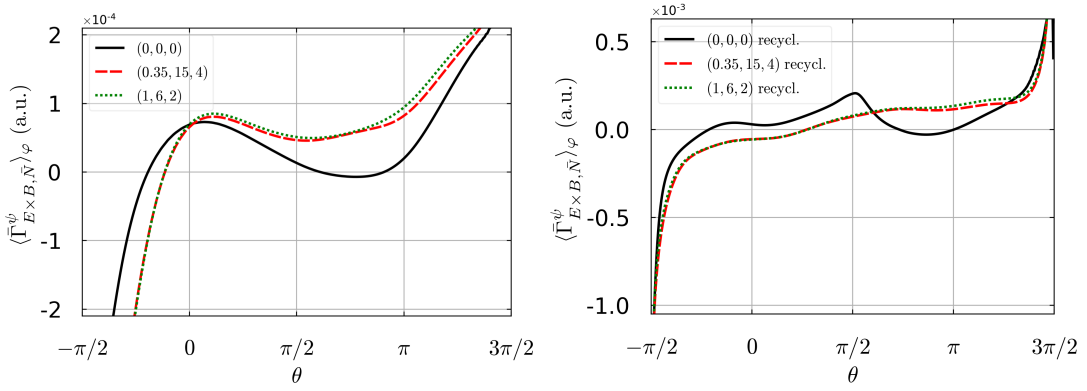


(c) No recycling

(d) Recycling

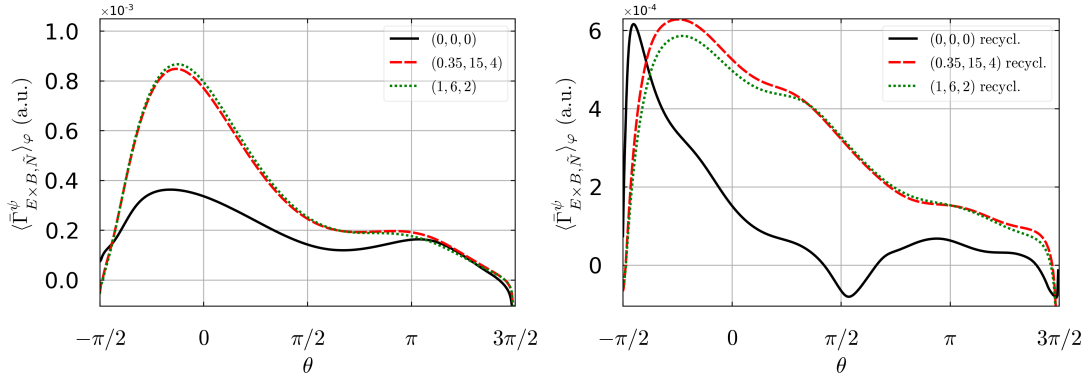


(e) No recycling

(f) Recycling

Figure 4.16.: Poloidal profiles of the $E \times B$ total mean flux $\bar{\Gamma}^{\psi}_{E\times B,N}$ (4.16a,4.16b), the mean-field mean $\bar{\Gamma}^{\psi}_{E\times B,\tilde{N}}$ (4.16c,4.16d) and the fluctuating-field mean $\bar{\Gamma}^{\psi}_{E\times B,\tilde{N}}$ (4.16e,4.16f) parts at $r/a = 1.1$ (SOL). Quantities are $(t,\varphi)$-averaged. (4.16a,4.16c,4.16e) cases without recycling. (4.16b,4.16d,4.16f) cases with recycling. $\theta = 0$ corresponds to the LFS midplane.

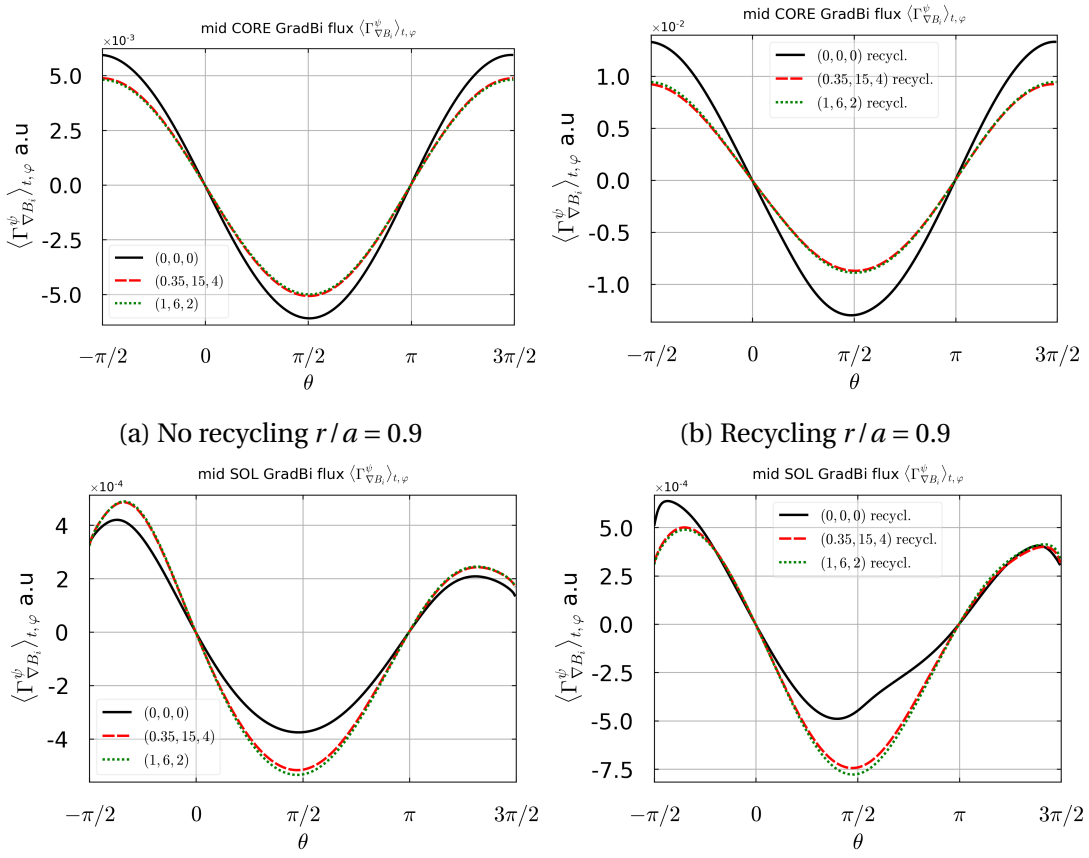


(a) No recycling $r/a = 0.9$

(b) Recycling $r/a = 0.9$

(c) No recycling $r/a = 1.1$

(d) recycling $r/a = 1.1$

Figure 4.17.: Poloidal profiles of the $\nabla B_i$ total mean flux $\bar{\Gamma}^{\psi}_{\nabla B_i,N}$ at $r/a = 0.9$ (CFR) (4.17a,4.17b) and at $r/a = 1.1$ (SOL) (4.17c,4.17d). Quantities are $(t,\varphi)$-averaged. (4.17a,4.17c) cases without recycling. (4.17b,4.17d) cases with recycling. $\theta = 0$ corresponds to the LFS midplane.

decreased by MPs, mainly from the mean-field mean part, whereas no ballooning can be seen in the SOL, even if MPs increase the $\bar{\Gamma}^{\psi}_{E\times B,N}$ flux (mainly the fluctuacting-field mean part this time). An increase of $\bar{\Gamma}^{\psi}_{\nabla B_e,N}$ flux is observed at the top and bottom, in the SOL, when MPs are switched on, mainly from the mean-field mean part of the flux.

#### 4.2.3.3. Poloidal distribution of $\langle\Gamma^{\psi}_{X,E_e}\rangle_{t,\varphi}$

Regarding the energy fluxes, we only study the $E\times B$ flux $\Gamma^{\psi}_{E\times B,E_e}$ as it is the major component of the flux in most of the domain (especially the outer part) according to

the previous section. This flux can be decomposed as follow:

$$\frac{2}{5}\overline{\Gamma^{\psi}_{E\times B,E_e}} = \overline{NT_e u^{\psi}_{E\times B}} = \underbrace{\bar{N}\bar{T}_e\bar{u}^{\psi}_{E\times B}}_{\text{mean-field}} + \underbrace{\bar{T}_e\overline{\tilde{N}\tilde{u}^{\psi}_{E\times B}}}_{\text{convected}} + \underbrace{\bar{N}\overline{\tilde{T}_e\tilde{u}^{\psi}_{E\times B}}}_{\text{conducted}} + \underbrace{\bar{u}^{\psi}_{E\times B}\overline{\tilde{N}\tilde{T}_e}}_{\text{negligible}} + \underbrace{\overline{\tilde{N}\tilde{T}_e\tilde{u}^{\psi}_{E\times B}}}_{\text{negligible}} \tag{4.11}$$

As for the particle flux, we note the total mean electron energy flux $\bar{\Gamma}^{\psi}_{E\times B,E_e}$, the mean-field mean flux $\bar{\Gamma}^{\psi}_{E\times B,\bar{E}_e}$, the convected mean flux $\bar{\Gamma}^{\psi}_{\text{convected},E_e}$ and the conducted mean flux $\bar{\Gamma}^{\psi}_{\text{conducted},E_e}$.

The averaged total mean flux, noted $\bar{\Gamma}^{\psi}_{E\times B,E_e}$, as well as the mean-field mean part $\bar{\Gamma}^{\psi}_{E\times B,\bar{E}_e}$ are shown in the SOL at ($r/a = 0.9$) and in the CFR ($r/a = 1.1$) on Figs. 4.18 and 4.20, respectively. In the CFR and in the solutions without recycling, the MPs increase the total flux $\Gamma^{\psi}_{E\times B,E_e}$ at the LFS (Fig. 4.18a), reminding of the increase of the particle ballooning. Comparing with the profiles of the solutions with recycling (Fig. 4.18b), the solution of reference shows a small increase of the $E\times B$ energy flux at the bottom of the LFS, and a reverse trend (negative flux) at the top LFS. These effects are damped in amplitude in the disturbed solutions with the MPs. Regarding now the decomposition, the solutions without recycling show that the mean-field mean $E\times B$ energy flux $\bar{\Gamma}^{\psi}_{E\times B,\bar{E}_e}$ amounts for less than 10% of the total flux (Fig. 4.18c), whereas it is at least 50% for the solutions with recycling (Fig. 4.18d). Into the SOL, and in the solutions without recycling, the convected (Fig. 4.19a) and conducted (Fig. 4.19c) fluxes are of similar amplitude, constituting the main part of the total flux. The existence of the conducted flux in the solution of reference without recycling is unexpected and still not well understood. The impact of MPs is opposite on the two components. For the convected flux, the MPs shift the profiles to lower values, globally decreasing the flux, while still preserving the ballooning structure at the LFS. On the contrary, the MPs increase the conducted flux, even changing its sign, creating a strong ballooning at the LFS, explaining the strong ballooning observed on the total flux in the disturbed solutions without recycling.

For the solutions with recycling, the convected flux in the SOL (Fig. 4.19b) plays a minor role with the balloning at the LFS and still the same decrease is observed due to MPs, even if the effects are quite different depending on the MP. Thus, the perturbartion $(1,6,2)$ creates a stronger decrease at the LFS compare to the perturbation $(0.35,15,4)$. The conducted flux (Fig. 4.19d) constitutes the other half of the flux (the first half being the mean-field mean component), showing a shift from convection to conduction fluxes between the solutions without and with recycling. This behaviour is not surprising due to the relocalization of the particles source at the limiter in the solutions with recycling, that leaves an energy flux in the core with a little particles flux to convect it. The behaviour of the conducted flux is similar to the mean-field one, and it is only shifted toward more negative values. This similarity is unfortunately still not understood.

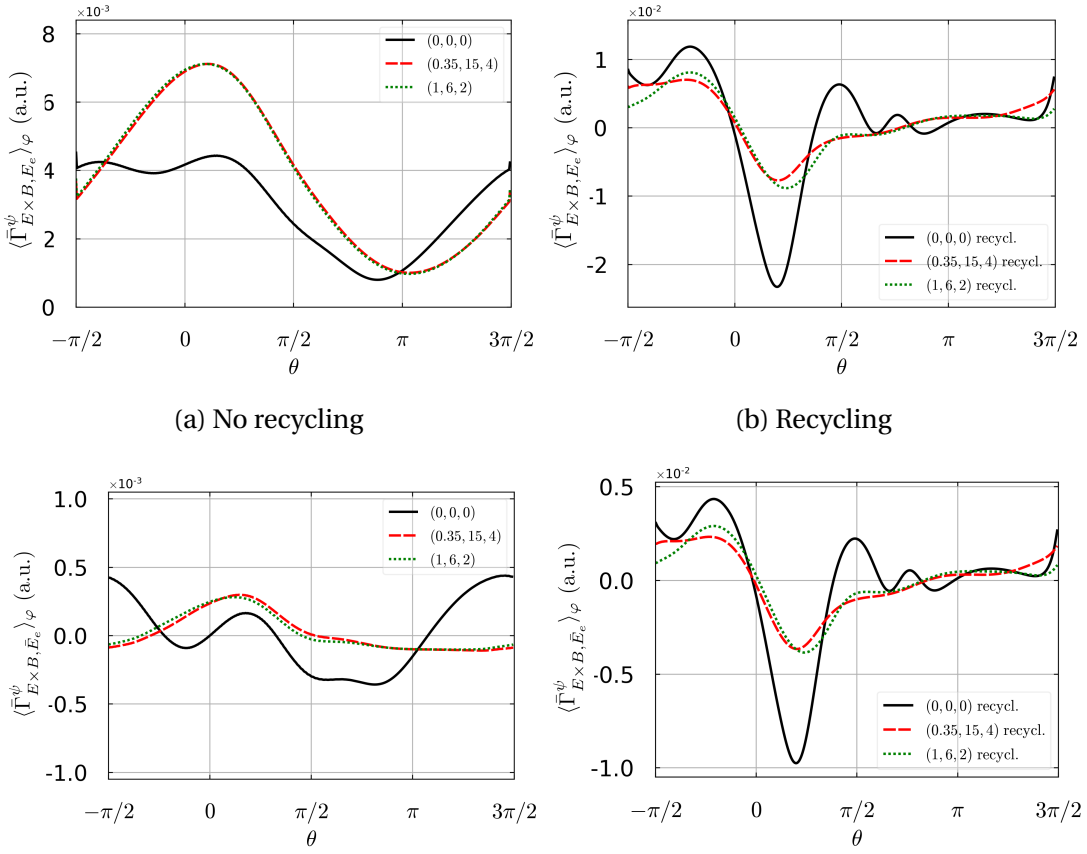


(a) No recycling

(b) Recycling

(c) No recycling

(d) Recycling

Figure 4.18.: Poloidal profiles of the $E \times B$ total mean energy flux $\bar{\Gamma}^{\psi}_{E\times B,E_e}$ (4.18a,4.18b) and mean-field mean energy flux $\bar{\Gamma}^{\psi}_{E\times B,\bar{E}_e}$ (4.18c,4.18c) time and $\varphi$ averaged at $r/a = 0.9$ (CFR). Cases without recycling (4.18a,4.18c). Cases with recycling (4.18b,4.18d)

Into the SOL ($r/a = 1.1$), and for the solutions without recycling, the total mean $E \times B$ energy flux (Fig. 4.20a) shows a ballooning structure at the LFS, which is amplified in the disturbed solutions by by MPs. For the solutions with recycling (Fig. 4.20b), the peak amplitude is half at the LFS, resulting in a less localized increase of the flux. We still observe an increase by a factor 2 due to the MPs in the disturbed solutions. Instead of being only at the LFS, the increase is observed at the top and HFS of the machine.

Looking at the decomposition, the mean-field mean component $\bar{\Gamma}^{\psi}_{E\times B,\bar{E}_e}$ is negligible in the both solutions without (Fig 4.20c) and with (Fig. 4.20d) recycling, by at least an order of magnitude. Thus most of the radial transport is made through convection and conduction. The solutions without recycling show that the convection (Fig. 4.21a) is around half of the conduction part (Fig 4.21c). A ballooning structure is seen at the

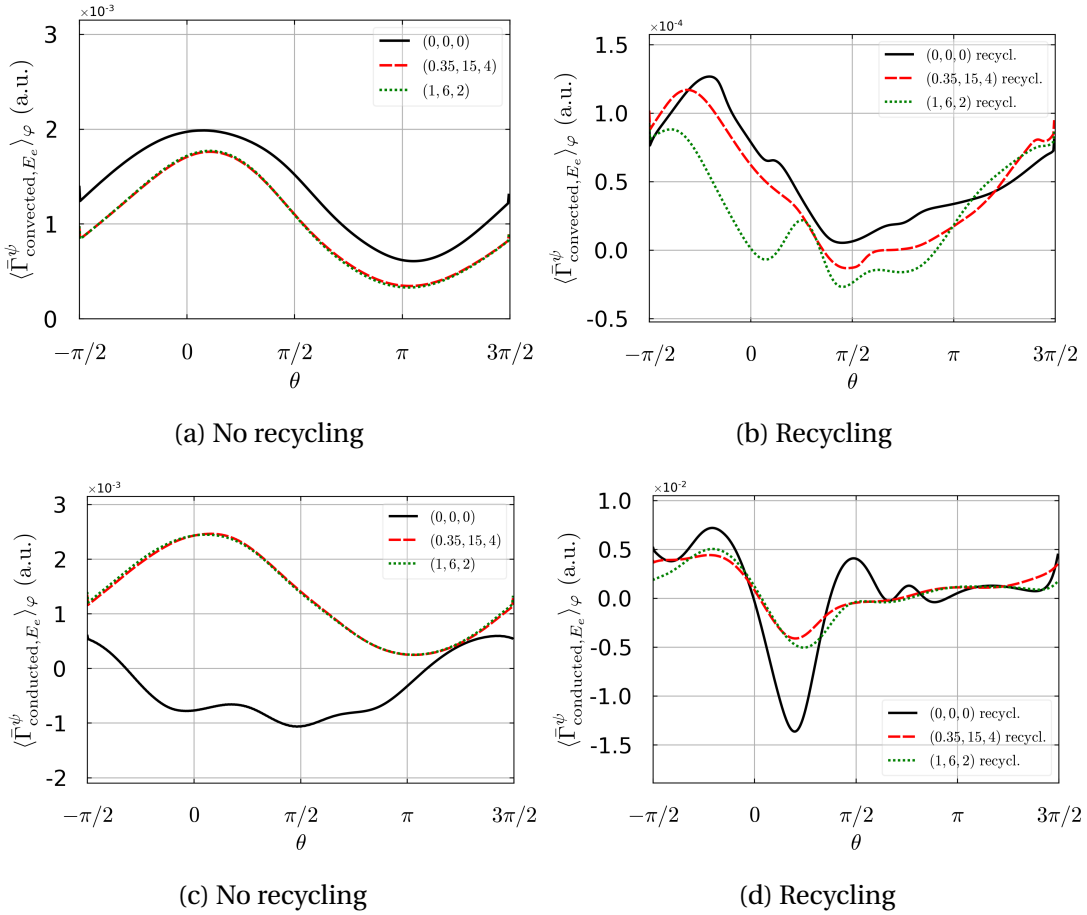


(a) No recycling

(b) Recycling

(c) No recycling

(d) Recycling

Figure 4.19.: Poloidal profiles of the $E \times B$ convected energy flux $\bar{\Gamma}^{\psi}_{\text{convected},E_e}$ (4.19a,4.19b) and conducted energy flux $\bar{\Gamma}^{\psi}_{\text{conducted},E_e}$ (4.19c,4.19c) time and $\varphi$ averaged at $r/a = 0.9$ (CFR). Cases without recycling (4.19a,4.19c). Cases with recycling (4.19b,4.19d)

LFS, which is amplified for both components of the flux in the disturbed solutions with the MPs. In the solutions with recycling, similar observations can be made.

With a two time larger amplitude, the conduction part in the solution of reference (without perturbation) with recycling (Fig. 4.21d) is less ballooned at the LFS compare to the non recycling reference. However, in the disturbed solutions the MPs increase the ballooning on a similar level in both solutions with and without recycling. The convection part in the solution of reference with recycling (Fig. 4.21b) is also lower than in the solution without recycling. In the disturbed solutions with the MPs, the convection part has the same amplitude with recycling or without.

In summary, we have seen that in the solutions without recycling the MPs increase the ballooning of the radial energy flux at LFS, both in the CFR and in the SOL.
In the solutions with recycling, a reverse trend (negative flux) is seen in the CFR at

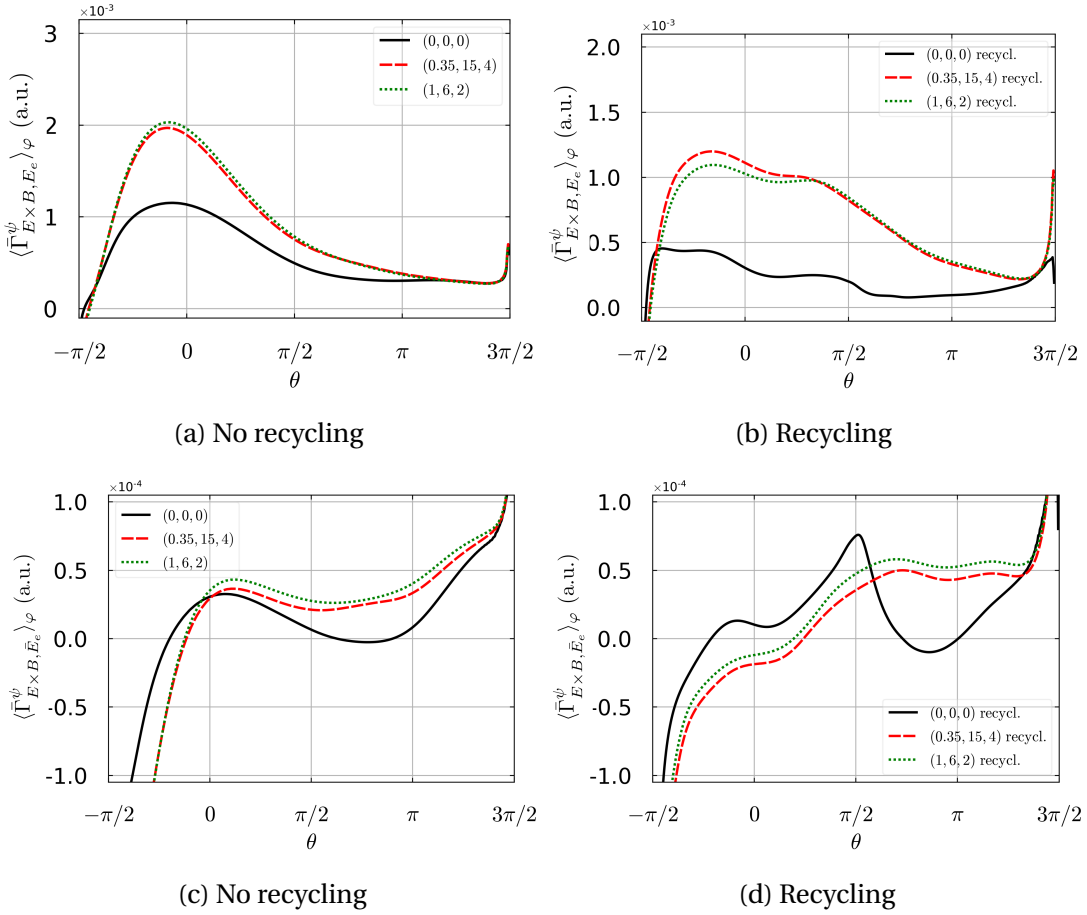


(a) No recycling

(b) Recycling

(c) No recycling

(d) Recycling

Figure 4.20.: Poloidal profiles of the $E \times B$ total mean energy flux $\bar{\Gamma}^{\psi}_{E\times B,E_e}$ (4.20a,4.20b) and mean-field mean energy flux $\bar{\Gamma}^{\psi}_{E\times B,\bar{E}_e}$ (4.20c,4.20c) time and $\varphi$ averaged at $r/a = 1.1$ (SOL). Cases without recycling (4.20a,4.20c). Cases with recycling (4.20b,4.20d)

the LFS, with a weaker ballooning in the disturbed solutions, while it is increased by the MPs in the SOL. We have also observed a reorganization of the energy flux between the convective and the conductive parts for the radial transport, which is more a consequence of the recyling than of the MPs themselves.

### 4.2.4. Density and power SOL width

We study the impact of the MPs on the density SOL width $\lambda_N$ and on the power SOL width $\lambda_q$. We already defined in Chap. 3 the density SOL width as the e-folding length of the density. In the same way, the power SOL width is the e-folding lentgh of the

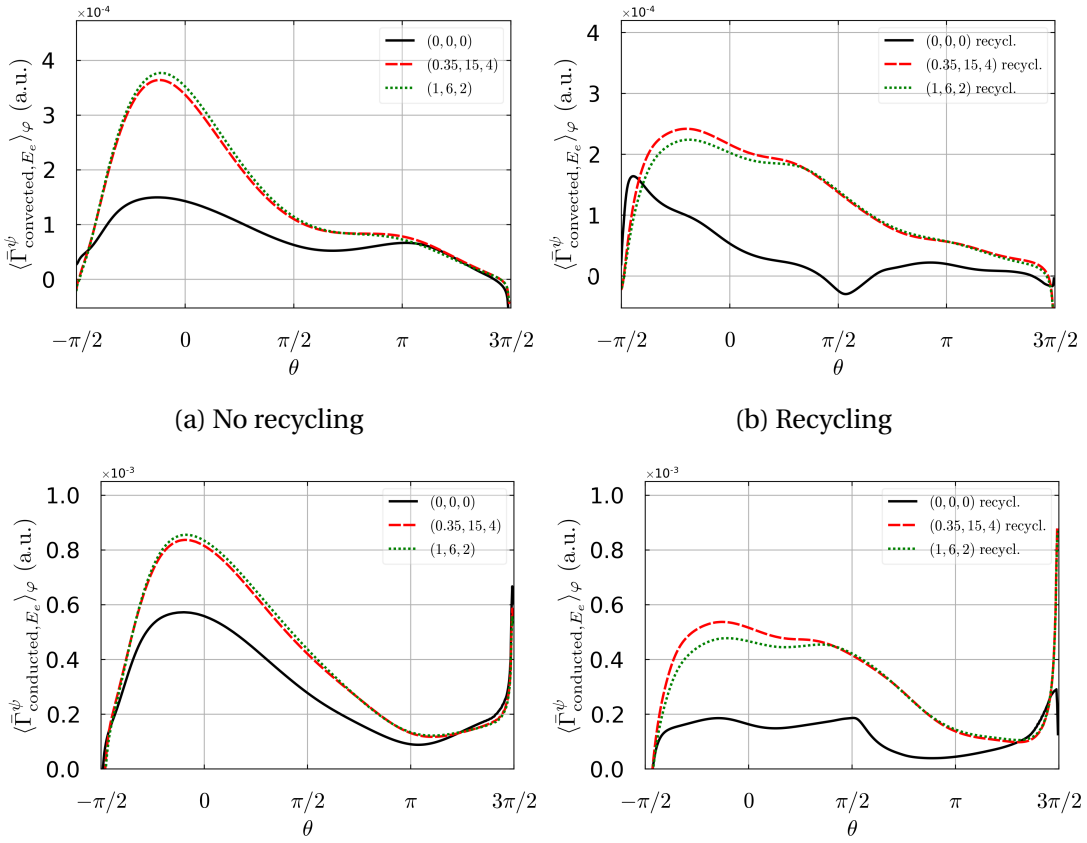


(a) No recycling

(b) Recycling

(c) No recycling

(d) Recycling

Figure 4.21.: Poloidal profiles of the $E \times B$ convected energy flux $\bar{\Gamma}^{\psi}_{\text{convected},E_e}$ (4.21a,4.21b) and conducted energy flux $\bar{\Gamma}^{\psi}_{\text{conducted},E_e}$ (4.21c,4.21c) time and $\varphi$ averaged at $r/a = 1.1$ (SOL). Cases without recycling (4.21a,4.21c). Cases with recycling (4.21b,4.21d)

parallel heat flux, defined as:

$$q_{\parallel} = q_{\parallel,e} + q_{\parallel,i} = \gamma_e N T_e \sqrt{T_e + T_i} + \gamma_i N T_i \sqrt{T_e + T_i} \tag{4.12}$$

with $\gamma_{e/i}$ the sheath heat transmission coefficient for electron and ion, respectively set at 4.5 and 2.5 for all non isothermal simulations. A reminder of the poloidal profile of $\lambda_N$ for the isothermal cases is plotted on Figs. 4.22a and 4.22b. The main result in the isothermal solutions is the mostly 5 to 10% decrease of the density SOL width in the disturbed solutions with respect to the solution of reference.

Figs 4.22 show both the density SOL width and the power SOL width for the non isothermal solutions. A complete opposite trend is observed here where disturbed solutions show increasing witdhs. In the solutions without recycling, $\lambda_N$ is plotted

on Fig. 4.22c. In the solution of reference, $\lambda_N$ is mostly around $30\rho_L$, and the MPs increase it all around the poloidal direction, especially at the top of the machine where the increase is of the order of 30%. In the solutions with recycling (Fig. 4.22d), $\lambda_N$ in the solution of reference is a bit higher (around $35\rho_L$) and the MPs increase this value to a peak at the top LFS. The form of the profile is also different, as the peak is well visible, compare to the almost flat profile in the disturbed solutions without recycling.

The power SOL width $\lambda_q$ in the solutions without recycling (Fig. 4.22e) is around $30\rho_L$ in the solution of reference and it shifts upward around $40\rho_L$ in the disturbed soluitons with MPs. The solutions with recycling are even more striking (Fig 4.22f), with similar value in the solution of reference (with a notable minimum at the HFS top), but a sharp increase at around $50\rho_L$ at the top of the machine in the disturbed solutions withMPs.

The trend between isothermal and non isothermal solutions is thus effectively opposite concerning the impact of the MPs. This is assuming a single exponential e-folding length for both isothermal and non-isothermal model. We have seen in Chap. 3, that, near the separatrix, the isothermal $\lambda_N$ actually increases with MPs.

## 4.3. Impact of MP on turbulence properties

The impact of on the fluctuations level of density and temperatures (electron and ion) is investigated first. Then, Probability Density Functions (PDF) and higher moments are studied to analyze the impact of MPs on the turbulence structures themselves.

### 4.3.1. Impact on fluctuations level

The evolution of the fluctuations level for the density, the electron and the ion temperatures in the radial direction, characterized here by the toroidal averaged of $\sigma_X / X$ (with $X$ the correspong field), are shown on Figs. 4.23, 4.24 and 4.25 respectively. To exhibit the differences on the poloidal asymmetry of the turbulence in the solutions with recycling and without, the fluctuations are plotted at the HFS and the LFS midplanes.

Figs. 4.23a and 4.23b show the density fluctuations at the HFS midplane. The fluctuations level in the CFR is low (below 0.1) and rather constant in the radial direction up to the vicinity of the separatrix. We still note that in the solutions with recycling the levels is even lower and near zero in the CFR close to the core. The MPs decrease the fluctuations in the solutions without recycling but increase them in the solutions with recycling, only for the perturbation (1,6,2). In the SOL, fluctuations levels increase to a maximum at the mid SOL, before decreasing. The profile is narrower for the solution of reference with recycling. The MPs seem to decrease the peak level of fluctuations,

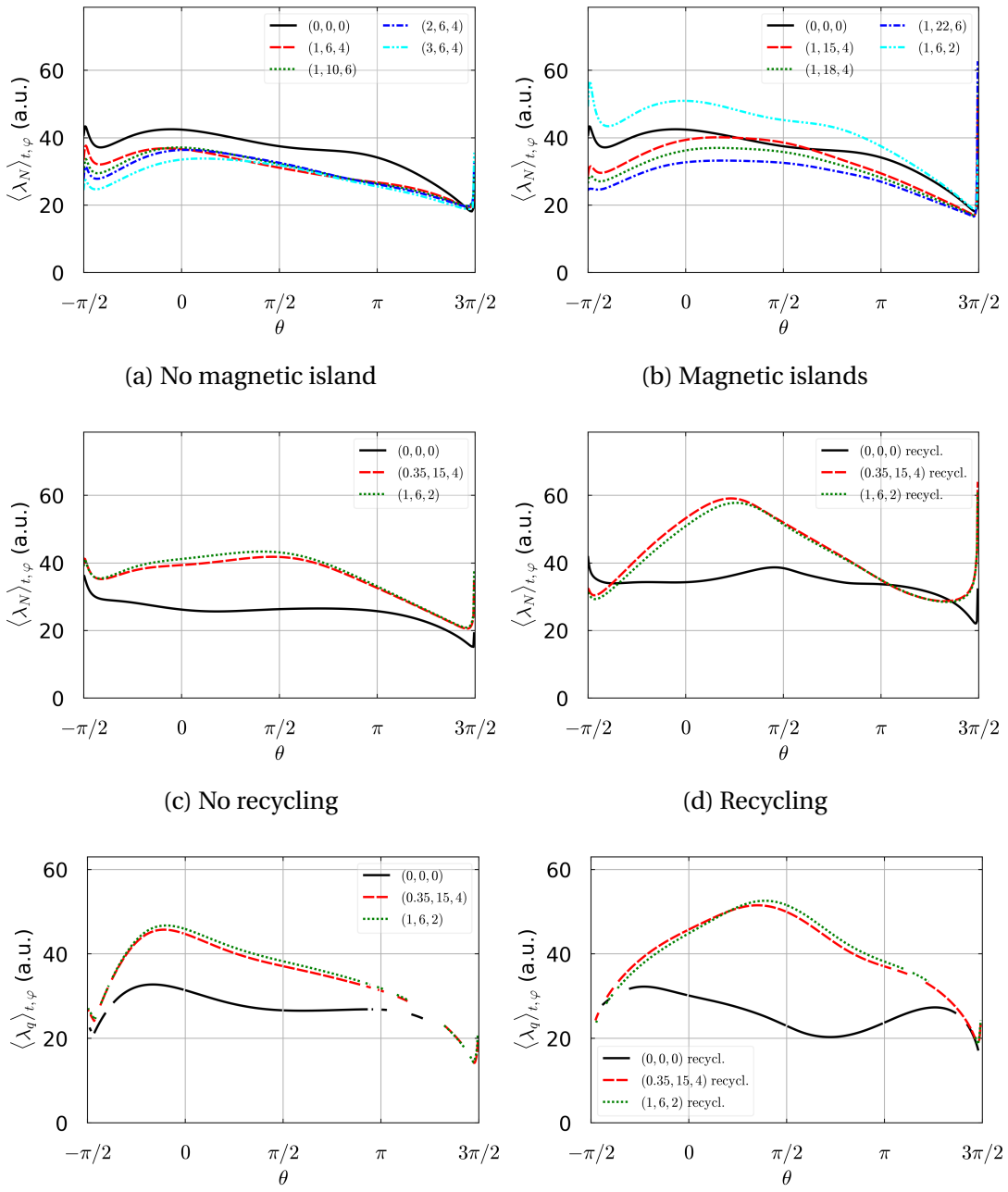


(a) No magnetic island

(b) Magnetic islands

(c) No recycling

(d) Recycling

(e) No recycling

(f) Recycling

Figure 4.22.: Poloidal profiles of $\lambda_N$ and $\lambda_q$, time and $\varphi$ averaged for the isothermal and non-isothermal cases. Cases without magnetic island ($\lambda_N$, isothermal) (4.22a). Cases with magnetic islands ($\lambda_N$, isothermal) (4.22b). Poloidal profiles of $\lambda_N$, the density SOL width (4.22c,4.22d), and $\lambda_q$, the power SOL width (4.22e,4.22f), time and $\varphi$ averaged for the non isothermal cases. Cases without recycling (4.22c,4.22e). Cases with recycling (4.22d,4.22f)

which is a bit similar to what has been observed in isothermal simulations at the HFS midplane.

The second diptic of profiles is the LFS midplane in the solutions without (Fig. 4.23c) and with (Fig. 4.23d) recycling. In the solutions without recycling, fluctuations are almost two times higher at the LFS than on the HFS in the CFR, with no impact of the MPs (quite similarly to isothermal cases). Then they peak at the mid SOL, almost two times higher than before decreasing in the far SOL (for the reference simulation). The MPs decrease the fluctuations in the mid and far SOL, and result in a mild increase in the vicinity of the separatrix in both closed and open flux surfaces. In the solutions with recycling, the density fluctuation levels are lower at the LFS (for one solution by almost a factor four) both in the CFR and in the SOL compare to the solutions without recycling. The decrease of density fluctuations in the CFR in the solutions with recycling is coherent with the weakening of the convective flux observed in the last section. On the contrary, in the solutions with recycling, MPs increase the fluctuations up to 50% in the SOL, with a flat profile from mid to far SOL (having almost an homogenous effect on the radial evolution of the fluctuations). Still, we note that, in the solutions with recycling, the fluctuations levels are lower than in the solutions without recycling. The decrease due to MPs in the solutions without recycling is higher than the increase level due to MPs in the solutions with recycling at the LFS midplane.

We look at now the electron (Figs. 4.24a and 4.24b) and ion (Figs 4.25a and 4.25b) temperatures fluctuation levels at the HFS midplane. The $T_e$ fluctuations are of similar order of magnitude (below 0.05) in both solutions of reference with and without recycling in the CFR, but they are a bit higher in the solutions without recycling in the SOL. The MPs in the disturbed solutions without recycling do not change the fluctuations in the CFR, and decrease them by around 30 to 50% (in relative variations) in the SOL. In the solutions with recycling, however, the MPs increase the fluctuations in the CFR by a factor up to five (for $(1,6,2)$) and flatten them to a plateau value similar to the distrubed solutions without recycling. The $T_i$ fluctuations (still HFS midplane) are 30% higher in the solutions with recycling than without. In the solutions without recycling, the MPs decrease the fluctuations both in the CFR and in the SOL. In the solutions with recycling, the MPs increase them at the CFR and decrease/flatten them in the SOL.

The LFS midplane shows, as usual, higher fluctuation levels for electron (Figs. 4.24c and 4.24d) and ion (Figs 4.25c and 4.25d). The shape of the profiles is quite similar to what happens at the HFS midplane. For $T_e$, in the solutions without recycling, there is almost no change (a slight increase) at the CFR when MPs are switched on but a decrease in the SOL. In the solutions with recycling, the MPs increase the fluctuations in the CFR and flatten the profiles in the SOL, with a global increase, resulting in similar level of fluctuations for the two source models. For $T_i$, we note in solutions without recycling a global decrease by around 20% of the fluctuations level when MPs are applied, whereas an increase of similar order happens in the solutions with

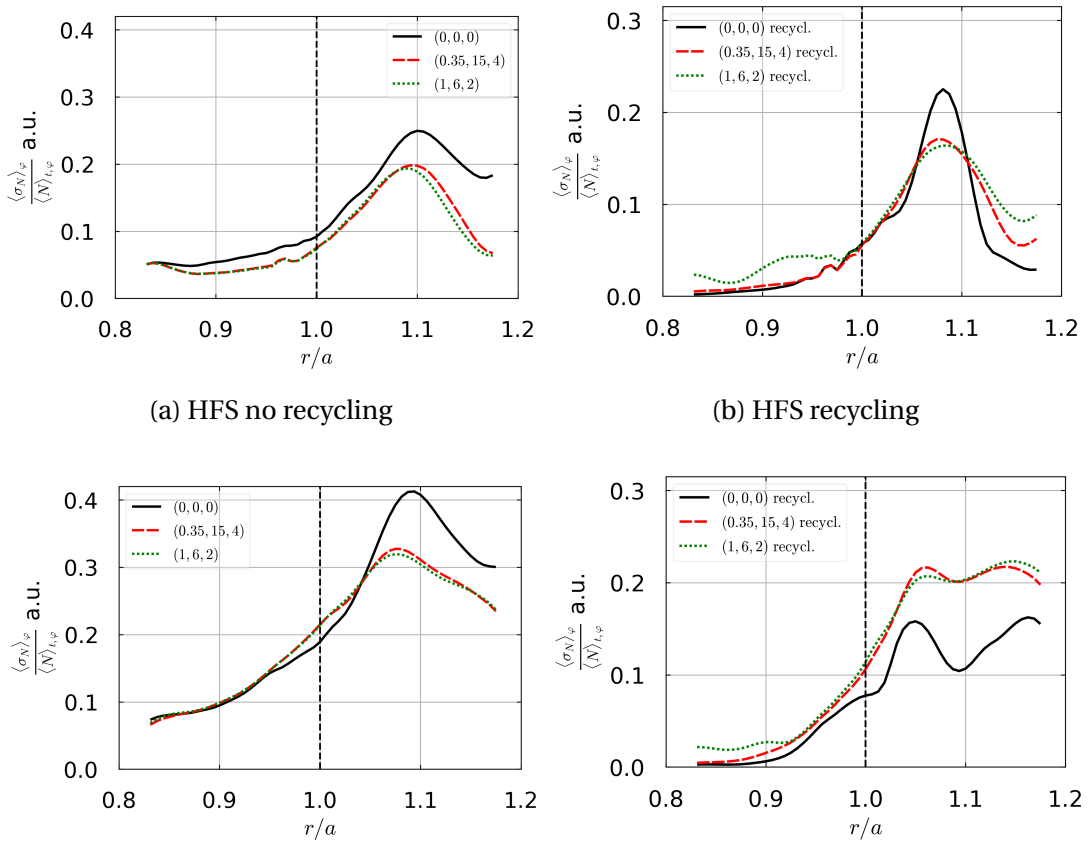


(a) HFS no recycling

(b) HFS recycling

(c) LFS no recycling

(d) LFS recycling

Figure 4.23.: Radial profiles of the standart deviation over time of the density averaged in the toroidal direction $\varphi$ and normalized by the $(t,\varphi)$-averaged density at the HFS (4.23a,4.23b) and at the LFS (4.23c,4.23d) midplane. Cases without recycling (4.23a,4.23c). Cases with recycling (4.23b,4.23d)

recycling.

As previously noted, in the solutions with recycling, a large part of the flux comes from the diffusive part in the CFR. Two hypothesis have been made:

- either the turbulence has been effectively damped by physical mechanims captured by our discretized system.
- either the physical response of the system leads to a shift of turbulence scales towards lower scales possibly badly or not captured by our discretization grid, in which case the drop of turbulent transport would be artifically enhanced in our results.

The lowering of the fluctuation levels in the CFR seen in the solutions with recycling for all the fields (and mainly the density $N$), at the HFS and LFS is consitent with the

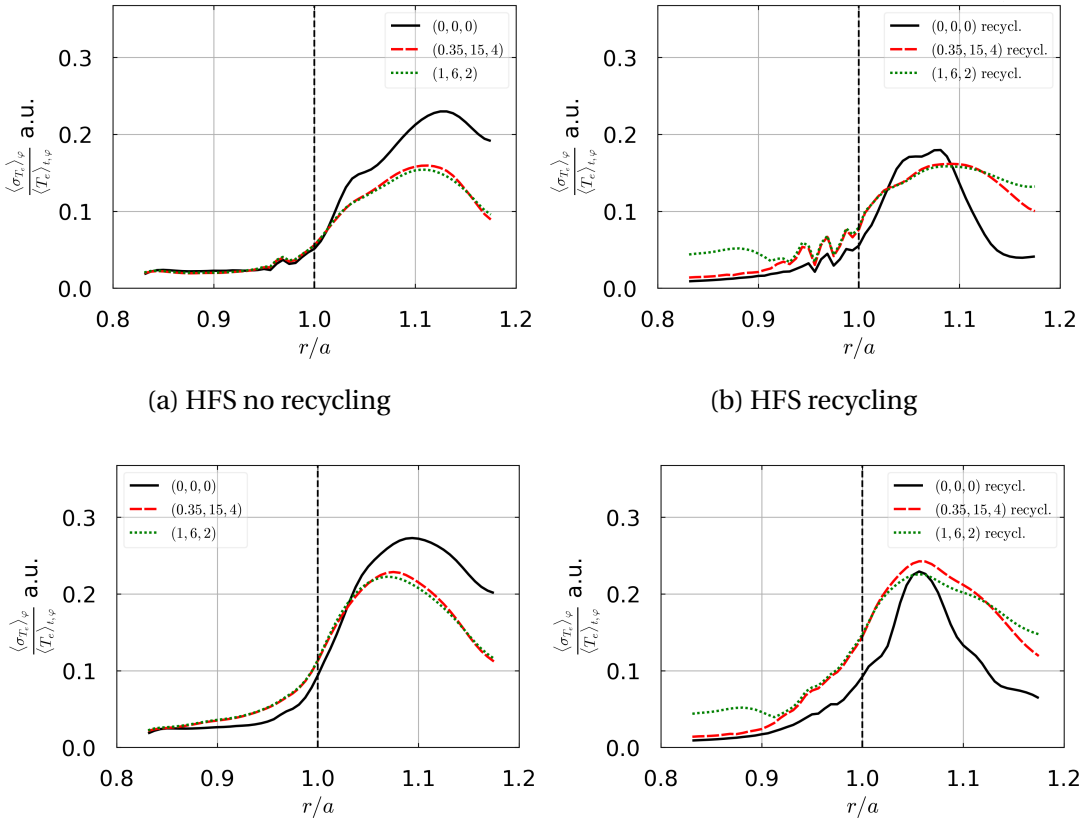


(a) HFS no recycling

(b) HFS recycling

(c) LFS no recycling

(d) LFS recycling

Figure 4.24.: Radial profiles of the standart deviation over time of the electron temperature averaged in the toroidal direction $\varphi$ and normalized by the $(t,\varphi)$-averaged electron temperature at the HFS (4.24a,4.24a) and at the LFS (4.24c,4.24a) midplane. Cases without recycling (4.24a,4.24c). Cases with recycling (4.24b,4.24d)

loss of turbulent fluxes (fluctuating-field mean ones for example) at these locations. This feature raises the question if the increase in temperature in the solutions with recycling, associated with a steepening of the temperature profiles, results in smaller fluctuations (in size), ill-captured by our mesh. Complementary simulations with a finer mesh would be needed to clarify this point.

In summary, the global trend is a decrease of the fluctuations levels in the solutions without recycling when MPs are switched on, with an opposite trend in the solutions with recycling.

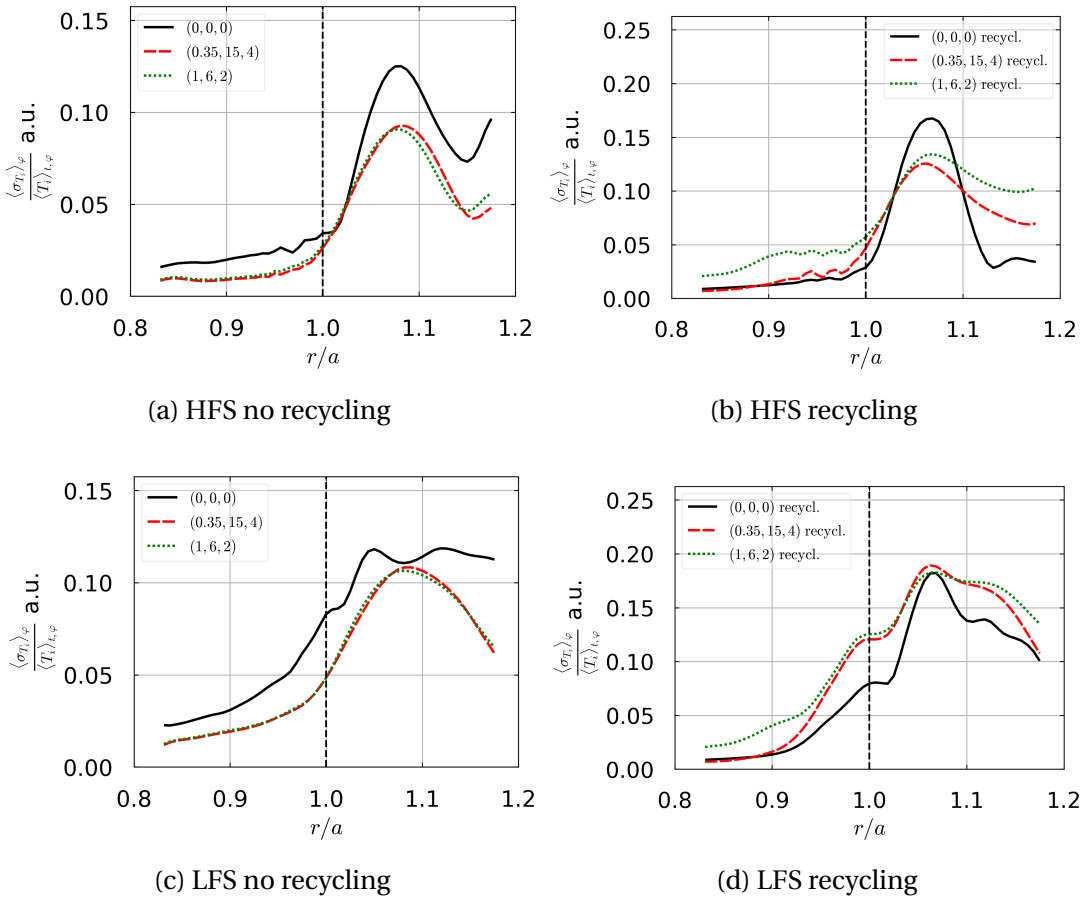


(a) HFS no recycling

(b) HFS recycling

(c) LFS no recycling

(d) LFS recycling

Figure 4.25.: Radial profiles of the standart deviation over time of the ion temperature averaged in the toroidal direction $\varphi$ and normalized by the $(t,\varphi)$-averaged ion temperature at the HFS (4.25a,4.25a) and at the LFS (4.25c,4.25a) midplane. Cases without recycling (4.25a,4.25c). Cases with recycling (4.25b,4.25d)

## 4.3.2. Turbulence intermittency for particle and energy

To better understand the effects of MPs on turbulence, we look at the Probability Density Functions of density events (Figs. 4.26), electron (Figs. 4.27) and ion (Figs. 4.28) temperature events. We choose the radial position $r/a = 0.98$ (near islands in the CFR) and $r/a = 1.1$ (in the SOL) at the LFS midpplane.

For the density events, the solutions without recycling at $r/a = 0.98$ (Fig. 4.26a) show nearly Gaussian PDFs with little impact of the MPs. In the solutions with recycling (Figs. 4.26b), the PDF in the solution of reference is still nearly Gaussian, albeit weakly skewed to the left (negative skewness). The MPs decrease visibly the skewness as the PDFs peak on the right and skew more on the left. In the middle of the SOL, at

$r/a = 1.1$, the PDFs of the solutions without recycling (Fig. 4.26c) show a very right skewed profiles (postive skewness), proof of an intermittent solution with bursts of higher than average density events. The MPs, in a similar fashion as what was observed in isothermal simulations, decrease the skewness, resulting in less skewed to the right (and peaked to the left) profiles. In the solutions with recycling, at $r/a = 1.1$ (Fig. 4.26d), the PDF of the solution of reference has a quasi opposite trend and skewed to the left. This result is surprising compare to other TOKAM3X simulations. Further investigations will be needed to understand this feature.

The MPs create a less negative skewness, resulting in more Gaussian shaped profiles. In all cases, the two MPs have similar effects on the PDFs, even if the amplitude and mode numbers are different. The conclusion for density events is quite like the one for isothermal simulations: the MPs decrease the intermittency into the SOL.

Regarding now the energy events, electron and ion temperatures are similar in behaviour and so are treated in parallel. At $r/a = 0.98$ and in solutions without recyclings, the electron temperature PDFs (Fig. 4.27a) are all nearly Gaussian with little influence of the MPs. A Gaussian shape is also observed for the ion temperature (Fig. 4.28a), but the solution of reference shows a higher amplitude than the disturbed solutions with MPs, showing an increase of the skewness. In the solutions with recycling now, at $r/a = 0.98$, the PDFs of the solution of the references for both $T_e$ (Fig. 4.27b) and $T_i$ (Fig. 4.28b) are still nearly Gaussian, even if it is a bit flatten for $T_i$. The PDFs in the distrued solutions with MPs skew to the left (negative skewness) for $T_e$ with a more pronounced effect for the case $(1,6,2)$. For the ion temperature (Fig. 4.28b) it is more peculiar as the reference flattened PDF, it flattens even more for the case $(0.35,15,4)$, but skews to the left (negative skewness) with a well-marked double bump for the case $(1,6,2)$. This double bump is not new in our simulations, since it was already observed in isothermal solutions at the same poloidal locations (not shown in Chap. 3). The resulting behaviour for turbulent events is still to be understood. We nevertheless can conclude that the impact of MPs on temperature events for the solutions with recycling seem more oriented toward an increase of intermittency (increase of positive skewness) in the CFR in the vicinity of the separatrix.

Into the SOL at $r/a = 1.1$ and in solutions without recycling, $T_e$ events are shown on Fig. 4.27c. The PDFs skew strongly to the right (positive skewness) and the MPs tend to increase the skewness in a similar way (no strong difference between the two modes). The solutions with recycling (Fig. 4.27d) still shows a profile skewed to the right (positive skewness) for the solution of reference but with a lower amplitude of the peak on the left. In the distrubed solutions, the MPs tend to increase (opposite to the density events) the skewness with a stronger effect for the case $(1,6,2)$ (the peak is 20% higher compare to $(0.35,15,4)$).

For the solutions without recycling, $T_i$ events at $r/a = 1.1$ are shown on Fig. 4.28c. The description is similar, with a right skewed profile (positive skewness) for the solution of reference and MPs which tend to shift more toward a Gaussian profile. The

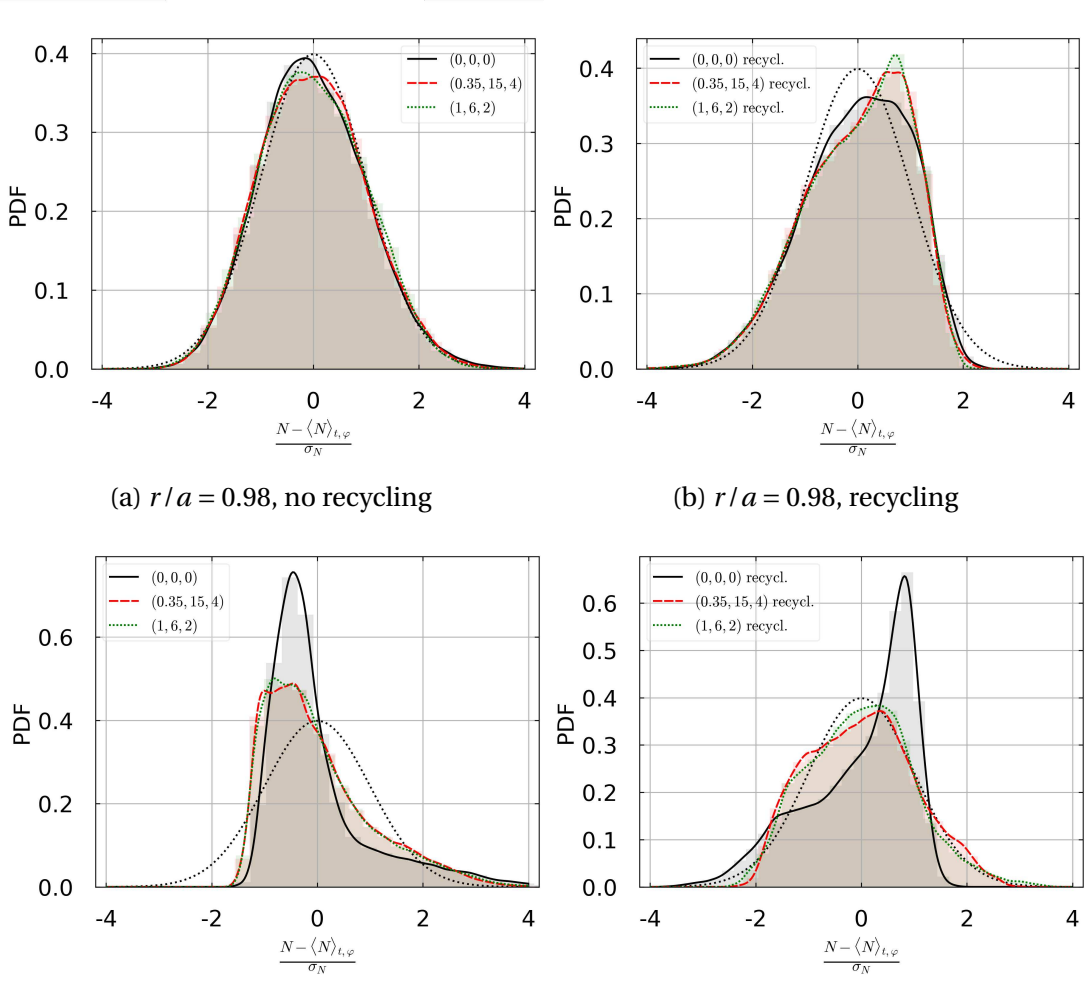


(a) $r/a = 0.98$, no recycling

(b) $r/a = 0.98$, recycling

(c) $r/a = 1.1$, no recycling

(d) $r/a = 1.1$, recycling

Figure 4.26.: Probability Density Functions of density events taken at the LFS mid-plane. $r/a = 0.98$ (4.26a,4.26b). $r/a = 1.1$ (4.26c,4.26d). The dotted black line is a perfect gaussian for help. The color area is the histogram while the curves are obtained through a density kernel method.

difference is that the reference is barely skewed for $T_i$ as compared to $T_e$ profiles. For the solution with recycling (Fig. 4.28d), the PDF for $T_i$ in the solution of reference is more flat than the one for $T_e$, and the MPs still increase the skewness to the right (increase of the positive skewness, to lesser extend), with still a more pronouced effect for the case $(1,6,2)$.

In summary, the global trends for temperature fluctuations are the following:

- In the core without recycling, MPs very midely move the skewness towards negative values compared with the quasi-Gaussian PDFs of the solution of reference.

- In the core with recycling, the negative skewness of the solution of reference gets amplified by the MPs, with a different behaviour (possible double-bump) depending on the mode number of the perturbation.
- In the SOL without recycling, the MPs reduce the strongly positive skewness of the PDF of the reference solution.
- In the SOL with recycling, the MPs on the contrary increase the weakly positive skewness of the PDF of the reference solution.

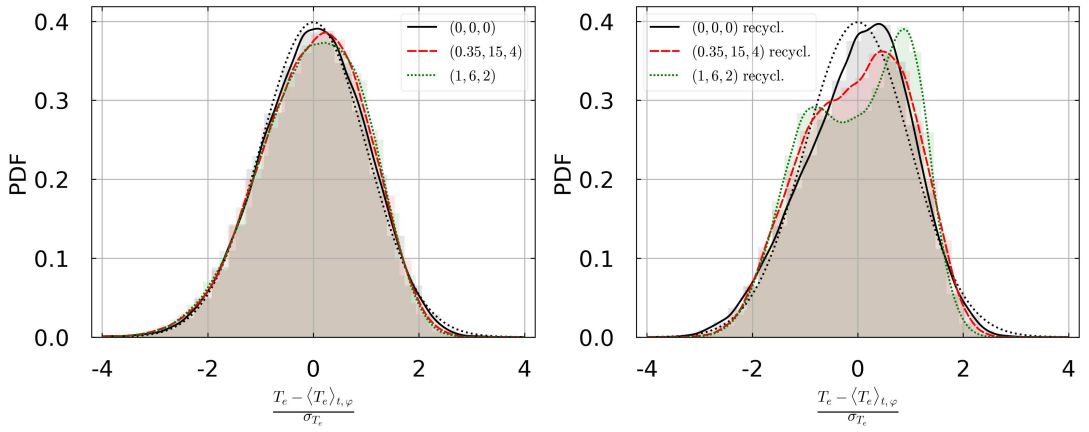


(a) $r/a = 0.98$, no recycling

(b) $r/a = 0.98$, recycling

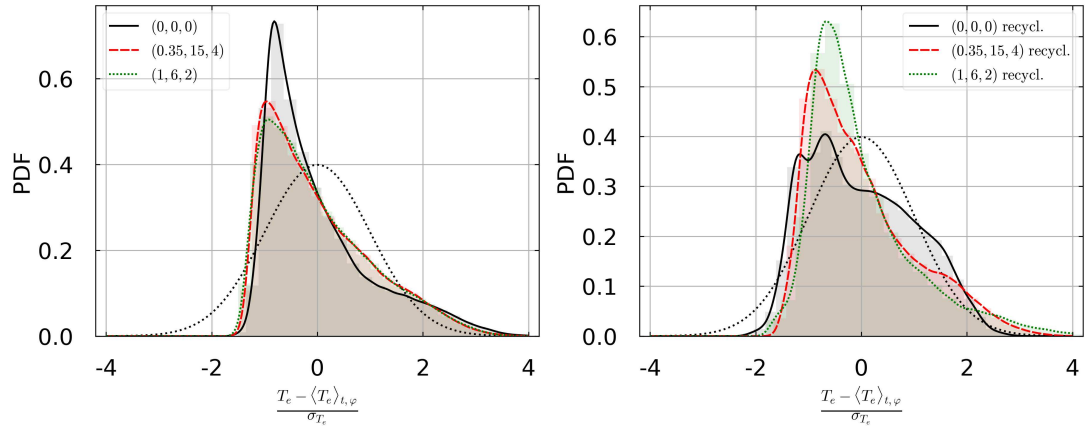


(c) $r/a = 1.1$, no recycling

(d) $r/a = 1.1$, recycling

Figure 4.27.: Probability Density Functions of electron temperature events taken at the LFS midplane. $r/a = 0.98$ (4.27a,4.27b). $r/a = 1.1$ (4.27c,4.27d). The dotted black line is a perfect gaussian for help. The color area is the histogram while the curves are obtained through a density kernel method.

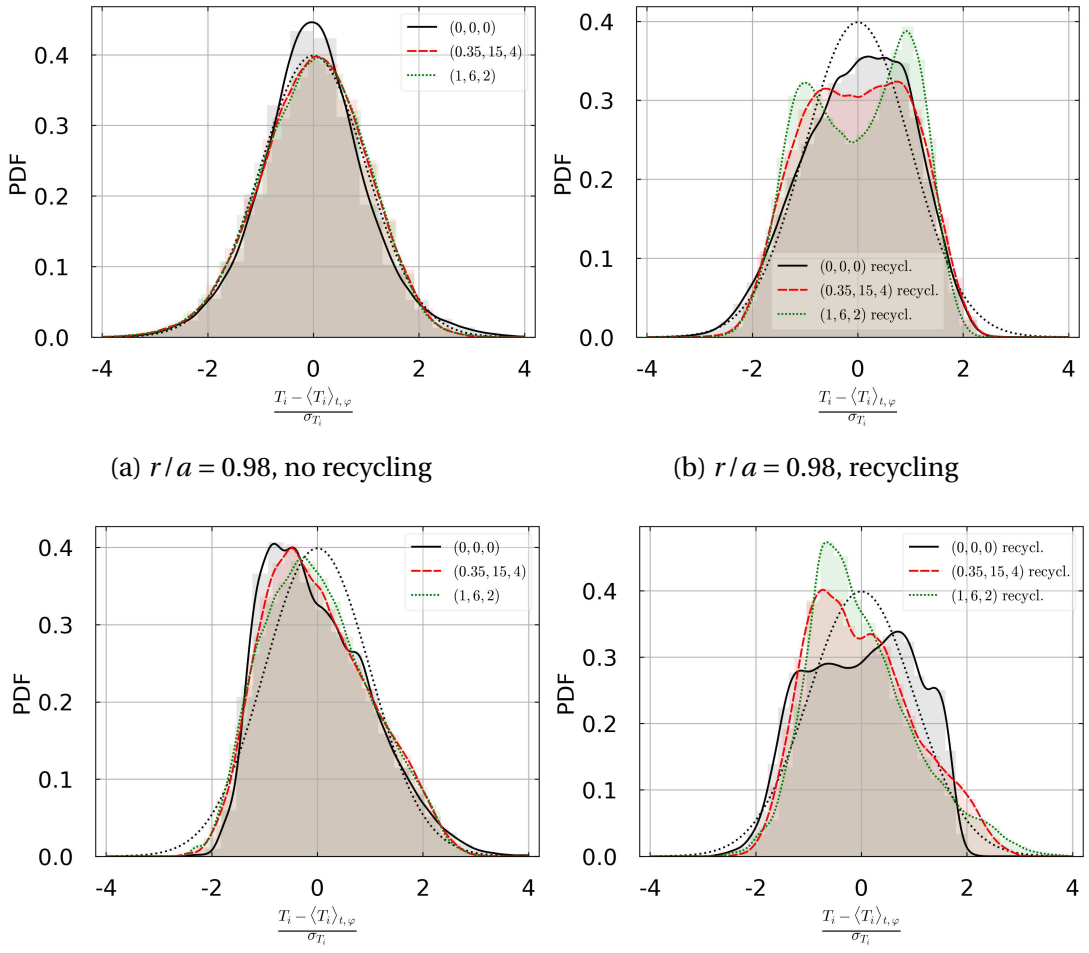


(a) $r/a = 0.98$, no recycling

(b) $r/a = 0.98$, recycling

(c) $r/a = 1.1$, no recycling

(d) $r/a = 1.1$, recycling

Figure 4.28.: Probability Density Functions of ion temperature events taken at the LFS midplane. $r/a = 0.98$ (4.28a,4.28b). $r/a = 1.1$ (4.28c,4.28d). The dotted black line is a perfect gaussian for help. The color area is the histogram while the curves are obtained through a density kernel method.

We have considered the PDFs at the LFS midplane (where the turbulence is more developped) at a specific radial position. To have a more thorough study of the possible impact of the MPs on the intermittency for both density and temperature events, we plot the radial skewness $\gamma_1$ at the LFS midplane, averaged in the toroidal direction, of $N$, $T_e$ and $T_i$ on Figs. 4.29.

In solutions without recycling, Fig. 4.29a in the CFR shows little impact of the MPs, with an almost zero constant value of the skewness on the whole region. This is well represented by the density PDF at $r/a = 0.98$ (Fig. 4.26a), with no intermittency for this part. The major change occurs first in the mid SOL and further out, with the

decrease of the skewness due to the MPs, well seen on the PDF 4.26c. For the electron temperature (Fig. 4.29c), the skewness changes from zero to a constant negative value in the CFR, which was seen on the PDF. 4.27a. We can improve the analysis by saying that MPs in the CFR in the solutions with recycling tend to create an intermittency of lower than average bursty events for $T_e$. No change in the skewness is observed at the separatrix and so until the mid SOL where the MP s decrease the skewness, which has been described on the PDF. 4.27c. Finally for $T_i$ (Fig. 4.29e), the behaviour induced by the MPs in the CFR is similar with $T_e$, with a global decrease to negative constant value (low burst-behaviour intermittency). The decrease of the skewness is on the whole radial profile, which is clearly seen on the mid SOL PDF 4.28c. The conclusion in the solutions without recycling is that the MPs decrease the high burst intermittency for density and temperature events. It is completed with the fact that the MPs can favor low burst intermittency in the CFR for temperature events.

Regarding now the solutions with recycling we analyze the skewness in the innermost part of the CFR. It is probably not so meaningfull due to the fact that the turbulence in this region is severely damped and so we limit ourself to the region near the separatrix and the SOL. For the density (Fig. 4.29b), the MPs tend to increase the skewness toward less negative values in the CFR, except near the separatrix, which was observed on the PDF 4.26b. In the SOL, the MPs still create a lower skewness before reverting the trend in the mid and far SOL, switching from negative (in the solution of reference) to positive (din distrubed solutions with MPs) skewness, a clearly observed phenomenon on the PDF 4.26d. For $T_e$ (Fig. 4.29d) and $T_i$ (Fig. 4.29f), the MPs midely increase the skewness in the CFR, near the separatrix to less negative values. The analysis of the impact of MPs in the solutions with recycling is thus confirmed to be an increase in high burst intermittency in the SOL for both density and temprature events. It is completed, thanks to the study of the skewness, by the observation of a loss of intermittency in the CFR (at least near the separatrix) when the MPs are switched on.

## 4.4. Conclusion on MPs in non-isothermal turbulent simulations

We have studied the impact of the MPs on electrostatic non isothermal fluid turbulence at the edge of a limiter plasma in a circular geometry. Single 3D mode MPs of small amplitude have been considered as well as two settings for the particle sources, one being located at the core and the other one at the limiter mimicking recycling. Results show an impact of MPs on both the plasma equilibrium and on the turbulence properties. The impact can be quite different depending on the source location mimicking or not the recycling.

Regarding the plasma equilibrium, the MPs lead to a decrease of the pressure profiles. However, only the solutions with recycling recover experimental trends

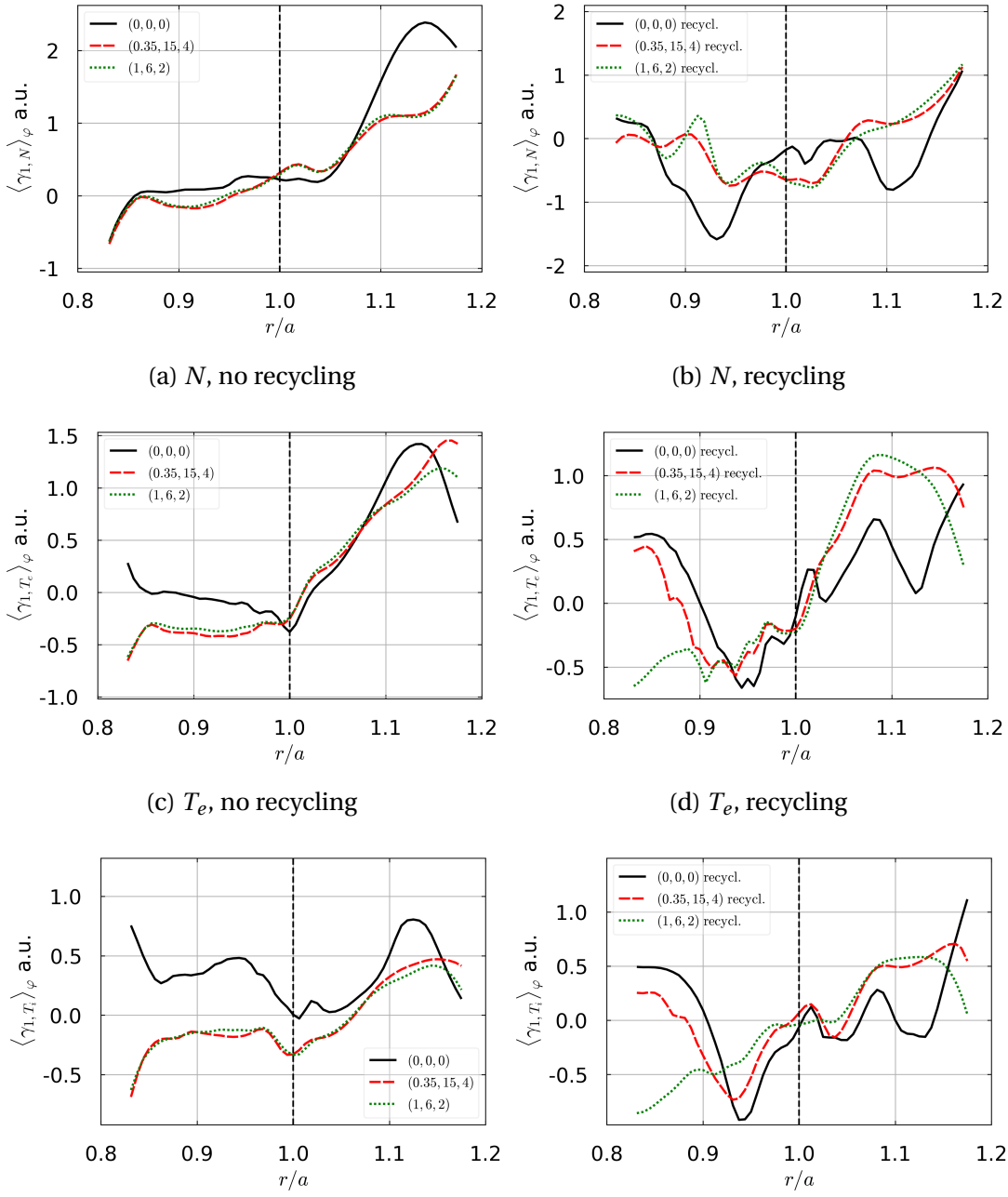


(a) $N$, no recycling

(b) $N$, recycling

(c) $T_e$, no recycling

(d) $T_e$, recycling

(e) $T_i$, no recycling

(f) $T_i$, recycling

Figure 4.29.: Radial profiles of the skewness $\gamma_1$ at LFS midplane, $\varphi$ averaged. Density skewness (4.29a,4.29b), electron temperature skewness (4.29c,4.29d), ion temperature skewness (4.29e,4.29f). Cases without recycling (4.29a,4.29c,4.29e). Cases with recycling (4.29b,4.29d,4.29f)

characterized by the loss of density in the edge of closed field lines region (the so-called density pump-out). The solutions without recycling show on the contrary a density pump-in. A decrease/flattening of the radial electric profile is recovered for both source locations. Without recycling, it is not associated to a change in the parallel velocity but it is when recycling is taken into account. Theses changes are associated to a complex flux reorganisation in the edge plasma, both for the mean and turbulence fluxes. Concerning particles fluxes, the mean-field mean changes are more important in the solutions with recycling than without, whereas for the turbulence ones changes are more important in the solutions without recycling. An more marked ballooning is seen in the solutions without recycling when the MPs are switched on, whereas in the solutions with recycling, a reverse trend with a negative particle flux exists in the CFR, decreased by MPs, and without any ballooning into the SOL. Still, the MPs increase the particle flux in this region. Concerning the energy fluxes, the MPs increase the ballooning in the solutions without recycling. In the solutions with recycling, a reverse trend with negative energy fluxes is seen in the CFR, with a weakening effect of the MPs, but with a ballooning in the SOL which is more marked with MPs. It is probably possible to explain most of the differences in the response of the solution to MPs depending on the particle source position, by considering the poloidal symmetry breaking induced by the localization of the source in the vicinity of the limiter in the recycling case. A deeper analysis would be necessary to backup this explanation.

Concerning the exhaust concern, isothermal simulations showed a decrease of the density SOL width due to the MPs. Here, non isothermal simulations exactly show the opposite trend for both the density and the power SOL width.

Regarding the turbulence properties, even if the nature of the edge turbulence can change a lot depending on the source locations (with or without recycling), the MPs impact the turbulence spatial distribution on the LFS/HFS asymmetries and on the radial profiles. The MPs have opposite effects in the solutions with or without recylcing. Without recycling, the turbulence intermittency weakens whereas the fluctuation levels decrease, especially in the SOL. With recycling, the MPs change the intermittency for density events, from large amplitude events to low amplitude ones in the CFR, but still conserve a classic intermittent behaviour for the temperature events. Moreover, the MPs have been seen to increase the fluctuation levels for both density and temperatures.

Finally, this study raises several questions. Most can be linked to the turbulence apparent weakening in the CFR in the solutions with recycling. Several progress can be made. The first is a study on a finer mesh to see if the turbulence weakening is due to an excessive dissipation related to turbulent scales smaller than the mesh resolution. A second progress is on the realism of the sources in the modeling of the recycling process. The correct way is to incorporate neutrals physics by running TOKAM3X-EIRENE coupled simulations in order to have a self-consitent recycling. In present simulations, the source of particules is very crude and it is not associated to a

new energy sink which could be the explanation for the sharp increase of the radial temperature profile, resulting in an apparent weakening of turbulence intensity in the CFR.

# 5. From turbulent to mean-field isothermal simulation, from circular to complex geometry

## Table of Content

At the end of Chapter 3, we saw that one can define anomalous transport coefficients from the output of direct turbulence simulations by taking the ratio of the average flux by the opposite of the average gradient of the transported quantity. Such diffusion coefficients can then be used in mean-field simulations to represent anomalous transport without modeling turbulence. Although this approach, referred to as the gradient-diffusion assumption, has been shown to have strong limits and to describe only very coarsly turbulent transport [50, 86], it is widely used in mean-field models to give a simple and quick representation of anomalous transport. It is currently the work-horse of edge plasma simulations with magnetic perturbations [45] under the assumption that the MPs do not impact these coefficients. We saw in Chap. 3 that effective diffusion coefficients post-calculated from TOKAM3X turbulence simulations demonstrate on the contrary an impact of the MPs on this description of transport. In this chapter, we adress the same issue in a different way by looking how mean plasma fields respond to MPs in mean-field simulations and comparing this to post-calculated mean-fields in turbulent cases. In order to compare on the same footing, we first use the TOKAM3X code in mean-field mode (no turbulence) with the isothermal model and compare the output with the turbulent simulations presented in Chap. 3. In a second part, we implement magnetic perturbations into the SOLEDGE3X-HDG.

## 5.1. From turbulence to mean-field simulations

As mentionned in the conclusion of Chap. 3, the numerical analysis of the impact of RMPs on the edge equilibrium plasma including neutrals recycling have only been performed using mean-field codes [45]. These studies relied on perpendicular diffusion coefficients to characterize anomalous radial transport. They are currently assumed to remain invariant when RMPs are switched on. We seek in this section to quantify the impact of such assumptions. 3D turbulence simulations are compared to corresponding 3D transport simulations in which velocity drifts have been switched off and the anomalous transport has been modeled by a constant diffusion coefficient.

### 5.1.1. Simulation settings

Concerning the turbulent simulations, we use the MP $(1,6,2)$ and $(1,22,6)$ already seen in Chapter 3. Concerning the mean-field simulations, the isothermal model is simplified into the system:

$$\begin{cases} \partial_t N + \boldsymbol{\nabla}\cdot(\Gamma_i \boldsymbol{b}) &= \boldsymbol{\nabla}\cdot(D_{\perp N}\boldsymbol{\nabla} N) + S_N \\ \partial_t \Gamma_i + \boldsymbol{\nabla}\cdot\left(\frac{\Gamma_i^2}{N}\boldsymbol{b}\right) &= -\nabla_\parallel(P_e+P_i) + \boldsymbol{\nabla}\cdot\left(D_{\perp\Gamma} N \boldsymbol{\nabla}(\frac{\Gamma_i}{N}) + D_{\perp N}\frac{\Gamma_i}{N}\boldsymbol{\nabla} N\right) + S_\Gamma \end{cases} \tag{5.1}$$

The effects of the perpendicular drifts are all expressed through the perpendicular coefficients $D_\perp$. Three mean-field simulations have been done with $D_\perp = 3.9\cdot 10^{-2}\rho_L^2\omega_c$, according to the results obtained with the turbulent transport in Chap. 3 (the perpen-

dicular diffusion takes into account the turbulent transport), and the perpendicular velocity $\vec{u}_\perp$ is set to zero. We keep the same geometry and physical parameters as the turbulent simulations used in Chap. 3. In addition, to avoid the occurence of small flow scales related to microturbulence the vorticity and the Ohm law equations are shunted. The perpendicular velocity $\vec{u}_\perp$ is put to zero and thus the radial transport is entirely modelled by $D_\perp$.

The only way to compare turbulent and mean-field simulations are the density and the ion momentum. In the following part, we concentrate on the density toroidal inhomogeneities defined as:

$$\delta N^0_\varphi = \frac{\langle N_{\mathrm{MP}} \rangle_t - \langle N_{(0,0,0)} \rangle_{t,\varphi}}{\langle N_{(0,0,0)} \rangle_{t,\varphi}} \tag{5.2}$$

This allows to see the toroidal as well as poloidal differences due to MP compared with the reference simulation. An other observation of interest is the 3D impact of the MPs themselves and could be seen through the density toroidal variation, noted:

$$\delta N_\varphi = \frac{\langle N_{\mathrm{MP}} \rangle_t - \langle N_{\mathrm{MP}} \rangle_{t,\varphi}}{\langle N_{\mathrm{MP}} \rangle_{t,\varphi}} \tag{5.3}$$

which allows to see the toroidal variations induced by the MPs, as well as, for the reference cases, to compare turbulent and mean-field simulations without MP.

### 5.1.2. Localized inhomogeneities on islands in transport simulations

In turbulent simulations, the MPs have been seen to play a role on averaged quantities as well as turbulent properties. We compare the toroidal density inhomogeneities $\delta N^0_\varphi$ on poloidal slices taken at $\varphi = 0$ on Figs 5.1. We choose the simulation of reference $(0,0,0)$, and two disturbed solutions with $(1,6,2)$ and $(1,15,4)$.

The Figs 5.1a,5.1c and 5.1e respectively show the mean-field solutions obtained for $(0,0,0)$, $(1,6,2)$ and $(1,15,4)$ without turbulence. The Figs 5.1b,5.1d and 5.1f correspond to the solutions with the same perturbations but obtained with the turbulence model.

The first difference to be noted in the two sets of simulations is the amplitude of the perturbation between mean-field and turbulent simulations without MP (fig. 5.1a,5.1b). The turbulence in the toroidal direction creates fluctuations around 10% of the density distribution, which is to compare with the perfectly axisymmetric mean-field simulation. This difference is probably due to the finite duration of our statistical interval and the strong correlation in the toroidal phasing between consecutive large scale events. In turbulent simulations, filaments develop in the toroidal direction (blobs in 2D) in the SOL. These filaments turn along the magnetic field lines. These latter naturally do not appear in a mean-field simulations as they are typical turbulent structures.

We can now compare the difference with MPs and we can clearly see the difference

in the amplitude of the perturbation between mean-field and turbulent simulations, being one order of magnitude stronger in the turbulent cases (see Figs 5.1). In the mean-field simulations (Figs. 5.1c and 5.1e), we clearly see the inhomogeneities near the location of the islands. They are located around the separatrix and the structures, then, spread in the SOL. Some inhomogeneities can be seen in the CFR but barely. We can note that they are more defined at the HFS, particularly for the MP (1,6,2) (Fig. 5.1c). In this case, the large structures at LFS seem to be more diluted in the SOL than the case (1,15,4) (Fig. 5.1e). The turbulent simulations clearly shows an influence of the islands as the structures look smaller in the SOL for the case with smaller islands (resp. Fig.5.1d,5.1f). Nevertheless, the toroidal inhomogeneities are not aligned with the magnetic islands and mainly appear after the separatrix, in the far SOL. It is really different compare to the mean-field simulations. We can also note in the case (1,15,4), fig. 5.1f, that a loss of density appear in the CFR at the LFS. This loss is a direct observation of the density pump-out studied in Chap. 3.

These results demonstrate that the MPs perturb turbulent transport in a non poloidally/toroidally symmetrical way, which in turn impacts the distribution of the transported field, i.e. the density in this case. The effect is non local and keeps a trace of the mode of the MP even in the SOL far from the magnetic islands. A possible explanation for these observations is that the instabilities driving turbulence develop with a specific poloidal phase and mode due to their interaction with the magnetic perturbation rather than with a random phase. The turbulent structures then keep trace of this initial phase during their radial propagation in the SOL. This way, the MPs generate a phase locking of turbulent structures and drive poloidally/toroidally non symmetric turbulent transport even away from the islands.

### 5.1.3. Density distribution on the limiter

In this section, a comparison is made of the density toroidal inhomogeneities $\delta N^0_\varphi$ at the limiter between turbulence and mean-field simulations. The geometry, equation model and MPs are all simpler than what can be found in [45], which is the most advanced study of the sort at the current date. Nevertheless, even a simpler model could provide insight on the physic at play. On Figs 5.2, we plot the density toroidal inhomogeneity at the limiter. The dotted horizontal line separates the HFS limiter (above) and the LFS one (below). The Figs 5.2a,5.2c and 5.2e are respectively the mean-field model with MP (0,0,0), (1,6,2) and (1,15,4). The Figs 5.2b,5.2d and 5.2f are respectively the turbulent model with MP (0,0,0), (1,6,2) and (1,15,4). Looking at the reference cases, without MP, we note, as expected, the homogeneous density distribution for the mean-field simulations (Fig. 5.2a) whereas the turbulence model shows fluctuations that spread in regular stripes but with weak amplitudes and without favorable side (Fig. 5.2b). When MPs are introduced, the results change sharply. In the (1,6,2) MP, mean-field model (Fig. 5.2c), we note a clear asymetry between LFS and HFS, with a predominant effect at LFS. The toroidal mode $n = 2$ is clearly visible (we remind

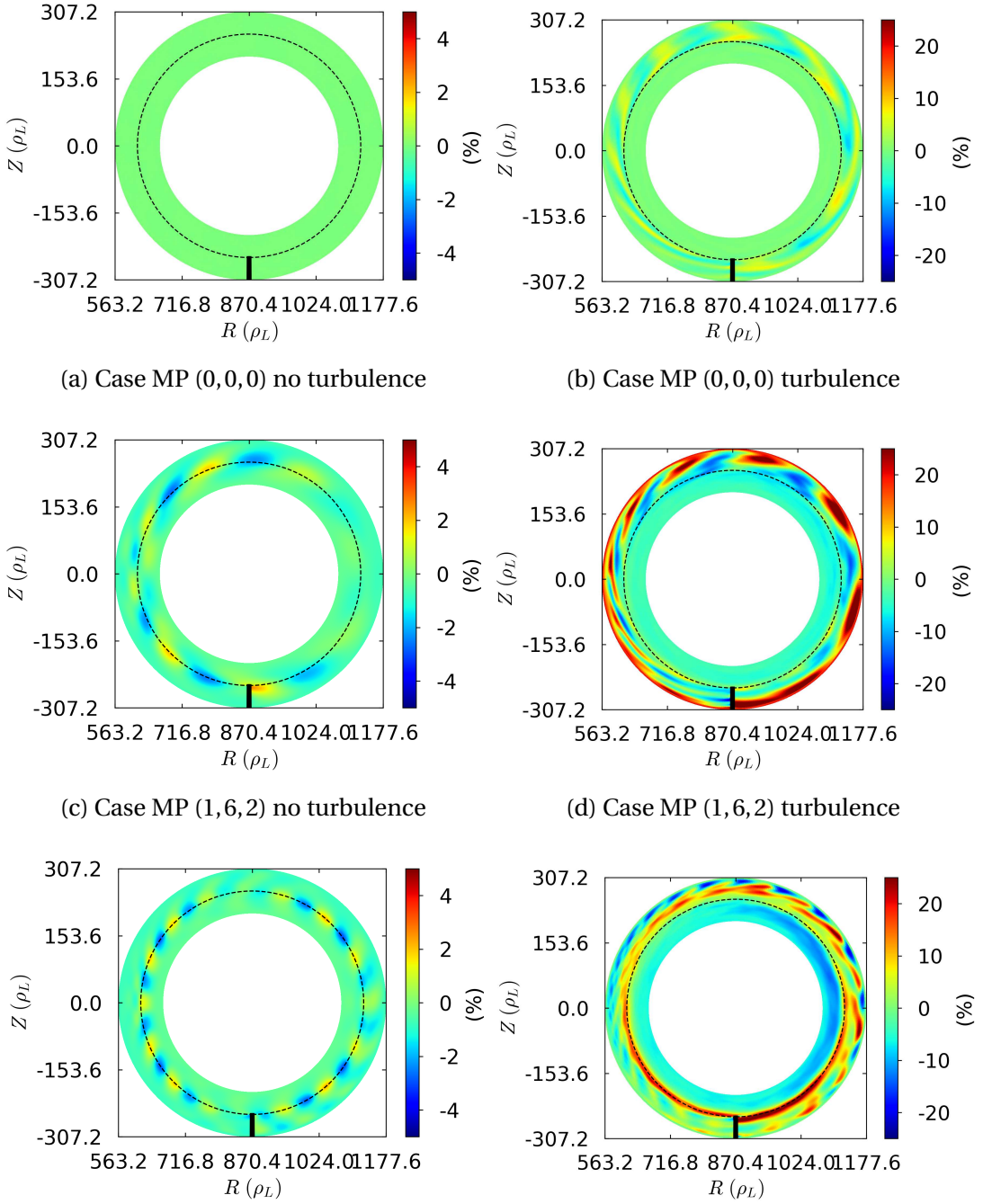


(a) Case MP (0,0,0) no turbulence

(b) Case MP (0,0,0) turbulence

(c) Case MP (1,6,2) no turbulence

(d) Case MP (1,6,2) turbulence

(e) Case MP (1,15,4) no turbulence

(f) Case MP (1,15,4) turbulence

Figure 5.1.: TOKAM3X simulations: poloidal slice at $\varphi = 0$ of density toroidal inhomogeneity as $\delta N^0_\varphi = (\langle N_{\mathrm{MP}} \rangle_t - \langle N_{(0,0,0)} \rangle_{t,\varphi}) / \langle N_{(0,0,0)} \rangle_{t,\varphi}$

the reader that the simulation is a half-torus). The same can be observed for (1,15,4) MP (Fig. 5.2e) with a smaller amplitude of density inhomogeneities. Fluctuations of similar amplitudes can still be seen at HFS but more concentrated at the upper level of the limiter. In mean-field simulations, the MP seems to actually impact mainly the target at the LFS rather than the HFS. The turbulence cases are more complex to analyse. No clear trend seems to appear concerning the mode numbers (fig. 5.2d,5.2f). We still can say that a larger density fluctuation occurs at the LFS limiter for both MP but the fluctuations at the HFS can not be neglected.

In order to highlight solely the non axysymmetric part of the perturbed density field, we now plot on Figs. 5.3 $\delta N_\varphi$ which excludes the toroidally symmetric part of the perturbation. The reference turbulent case is already plotted on Fig. 5.2b ($\delta N^0_\varphi = \delta N_\varphi$ for the reference case). Figs. 5.3 show only the turbulence cases as the mean-field ones are no different from the density toroidal inhomogeneities seen on Figs. 5.2. We can clearly see the difference in the turbulence cases between $N^0_\varphi$ and $\delta N_\varphi$. The mode (1,6,2) shows clearly the $n = 2$ mode (see Fig. 5.3a), and (1,15,4) does as well for $n = 4$ (see Fig. 5.3b). We note that the impact for the toroidal variations created by MPs is stronger in the HFS part of the limiter.

The conclusion at this point is the importance of accurately modeled 3D turbulent processes coupled with MP. It should be taken as an encouragement to pursue the development of turbulence codes to handle plasma simulations in realistic geometries with magnetic perturbations. In mean-field simulations, the response of the plasma to the MP is local and exhibits the same mode number as the MP. In turbulence simulations, the response of the plasma is more complex with an impact not only on the mode number corresponding to the MP but also on axisymmetric modes. Turbulence introduces non locality in the plasma response, the largest perturbation on the density being localized radially downstream of the magnetic islands probably due to phase locking of instabilities by the MPs.

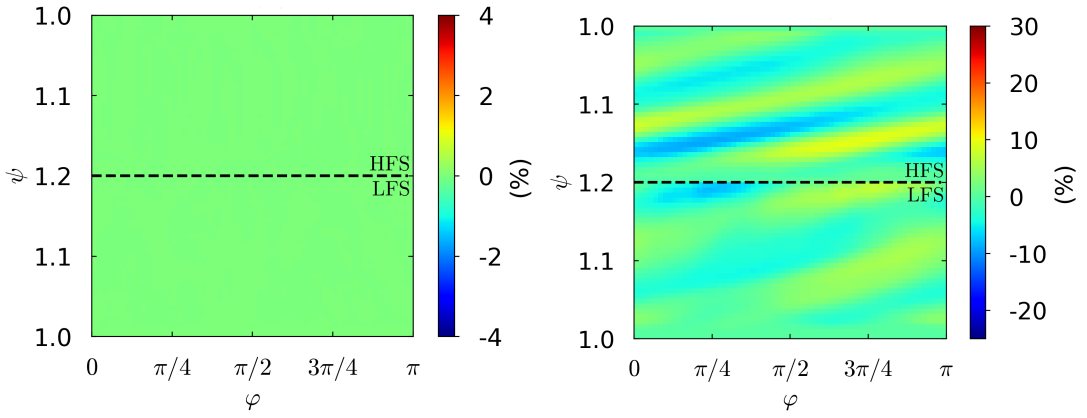


(a) Case MP (0,0,0) no turbulence




(b) Case MP (0,0,0) turbulence

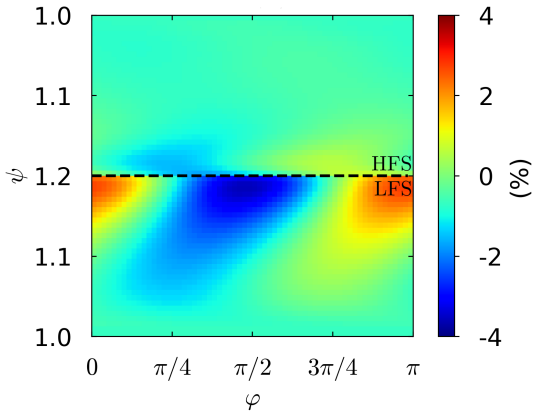


(c) Case MP (1,6,2) no turbulence

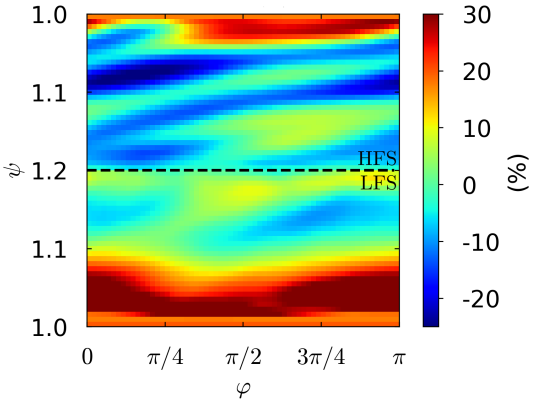


(d) Case MP (1,6,2) turbulence

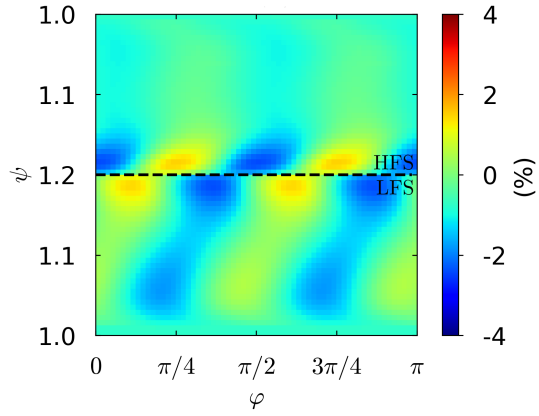


(e) Case MP (1,15,4) no turbulence

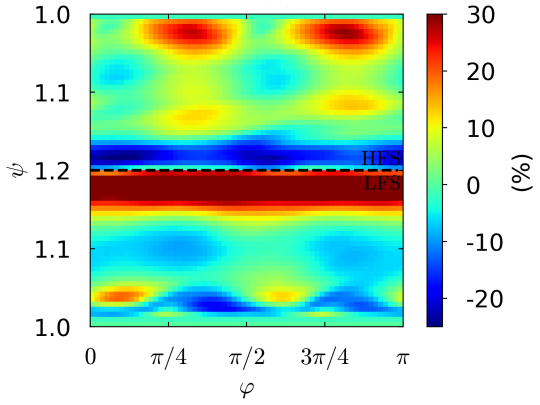


(f) Case MP (1,15,4) turbulence

Figure 5.2.: TOKAM3X simulations: density toroidal inhomogeneity as $\delta N^0_\varphi = (\langle N_{\mathrm{MP}}\rangle_t - \langle N_{(0,0,0)}\rangle_{t,\varphi})/\langle N_{(0,0,0)}\rangle_t$ at the limiter, above the dotted line is the HFS and below is the LFS

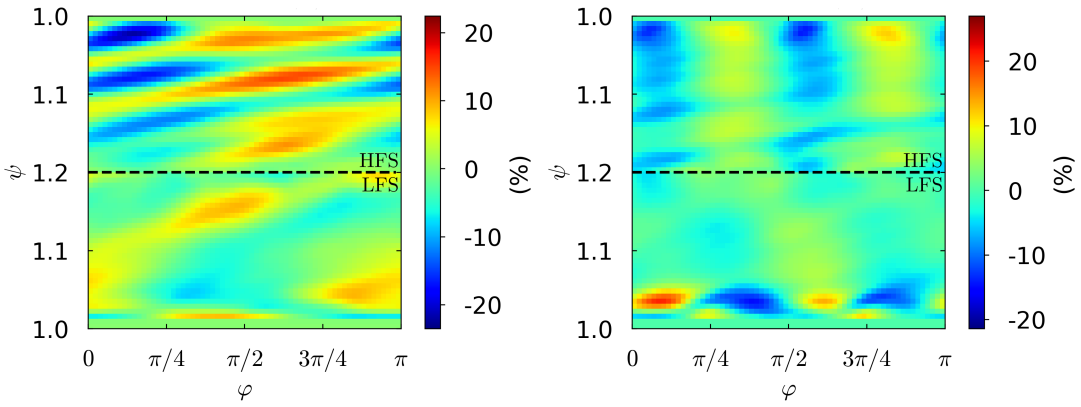


(a) Case MP (1,6,2) turbulence

(b) Case MP (1,15,4) turbulence

Figure 5.3.: TOKAM3X simulations: density toroidal variation as $\delta N_\varphi = (\langle N_{\mathrm{MP}}\rangle_t - \langle N_{\mathrm{MP}}\rangle_{t,\varphi})/\langle N_{\mathrm{MP}}\rangle_t$ at the limiter, above the dotted line is the HFS and below is the LFS

## 5.2. From single mode to multi-modes magnetic perturbations

Until this point, we have only focused on single mode MPs in order to isolate their basic effect on the plasma. RMPs are in reality composed of a superposition of modes. Unfortunately, we have not been able to address RMPs with realistic spectra with TOKAM3X used in turbulent mode due to unidentified and, to date unsolved, numerical instabilities when applying realistic RMPs. Nevertheless, first steps towards real RMP spectra have been achieved with mean-field simulations. As the mean-field simulations are numerically more stable we manage to input a more complex MP and can used higher amplitude of perturbations.

### 5.2.1. Simulation settings

To be more realistic, a set of rectangular magnetic coils has been modeled around the torus of the simulation. It is a set of two rows (upper and lower) of four rectangular coils. The magnetic field produced by these coils is computed throught the Biot and Savard law in a very similar way as what is done in [84]:

$$\boldsymbol{B}_{\mathrm{coils}}(P) = \frac{\mu_0}{4\pi}\sum_{i=1}^{n_{\mathrm{coils}}}\left(\oint_{C_i}\frac{I_i\delta\boldsymbol{r}\times\boldsymbol{r}}{r^3}\right) \tag{5.4}$$

where a summation is done on all coils. $\mu_0$ is the vacuum magnetic permeability, $I_i$ is the current in the coil numbered $i$, $\boldsymbol{r}$ is the vector between a point $P$ of the simulation domain and a point along the coil contour $C$ and $\delta\boldsymbol{r}$ is the infinitesimal

vector for integration along the contour of the coil. The magnetic field is expressed in the cylindrical basis. To obtain the contravariant coordinates of the coil, we apply the following transformation:

$$\begin{pmatrix} B^{\psi}_{\text{coils}} \\ B^{\theta^*}_{\text{coils}} \\ B^{\varphi}_{\text{coils}} \end{pmatrix} = \boldsymbol{J}^{-1} \begin{pmatrix} B^{R}_{\text{coils}} \\ B^{Z}_{\text{coils}} \\ B^{\phi}_{\text{coils}} \end{pmatrix} \tag{5.5}$$

where $\boldsymbol{J}$ is the local Jacobian matrix (defined in Appendix B). The contravariant coordinates of the coils are then added to the equilibrium magnetic field $\boldsymbol{B}_0$. A 3D illustration is given in Figs 5.4a on the left. The RMP coils are the red rectangles and some field lines of the simulation domain are shown in green.

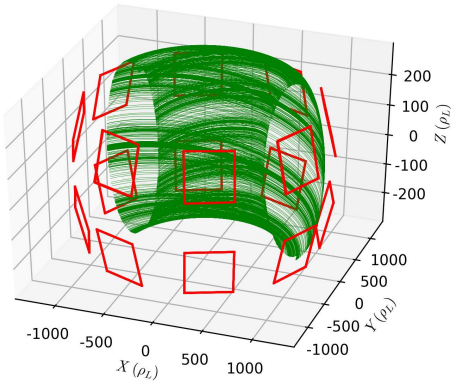


(a) RMP coils

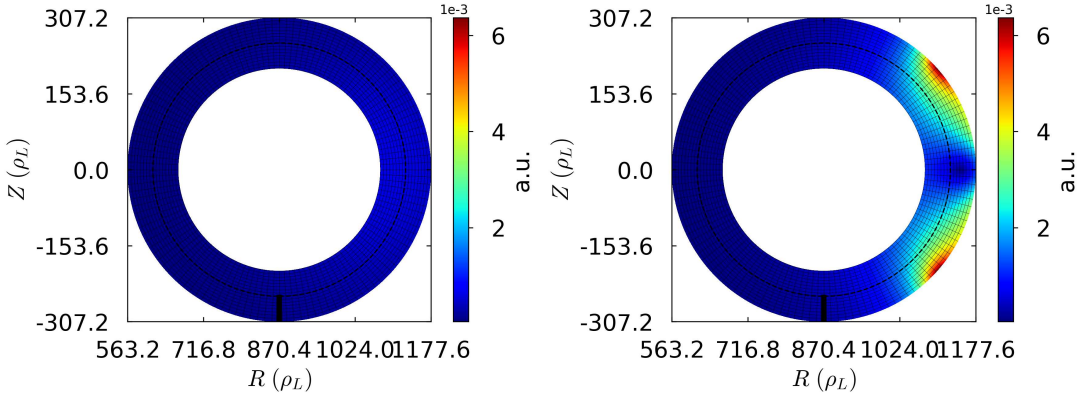


(b) $\tilde{B}$ field $\varphi = 0$

(c) $\tilde{B}$ field $\varphi = \pi/8$

Figure 5.4.: 3D plot of the RMP coils (in red) with some fieldlines in green 5.4a. Poloidal 2D slice of the norm of the perturbated magnetic field $\tilde{\boldsymbol{B}}$ at $\varphi = 0$ 5.4b and $\varphi = \pi/8$ 5.4c for the realistic RMP

The Biot and Savart law expressed in equation 5.4 can be simplified for a constant

| Even configuration | | | | | | | |
|---|---|---|---|---|---|---|---|
| + | - | + | - | + | - | + | - |
| + | - | + | - | + | - | + | - |

| Odd configuration | | | | | | | |
|---|---|---|---|---|---|---|---|
| + | - | + | - | + | - | + | - |
| - | + | - | + | - | + | - | + |

Table 5.1.: The even and odd configuration. The ± sign directly translates the sign of the current in the coil.

coil current as:

$$\boldsymbol{B}_{\text{coils}}(P) = \frac{\mu_0 I_{\text{coil}}}{4\pi} \sum_{i=1}^{n_{\text{coils}}} \left( \oint_{C_i} \frac{\delta_i \delta \boldsymbol{r} \times \boldsymbol{r}}{r^3} \right) \tag{5.6}$$

where $I_{\text{coil}}$ is a constant current into each RMP coil, which is realistic in the chosen configuration, as each coil is identical. $\delta_i = \pm 1$ is the parity of the coil. If the current goes into a specific direction inside a coil, the direct neighbour is set so that the current goes the other way. For a RMP case with 2 rows of 8 set of coils, one can implement two kind of configurations: the even and odd configurations, as shown in Table 5.1. The ± signs correspond to the current direction.

In this thesis, we only use the even configuration. A study about even and odd configurations has already been done in the thesis [83] with the MHD code JOREK [26, 60].

The equation 5.6 is still not dimensionless. We thus introduce the toroidal current $I_{\text{tor}}$, seen in Chap. 2, as well as $F = \mu_0 I_{\text{tor}}/(2\pi)$, which is a parameter of the code that caracterizes the amplitude of the dimensionless equilibrium magnetic field $\boldsymbol{b}_0$. It is generally set to 1. We can then write the equation 5.6 as:

$$\boldsymbol{B}_{\text{coils}}(P) = F\epsilon_{\text{RMP}} \sum_{i=1}^{n_{\text{coils}}} \left( \oint_{C_i} \frac{\delta_i \delta \boldsymbol{r} \times \boldsymbol{r}}{r^3} \right) \tag{5.7}$$

with $\epsilon_{\text{RMP}} = 0.5 I_{\text{coil}}/I_{\text{tor}} \ll 1$. To keep a similar notation as what was done for the MP, the realistic RMP is noted rmp $(a, i_{\text{row}}, i_{\text{col}})$, where $\epsilon_{\text{RMP}} = a \cdot 10^{-3}$, $i_{\text{row}}$ is the number of rows of coils and $i_{\text{col}}$ the number of coils in a row. The TOKAM3X code has been implemented with the possibility to create coils such that $i_{\text{row}} = 1 \ldots 2$ (1 or 2 rows of coils) and any number of evenly spaced (in the toroidal direction) coils in a row. In this thesis, we choose $i_{\text{row}} = 2$ and $i_{\text{col}} = 8$ (in even configuration).

To ensure a comparable result between a single mode MP and a realistic RMP, we choose to have an equivalent amplitude of magnetic perturbation at the point in the simulation exhibiting the largest perturbation. We choose a maximal amplitude

of the order of $10^{-3}B_0$. This corresponds to single mode MP $(10,6,2)$ and $(10,15,4)$, whereas the realistic RMP is $(0.1,2,8)$. The form of the realistic RMP can be seen on Figs 5.4b and 5.4b. Those two poloidal slices taken at $\varphi = 0$ and $\varphi = \pi/8$ shows the relative amplitude of the magnetic perturbation ($|\boldsymbol{B} - \boldsymbol{B}_0|/|\boldsymbol{B}_0|$). With the scale, it clearly shows an amplitude of the order of $10^{-3}B_0$. We complete it by the poloidal spectrum of the three different cases (two single mode MP and one realistic RMP) taken at $r/a = 0.9$ (to see if the RMP goes in the CFR) and $\varphi = \pi/8$. Whereas we can clearly see, for the single mode, the expected mode $m$ (with the resonance due to the magnetic curvature), the realistic RMP shows a full spectrum of poloidal mode numbers $m \in [4 \dots 50]$. Concerning the toroidal mode number $n$, the single mode MPs show (as stated in Chapter 3) the main toroidal mode number corresponding to the perturbation. The realistic RMP is more complex with the expected mode $n = 4$ (corresponding to the coils configuration in a row: 8 coils, whose current switches between two neigbours in a row, create a $n = 4$ oscillation), but other modes exist such as $n = 12, 20$ of similar amplitudes due to the toroidal shaping of the coils.

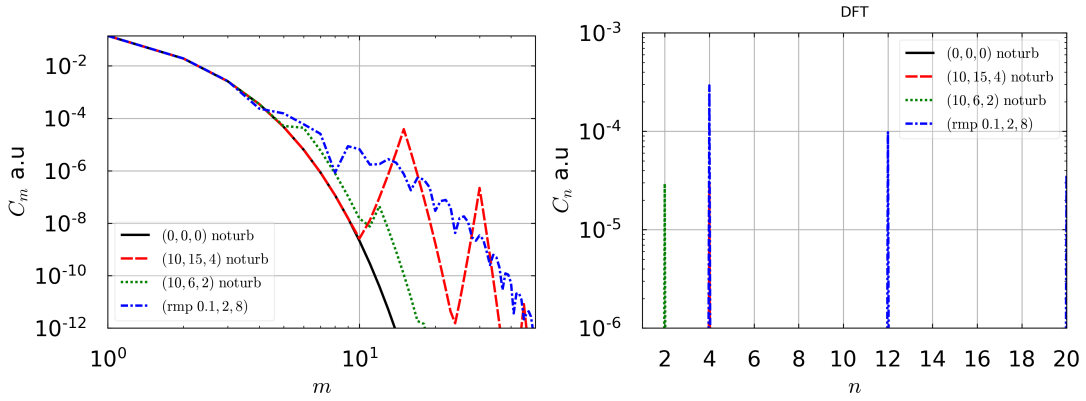


(a) Poloidal DFT of $|\boldsymbol{B}|$

(b) Toroidal DFT of $|\boldsymbol{B}|$

Figure 5.5.: Spectrum of $|\boldsymbol{B}|$ along the poloidal direction at $r/a = 0.9$, $\varphi = \pi/8$ 5.5a. Spectrum of $|\boldsymbol{B}|$ along the toroidal direction at $r/a = 0.9$, $\theta^* = 0$ (LFS midplane) 5.5b.

The addition of several mode numbers in both directions have a direct impact on the island formation. This can be observed on the Poincaré map on Figs 5.6. The Fig 5.6a shows the Poincaré map for the case MP $(10,6,2)$. We can clearly observe large magnetic islands with a stochastic region at $3.50 \leq q \leq 3.55$. We note that the magnetic islands are not well defined and that the magnetic field lines seem to fill all the available space (with the exception of the islands, that look like empty elongated structures), forming a stochastic field region. The Fig 5.6b shows the Poincaré map for the case RMP, even configuration, $(0.1,2,8)$. The first observation is the size of the islands, extremely small in the CFR, where the flux surfaces are almost unperturbed. The SOL is more perturbated with islands of equivalent size at $5.25 \leq q \leq 6.0$, but more numerous compare to $(1,6,2)$. The islands then shrink the more it goes toward the

CFR. This is due to a major difference between the single mode MP and the realistic RMP: the radial dependency of the amplitude of the MP. For realistic RMP, the strength of the MP decreases the more it goes inside the plasma.

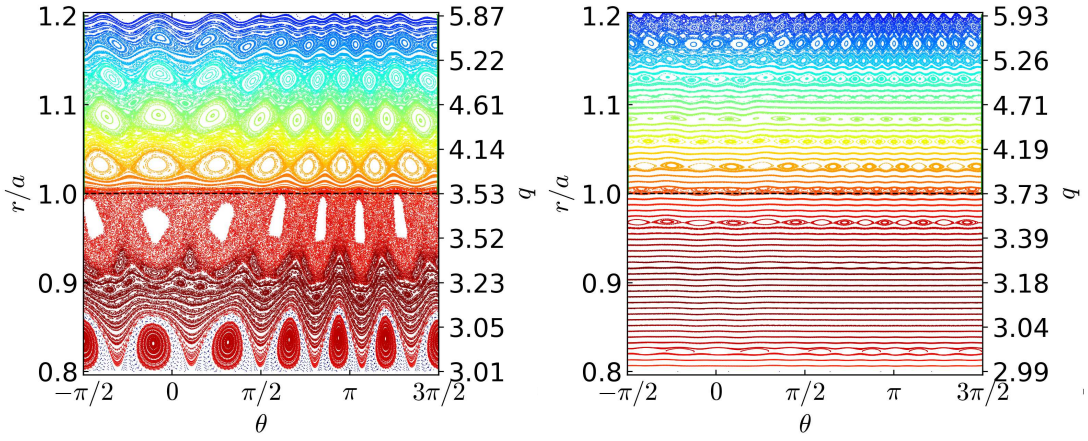


(a) MP (10,6,2) (b) RMP (0.1,2,8)

Figure 5.6.: Poincaré map for MP (10,6,2)5.6a and RMP (0.1,2,8)5.6b

This radial dependency should have interesting behaviour on the turbulence itself. Unfortunately, the turbulent model of TOKAM3X is not yet stable enough to manage the realistic RMP. In the following part, we study the difference in the density 2D profiles obtained from solutions with realistic and single mode MP of similar amplitude.

### 5.2.2. Impact of RMPs on the mean density distribution

Following the steps done in the first section, the density fluctuation in the toroidal direction is plotted on Figs 5.7. The first two Figs 5.7a,5.7b show the density toroidal inhomogeneities $\delta N^0_\varphi$ for the single mode MP (10,6,2) and (10,15,4). The 4 others Figs. are successive poloidal slices for the RMP (0.1,2,8) at $\varphi = 0$ (fig. 5.7c), $\varphi = \pi/8$ (fig. 5.7d), $\varphi = \pi/4$ (fig. 5.7e), $\varphi = 3\pi/8$ (fig. 5.7f) of density fluctuations. The first comparison that can be done is the fluctuation level. Realistic RMP, for an equivalent amplitude, modifies only barely the density. The fluctuation are only of a few percents. The single mode MP, whom amplitude has been multiplied by 10, shows a quasi linear increase in density fluctuation level with repect to the former cases (see Figs. 5.1). It is interesting to note that in the mean field simulations, an increase of the MP amplitude relates directly with an increase in the amplitude of the density inhomogeneity. It was not so strinking for the turbulence model as shown in Fig. 5.8. When we compare the turbulent case (1,6,4) (Fig. 5.8a) and (3,6,4) (Fig. 5.8b) we still note an increase in the level of density fluctuations, but not as much as a factor three, like what would

be observed in a mean-field simulation. The density inhomogeneity in the turbulent model seems to spread farther in the SOL.

Going back into the mean field model and the RMP case, we can see on Figs 5.7c, 5.7d, 5.7e and 5.7f that the density fluctuations follow the form of the MP. The HFS region shows little change whereas, at LFS, fluctuations become completely non-axisymmetric. The density fluctuation is positive with a positive perturbated magnetic field (Fig. 5.7d) and negative otherwise (Fig. 5.7f). Seeing that the realistic RMP mainly modifies the LFS region, the 2D map of the density fluctuations on the limiter (Fig. 5.9) shows, as expected, mainly fluctuations at the LFS region. The fluctuations shape in lobe-like structures at the LFS. This is observed in experiment on MAST [124] for example, although in a different magnetic geometry.

## 5.3. Modeling of the impact of MPs in realistic plasma and wall geometry with the SOLEDGE3X-HDG code

The SOLEDGE3X-HDG code is a transport code able to compute isothermal and non-isothermal models in complex geometries. At the time this work was carried out, a new 3D version of the code had just been released but had never been used appart from basic verification tests. The model solved by the code is currently a mean-field model but developments are already relatively advanced to extend it towards turbulence. The SOLEDGE3X-HDG code relies on a finite element HDG approach which offers greater geometrical flexibility compared with the numerical discretization used in TOKAM3X or other edge codes. It opens the path to simulations in 3D realistic geometry, for the plasma but also for the wall, with any type of magnetic topology, toroidally symmetric or not, eventually with turbulence. In this thesis, we propose the first physical application of the SOLEDGE3X-HDG code to 3D magnetic equilibria. We wish to see the capabilities of SOLEDGE3X-HDG to react to 3D MPs. As the code is vastly different from TOKAM3X, even its mean-field version, we do not aim towards a comparison of both codes. Still, we use the results found in the previous sections to see if compararable trends can be highlighted. We choose to approach the problem by changing the geometry of the simulation applying the same RMP-like (multi-modes) MP.

### 5.3.1. Simulations settings

Capitalizing on the geometrical flexibility of the code, we have performed simulations in three kind of circular geometries with limiter at the bottom: a vertical infinitely thin limiter (see Fig. 5.10a), a vertical limiter (see Fig. 5.10b), a realistic horizontal limiter (see Fig. 5.10c). The simulated domain is a region of $250\rho_L$ and the inner radius of the torus is $500\rho_L$. The perpendicular transport is set through a diffusion coefficient

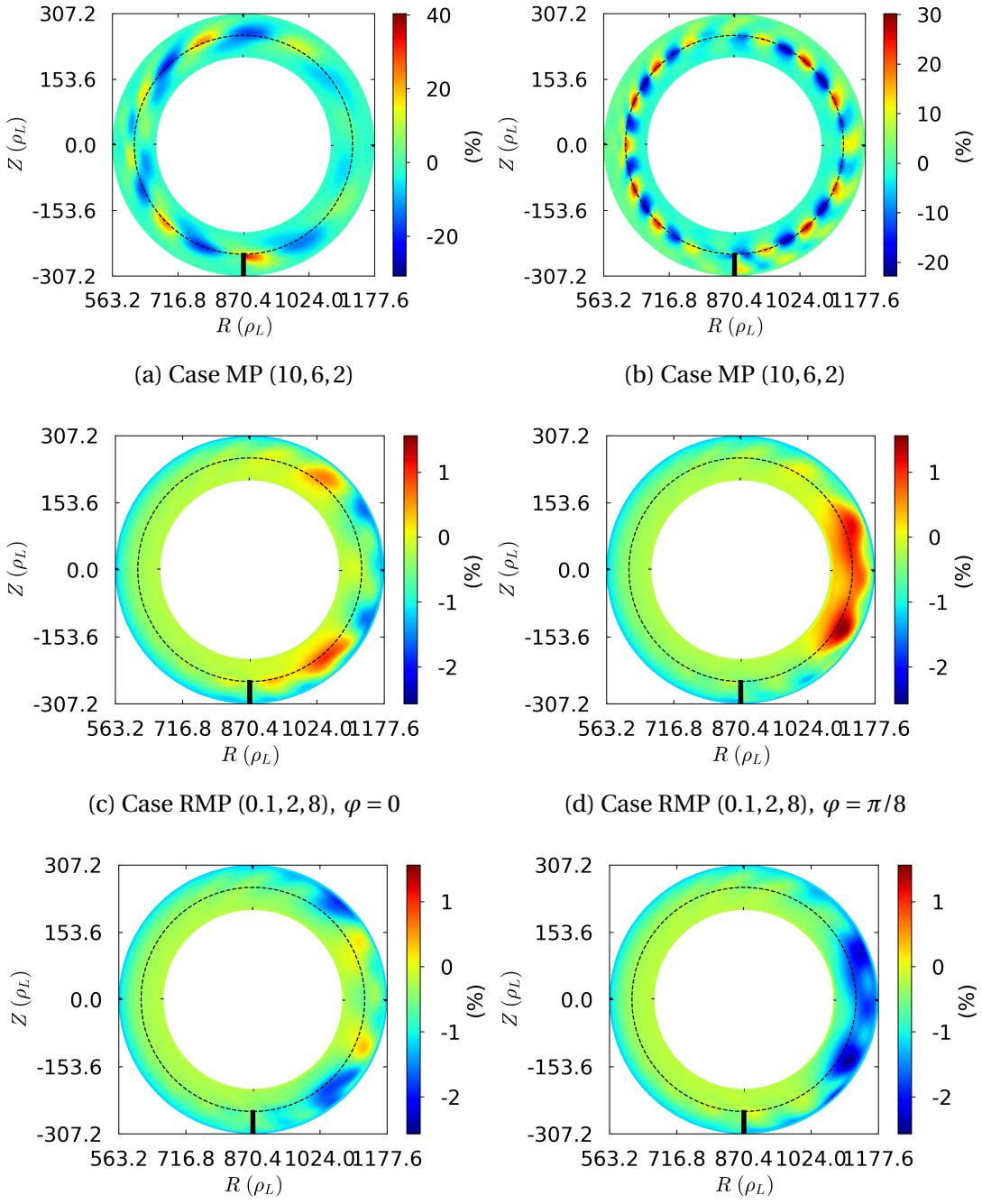


(a) Case MP (10,6,2)

(b) Case MP (10,6,2)

(c) Case RMP (0.1,2,8), $\varphi = 0$

(d) Case RMP (0.1,2,8), $\varphi = \pi/8$

(e) Case RMP (0.1,2,8), $\varphi = \pi/4$

(f) Case RMP (0.1,2,8), $\varphi = 3\pi/8$

Figure 5.7.: TOKAM3X simulations: density inhomogeneity as $\delta N^0_\varphi = (\langle N_{\mathrm{MP}}\rangle_t - \langle N_{(0,0,0)}\rangle_{t,\varphi})/\langle N_{(0,0,0)}\rangle_t$ for the cases (10,6,2) (5.7a), (10,15,4) (5.7b) and RMP (0.1,2,8) at $\varphi = 0$ (5.7c), $\varphi = \pi/8$ (5.7d), $\varphi = \pi/4$ (5.7e) and $\varphi = 3\pi/8$ (5.7f)

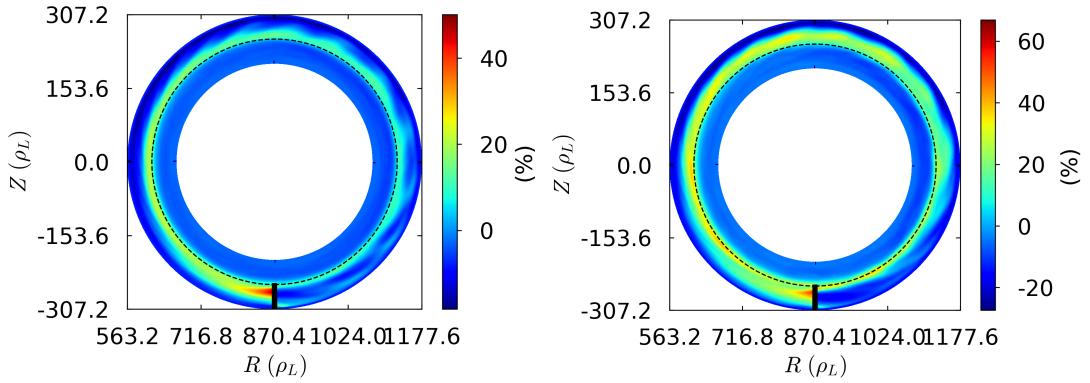


(a) MP (1,6,4) (b) MP (3,6,4)

Figure 5.8.: TOKAM3X simulations: Density inhomogeneity as $\delta N_\varphi^0 = (\langle N_{\mathrm{MP}}\rangle_t - \langle N_{(0,0,0)}\rangle_{t,\varphi})/\langle N_{(0,0,0)}\rangle_t$ for the cases (1,6,4) (5.8b) and (3,6,4) (5.8b) with the turbulent model at $\varphi = 0$

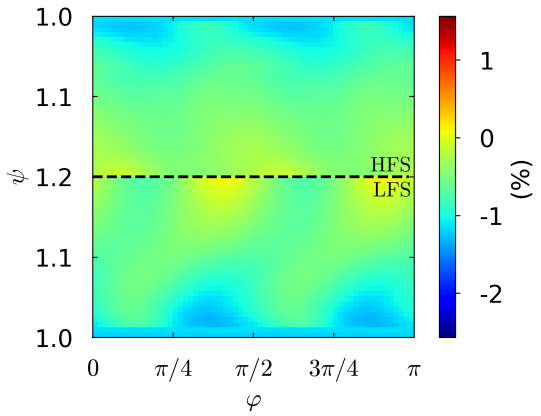


Figure 5.9.: TOKAM3X simulations: density inhomogeneity as $\delta N_\varphi^0 = (\langle N_{\mathrm{MP}}\rangle_t - \langle N_{(0,0,0)}\rangle_{t,\varphi})/\langle N_{(0,0,0)}\rangle_t$ at the limiter for the realistic RMP (0.1,2,8), above the dotted line is the HFS and below is the LFS

at $D_\perp = 0.038$, wich corresponds, in dimensional unit, to a diffusion of 1 $\mathrm{m}^2 \cdot \mathrm{s}^{-1}$. We should note that the perpendicular velocity $\boldsymbol{u}_\perp$ is set to zero so that the perpendicular transport is fully diffusive. A reference value of $T_0 = 50$ eV and $B_0 = 2$ T are chosen at the edge plasma. The aspect ratio is $\mathscr{A} = 3.4$ and the safety factor at the edge is $q = 3.5$.

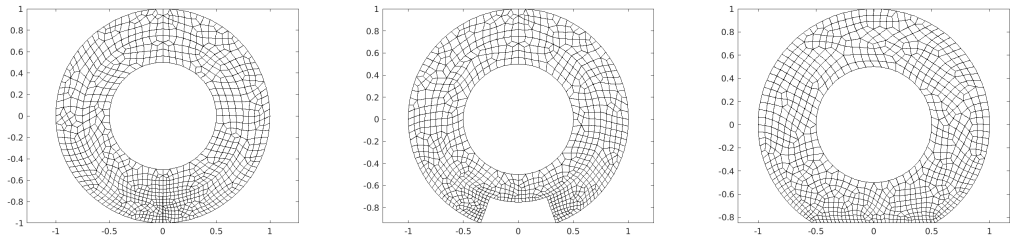

(a) Infinitely thin limiter (b) Vertical limiter (c) Horizontal limiter

Figure 5.10.: Three types of bottom limiters. Non field-aligned mesh configurations.

The equilibrium magnetic field is analytically set as (cylindrical basis):

$$\boldsymbol{B}_0 = \begin{cases} B_R = -\dfrac{B_0 y}{xq\sqrt{1-\frac{r}{R_0}^2}} \\ B_Z = B_0 \dfrac{x-R_0}{xq\sqrt{1-\frac{r}{R_0}^2}} \\ B_\phi = B_0 \dfrac{R_0}{r} \end{cases} \tag{5.8}$$

with $r = \sqrt{(x-R_0)^2 + y^2}$. The magnetic perturbation is added through a set of magnetic coils in the same framework as TOKAM3X. A row of rectangular coils are set above and below the midplane of the torus. In these simulation, the toroidal elongation of each coil is $\pi/8$, which create, for a simulation domain on a $\pi/2$ torus (for symmetry), the result shows on Fig. 5.11. The coils are set in even configuration.

For each perturbated simulation, a reference simulation without perturbation is run. The amplitude of the magnetic perturbation is set so that $|\boldsymbol{B}_{\mathrm{RMP}}|/|\boldsymbol{B}| \sim 10^{-3}$ at the maximum of the perturbation, as seen on Fig. 5.12

### 5.3.2. RMP in different limiter configurations

To study the effect of the geometry, we take a look at the density toroidal inhomogeneities $\delta N_\varphi^0$ and the density toroidal variations $\delta N_\varphi$. In SOLEDGE3X-HDG the average in time is implicit as the simulation is steady-state. We plot for 3 different positions (from $\pi/8$ to $\pi/4$ by $3\pi/4$ step) poloidal slices of $\delta N_\varphi^0$ and $\delta N_\varphi$ for the infinitely thin limiter (see Fig. 5.13), the vertical limiter (see Fig. 5.14) and the horizontal limiter (see Fig. 5.15). The first remark is the similar behaviour between the infinitely thin limiter simulation with SOLEDGE3X-HDG and the one of TOKAM3X, at the LFS with a large scale structure. We note nevertheless that the SOLEDGE3X-HDG simulation shows small scale perturbations at the external boundaries of the domain, which is not visible in TOKAM3X. This is most certainly due to the difference in boundary conditions.

We can observe similar structures between the 3 geometries with few differences. Starting with the infinitely thin limiter, we note that the positive RMP induces an

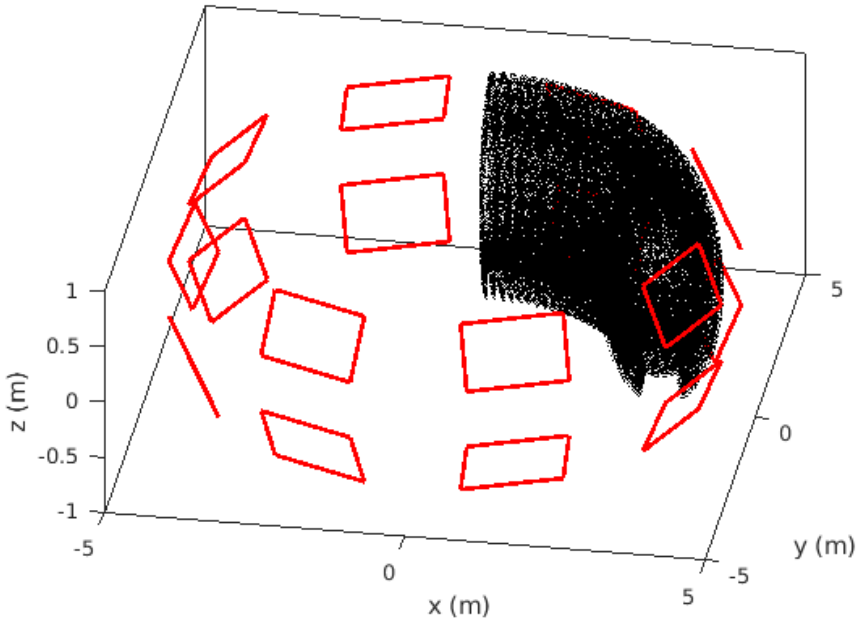


Figure 5.11.: Coils distributions (red) for the different simulations. The grey zone shows the simulation domain. The coils are in even configuration.

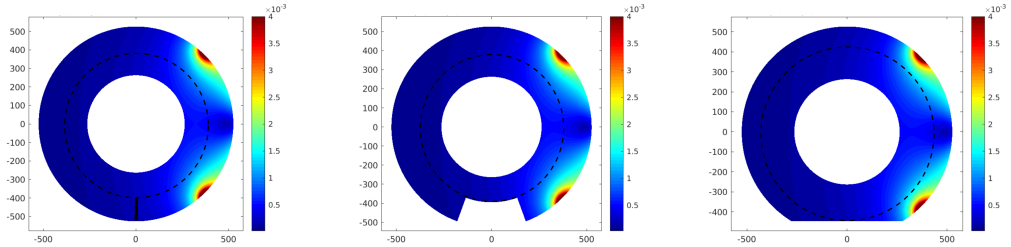

(a) Infinitely thin limiter (b) Vertical limiter (c) Horizontal limiter

Figure 5.12.: $|\boldsymbol{B}_{\text{pert}}|/|\boldsymbol{B}|$ at $\varphi = \pi/10$

increase of the density at the LFS (see Figs. 5.13a and 5.13b) both for $\delta N^0_\varphi$, which mark a direct impact of the RMP on the unperturbed equilibrium, and for the $\delta N_\varphi$, which underline the 3D effects of RMP even with mean-field simulations. The negative RMP creates a loss (see Figs. 5.13e and 5.13f). This is also observed for the vertical limiter (see resp. Figs. 5.14a and 5.14b then 5.14e and 5.14f) and the horizontal one (see resp. Figs. 5.15a and 5.15b then 5.15e and 5.15f). The density fluctuations at the limiter is stronger on the LFS part. The few differences we can observe are the spreading of the density perturbations, which is mostly due to the difference of the SOL thickness.

The conclusion to this part is twofolds. First is the capability of SOLEDGE3X-HDG

to efficiently deal with a full 3D isothermal simulation with RMP-like perturbations. Second, limiter configurations in circular geometries does not seem to change much the density fluctuations (both $\delta N_\varphi^0$ and $\delta N_\varphi$) at the target.

## 5.4. Modeling of the ripple for different geometries with SOLEDGE3X-HDG

In this part, we take a look to a different kind of 3D magnetic perturbations: the ripple. This perturbation is due to the finite number of toroidal field coils. An illustration is given in Figs. 5.16[1]. As we can see, the strength of the magnetic field intensity is stronger near the coils and weaker between two coils. The more the number of toroidal coils $N$ increase, the less is the impact. The effects of the ripple can be numerous and could lead to particles and heat flux losses [109, 115]. This section aims to show the capability of SOLEDGE3X-HDG to deal with a ripple in various geometries.

### 5.4.1. Simulations settings

The ripple perturbations is applied to the same geometries and parameters. We also extend the study to the more realistic geometry of WEST, in diverted configuration. The mesh of the X-point configuration is shown on Fig 2.5b. For WEST, $\mathscr{A} = 2.5$ and the diffusive coefficient is chosen artificially larger $D_\perp = 0.1$ (adimensional unit). The other parameters are left unchanged.

To create a ripple, a set of $N$ toroidal coils is created in the same framework as the RMP coils. The Biot and Savard law allows then to obtain a toroidal magnetic field with ripple $B_{\text{tot}}$. The toroidal average $B_{\text{eq}} = \langle B_{\text{tot}} \rangle_\varphi$ of this field is then calculated, corresponding to an equilibrium magnetic field. This equilibrium is then substracted to the total field, leaving only the ripple perturbation:

$$B_{\text{ripple}} = B_{\text{tot}} - B_{\text{eq}} \tag{5.9}$$

The ripple is then added to the 2D equilibrium field computed by the code (for the circular geometries, already explained in the previous section) or the one taken from a file (for the WEST geometry).

To create the toroidal coils, we create a set of points $(x_c, y_c, z_c)$ defined as:

$$\begin{cases} x_c = (R_0 + br_0 \cos(\theta + \delta_t \sin(\theta))) \cos(\varphi) \\ y_c = (R_0 + br_0 \cos(\theta + \delta_t \sin(\theta))) \sin(\varphi) \\ z_c = \kappa_e br_0 \sin(\varphi) \end{cases} \tag{5.10}$$

[1] source: http://ressources.univ-lemans.fr/AccesLibre/UM/Pedago/physique/02/electri/toremagne.html

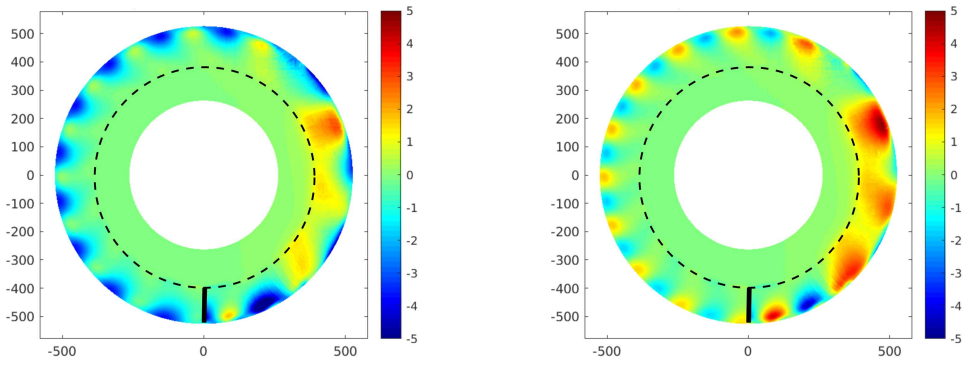

(a) $\delta N^0_\varphi, \varphi = \pi/8$



(b) $\delta N_\varphi, \varphi = \pi/8$

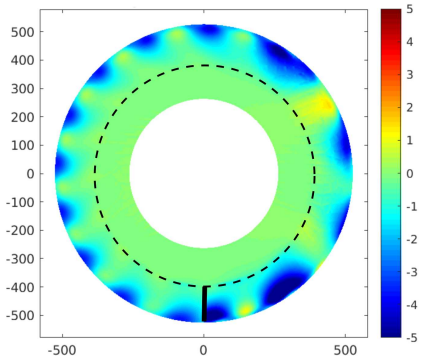

(c) $\delta N^0_\varphi, \varphi = \pi/4$

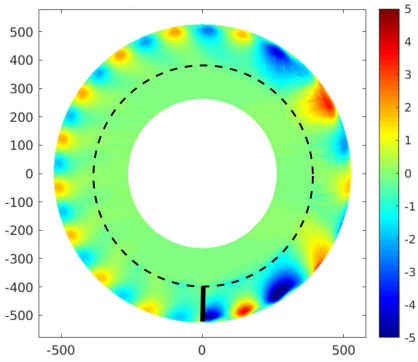

(d) $\delta N_\varphi, \varphi = \pi/4$

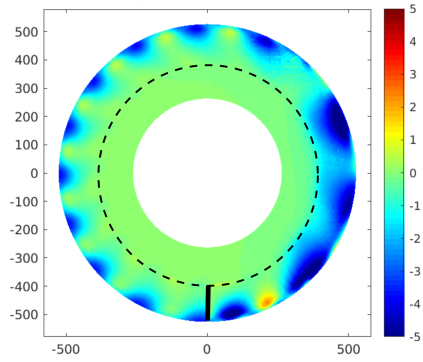

(e) $\delta N^0_\varphi, \varphi = 3\pi/8$

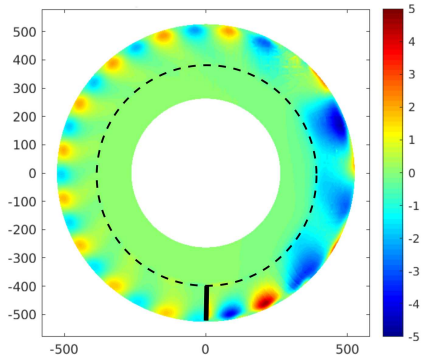

(f) $\delta N_\varphi, \varphi = 3\pi/8$

Figure 5.13.: SOLEDGE3X-HDG simulations: density toroidal inhomogeneities (5.13a,5.13c,5.13e) noted $\delta N^0_\varphi$ and density toroidal variations (5.13b,5.13d,5.13f) noted $\delta N_\varphi$ for the infinitely thin limiter at different poloidal slices with RMP

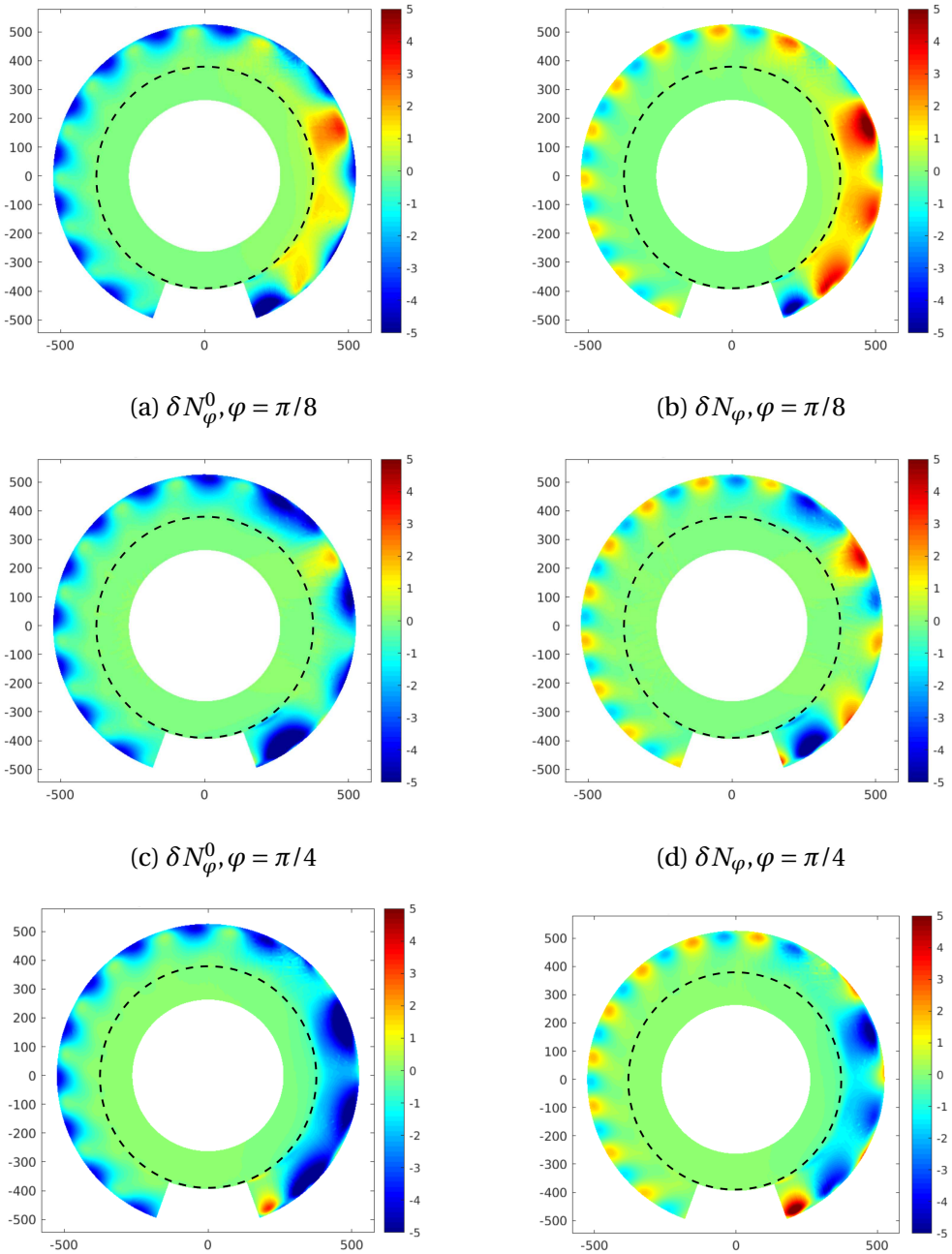

(a) $\delta N^0_\varphi, \varphi = \pi/8$

(b) $\delta N_\varphi, \varphi = \pi/8$

(c) $\delta N^0_\varphi, \varphi = \pi/4$

(d) $\delta N_\varphi, \varphi = \pi/4$

(e) $\delta N^0_\varphi, \varphi = 3\pi/8$

(f) $\delta N_\varphi, \varphi = 3\pi/8$

Figure 5.14.: SOLEDGE3X-HDG simulations: density toroidal inhomogeneities (5.14a,5.14c,5.14e) noted $\delta N^0_\varphi$ and density toroidal variations (5.14b,5.14d,5.14f) noted $\delta N_\varphi$ for the vertical limiter at different poloidal slices with RMP

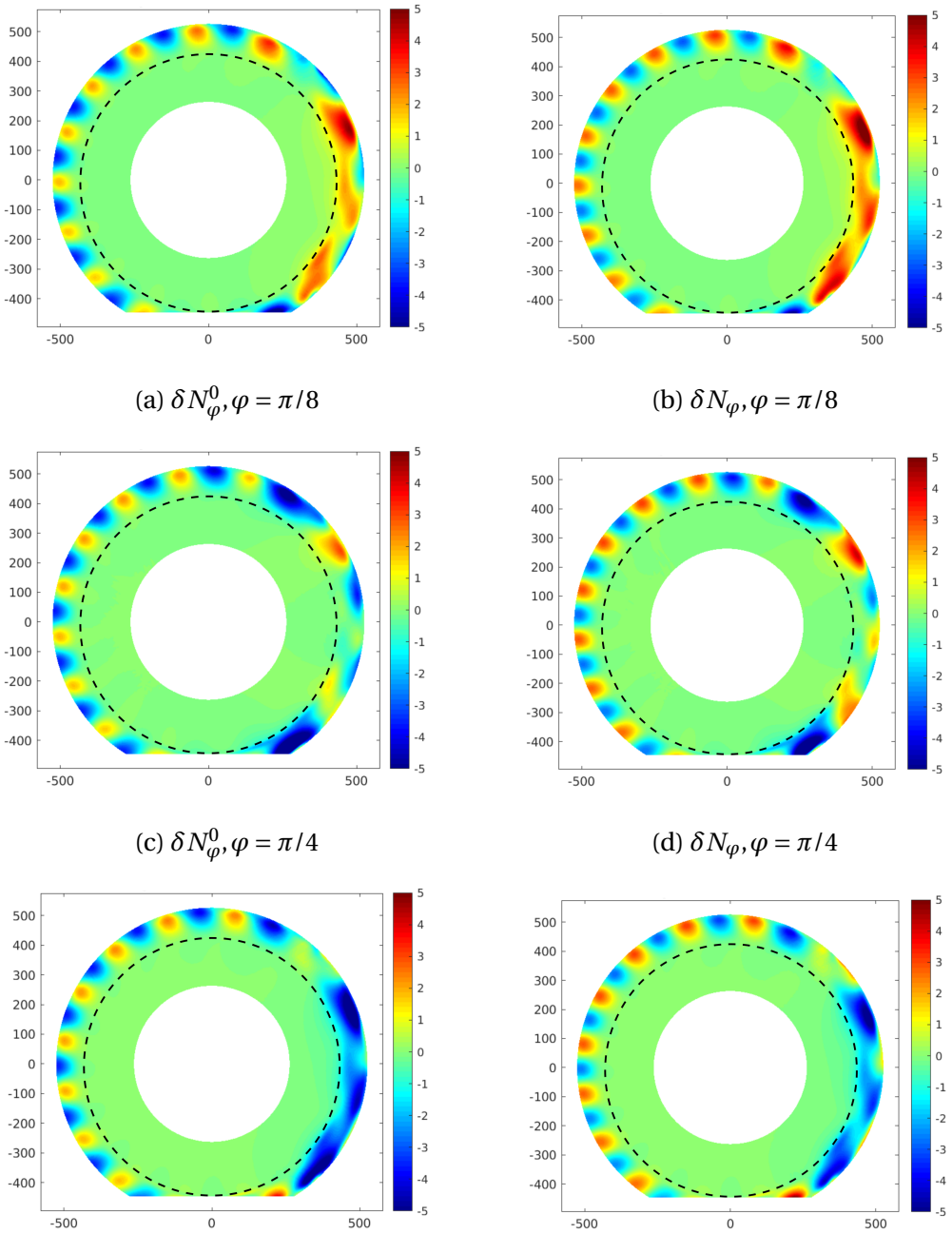

(a) $\delta N_\varphi^0, \varphi = \pi/8$

(b) $\delta N_\varphi, \varphi = \pi/8$

(c) $\delta N_\varphi^0, \varphi = \pi/4$

(d) $\delta N_\varphi, \varphi = \pi/4$

(e) $\delta N_\varphi^0, \varphi = 3\pi/8$

(f) $\delta N_\varphi, \varphi = 3\pi/8$

Figure 5.15.: SOLEDGE3X-HDG simulations: density toroidal inhomogeneities (5.15a,5.15c,5.15e) noted $\delta N_\varphi^0$ and density toroidal variations (5.15b,5.15d,5.15f) noted $\delta N_\varphi$ for the horizontal limiter at different poloidal slices with RMP

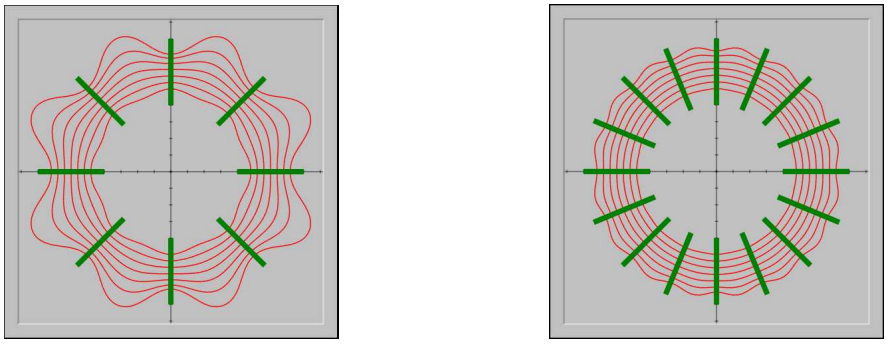

(a) $N = 8$ (b) $N = 16$

Figure 5.16.: Illustration of the ripple by plotting the magnetic field lines (in red) generated by a set of $N$ poloidal coils (in green). Adapted from there

with $\theta \in [0, 2\pi]$, $b > 1$ a constante, $r_0$ the inner radius of the torus (with the SOL), $\delta_t$ the triangularity, fixed at 0 for all simulations, and $\kappa_e$ the ellipticity fixed at 1 for all simulation. $b$ is chosen to have the coils far enough of the simulation box, so that the approximation of a coil being an infinitly thin line does not invalidate the form of the magnetic field.

We choose to set $N = 18$ toroidal coils for each simulation (same number as WEST). For symetry reasons, only $2\pi/9$ of the torus is simulated. The Fig 5.17 shows in red the coils and in black the simulation domain for the vertical limiter and WEST geometries.

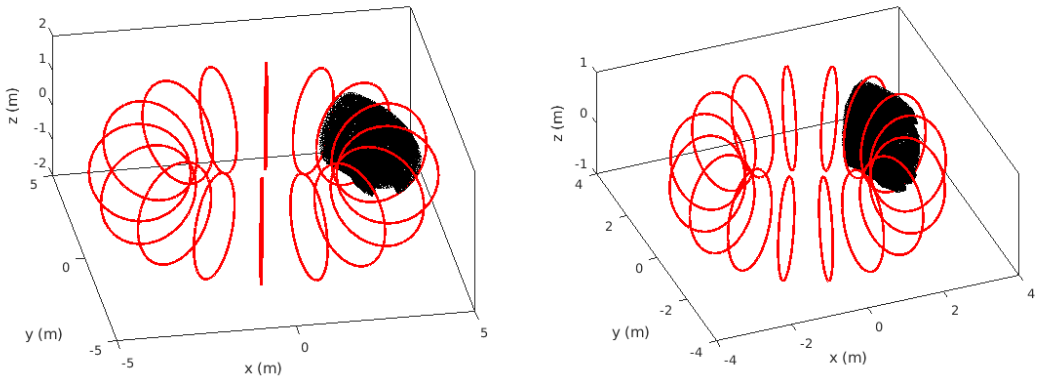


(a) Infinitely thin limiter (b) WEST

Figure 5.17.: Toroidal coils (red) with the simulation domain (black) for the infinitely thin limiter (Fig. 5.17a) and WEST (Fig. 5.17b) geometries.

### 5.4.2. Ripple on different limiter configurations

The first observation we can make is on the ripple itself. We plot on Figs 5.18 the 2D map of the module of the perturbation for the infinitely thin limiter (the other geometries having the same kind of profile) for different poloidal slices. We can clearly see the modulation of the field at the LFS region.

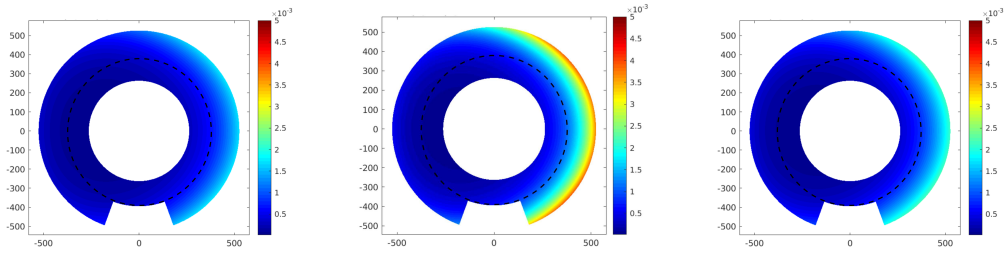

(a) $\varphi = 0$ (b) $\varphi = \pi/15$ (c) $\varphi = 2\pi/15$

Figure 5.18.: $|\boldsymbol{B}_{\text{pert}}|/|\boldsymbol{B}|$ at different toroidal position for the vertical limiter

The next step is the observation of $\delta N_\varphi^0$ and $\delta N_\varphi$. According to the litterature cited in Chap 1, the ripple should have little 3D impact on the axisymmetry of the plasma. Consequently, we can expect $\delta N_\varphi^0$ to change but $\delta N_\varphi$ should show little variations. As seen for all geometries (see on the left side on Figs. 5.19, 5.20 and 5.21), the ripple creates a positive $\delta N_\varphi^0$ at the LFS of the machine and a negative one at the HFS from the limiter and up to the top. The ripple is known to produce alternate patterns of positive and negative density flux at the limiter. We can take a look at the density toroidal variations, on the right side of each set of Figs. For all geometries, we clearly have a alternate pattern of positive and negative density fluctuations $\delta N_\varphi$ at the LFS, whereas, in opposite phasis, we see a similar phenomenon at the HFS, albeit at lower amplitude. On a side note, $\delta N_\varphi^0$ varies around $\pm 20\%$ of the average density and show that the ripple can considerably change the equilibrium of the plasma. But $\delta N_\varphi$ is actually small, barely $\pm 2\%$ of the average density. Furthermore, we note that these variations are too small to be correctly captured by SOLEDGE3X-HDG for the horizontal limiter, as oscillation are clearly visible (see Figs. 5.21 on the right). These oscillations are probably related to specific issues due to boundary conditions in grazing incidence angles (specific of the horizontal limiteur case) and could probably be removed with a finer mesh or specific treatment of boundary conditions when the magnetic field is tangential to the wall.

SOLEDGE3X-HDG seems capable to reproduce a ripple-like MP for simple geometries. Even if the horizontal limiter configuration would require probably a finer mesh.

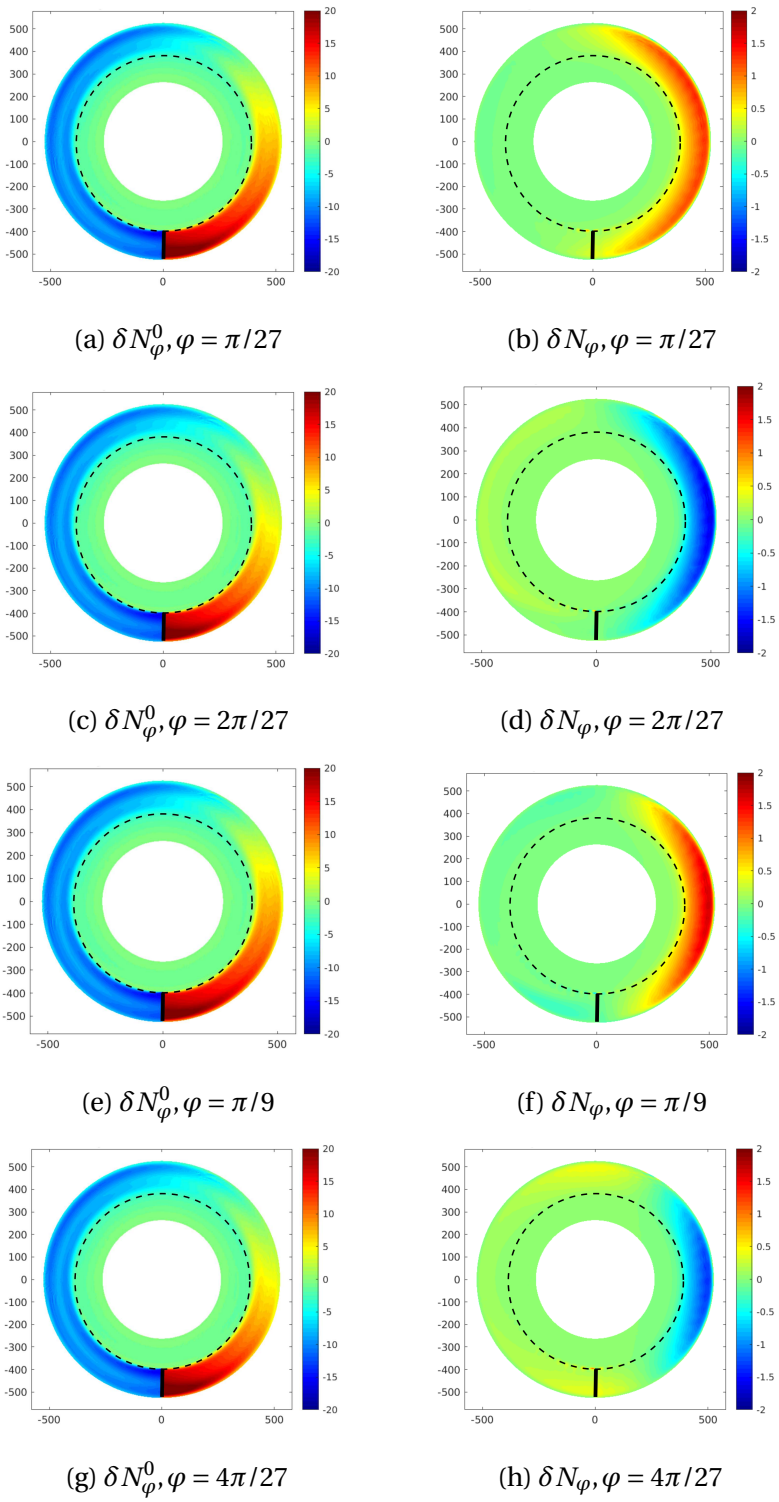

(a) $\delta N^0_\varphi, \varphi = \pi/27$ (b) $\delta N_\varphi, \varphi = \pi/27$

(c) $\delta N^0_\varphi, \varphi = 2\pi/27$ (d) $\delta N_\varphi, \varphi = 2\pi/27$

(e) $\delta N^0_\varphi, \varphi = \pi/9$ (f) $\delta N_\varphi, \varphi = \pi/9$

(g) $\delta N^0_\varphi, \varphi = 4\pi/27$ (h) $\delta N_\varphi, \varphi = 4\pi/27$

Figure 5.19.: SOLEDGE3X-HDG simulations: density toroidal inhomogeneities (5.19a,5.19c,5.19e,5.19g) noted $\delta N^0_\varphi$ and density toroidal variations (5.19b,5.19d,5.19f,5.19h) noted $\delta N_\varphi$ for the infinitely thin limiter at different poloidal slices with ripple-like MP

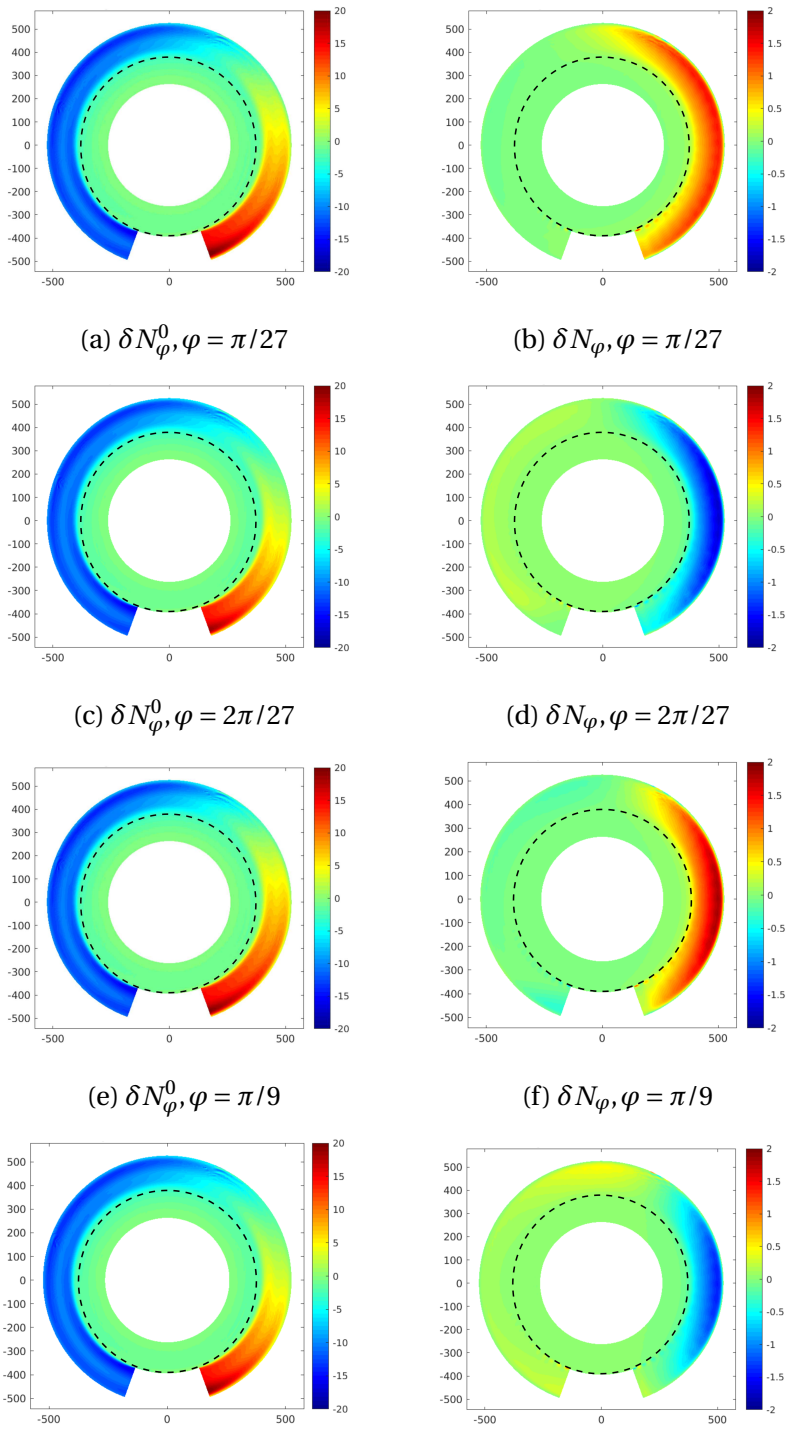

(a) $\delta N^0_\varphi, \varphi = \pi/27$ (b) $\delta N_\varphi, \varphi = \pi/27$

(c) $\delta N^0_\varphi, \varphi = 2\pi/27$ (d) $\delta N_\varphi, \varphi = 2\pi/27$

(e) $\delta N^0_\varphi, \varphi = \pi/9$ (f) $\delta N_\varphi, \varphi = \pi/9$

(g) $\delta N^0_\varphi, \varphi = 4\pi/27$ (h) $\delta N_\varphi, \varphi = 4\pi/27$

Figure 5.20.: SOLEDGE3X-HDG simulations: density toroidal inhomogeneities (5.20a,5.20c,5.20e,5.20g) noted $\delta N^0_\varphi$ and density toroidal variations (5.20b,5.20d,5.20f,5.20h) noted $\delta N_\varphi$ for the vertical limiter at different poloidal slices with ripple-like MP

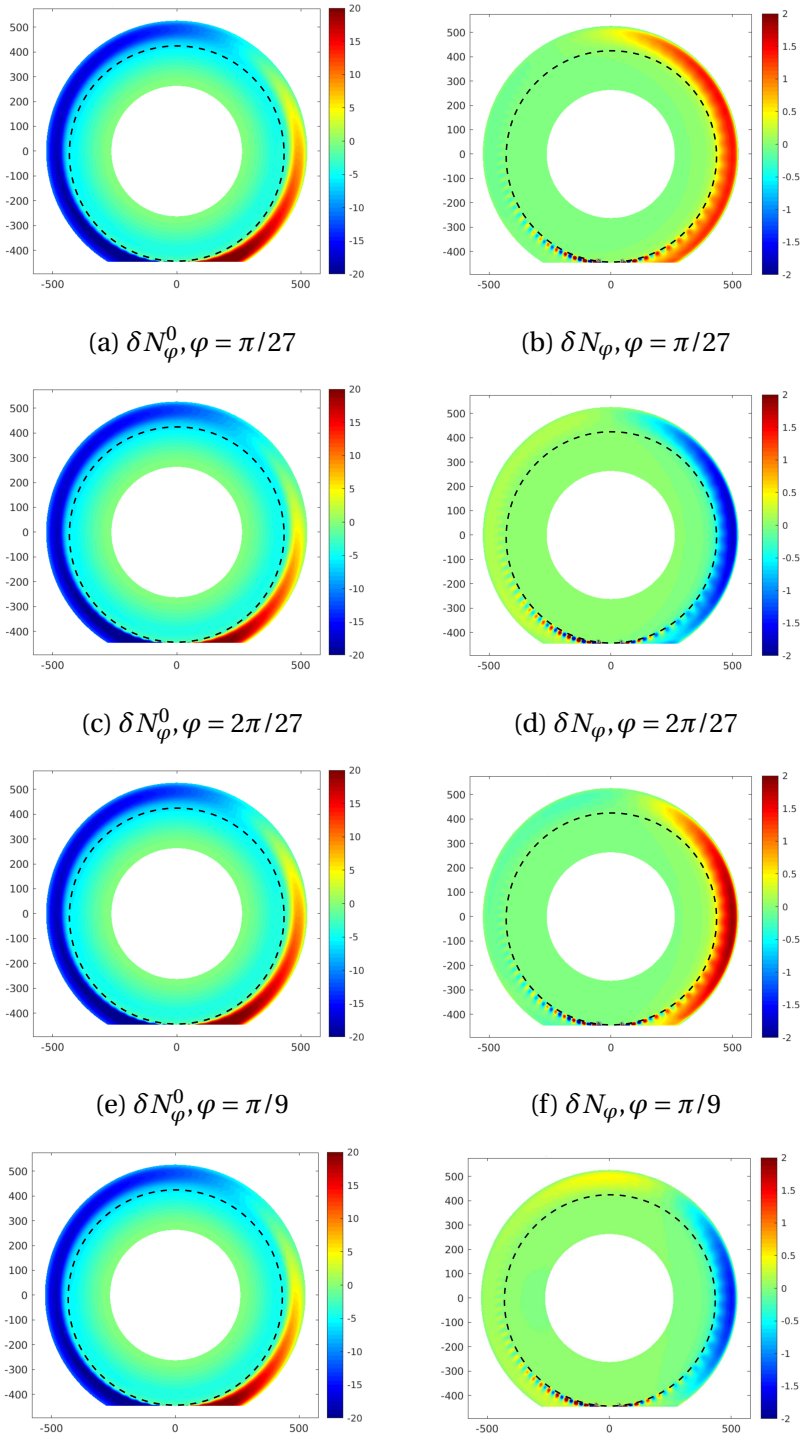

(a) $\delta N^0_\varphi, \varphi = \pi/27$ (b) $\delta N_\varphi, \varphi = \pi/27$

(c) $\delta N^0_\varphi, \varphi = 2\pi/27$ (d) $\delta N_\varphi, \varphi = 2\pi/27$

(e) $\delta N^0_\varphi, \varphi = \pi/9$ (f) $\delta N_\varphi, \varphi = \pi/9$

(g) $\delta N^0_\varphi, \varphi = 4\pi/27$ (h) $\delta N_\varphi, \varphi = 4\pi/27$

Figure 5.21.: SOLEDGE3X-HDG simulations: density toroidal inhomogeneities (5.21a,5.21c,5.21e,5.21g) noted $\delta N^0_\varphi$ and density toroidal variations (5.21b,5.21d,5.21f,5.21h) noted $\delta N_\varphi$ for the horizontal limiter at different poloidal slices with ripple-like MP

### 5.4.3. The ripple from limiter to divertor

The last simulation we have tried is the WEST geometry with a ripple of one order of magnitude lower than the circular simulations, due to computational limits. We plot on Figs. 5.22 $\delta N_\varphi^0$ (left) and $\delta N_\varphi$ (right) at different toroidal positions. The limit observed with the horizontal limiter can also be observed here at the boundary, where the density becomes very low, creating spurious oscillations. The code still converges and thus we can concentrate around the lower and upper X-point. For $\delta N_\varphi^0$, we can observe the increase of density fluctuations at the bottom inner and top outer target, whereas the bottom outer and top inner targets show a decrease of density. For $\delta N_\varphi$, at the bottom limiter, we can distinguish alternating pattern of positive and negative density fluctuations.

## 5.5. Conclusion on transport simulations

A comparison between self-consistent turbulence simulations and mean-field simulations, in which radial transport is prescribed via a gradient-diffusion assumption, shows a significant difference in the response of the plasma to MPs. The amplitude of the non-axisymmetric density perturbation is much more pronounced in the turbulent simulations than in the mean-field ones. Moreover, its spatial localization also changes, the effect of magnetic islands remaining local in the mean-field simulations while non local effects are important with turbulent simulations. These results suggest that the assumption of unperturbed perpendicular transport in mean-field simulations with MPs is probably an oversimplification and calls for further studies on the significant role played by turbulence on the response of the plasma to magnetic perturbations.

A study over more realistic RMP in mean-field simulations with TOKAM3X and SOLEDGE3X-HDG, has shown that the impact of this more localized perturbation is somewhat smaller on the density variations for the same amplitude as single mode MPs.

Finally, the mean-field code SOLEDGE3X-HDG has shown a promising ability to treat 3D MPs. Satisfying results have been obtained for the realistic RMP but more work is needed to obtain a correct ripple-like MP, especially in complex geometries. Still, the first results obtained in this thesis are promising for the 3D capabilities of the SLOEDGE3X-HDG code.

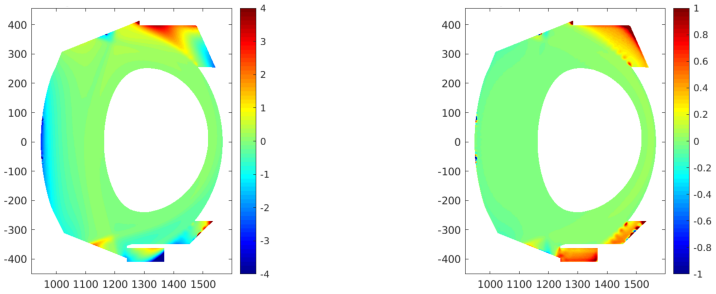

(a) $\delta N_\varphi^0, \varphi = \pi/27$ (b) $\delta N_\varphi, \varphi = \pi/27$

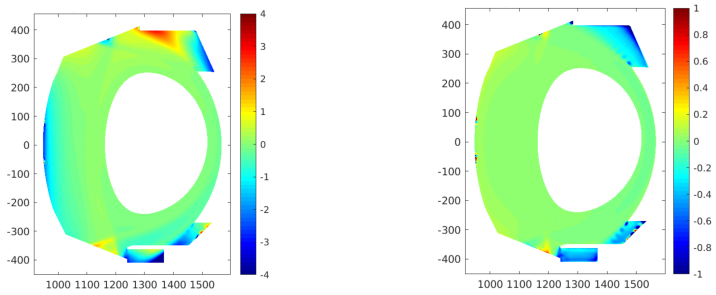

(c) $\delta N_\varphi^0, \varphi = 2\pi/27$ (d) $\delta N_\varphi, \varphi = 2\pi/27$

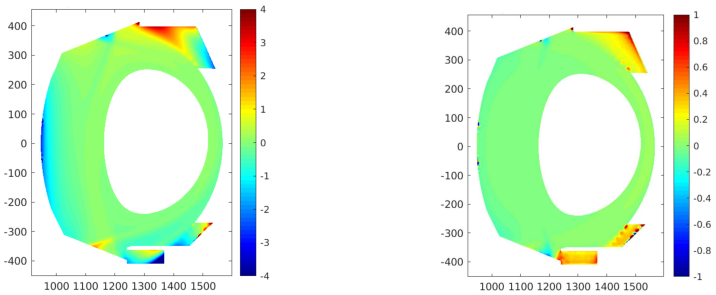

(e) $\delta N_\varphi^0, \varphi = \pi/9$ (f) $\delta N_\varphi, \varphi = \pi/9$

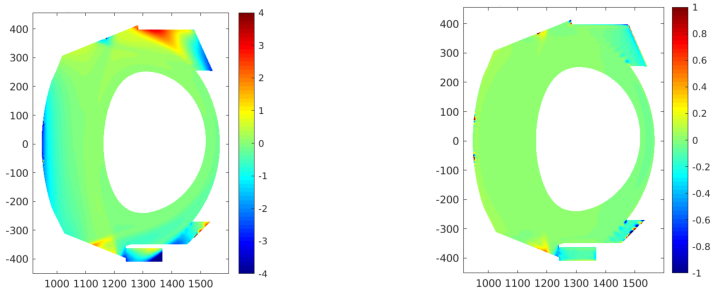

(g) $\delta N_\varphi^0, \varphi = 4\pi/27$ (h) $\delta N_\varphi, \varphi = 4\pi/27$

Figure 5.22.: SOLEDGE3X-HDG simulations: density toroidal inhomogeneities (5.22a,5.22c,5.22e,5.22g) noted $\delta N_\varphi^0$ and density toroidal variations (5.22b,5.22d,5.22f,5.22h) noted $\delta N_\varphi$ for WEST at different poloidal slices with ripple-like MP

# Conclusion

A study of the impact of 3D magnetic perturbations on turbulence and plasma equilibrium on the edge plasma has carried out. For the first time, the state-of-the-art fluid simulation code TOKAM3X has been used to simulate isothermal and non-isothermal edge-plasmas of tokamak, including single mode magnetic perturbations. A comparison between turbulence (TOKAM3X) and mean-field models (TOKAM3X, SOLEDGE3X-HDG) had been also carried out.

Single mode magnetic perturbations have been applied on isothermal limiter plasmas in circular geometry. Depending on the perturbations wavenumbers, magnetic islands may occur inside the computational domain. A dependency on the amplitude and wavenumbers of the perturbation, especially if it corresponds to resonance with magnetic islands, has been seen on the plasma equilibrium and, to a lesser extent, on the turbulence properties. Magnetic perturbations lead thus to changes on plasma rotation and flows, with solutions recovering experimental key features such as the density pump-out or the reversal of parallel velocities.

The density SOL width increases just after the separatrix when MPs are switched on but otherwise decreases in the rest of the SOL. Concerning the turbulence properties, the fundamental nature of turbulence is not changed much, with still intermittent events in the SOL, even if MPs tend to decrease it in the SOL, especially when magnetic islands are present. Density fluctuations are shown to decrease in the SOL when MPs are switched and an increase of the ballooning of the $E \times B$ turbulence is observed in the SOL.

In non-isothermal plasmas, the impact of the sources location has been investigated mimicking or not the recycling due to plasma wall interactions. In simulations without recycling the particles and energy sources are assumed coming from the core and have been located at the inner radius of the computational domain. On the contrary, in simulations with recycling assuming that 90% of the particles come from the limiter and 10% from the core, the main source has been located at the limiter. Experimental features such as the density pump-out and the reversal of parallel velocities are recovered in the recycling cases only, even if a pressure loss and a decrease of the radial electric profile are observed on both simulations. These different behaviors are associated to complex flux reorganizations. The simulations without recycling show an increase in the particle ballooning, whereas the simulations with recycling and MPs show a reverse particle ballooning in the CFR and no impact of the magnetic perturbations in the SOL. On the energy part, the MPs increase the ballooning in

the simulations without recycling, in both the CFR and the SOL. With recycling, this stronger ballooning is only visible in the SOL (whereas the reverse energy flux decreases). The ballooning behavior seems quite different with respect to the isothermal simulations, but are actually similar since the particle ballooning in isothermal cases should be compared with the energy ballooning in non isothermal simulations.

On the power exhaust concern, non isothermal simulations have shown a clear difference with isothermal ones, as both the density SOL width and power SOL width increase in both cases when MPs are switched on. Finally, on turbulent properties, for non recycling cases, density and temperature fluctuations decrease with MPs as well as the intermittency. In simulations without recycling, the density and temperature fluctuations increase, especially in the SOL, whereas the intermittency reverses in the CFR for density events, but not for the temperature events.

The complexity of the changes of the turbulent transport in both isothermal and non isothermal simulations have raised the question of the limit of mean-field simulations when considering 3D MPs. A comparison between mean-field and turbulent isothermal simulations with single mode perturbations has been done with TOKAM3X. It has been shown that the amplitude of the non-axisymmetric density perturbation is more pronounced in turbulent simulations. The spatial localization of the density toroidal inhomogeneities due to MPs is also different with non local effects probably due to a phase-locking of turbulent structures on magnetic perturbations in turbulent cases. It suggests that the assumption of unperturbed perpendicular transport in mean-field simulations is probably an oversimplification, which calls for further studies on the topic.

Still, present mean-field simulations have allowed for much more complex MPs and geometries that what have been done in the turbulent framework of this thesis. As such, an attempt in mean-field simulations with both TOKAM3X and SOLEDGE3X-HDG has been performed with more realistic MPs and make a first step towards realistic magnetic perturbations such as RMPs or ripple. Thus perturbations mimicking realistic RMP coils and magnetic field have been implemented in TOKAM3X. Solutions show in mean-field simulations that the impact of realistic MP is more localized on the LFS region of the machine. The amplitude of the density toroidal inhomogeneities are also much lower for the same peak amplitude of the magnetic perturbation. The same perturbation have been applied to SOLEDGE3X-HDG, using for the first time its 3D framework. More complex geometries have been studied, showing little changes on the response of the plasma in the volume but underlining that the impact on wall fluxes and conditions is strongly dependent on the wall geometry. Finally a generalization of the study of magnetic perturbation to the case of ripple has been performed, including on a real WEST tokamak geometry, highlighing that the ripple leads to strong density toroidal inhomogeneities (the equilibrium compare to a case without ripple change a lot) but little density toroidal variations (the density variation in the toroidal direction are weak). Overall, the studies with the SOLEDGE3X-HDG code demonstrate promising capabilities at handling complex geometries in 3D magnetic configurations,

but also point out specific issues (boundary conditions, stability of small scales) that will need improvement before exhaustive use of the code's capabilities can be made.

In summary, this thesis offers a first insight on the impact of 3D magnetic perturbations in self-consistent turbulence simulations. Results hightlight some fundamental limits concerning the modeling of the edge plasma with 3D magnetic fields under the gradient-diffusion assumption with constant diffusion coefficients. They call for urgent additional studies in order to rapidely provide guide-lines to mean-field simulations which will remain the work-horse for ITER studies in the upcoming few years. Although existing numerical tools have shown their capabilities to adress these issues, some limits have been identified that need to be worked on in order to extend our conclusions to more realistic configurations and conditions. Concerning the TOKAM3X code, such development has been undertaken in parallel to the course of this PhD, leading to a new version called SOLEDGE3X with more advanced geometrical flexibility. The exploitation of this new code together with the continuous progress of the SOLEDGE3X-HDG code will allow to pursue these studies in the near future and bring more detailed conclusions on the topic.

# Bibliography


[1] Justin R. Angus et al. In: *Phys. Plasmas* 21.1 (2014), p. 012514 (cit. on p. 24).

[2] P. Barabaschi et al. In: *Nucl. Fusion* 59.11 (2019), p. 112005 (cit. on p. 18).

[3] C. Baudoin. "Numerical evaluations of mechanisms governing the heat transport in the edge plasma of tokamaks". PhD thesis. Aix-Marseille Université, 2018 (cit. on pp. 22, 43).

[4] C. Baudoin et al. In: *Contr. Plasma Phys.* 58.6-8 (2018), pp. 484–489 (cit. on pp. 36, 57).

[5] M. Becoulet et al. In: *Nucl. Fusion* 52 (2012), p. 054003 (cit. on p. 33).

[6] M. Bécoulet et al. In: *Nucl. Fusion* 45 (2005), p. 1284 (cit. on p. 33).

[7] M Bécoulet et al. In: *Plasma Phys. Control. Fusion* 45.12A (2003), A93–A113 (cit. on p. 32).

[8] P. Beyer et al. In: *Phys. Plasmas* 5.12 (1998), pp. 4271–4279 (cit. on p. 35).

[9] P. Beyer et al. In: *Plasma Phys. Control. Fusion* 44.10 (2002), p. 2167 (cit. on p. 35).

[10] P Beyer et al. In: *Plasma Phys. Control. Fusion* 53.5 (2011), p. 054003 (cit. on p. 35).

[11] K Bodi, G Ciraolo, Ph Ghendrih, et al. "Impact of the Boussinesq approximation in tokamak scrape–off layer turbulence". In: *EPS Conference on Plasma Physic.* 2011 (cit. on p. 51).

[12] Xavier Bonnin et al. In: *Plasma and Fusion Research* 11 (2016), pp. 1403102–1403102 (cit. on p. 37).

[13] Allen H. Boozer. In: *Rev. Mod. Phys.* 76 (4 2005), pp. 1071–1141 (cit. on p. 20).

[14] C. Bourdelle et al. In: *Nucl. Fusion* 55.6 (2015), p. 063017 (cit. on p. 18).

[15] S.I. Braginskii. In: *Rev. Plasma Phys.* 1 (1965), p. 205 (cit. on pp. 41–43).

[16] D P Brennan et al. In: *Jour. Phys.: Conf. Series* 46 (2006), pp. 63–72 (cit. on p. 33).

[17] H. Bufferand. "Development of a Fluid Code for Tokamak Edge Plasma Simulation - Investigation on non-local Transport". PhD thesis. Aix-Marseille Université, 2012 (cit. on p. 37).

[18] H. Bufferand et al. "Implementation of drift velocities and currents in SOLEDGE2D–EIRENE". In: *Nucl. Materials and Energy* 12 (2017), pp. 852–857 (cit. on pp. 25, 37, 39, 45).

[19] F. Chen. *Introduction to Plasma Physics and Controlled Fusion*. Third Edition. Springer International Publishing, 2016 (cit. on p. 23).

[20] L. Chôné et al. In: *Phys. Plasmas* 21.7 (2014), p. 070702 (cit. on p. 27).

[21] S. Coda et al. In: *Nucl. Fusion* 57.10 (2017), p. 102011 (cit. on p. 18).

[22] J.W. Coenen et al. In: *Nucl. Fusion* 51 (2011), p. 063030 (cit. on p. 69).

[23] C. Colin et al. In: *Journal of Nuclear Materials* 463 (2015), pp. 654–658 (cit. on p. 30).

[24] J.W. Connor et al. In: *Nucl. Fusion* 13.2 (1973), pp. 221–225 (cit. on p. 31).

[25] N. Cruz et al. In: *Fusion Engineering and Design* 129 (2018), pp. 247–252 (cit. on p. 32).

[26] O. Czarny et al. In: *Jour. Comput. Phys.* 227.16 (2008), pp. 7423–7445 (cit. on p. 142).

[27] W.D. D'haeseleer, W.N.G. Hitchon, J.D. Callen, et al. *Flux Coordinates and Magnetic Field Structure*. Springer, 1991 (cit. on pp. 53, 178, 179).

[28] A. Dinklage et al. In: *Nature Phys.* 14.8 (2018), pp. 855–860 (cit. on p. 18).

[29] Rosa Donat et al. In: *Jour. Comput. Phys.* 125.1 (1996), pp. 42–58 (cit. on p. 55).

[30] B D Dudson et al. In: *Plasma Phys. Control. Fusion* 53.5 (2011), p. 054005 (cit. on p. 33).

[31] B. D. Dudson et al. In: *Jour. Plasma Phys.* 81.1 (2015), p. 365810104 (cit. on p. 36).

[32] B.D. Dudson et al. In: *Computer Phys. Comm.* 180.9 (2009), pp. 1467–1480 (cit. on p. 36).

[33] ITER Physics Basis Editors et al. In: *Nucl. Fusion* 39.12 (1999), pp. 2137–2174 (cit. on pp. 30, 32).

[34] T. Eich et al. In: *Nucl. Fusion* 53.9 (2013), p. 093031 (cit. on p. 30).

[35] T. Eich et al. In: *Nucl. Materials and Energy* 12 (2017), pp. 84–90 (cit. on p. 32).

[36] T. E. Evans et al. In: *Phys. Rev. Lett.* 92 (23 2004), p. 235003 (cit. on p. 33).

[37] T. E. Evans et al. In: *Nature Phys.* 2.6 (2006), pp. 419–423 (cit. on p. 33).

[38] T.E. Evans. In: *Plasma Phys. Control. Fusion* 57 (2015), p. 123001 (cit. on pp. 32, 33).

[39] T.E. Evans et al. In: *Jour. Nucl. Materials* 337-339 (2005), pp. 691–696 (cit. on p. 32).

[40] T.E. Evans et al. In: *Nucl. Fusion* 48.2 (2008), p. 024002 (cit. on p. 67).

[41] D.M. Fan et al. In: *Nucl. Materials and Energy* 18 (2019), pp. 105–110 (cit. on p. 57).

[42] N. Fedorczak et al. In: *Nucl. Materials and Energy* 12 (2017), pp. 838–843 (cit. on p. 24).

[43] N Fedorczak et al. In: *Plasma Phys. Control. Fusion* 55.12 (2013), p. 124024 (cit. on p. 27).

[44] Y. Feng et al. In: *Contr. Plasma Phys.* 54.4-6 (2014), pp. 426–431 (cit. on pp. 34, 37).

[45] H. Frerichs et al. In: *Phys. Plasmas* 23.6 (2016), p. 062517 (cit. on pp. 25, 34, 86, 134, 136).

[46] H. Frerichs et al. In: *Nucl. Materials and Energy* 18 (2019), pp. 62–66 (cit. on p. 33).

[47] D. Galassi. "Numerical Modelling of Transport and Turbulence in Tokamak Edge Plasma with Divertor Configuration". PhD thesis. Aix-Marseille Université and Università di Bologna, 2017 (cit. on pp. 21, 43, 51, 178).

[48] D. Galassi et al. In: *Fluids* 4.1 (2019), p. 50 (cit. on pp. 36, 57).

[49] O. E. Garcia et al. In: *Phys. Plasmas* 13.8 (2006), p. 082309 (cit. on p. 24).

[50] O.E. Garcia et al. In: *Jour. Nucl. Materials* 363-365 (2007), pp. 575–580 (cit. on p. 134).

[51] Ph Ghendrih et al. In: *Plasma Phys. Control. Fusion* 53.5 (2011), p. 054019 (cit. on p. 48).

[52] G. Giorgiani et al. In: *Contr. Plasma Phys.* 58.6-8 (2018), pp. 688–695 (cit. on pp. 37, 58, 60).

[53] G. Giorgiani et al. In: *Jour. Comp. Phys.* 374 (2018), pp. 515–532 (cit. on pp. 37, 58–60).

[54] G. Giorgiani et al. In: *Nucl. Materials and Energy* 19 (2019), pp. 340–345 (cit. on pp. 37, 39, 58).

[55] V. Grandgirard et al. In: *Computer Phys. Comm.* 207 (2016), pp. 35–68 (cit. on p. 40).

[56] J.R. Harrison et al. In: *Nucl. Fusion* 59.11 (2019), p. 112011 (cit. on p. 18).

[57] D.N. Hill. In: *Jour. Nucl. Materials* 241-243 (1997), pp. 182–198 (cit. on p. 27).

[58] F. L. Hinton et al. In: *Phys. Fluids* 14.1 (1971), pp. 116–123 (cit. on p. 45).

[59] F. L. Hinton et al. In: *Rev. Mod. Phys.* 48.2 (1976), pp. 239–308 (cit. on pp. 23, 54).

[60] G.T.A Huysmans et al. In: *Nucl. Fusion* 47.7 (2007), pp. 659–666 (cit. on p. 142).

[61] Y. M. Jeon et al. In: *Phys. Rev. Lett.* 109 (3 2012), p. 035004 (cit. on p. 33).

[62] Alexander Kendl et al. In: *Phys. Plasmas* 17.7 (2010), p. 072302 (cit. on p. 33).

[63] A Kirk et al. In: *Plasma Phys. Control. Fusion* 55.4 (2013), p. 045007 (cit. on p. 32).

[64] P.T. Lang et al. In: *Nucl. Fusion* 53.4 (2013), p. 043004 (cit. on p. 32).

[65] J D Lawson. In: *Proc. Physic. Society* 70.1 (1957), pp. 6–10 (cit. on p. 17).

[66] M. Leconte et al. In: *Nucl. Fusion* 50.5 (2010), p. 054008 (cit. on p. 35).

[67] M. Leconte et al. In: *Phys. Plasmas* 19.5 (2012), p. 055903 (cit. on p. 35).

[68] A W Leonard. In: *Plasma Phys. Control. Fusion* 60.4 (2018), p. 044001 (cit. on p. 31).

[69] A. W. Leonard. In: *Phys. Plasmas* 21.9 (2014), p. 090501 (cit. on p. 28).

[70] Y. Liang et al. In: *Phys. Rev. Lett.* 98 (26 2007), p. 265004 (cit. on pp. 33, 67).

[71] P.C. Liewer. In: *Nucl. Fusion* 25.5 (1985), pp. 543–621 (cit. on p. 24).

[72] X. Litaudon et al. In: *Nucl. Fusion* 57.10 (2017), p. 102001 (cit. on p. 18).

[73] Xu-Dong Liu et al. In: *Jour. Comput. Phys.* 115.1 (1994), pp. 200–212 (cit. on p. 55).

[74] Y R Martin et al. In: *Jour. Phys.: Conf. Series* 123 (2008), p. 012033 (cit. on p. 28).

[75] J.E. Menard et al. In: *Nucl. Fusion* 57.10 (2017), p. 102006 (cit. on p. 18).

[76] H. Meyer et al. In: *Nucl. Fusion* 59.11 (2019), p. 112014 (cit. on p. 18).

[77] S. Mordijck et al. In: *Plasma Phys. Control. Fusion* 58.1 (2015), p. 014003 (cit. on p. 34).

[78] S Mordijck et al. In: *Plasma Phys. Control. Fusion* 53.12 (2011), p. 122001 (cit. on p. 34).

[79] A. Mosetto et al. In: *Phys. Plasmas* 19.11 (2012), p. 112103 (cit. on p. 24).

[80] A. Mosetto et al. In: *Phys. Plasmas* 20.9 (2013), p. 092308 (cit. on p. 24).

[81] R. A. Moyer et al. In: *Rev. Scientific Instruments* 89.10 (2018), 10E106 (cit. on p. 34).

[82] N. Nace. "Dynamics of Driven and Spontaneous Transport Barriers in the Edge of Plasma of Tokamaks". PhD thesis. Aix-Marseille Université, 2018 (cit. on pp. 26, 40, 43, 45).

[83] E. Nardon. "Edge Localized Modes Control by Resonant Magnetic Perturbations". PhD thesis. École Polytechnique, 2007 (cit. on pp. 27, 32, 142).

[84] E. Nardon et al. In: *Phys. Plasmas* 14 (2007), p. 092501 (cit. on pp. 33, 140).

[85] E. Nardon et al. In: *Jour. Nucl. Materials* 363 (2007), pp. 1071–1075 (cit. on p. 32).

[86] V. Naulin. In: *Jour. Nucl. Materials* 363-365 (2007), pp. 24–31 (cit. on p. 134).

[87] F Nespoli et al. In: *Plasma Phys. Control. Fusion* 59.5 (2017), p. 055009 (cit. on p. 24).

[88] F. Orain et al. In: *Plasma Phys. Control. Fusion* 57.1 (2014), p. 014020 (cit. on pp. 32, 33).

[89] H.K. Park et al. In: *Nucl. Fusion* 59.11 (2019), p. 112020 (cit. on p. 18).

[90] Paola Paruta et al. In: *Phys. Plasmas* 25.11 (2018), p. 112301 (cit. on p. 36).

[91] J. Peer et al. In: *Nucl. Fusion* 57.8 (2017), p. 086026 (cit. on p. 35).

[92] C.C. Petty et al. In: *Nucl. Fusion* 59.11 (2019), p. 112002 (cit. on p. 18).

[93] D E Post and R Behrisch. *Physics of plasma-wall interactions in controlled fusion*. Springer, 1984 (cit. on p. 49).

[94] R.F. Post. In: *Nucl. Fusion* 27.10 (1987), pp. 1579–1739 (cit. on p. 18).

[95] D. Reiser. In: *Phys. Plasmas* 14 (2007), p. 082314 (cit. on p. 35).

[96] D. Reiser et al. In: *Phys. Plasmas* 12.12 (2005), p. 122308 (cit. on p. 35).

[97] D. Reiser et al. In: *Phys. Plasmas* 16.4 (2009), p. 042317 (cit. on p. 35).

[98] D. Reiter et al. In: *Fusion Science and Technology* 47.2 (2005), pp. 172–186 (cit. on p. 37).

[99] T.T. Ribeiro et al. In: *Plasma Pys. Control. Fusion* 47.10 (2005), p. 1657 (cit. on p. 24).

[100] P Ricci et al. In: *Plasma Phys. Control. Fusion* 54.12 (2012), p. 124047 (cit. on p. 36).

[101] P.L Roe. In: *Jour. Comput. Phys.* 43.2 (1981), pp. 357–372 (cit. on p. 55).

[102] A. Samain et al. In: *Jour. Nucl. Materials* 128-129 (1984), pp. 395–399 (cit. on p. 35).

[103] Y. Sarazin et al. In: *Phys. Plasmas* 5.12 (1998), pp. 4214–4228 (cit. on pp. 24, 81).

[104] Y. Sarazin et al. In: *Jour. Nucl. Materials* 313-316 (2003), pp. 796–803 (cit. on p. 25).

[105] O. Schmitz et al. In: *Phys. Rev. Lett.* 103 (16 2009), p. 165005 (cit. on p. 33).

[106] P.P.J.M. Schram. *Kinetic Theory of Gases and Plasmas*. Springer Science + Business Media, 1991 (cit. on p. 171).

[107] B.D. Scott. In: *Phys. Plasmas* 12.6 (2005), p. 062314 (cit. on p. 24).

[108] Bruce D Scott. In: *Plasma Phys. Control. Fusion* 49.7 (2007), S25–S41 (cit. on pp. 24, 25).

[109] K.C. Shaing et al. In: *Nucl. Fusion* 22.8 (1982), pp. 1061–1068 (cit. on pp. 31, 150).

[110] M Shimada et al. In: *Nucl. Fusion* 47.6 (2007), S1–S17 (cit. on p. 32).

[111] Weston M. Stacey. In: *Phys. Plasmas* 20.9 (2013), p. 092508 (cit. on p. 27).

[112] P.C. Stangeby. *The Plasma Boundary of Magnetic Fusion Devices*. CRC Press, 2000 (cit. on pp. 28, 46–49).

[113] A. Stegmeir et al. In: *Phys. Plasmas* 26.5 (2019), p. 052517 (cit. on p. 36).

[114] Andreas Stegmeir et al. In: *Plasma Phys. Control. Fusion* 60.3 (2018), p. 035005 (cit. on p. 36).

[115] T.E. Stringer. In: *Nucl. Fusion* 12.6 (1972), pp. 689–694 (cit. on pp. 31, 150).

[116] W. Suttrop et al. In: *Phys. Rev. Lett.* 106 (22 2011), p. 225004 (cit. on p. 33).

[117] P. Tamain. "Étude des Flux de Matière dans le Plasma de Bord des Tokamaks : Alimentation, Transport et Turbulence". PhD thesis. Aix-Marseille Université, 2007 (cit. on pp. 43, 51).

[118] P. Tamain et al. In: *Plasma Phys. Control. Fusion* 52 (2010), p. 075017 (cit. on pp. 34, 67, 69, 71, 81).

[119] P. Tamain et al. In: *Jour. Comput. Phys.* 229.2 (2010), pp. 361–378 (cit. on p. 25).

[120] P. Tamain et al. In: *Contr. Plasma Phys.* 54.4-6 (2014), pp. 555–559 (cit. on p. 24).

[121] P. Tamain et al. In: *Plasma Phys. Control. Fusion* 57.5 (2015), p. 054014 (cit. on pp. 36, 57).

[122] P. Tamain et al. In: *Jour. Comp. Phys.* 321 (2016), pp. 606–623 (cit. on pp. 36, 39).

[123] Tetsuo Tanabe. *Tritium: Fuel of fusion reactors*. Springer, 2017 (cit. on p. 16).

[124] A.J. Thornton et al. In: *Nucl. Fusion* 54.6 (2014), p. 064011 (cit. on pp. 34, 145).

[125] M. Z. Tokar et al. In: *Phys. Rev. Lett.* 98 (9 2007), p. 095001 (cit. on p. 32).

[126] Shih-tung Tsai et al. In: *Phys. Fluids* 13.8 (1970), pp. 2108–2114 (cit. on p. 45).

[127] F.L. Waelbroeck. In: *Nucl. Fusion* 49 (2009), p. 104025 (cit. on p. 32).

[128] F Wagner. In: *Plasma Phys. Control. Fusion* 49.12B (2007), B1–B33 (cit. on pp. 22, 27).

[129] F. Wagner et al. In: *Phys. Rev. Lett.* 49 (19 1982), pp. 1408–1412 (cit. on p. 27).

[130] B.N. Wan et al. In: *Nucl. Fusion* 57.10 (2017), p. 102019 (cit. on p. 18).

[131] S.X. Wang et al. In: *Nucl. Fusion* 58.11 (2018), p. 112013 (cit. on p. 69).

[132] J. Wesson. *Tokamaks*. Third Edition. International Series of Monographes on Physics. Oxford Science Publications, 2004 (cit. on pp. 20, 24, 32, 41).

[133] A. J. Wootton et al. In: *Phys. Fluids B: Plasma Phys.* 2.12 (1990), pp. 2879–2903 (cit. on p. 24).

[134] S J Zweben et al. In: *Plasma Phys. Control. Fusion* 49.7 (2007), S1–S23 (cit. on p. 24).

# APPENDIX

# A. Derivation of the fluid model

## A.1. From particle to Vlasov-Boltzmann equations

From [106], we detail here the calculation to obtain the Boltzmann-Vlasov equations. Starting from the particle descritpion, we have:

$$m_j \mathrm{d}_t \boldsymbol{v}_j = q_j(\boldsymbol{E}_j + \boldsymbol{v}_j \times \boldsymbol{B}_j) \tag{A.1}$$

where $\boldsymbol{E}_j$ and $\boldsymbol{B}_j$ stand for a local description of the electric and magnetic fields, composed of the external fields and the complex interaction of the particle with the others. Both fields follow the Maxwell's equations:

$$\begin{cases} \boldsymbol{\nabla} \cdot \boldsymbol{E}_j &= \rho_j/\epsilon_0 \\ \boldsymbol{\nabla} \cdot \boldsymbol{B}_j &= 0 \\ \boldsymbol{\nabla} \times \boldsymbol{E}_j &= -\partial_t \boldsymbol{B}_j \\ \boldsymbol{\nabla} \times \boldsymbol{B}_j &= \mu_0(\boldsymbol{j}_j + \epsilon_0 \partial_t \boldsymbol{E}_j) \end{cases} \tag{A.2}$$

where $\rho_j$ and $\boldsymbol{j}_j$ are the local charge and current densities, written:

$$\begin{cases} \rho_j(t,\boldsymbol{x}) &= \displaystyle\sum_{k=1}^{N_j} q_k \delta(\boldsymbol{x} - \boldsymbol{x}_k) \\ \boldsymbol{j}_j(t,\boldsymbol{x}) &= \displaystyle\sum_{k=1}^{N_j} q_k \delta(\boldsymbol{x} - \boldsymbol{x}_k)\boldsymbol{v}_k \end{cases} \tag{A.3}$$

The particle description can be extended into a microscopic distribution function $\mathscr{N}_s$ for each specie $s$ in the 6D phase space, leading to the Kilmontovitch equation. We note thus:

$$\mathscr{N}_s(t,\boldsymbol{x},\boldsymbol{v}) = \sum_{k=1}^{N_{j_s}} \delta(\boldsymbol{x} - \boldsymbol{x}_k)\delta(\boldsymbol{v} - \boldsymbol{v}_k) \tag{A.4}$$

where $N_{j_s}$ notes the number of particles of specie $s$, verifying $\sum_s N_{j_s} = N_j$. $\mathscr{N}_s$ is a discrete function in the phase space. Writinf the conservation law for particles $\mathrm{d}\mathscr{N}_s = 0$, we obtain (Lorentz force and $\boldsymbol{v}$ are divergence free in $\boldsymbol{v}$ space):

$$\partial_t \mathscr{N}_s + \boldsymbol{v} \cdot \boldsymbol{\nabla}_x \mathscr{N}_s + \frac{q_s}{m_s}(\boldsymbol{E}_j + \boldsymbol{v} \times \boldsymbol{B}_j) \cdot \boldsymbol{\nabla}_v \mathscr{N}_s = 0 \tag{A.5}$$

by recognizing that $\dot{\boldsymbol{x}} = \boldsymbol{v}$ and $\dot{\boldsymbol{v}} = \frac{q_s}{m_s}(\boldsymbol{E}_j + \boldsymbol{V}_j \times \boldsymbol{B}_j)$. This equation cannot be solved numerically as it describes still a too large number of microscopic states. Futhermore, the results will be a huge amount of data that are not directly physical quantities (average properties such as density, velocity, etc.) and so hardly relevant for a physicist.

To obtain more physical measures, the equations A.5 are averaged with the following method:

$$\left\{\begin{array}{lcll} \mathcal{N}_s(t,\boldsymbol{x},\boldsymbol{v}) & = & f_s(t,\boldsymbol{x},\boldsymbol{v}) + \delta\mathcal{N}_s(t,\boldsymbol{x},\boldsymbol{v}) & \text{with} \quad <\mathcal{N}_s> = f_s \\ \boldsymbol{E}_j(t,\boldsymbol{x}) & = & \boldsymbol{E}(t,\boldsymbol{x}) + \delta\boldsymbol{E}(t,\boldsymbol{x}) & \text{with} \quad <\boldsymbol{E}_j> = \boldsymbol{E} \\ \boldsymbol{B}_j(t,\boldsymbol{x}) & = & \boldsymbol{B}(t,\boldsymbol{x}) + \delta\boldsymbol{B}(t,\boldsymbol{x}) & \text{with} \quad <\boldsymbol{B}_j> = \boldsymbol{B} \end{array}\right.$$

To complete the averaging, we add the charge and the current from the Maxwell's equations:

$$\left\{\begin{array}{lcll} \rho_s(t,\boldsymbol{x}) & = & <\rho_j(t,\boldsymbol{x})> & = \sum_s q_s \int_\Omega f_s \mathrm{d}^3\boldsymbol{v} \\ \boldsymbol{j}_s(t,\boldsymbol{x}) & = & <\boldsymbol{j}_j(t,\boldsymbol{x})> & = \sum_s q_s \int_\Omega \boldsymbol{v} f_s \mathrm{d}^3\boldsymbol{v} \end{array}\right.$$

Thus equation A.5 write:

$$\partial_t(f_s + \delta\mathcal{N}_s) + \boldsymbol{v}\cdot\boldsymbol{\nabla}_{\boldsymbol{x}}(f_s + \delta\mathcal{N}_s) + \frac{q_s}{m_s}(\boldsymbol{E} + \delta\boldsymbol{E} + \boldsymbol{v}\times(\boldsymbol{B} + \delta\boldsymbol{B}))\cdot\boldsymbol{\nabla}_{\boldsymbol{v}}(f_s + \delta\mathcal{N}_s) = 0$$

Averaging leads to (using $\boldsymbol{\nabla}\cdot(a+b) = \boldsymbol{\nabla}\cdot a + \boldsymbol{\nabla}\cdot b$ and $<\partial_{x_i} f> = \partial_{x_i} <f>$):

$$\partial_t f_s + \boldsymbol{v}\cdot\boldsymbol{\nabla}_{\boldsymbol{x}} f_s + \frac{q_s}{m_s}(\boldsymbol{E} + \boldsymbol{v}\times\boldsymbol{B})\cdot\boldsymbol{\nabla}_{\boldsymbol{v}} f_s + \frac{q_s}{m_s} <(\delta\boldsymbol{E} + \boldsymbol{v}\times\delta\boldsymbol{B})\cdot\boldsymbol{\nabla}_{\boldsymbol{v}}(\delta\mathcal{N}_s)> = 0$$

and by noting $C_s = -\frac{q_s}{m_s} <(\delta\boldsymbol{E} + \boldsymbol{v}\times\delta\boldsymbol{B})\cdot\boldsymbol{\nabla}_{\boldsymbol{v}}(\delta\mathcal{N}_s)>$, we achieve the Boltzmann equations:

$$\partial_t f_s + \boldsymbol{v}\cdot\boldsymbol{\nabla}_{\boldsymbol{x}} f_s + \frac{q_s}{m_s}(\boldsymbol{E} + \boldsymbol{v}\times\boldsymbol{B})\cdot\boldsymbol{\nabla}_{\boldsymbol{v}} f_s = C_s \tag{A.6}$$

## A.2. Fluid equation derivations

In this part, we precise the computation for $n = 0\cdots 2$ in equation 2.4. We assume the distribution function $f_s$ to be exponentially vanishing (see expression 2.5), that is:

$$\forall n \in \mathbb{N},\ \lim_{|\boldsymbol{v}|\to\infty} \boldsymbol{v}^{\otimes n} f_s = 0 \tag{A.7}$$

Using commutative properties, equation 2.4 writes $\forall n \in \mathbb{N}$:

$$\partial_t \int_\Omega \boldsymbol{v}_s^{\otimes n} f_s \mathrm{d}^3\boldsymbol{v} + \boldsymbol{\nabla}_{\boldsymbol{x}}\cdot\int_\Omega \boldsymbol{v}_s^{\otimes n+1} f_s \mathrm{d}^3\boldsymbol{v} + \int_\Omega \boldsymbol{v}_s^{\otimes n}\boldsymbol{\nabla}_{\boldsymbol{v}}\cdot\left(\frac{q_s}{m_s}(\boldsymbol{E} + \boldsymbol{v}\times\boldsymbol{B}) f_s\right)\mathrm{d}^3\boldsymbol{v} = \int_\Omega \boldsymbol{v}_s^{\otimes n} C_s \mathrm{d}^3\boldsymbol{v} \tag{A.8}$$

### A.2.1. The continuity equation $n = 0$

Equation A.8 becomes:

$$\partial_t \underbrace{\int_\Omega f_s \mathrm{d}^3\boldsymbol{v}}_{\equiv n_s} + \boldsymbol{\nabla}_{\boldsymbol{x}} \cdot \underbrace{\int_\Omega \boldsymbol{v} f_s \mathrm{d}^3\boldsymbol{v}}_{\equiv \Gamma \equiv n_s \boldsymbol{u}_s} + \underbrace{\int_\Omega \boldsymbol{\nabla}_{\boldsymbol{v}} \cdot \left(\frac{q_s}{m_s}(\boldsymbol{E} + \boldsymbol{v} \times \boldsymbol{B}) f_s\right) \mathrm{d}^3\boldsymbol{v}}_{\equiv (\mathrm{i})_{A.9}} = \underbrace{\int_\Omega C_s \mathrm{d}^3\boldsymbol{v}}_{\equiv S_s} \tag{A.9}$$

Using as definitions $n_s$ the particle density, the momentum $\Gamma \equiv n_s \boldsymbol{u}_s$, with $\boldsymbol{u}_s$ the fluid velocity and the collisional particle source $S_s$, we only have to calculate $(\mathrm{i})_{A.9}$:

$$(\mathrm{i})_{A.9} = \lim_{\boldsymbol{v} \to +\infty} \left[\frac{q_s}{m_s}(\boldsymbol{E} + \boldsymbol{v} \times \boldsymbol{B}) f_s\right]_{-\boldsymbol{v}}^{+\boldsymbol{v}} = 0 \tag{A.10}$$

by property of $f_s$ (exponentially vanishing). This gives the continuity equation:

$$\partial_t n_s + \boldsymbol{\nabla} \cdot (n_s \boldsymbol{u}_s) = S_s \tag{A.11}$$

### A.2.2. The momentum equation $n = 1$

Equation A.8 becomes:

$$\partial_t \underbrace{\int_\Omega \boldsymbol{v} f_s \mathrm{d}^3\boldsymbol{v}}_{\equiv n_s \boldsymbol{u}_s} + \boldsymbol{\nabla}_{\boldsymbol{x}} \cdot \underbrace{\int_\Omega \boldsymbol{v}^{\otimes 2} f_s \mathrm{d}^3\boldsymbol{v}}_{(\mathrm{i})_{A.12}} + \underbrace{\int_\Omega \boldsymbol{v} \boldsymbol{\nabla}_{\boldsymbol{v}} \cdot \left(\frac{q_s}{m_s}(\boldsymbol{E} + \boldsymbol{v} \times \boldsymbol{B}) f_s\right) \mathrm{d}^3\boldsymbol{v}}_{(\mathrm{ii})_{A.12}} = \underbrace{\int_\Omega \boldsymbol{v} C_s \mathrm{d}^3\boldsymbol{v}}_{(\mathrm{iii})_{A.12}} \tag{A.12}$$

The velocity particle $\boldsymbol{w}_s$ in the moving frame of the fluid $\boldsymbol{u}_s$ is defined as: $\boldsymbol{w}_s = \boldsymbol{v} - \boldsymbol{u}_s$ with by definition $\int_\Omega \boldsymbol{w}_s f_s \mathrm{d}^3\boldsymbol{v} = 0$. Thus we have the following calculations:

$$\begin{aligned}
(\mathrm{i})_{A.12} &= \int_\Omega (\boldsymbol{u}_s + \boldsymbol{w}_s) \otimes (\boldsymbol{u}_s + \boldsymbol{w}_s) f_s \mathrm{d}^3\boldsymbol{v} \\
&= \int_\Omega \boldsymbol{u}_s \otimes \boldsymbol{u}_s f_s \mathrm{d}^3\boldsymbol{v} + \int_\Omega \boldsymbol{u}_s \otimes \boldsymbol{w}_s f_s \mathrm{d}^3\boldsymbol{v} + \int_\Omega \boldsymbol{w}_s \otimes \boldsymbol{u}_s f_s \mathrm{d}^3\boldsymbol{v} + \underbrace{\int_\Omega \boldsymbol{w}_s \otimes \boldsymbol{w}_s f_s \mathrm{d}^3\boldsymbol{v}}_{\equiv \overline{\overline{\boldsymbol{\Pi}}}_s^{\mathrm{tot}} / m_s} \\
&= \boldsymbol{u}_s \otimes \boldsymbol{u}_s \int_\Omega f_s \mathrm{d}^3\boldsymbol{v} + \boldsymbol{u}_s \otimes \underbrace{\int_\Omega \boldsymbol{w}_s f_s \mathrm{d}^3\boldsymbol{v}}_{=0} + \underbrace{\int_\Omega \boldsymbol{w}_s f_s \mathrm{d}^3\boldsymbol{v}}_{=0} \otimes \boldsymbol{u}_s + \frac{1}{m_s} \overline{\overline{\boldsymbol{\Pi}}}_s^{\mathrm{tot}} \\
&= n_s \boldsymbol{u}_s \otimes \boldsymbol{u}_s + \frac{1}{m_s} \overline{\overline{\boldsymbol{\Pi}}}_s^{\mathrm{tot}}
\end{aligned}$$

with the total pressure tensor $\overline{\overline{\boldsymbol{\Pi}}}_s^{\mathrm{tot}} = p_s \mathbb{1} + \overline{\overline{\boldsymbol{\Pi}}}_s^{\mathrm{clos}}$. $p_s = \mathrm{Tr}(\overline{\overline{\boldsymbol{\Pi}}}_s^{\mathrm{tot}})/3$ is the scalar isotropic pressure and $\overline{\overline{\boldsymbol{\Pi}}}_s^{\mathrm{clos}}$, the residual stress tensor.

The second term is calculated with an integration by part and this writes:

$$\begin{aligned}(\text{ii})_{A.12} &= \underbrace{\left[\boldsymbol{v}\cdot\frac{q_s}{m_s}(\boldsymbol{E}+\boldsymbol{v}\times\boldsymbol{B})f_s\right]_{-\infty}^{\infty}}_{=0} - \int_\Omega \frac{q_s}{m_s}(\boldsymbol{E}+\boldsymbol{v}\times\boldsymbol{B})f_s \mathrm{d}^3\boldsymbol{v} \\ &= -\frac{q_s}{m_s}\left(\boldsymbol{E}\int_\Omega f_s \mathrm{d}^3\boldsymbol{v} + \int_\Omega \boldsymbol{v} f_s \mathrm{d}^3\boldsymbol{v}\times\boldsymbol{B}\right) \\ &= -\frac{q_s}{m_s} n_s(\boldsymbol{E}+\boldsymbol{u}_s\times\boldsymbol{B})\end{aligned}$$

Finally the collisional term gives:

$$\begin{aligned}(\text{iii})_{A.12} &= \int_\Omega (\boldsymbol{u}_s+\boldsymbol{w}_s)C_s \mathrm{d}^3\boldsymbol{v} = \boldsymbol{u}_s\int_\Omega C_s \mathrm{d}^3\boldsymbol{v} + \int_\Omega \boldsymbol{w}_s C_s \mathrm{d}^3\boldsymbol{v} \\ &= \boldsymbol{u}_s S_s + \int_\Omega \boldsymbol{w}_s C_s = \frac{1}{m_s}\boldsymbol{R}_s\end{aligned}$$

with $\boldsymbol{R}_s \equiv m_s\int_\Omega \boldsymbol{v}_s C_s \mathrm{d}^3\boldsymbol{v}$ the collisional momentum source. Finally the momentum equation writes:

$$\partial_t(m_s n_s \boldsymbol{u}_s) + \boldsymbol{\nabla}\cdot\left(m_s n_s \boldsymbol{u}_s\otimes\boldsymbol{u}_s + \overline{\overline{\boldsymbol{\Pi}}}_s^{\text{tot}}\right) = q_s n_s(\boldsymbol{E}+\boldsymbol{u}_s\times\boldsymbol{B}) + \boldsymbol{R}_s \tag{A.13}$$

or in non-conservative form:

$$m_s n_s \partial_t \boldsymbol{u}_s + m_s n_s(\boldsymbol{u}_s\cdot\boldsymbol{\nabla})\boldsymbol{u}_s = -\boldsymbol{\nabla}p_s - \boldsymbol{\nabla}\cdot\overline{\overline{\boldsymbol{\Pi}}}_s^{\text{res}} + q_s n_s(\boldsymbol{E}+\boldsymbol{u}_s\times\boldsymbol{B}) + \boldsymbol{R}_s \tag{A.14}$$

where we used $\boldsymbol{\nabla}\cdot(m_s n_s \boldsymbol{u}_s\otimes\boldsymbol{u}_s) = \boldsymbol{u}_s\boldsymbol{\nabla}\cdot(m_s n_s\boldsymbol{u}_s) + m_s n_s(\boldsymbol{u}_s\cdot\boldsymbol{\nabla})\boldsymbol{u}_s$ and the continuity equation A.11

### A.2.3. The energy equation $n=2$

Equation A.8 becomes:

$$\underbrace{\partial_t\int_\Omega \boldsymbol{v}^{\otimes 2} f_s \mathrm{d}^3\boldsymbol{v}}_{(\text{i})_{A.15}} + \underbrace{\boldsymbol{\nabla}_{\boldsymbol{x}}\cdot\int_\Omega \boldsymbol{v}^{\otimes 3} f_s \mathrm{d}^3\boldsymbol{v}}_{(\text{ii})_{A.15}} + \underbrace{\int_\Omega \boldsymbol{v}^{\otimes 2}\boldsymbol{\nabla}_{\boldsymbol{v}}\cdot\left(\frac{q_s}{m_s}(\boldsymbol{E}+\boldsymbol{v}\times\boldsymbol{B})f_s\right)\mathrm{d}^3\boldsymbol{v}}_{(\text{iii})_{A.15}} = \underbrace{\int_\Omega \boldsymbol{v}^{\otimes 2} C_s \mathrm{d}^3\boldsymbol{v}}_{(\text{iv})_{A.15}} \tag{A.15}$$

The first term is exactly the same as above $(\text{i})_{A.12}$, so:

$$(\text{i})_{A.15} = n_s\boldsymbol{u}_s\otimes\boldsymbol{u}_s + \frac{1}{m_s}\overline{\overline{\boldsymbol{\Pi}}}_s^{\text{tot}}$$

The second term follows the same development:

$$\begin{aligned}(\text{ii})_{A.15} &= \int_\Omega (\boldsymbol{u}_s + \boldsymbol{w}_s)^{\otimes 3} f_s \mathrm{d}^3\boldsymbol{v} = \cdots \\ &= n_s \boldsymbol{u}_s^{\otimes 3} + \frac{1}{m_s}\left(\overline{\overline{\boldsymbol{\Pi}}}_s^{\mathrm{tot}} \otimes \boldsymbol{u}_s + \boldsymbol{u}_s \otimes \overline{\overline{\boldsymbol{\Pi}}}_s^{\mathrm{tot}}\right) + \int_\Omega \boldsymbol{w}_s \otimes \boldsymbol{u}_s \otimes \boldsymbol{w}_s f_s \mathrm{d}^3\boldsymbol{v} + \frac{2}{m_s}\overline{\overline{\overline{\boldsymbol{Q}}}}_s\end{aligned}$$

with $\overline{\overline{\overline{\boldsymbol{Q}}}}_s = \frac{1}{2} m_s \int_\Omega \boldsymbol{w}_s^{\otimes 3} f_s \mathrm{d}^3\boldsymbol{v}$ the pressure flux tensor.
The third term leads to, with the same method as before (integration by part):

$$\begin{aligned}(\text{iii})_{A.15} &= -\int_\Omega \left(\frac{q_s}{m_s}(\boldsymbol{E} + \boldsymbol{v} \times \boldsymbol{B}) f_s\right) \otimes \boldsymbol{v} \mathrm{d}^3\boldsymbol{v} - \int_\Omega \boldsymbol{v} \otimes \left(\frac{q_s}{m_s}(\boldsymbol{E} + \boldsymbol{v} \times \boldsymbol{B}) f_s\right) \mathrm{d}^3\boldsymbol{v} = \cdots \\ &= -\frac{q_s}{m_s} n_s (\boldsymbol{E} \otimes \boldsymbol{u}_s + \boldsymbol{u}_s \otimes \boldsymbol{E}) - \frac{2}{m_s}\overline{\overline{\overline{\boldsymbol{W}}}}_s^{\boldsymbol{v}\times\boldsymbol{B}}\end{aligned}$$

with the work tensor of the Lorentz force $\overline{\overline{\overline{\boldsymbol{W}}}}_s^{\boldsymbol{v}\times\boldsymbol{B}} \equiv \frac{1}{2} q_s \int_\Omega ((\boldsymbol{v} \times \boldsymbol{B}) \otimes \boldsymbol{v} + \boldsymbol{v} \otimes (\boldsymbol{v} \times \boldsymbol{B})) f_s \mathrm{d}^3\boldsymbol{v}$
Finally, the last collisional term gives:

$$\begin{aligned}(\text{iv})_{A.15} &= \int_\Omega (\boldsymbol{u}_s + \boldsymbol{w}_s)^{\otimes 2} C_s \mathrm{d}^3\boldsymbol{v} = \cdots \\ &= \frac{2}{m_s}\overline{\overline{\boldsymbol{H}}}_s + \frac{1}{m_s}(\boldsymbol{R}_s \otimes \boldsymbol{u}_s + \boldsymbol{u}_s \otimes \boldsymbol{R}_s) + \boldsymbol{u}_s \otimes \boldsymbol{u}_s S_s\end{aligned}$$

with the collisional pressure source tensor $\overline{\overline{\boldsymbol{H}}}_s = \int_\Omega C_s \boldsymbol{w}_s \otimes \boldsymbol{w}_s f_s \mathrm{d}^3\boldsymbol{v}$. It is useful to note the energy tensor $\overline{\overline{\boldsymbol{\epsilon}}}_s$ such that:

$$n_s \overline{\overline{\boldsymbol{\epsilon}}}_s \equiv \frac{1}{2} m_s n_s \boldsymbol{u}_s \otimes \boldsymbol{u}_s + \frac{1}{2}\overline{\overline{\boldsymbol{\Pi}}}_s^{\mathrm{tot}} \tag{A.16}$$

Leading to the energy tensor equation:

$$\begin{aligned}&\partial_t (n_s \overline{\overline{\boldsymbol{\epsilon}}}_s) + \boldsymbol{\nabla} \cdot \left(\frac{1}{2} n_s (\overline{\overline{\boldsymbol{\epsilon}}}_s \otimes \boldsymbol{u}_s + \boldsymbol{u}_s \otimes \overline{\overline{\boldsymbol{\epsilon}}}_s) + \frac{1}{2}\int_\Omega m_s \boldsymbol{w}_s \otimes \boldsymbol{u}_s \otimes \boldsymbol{w}_s f_s \mathrm{d}^3\boldsymbol{v} + \overline{\overline{\overline{\boldsymbol{Q}}}}_s\right) \\ &= \frac{1}{2} q_s n_s (\boldsymbol{E} \otimes \boldsymbol{u}_s + \boldsymbol{u}_s \otimes \boldsymbol{E}) + \overline{\overline{\overline{\boldsymbol{W}}}}_s^{\boldsymbol{v}\times\boldsymbol{B}} + \overline{\overline{\boldsymbol{H}}}_s + \frac{1}{2}(\boldsymbol{R}_s \otimes \boldsymbol{u}_s + \boldsymbol{u}_s \otimes \boldsymbol{R}_s) + \frac{1}{2} m_s \boldsymbol{u}_s \otimes \boldsymbol{u}_s S_s\end{aligned} \tag{A.17}$$

This tensor equation gives information on the total energy in each direction, which is considered mostly useless, so that only the total energy in the system is kept by taking the trace Tr of the equation above. The total energy is noted $E_s^{\mathrm{tot}} = \frac{1}{2} m_s n_s |\boldsymbol{u}_s|^2 + \frac{3}{2} p_s$, with the scalar pressure $p_s = \frac{1}{3}\mathrm{Tr}\left(\overline{\overline{\boldsymbol{\Pi}}}_s^{\mathrm{tot}}\right)$. The collisional energy source is noted $Q_{C_s} = \frac{1}{2} m_s \int_\Omega |\boldsymbol{w}_s|^2 C_s \mathrm{d}^3\boldsymbol{v}$ and the heat flux $\boldsymbol{q}_s = \frac{1}{2} m_s \int_\Omega |\boldsymbol{w}_s|^2 \boldsymbol{w}_s f_s \mathrm{d}^3\boldsymbol{v}$. The energy equation

thus writes:

$$\partial_t E_s^{\text{tot}} + \boldsymbol{\nabla}\cdot\left(E_s^{\text{tot}}\boldsymbol{u}_s + \boldsymbol{u}_s\cdot\overline{\overline{\boldsymbol{\Pi}}}_s^{\text{tot}} + \boldsymbol{q}_s\right) = n_s q_s \boldsymbol{E}\cdot\boldsymbol{u}_s + Q_{C_s} + \boldsymbol{R}_s\cdot\boldsymbol{u}_s + \frac{1}{2}m_s|\boldsymbol{u}_s|^2 S_s \quad \text{(A.18)}$$

or using the continuity and momentum equations, in a non conservative form:

$$\partial_t\left(\frac{3}{2}p_s\right) + \boldsymbol{\nabla}\cdot\left(\frac{3}{2}p_s\boldsymbol{u}_s\right) + \left(\overline{\overline{\boldsymbol{\Pi}}}_s^{\text{tot}}\cdot\boldsymbol{\nabla}\right)\cdot\boldsymbol{u}_s + \boldsymbol{\nabla}\cdot\boldsymbol{q}_s = Q_{C_s} \quad \text{(A.19)}$$

## A.3. Drift approximations

In this section, we show that the diamagnetic drift $\boldsymbol{u}_*$ can be expressed as $\boldsymbol{u}_{\nabla B} = \pm 2T_s\frac{1}{\boldsymbol{B}}$ in the divergence operator as both divergence are roughly the same.

$$\begin{aligned}
\boldsymbol{\nabla}\cdot(n_s\boldsymbol{u}_*) &= \boldsymbol{\nabla}\cdot\left(\frac{n_s\boldsymbol{B}\times\boldsymbol{\nabla}p_s}{n_s q_s B^2}\right) = \boldsymbol{\nabla}\left(\frac{1}{B^2}\right)\cdot(\boldsymbol{B}\times\boldsymbol{\nabla}p_s) + \frac{1}{B^2}\boldsymbol{\nabla}\cdot(\boldsymbol{B}\times\boldsymbol{\nabla}p_s)\\
&= \boldsymbol{\nabla}\left(\frac{1}{B^2}\right)\cdot(\boldsymbol{B}\times\boldsymbol{\nabla}p_s) + \frac{1}{B^2}\left[\underbrace{(\boldsymbol{\nabla}\times\boldsymbol{B})}_{\approx 0}\cdot\boldsymbol{\nabla}p_s - \boldsymbol{B}\cdot\underbrace{(\boldsymbol{\nabla}\times\boldsymbol{\nabla}p_s)}_{\equiv 0}\right]\\
&= \boldsymbol{\nabla}\left(\frac{1}{B^2}\right)\cdot(\boldsymbol{B}\times\boldsymbol{\nabla}p_s)
\end{aligned}$$

In this work, the electrostatic hypothesis assumes $\boldsymbol{\nabla}\times\boldsymbol{B} = \mu_0\boldsymbol{j}$. The current $\boldsymbol{j}$ can be split into the current generated by the toroidal coils, which is zero in the plasma by construction (all the current is inside the coils) and the plasma current driven by transformer effect to generate the poloidal field and local currents circulating in the edge plasma due to boundary conditions or fluctuations. Due to the resistivity gradient between the center of the plasma and the edge, it is safe to assume that most of the plasma current goes through the center of the plasma, i.e. outside the simulated domain in our simulations. As for the last component, it is neglected in the electrostatic approach under the low $\beta$ assumption. Consequently the Ampere'slaw can be reduced to $\boldsymbol{\nabla}\times\boldsymbol{B}\approx 0$. Now we calculate the divergence of the curvature drift, assuming $p_s = n_s T_s$:

$$\begin{aligned}
\boldsymbol{\nabla}\cdot(n_s\boldsymbol{u}_{\nabla B}) &= \boldsymbol{\nabla}\cdot\left(2p_s\frac{\boldsymbol{B}\times\boldsymbol{\nabla}B}{B^3}\right) = \boldsymbol{\nabla}\left(\frac{2p_s}{B^3}\right)\cdot(\boldsymbol{B}\times\boldsymbol{\nabla}B) + \left(\frac{2p_s}{B^3}\right)\underbrace{\boldsymbol{\nabla}\cdot(\boldsymbol{B}\times\boldsymbol{\nabla}B)}_{\approx 0 \text{ same as } \boldsymbol{\nabla}\cdot(\boldsymbol{B}\times\boldsymbol{\nabla}p_s)}\\
&= \frac{2}{B^3}\boldsymbol{\nabla}p_s\cdot(\boldsymbol{B}\times\boldsymbol{\nabla}B) + 2p_s\left(\frac{1}{B^3}\right)\cdot(\boldsymbol{B}\times\boldsymbol{\nabla}B)\\
&= -\frac{2}{B^3}\boldsymbol{\nabla}B\cdot(\boldsymbol{B}\times\boldsymbol{\nabla}p_s) - \frac{6p_s}{B^4}\underbrace{\boldsymbol{\nabla}\boldsymbol{B}\cdot(\boldsymbol{B}\times\boldsymbol{\nabla}B)}_{\equiv 0}\\
&= \boldsymbol{\nabla}\left(\frac{1}{B^2}\right)\cdot(\boldsymbol{B}\times\boldsymbol{\nabla}p_s)
\end{aligned}$$

Thus $\boldsymbol{\nabla} \cdot (n_s \boldsymbol{u}_*) = \boldsymbol{\nabla} \cdot (n_s \boldsymbol{u}_{\nabla B})$

# B. Magnetic geometry: general concept and TOKAM3X approach

TOKAM3X is based on a flux surface aligned coordinate system, allowing complex magnetic configurations. In the following part we describe the mathematical concept of curvilinear coordinates and set the general approach assuming a full 3D code. Then we introduce the hypothesis done in TOKAM3X and detail the notation used in the code. The interested reader can take a look to [27] and [47] for more information.
In the whole part, we use the Einstein's summation convention:

$$A^i B_i = \sum_i A^i B_i$$

## B.1. Curvilinear coordinates

The magnetic field in a tokamak is usually known from experiments and reconstructs through code such as EFIT. The magnetic field in output is expressed in the cylindrical coordinates, $\boldsymbol{B} = \boldsymbol{B}(R, Z, \phi)$, where $R$ is the major radius, $Z$ is the vertical axis from the magnetic axis and $\phi$ is the curvilinear coordinate along the toroidal direction.[1]
Because of the anisotropy of the transport process between parallel (to the magnetic field) and perpendicular directions, a coordinate system based on the magnetic topology is used to be aligned with magnetic flux surfaces. For any orthonormal euclidian coordinates $\boldsymbol{r} = \boldsymbol{r}(x, y, z)$ (here cylindrical ones for example) in an euclidian orthonormal basis $(\hat{\boldsymbol{e}}_x, \hat{\boldsymbol{e}}_y, \hat{\boldsymbol{e}}_z)$, we define a set of three scalar $(u^1, u^2, u^3)$ representing the general curvilinear coordinates. For any point $\boldsymbol{r}$ we have thus:

$$\begin{aligned}
\boldsymbol{r} &= \boldsymbol{r}(x, y, z) = \boldsymbol{r}(u^1, u^2, u^3) \\
x &= x(u^1, u^2, u^3) \\
y &= y(u^1, u^2, u^3) \\
z &= z(u^1, u^2, u^3)
\end{aligned}$$

For every point in 3D space, we define a curve along which two parameters are

[1] I remind the reader that these three coordinates are all with the dimension of a length [L]: $\phi$ is not an angle!

constant and the last one is free. These coordinates curves define thus at every point a set of vectors, tangent to the three coordinates curves.

$$\boldsymbol{e}_i = \frac{\partial \boldsymbol{r}}{\partial u^i} \quad i \in (1,2,3) \tag{B.1}$$

where,

$$\frac{\partial \boldsymbol{r}}{\partial u^i} = \frac{\partial x}{\partial u^i}\hat{\boldsymbol{e}}_x + \frac{\partial y}{\partial u^i}\hat{\boldsymbol{e}}_y + \frac{\partial z}{\partial u^i}\hat{\boldsymbol{e}}_z \tag{B.2}$$

These *tangent basis* vectors set the *covariant basis*, that is generally not orthogonal. We define a dual (or reciprocal) basis as the three curves form three surfaces. The vector orthogonal to these surfaces are the *contravariant basis* vectors, defined as:

$$\boldsymbol{e}^i = \boldsymbol{\nabla} u^i \quad i \in (1,2,3) \tag{B.3}$$

where,

$$\boldsymbol{\nabla} u^i = \frac{\partial u^i}{\partial x}\hat{\boldsymbol{e}}_x + \frac{\partial u^i}{\partial y}\hat{\boldsymbol{e}}_y + \frac{\partial u^i}{\partial z}\hat{\boldsymbol{e}}_z \tag{B.4}$$

Due to the local construction of those two basis, we define the Jacobian matrix $\bar{\boldsymbol{J}}$ as:

$$\bar{\boldsymbol{J}} = \begin{pmatrix} \frac{\partial x}{\partial u^1} & \frac{\partial x}{\partial u^2} & \frac{\partial x}{\partial u^3} \\ \frac{\partial y}{\partial u^1} & \frac{\partial y}{\partial u^2} & \frac{\partial y}{\partial u^3} \\ \frac{\partial z}{\partial u^1} & \frac{\partial z}{\partial u^2} & \frac{\partial z}{\partial u^3} \end{pmatrix} \qquad \bar{\boldsymbol{J}}^{-1} = \bar{\mathfrak{J}} \begin{pmatrix} \frac{\partial u^1}{\partial x} & \frac{\partial u^1}{\partial y} & \frac{\partial u^1}{\partial z} \\ \frac{\partial u^2}{\partial x} & \frac{\partial u^2}{\partial y} & \frac{\partial u^2}{\partial z} \\ \frac{\partial u^3}{\partial x} & \frac{\partial u^3}{\partial y} & \frac{\partial u^3}{\partial z} \end{pmatrix}$$

which allows to switch from a classical set of euclidiean coordinates $\bar{X}_i$ to a covariant ones $X_i$:

$$\bar{X}_i = J_{ij} X_j$$

or to contravariant ones $X^i$:

$$\bar{X}^i = J^{-1}_{ij} X^j$$

We remind the reader that in euclidean basis $\bar{X}_i = \bar{X}^i$. We can define the Jacobian, that is the determinant of the Jacobian matrix:

$$J \equiv \frac{\partial \boldsymbol{r}}{\partial u^i} \cdot \frac{\partial \boldsymbol{r}}{\partial u^j} \times \frac{\partial \boldsymbol{r}}{\partial u^k} \quad (i,j,k) \text{ in cycl. order}$$

or

$$J^{-1} \equiv \boldsymbol{\nabla} u^i \cdot \boldsymbol{\nabla} u^j \times \boldsymbol{\nabla} u^k \quad (i,j,k) \text{ in cycl. order}$$

By construction we have the following properties and definitions (see [27] for more details).

### B.1.1. Relation covariant and contravariant

$$\begin{aligned}
\boldsymbol{e}_i &= J(\boldsymbol{e}^j \times \boldsymbol{e}^k) \quad (i,j,k) \text{ in cycl. order} \\
\boldsymbol{e}^i &= J^{-1}(\boldsymbol{e}_j \times \boldsymbol{e}_k) \quad (i,j,k) \text{ in cycl. order} \\
\boldsymbol{e}^i \cdot \boldsymbol{e}_i &= \delta^i_j \\
&= 1 \quad \text{if} \quad i = j \\
&= 0 \quad \text{otherwise}
\end{aligned}$$

For any vector $\boldsymbol{X}$, we can express it in covariant or contravariant basis. In convariant basis, the components are the contravariant ones (upper index) and inversely.

$$\begin{aligned}
\boldsymbol{X} &= X_i \boldsymbol{e}^i \quad \text{(Covariant components in contravariant basis)} \\
X_i &\equiv \boldsymbol{X} \cdot \boldsymbol{e}_i \\
\boldsymbol{X} &= X^i \boldsymbol{e}_i \quad \text{(Contravariant components in covariant basis)} \\
X^i &\equiv \boldsymbol{X} \cdot \boldsymbol{e}^i
\end{aligned}$$

### B.1.2. Metric tensor

These two basis set a metric defined by:

$$\begin{aligned}
g_{ij} &\equiv \boldsymbol{e}_i \cdot \boldsymbol{e}_j = g_{ji} \\
g^{ij} &\equiv \boldsymbol{e}^i \cdot \boldsymbol{e}^j = g^{ji}
\end{aligned}$$

Computing the metric tensor is not trivial at all but we can show that a local approximation is:

$$\begin{aligned}
(g_{ij}) &= \bar{\boldsymbol{J}}^T \bar{\boldsymbol{J}} \quad \text{locally} \\
(g^{ij}) &= \bar{\mathfrak{J}}^T \bar{\mathfrak{J}} \quad \text{locally}
\end{aligned}$$

The following properties can then be infered:

$$\begin{aligned}
X_i &= g_{ij} X^j \\
X^i &= g^{ij} X_j \\
\boldsymbol{e}_i &= g_{ij} \boldsymbol{e}^j \\
\boldsymbol{e}^i &= g^{ij} \boldsymbol{e}_j \\
g_{ik} g^{kj} &= \delta^j_i \\
g^{ik} g_{kj} &= \delta^i_j
\end{aligned}$$

And finally as a side note:

$$g = \det(g_{ij}) = J^2$$
$$g^{-1} = \det\left(g^{ij}\right) = J^{-2}$$

### B.1.3. Operator and other useful relations

We can write the differential arc length, area element and volume element as:

$$\mathrm{d}l = J|\boldsymbol{\nabla} u^j \times \boldsymbol{\nabla} u^k|\mathrm{d}u^i$$
$$\mathrm{d}S = J|\boldsymbol{\nabla} u^i|\mathrm{d}u^j \mathrm{d}u^k$$
$$\mathrm{d}V = J\mathrm{d}u^1\mathrm{d}u^2\mathrm{d}u^3$$

The gradient, divergence and curl are then defined as:

$$\boldsymbol{\nabla} = \boldsymbol{e}^i \frac{\partial}{\partial u^i}$$
$$\boldsymbol{\nabla} \cdot \boldsymbol{X} = J^{-1} \frac{\partial}{\partial u^i}(JX^i)$$
$$\boldsymbol{\nabla} \times \boldsymbol{X} = J^{-1} \sum_k \left( \frac{\partial X_j}{\partial u^i} - \frac{\partial X_i}{\partial u^j} \right) \boldsymbol{e}_k \quad (i,j,k) \text{ in cycl. order}$$

## B.2. Magnetic based coordinate system

Now the definitions and properties for curvilinear coordinates are set. In tokamak, the existence of flux surfaces is assumed. These surfaces, tangent in every point to the magnetic field lines, are labelled by a coordinate $\psi$. The curvilinear coordinate $\theta^*$ varies along magnetic flux surfaces in the poloidal plane. Finally $\zeta$ is the curvilinear coordinate along the toroidal plane.
At this point, TOKAM3X makes some assumptions or uses different notations:

- $\theta^*$ is a poloidal curvilinear angle varying in $[0, 2\pi]$, which is the same as $\theta$ in circular geometry.
- $(g_{ij})$ is noted $\mathbb{G}$ or gmat in the code and $(g^{ij})$ is noted $\mathbb{H}$ or hmat in the code.
- $\zeta$ is considered to be the same as $\varphi$ the toroidal angle in cylindrical coordinates (careful: not the cylindrical curvilinear coordinate $\phi$) because tokamaks are axisymmetrical machines so that the flux surface are not much deformed in the toroidal direction. We consider $\zeta$ to be a local index in the toroidal direction.
- The discretization of the domain transforms $(\psi, \theta^*, \varphi)$ basis into $(i_\psi, i_\theta, i_\varphi)$ basis.

From the last point, a lot of assumption can be made and simplify the metric. The Jacobian matrix becomes:

$$\bar{\boldsymbol{J}} = \begin{pmatrix} \dfrac{\partial R}{\partial i_\psi} & \dfrac{\partial R}{\partial i_\theta} & 0 \\ \dfrac{\partial Z}{\partial i_\psi} & \dfrac{\partial Z}{\partial i_\theta} & 0 \\ 0 & 0 & \dfrac{\mathrm{d}\phi}{\mathrm{d}i_\varphi} \end{pmatrix} \tag{B.5}$$

This structure is correct for 2D magnetic field but wrong in fully 3D magnetic field. Still we preserved this form for small 3D perturbations on the 2D magnetic field, assuming that the main 2D structure is still preserved, and thus flux surfaces. In this case, we have:

$$\boldsymbol{e}_\varphi \cdot \boldsymbol{e}_\psi = \boldsymbol{e}_\varphi \cdot \boldsymbol{e}_{\theta^*} = \boldsymbol{e}^\varphi \cdot \boldsymbol{e}^\psi = \boldsymbol{e}^\varphi \cdot \boldsymbol{e}^{\theta^*} = 0 \quad , \quad \boldsymbol{e}^\varphi \times \boldsymbol{e}_\varphi = 0 \tag{B.6}$$

This way allows to reduce memory usage and computation time as we can write:

$$\bar{\boldsymbol{J}}_{\mathrm{TK3X}} = \begin{pmatrix} \dfrac{\partial R}{\partial i_\psi} & \dfrac{\partial R}{\partial i_\theta} \\ \dfrac{\partial Z}{\partial i_\psi} & \dfrac{\partial Z}{\partial i_\theta} \end{pmatrix} \quad , \quad \frac{\mathrm{d}\phi}{\mathrm{d}i_\varphi} = ||\boldsymbol{e}_{i_\varphi}|| = \frac{\mathrm{d}\phi}{\mathrm{d}\varphi}\frac{\mathrm{d}\varphi}{\mathrm{d}i_\varphi} = R\frac{\mathrm{d}\varphi}{\mathrm{d}i_\varphi} \tag{B.7}$$

where:

$$\frac{\mathrm{d}\varphi}{\mathrm{d}i_\varphi} = \frac{L_\varphi}{N_\varphi} \tag{B.8}$$

represents the angular extension along the toroidal direction (dphi_diphi in the code). Thus we have:

$$J = \det\left(\bar{\boldsymbol{J}}\right) = \det\left(\bar{\boldsymbol{J}}_{\mathrm{TK3X}}\right) R\frac{\mathrm{d}\varphi}{\mathrm{d}i_\varphi} = J_{\mathrm{TK3X}} R\frac{\mathrm{d}\varphi}{\mathrm{d}i_\varphi} \tag{B.9}$$

Since the magnetic field is divergence-free, it is written:

$$\boldsymbol{B} = \boldsymbol{\nabla} \times \boldsymbol{A} \tag{B.10}$$

with (correct only with curvilinear angles):

$$\boldsymbol{A} = \Psi_p \boldsymbol{\nabla}\varphi + \Psi_t \boldsymbol{\nabla}\theta^* = \Psi_p \boldsymbol{e}^\varphi + \Psi_t \boldsymbol{e}^{\theta^*} \tag{B.11}$$

$\Psi_p$ and $\Psi_t$ are respectively the poloidal and toroidal flux of magnetic field. A general (3D) way assume them to be fonction of the three variables $(\psi, \theta^*, \varphi)$. But we assume them to be of the form:

$$\Psi_t = \Psi_t^0(\psi, \theta^*) \tag{B.12}$$

$$\Psi_p = \left(1 + \epsilon_p(\psi, \theta^*, \varphi)\right)\Psi_p^{0,3\mathrm{D}}(\psi, \varphi) = \left(1 + \epsilon_p(\psi, \theta^*, \varphi)\right)\Psi_p^0(\psi)\frac{\mathrm{d}\varphi}{\mathrm{d}i_\varphi} \tag{B.13}$$

with $||\epsilon_p|| \ll 1$ and $\Psi_p^{0,3D}$ the 3D poloidal flux function can be reduced to a 2D one $\Psi_p^0$ multiplied by the toroidal angular elongation $\mathrm{d}\varphi/\mathrm{d}i_\varphi$.

The calculation of the magnetic field gives then, using $\boldsymbol{\nabla}\times\boldsymbol{\nabla}=\mathbf{0}$:

$$\boldsymbol{B}=\frac{\partial\psi_t}{\partial\psi}J^{-1}\boldsymbol{e}_\varphi-\left(\frac{\partial\psi_p}{\partial\psi}(1+\epsilon_p)+\psi_p\frac{\partial\epsilon_p}{\partial\psi}\right)\frac{\mathrm{d}\varphi}{\mathrm{d}\varphi}J^{-1}\boldsymbol{e}_{\theta^*}+\psi_p\frac{\partial\epsilon_p}{\partial\theta^*}J^{-1}\boldsymbol{e}_\psi \tag{B.14}$$

In TOKAM3X, the basis vectors are normalized (noted $\hat{\boldsymbol{e}}_i$) such that:

$$\begin{aligned}\boldsymbol{B}&=B^\varphi\boldsymbol{e}_\varphi+B^{\theta^*}\boldsymbol{e}_{\theta^*}+B^\psi\boldsymbol{e}_\psi\\&=B^\varphi||\boldsymbol{e}_\varphi||\frac{\boldsymbol{e}_\varphi}{||\boldsymbol{e}_\varphi||}+B^{\theta^*}||\boldsymbol{e}_{\theta^*}||\frac{\boldsymbol{e}_{\theta^*}}{||\boldsymbol{e}_{\theta^*}||}+B^\psi||\boldsymbol{e}_\psi||\frac{\boldsymbol{e}_\psi}{||\boldsymbol{e}_\psi||}\\&=B^\varphi\sqrt{g_{\varphi\varphi}}\hat{\boldsymbol{e}}_\varphi+B^{\theta^*}\sqrt{g_{\theta^*\theta^*}}\hat{\boldsymbol{e}}_{\theta^*}+B^\psi\sqrt{g_{\psi\psi}}\hat{\boldsymbol{e}}_\psi\\&=B^{\mathrm{tor}}\hat{\boldsymbol{e}}_\varphi+B^{\mathrm{pol}}\hat{\boldsymbol{e}}_{\theta^*}+B^{\mathrm{psi}}\hat{\boldsymbol{e}}_\psi\end{aligned} \tag{B.15}$$

In the former version of TOKAM3X, $\epsilon_p=0$ so that $B^\psi=0$. By choosing $\Psi_t^0$ such that:

$$\frac{\partial\Psi_t^0}{\partial\psi}=\frac{FJ}{R\sqrt{g_{\varphi\varphi}}}$$

This expression can be check with the Ampère's law along a magnetic field line (toroidal direction):

$$\oint\boldsymbol{B}\cdot\mathrm{d}\boldsymbol{l}=2\pi F=\mu_0 I_{\mathrm{tor}}$$

Thus:

$$F=\frac{\mu_0 I_{\mathrm{tor}}}{2\pi}$$

## B.3. Parallel gradient, drifts velocities and fluxes

This section is memento giving the global expressions of useful quantities in both mathematical and TOKAM3X notations. Here are the correspondances between the code (left) and mathematical notations (right). We always assume the Einstein convention on the mathematical notations.

$$\begin{aligned}B^{\mathrm{tor}}&=B^{i_\varphi}\sqrt{g_{i_\varphi i_\varphi}}\\B^{\mathrm{pol}}&=B^{i_\theta}\sqrt{g_{i_\theta i_\theta}}\\B^{\mathrm{psi}}&=B^{i_\psi}\sqrt{g_{i_\psi i_\psi}}\end{aligned}$$

We note:

$$\boldsymbol{b}=\frac{\boldsymbol{B}}{|\boldsymbol{B}|}$$

with:

$$\begin{aligned} B &= |\boldsymbol{B}| = \sqrt{g_{ij}B^iB^j} \\ &\underset{\text{TK3X}}{=} \left( B^{\text{tor}^2} + B^{\text{pol}^2} + B^{\text{pol}}B^{\text{psi}}\frac{g_{i_\theta i_\psi}}{\sqrt{g_{i_\theta i_\theta}g_{i_\psi i_\psi}}} + B^{\text{psi}}B^{\text{pol}}\frac{g_{i_\psi i_\theta}}{\sqrt{g_{i_\theta i_\theta}g_{i_\psi i_\psi}}} + B^{\text{psi}^2} \right) \end{aligned}$$

Let a scalar $f$, then the parallel gradient is written:

$$\nabla_\parallel f = \boldsymbol{b}\cdot\boldsymbol{\nabla} f = \frac{B^i}{B}\frac{\partial f}{\partial u^i} \tag{B.16}$$

$$\underset{\text{TK3X}}{=} \frac{B^{\text{tor}}}{B\sqrt{g_{i_\varphi i_\varphi}}}\frac{\partial f}{\partial i_\varphi} + \frac{B^{\text{pol}}}{B\sqrt{g_{i_\theta i_\theta}}}\frac{\partial f}{\partial i_\theta} + \frac{B^{\text{psi}}}{B\sqrt{g_{i_\psi i_\psi}}}\frac{\partial f}{\partial i_\psi} \tag{B.17}$$

The perpendicular gradient is exactly the gradient minus the parallel gradient along the magnetic (parallel) direction. We skip this easy step and directly calculate the drift velocities. Each drift velocity is of the form:

$$\boldsymbol{u}_{\text{drift}} = \frac{\boldsymbol{B}\times\boldsymbol{\nabla} f}{B^2}$$

Passing $\boldsymbol{B}$ in the contravariant basis gives an easier computation:

$$\boldsymbol{B} = (B^i\boldsymbol{e}_i\cdot\boldsymbol{e}_j)\boldsymbol{e}^j = (B^i g_{ij})\boldsymbol{e}^j$$

Then:

$$\begin{aligned} \boldsymbol{u}_{\text{drift}} &= \frac{B^i}{B^2}g_{ij}\boldsymbol{e}^j\times\boldsymbol{e}^k\frac{\partial f}{\partial u^k} \\ &= \frac{B^i}{JB^2}g_{ij}\frac{\partial f}{\partial u^k}\boldsymbol{e}_l \end{aligned}$$

For each contravariant component of the drift velocity $u^i = \boldsymbol{u}\cdot\boldsymbol{e}^i/|\boldsymbol{e}^i|$, we have

therefore:

$$
\begin{aligned}
u^{\psi} &= \frac{B^{\psi}}{JB^2\sqrt{g^{\psi\psi}}}\left(g_{\psi\theta^*}\frac{\partial f}{\partial u^{\zeta}} - g_{\psi\zeta}\frac{\partial f}{\partial u^{\theta^*}}\right) \\
&+ \frac{B^{\theta^*}}{JB^2\sqrt{g^{\psi\psi}}}\left(g_{\theta^*\theta^*}\frac{\partial f}{\partial u^{\zeta}} - g_{\theta^*\zeta}\frac{\partial f}{\partial u^{\theta^*}}\right) \\
&+ \frac{B^{\zeta}}{JB^2\sqrt{g^{\psi\psi}}}\left(g_{\zeta\theta^*}\frac{\partial f}{\partial u^{\zeta}} - g_{\zeta\zeta}\frac{\partial f}{\partial u^{\theta^*}}\right) \\
&\underset{\text{TK3X}}{=} \frac{B^{\text{psi}}}{JB^2\sqrt{g_{i_\psi i_\psi}}\sqrt{g^{i_\psi i_\psi}}}\left(g_{i_\psi i_\theta}\frac{\partial f}{\partial u^{i_\varphi}}\right) \\
&+ \frac{B^{\text{pol}}}{JB^2\sqrt{g_{i_\theta i_\theta}}\sqrt{g^{i_\psi i_\psi}}}\left(g_{i_\theta i_\theta}\frac{\partial f}{\partial u^{i_\varphi}}\right) \\
&- \frac{B^{\text{tor}}}{JB^2\sqrt{g_{i_\phi i_\phi}}\sqrt{g^{i_\psi i_\psi}}}\left(g_{i_\varphi i_\varphi}\frac{\partial f}{\partial u^{i_\theta}}\right)
\end{aligned}
$$

$$
\begin{aligned}
u^{\theta^*} &= \frac{B^{\psi}}{JB^2\sqrt{g^{\theta^*\theta^*}}}\left(g_{\psi\zeta}\frac{\partial f}{\partial u^{\psi}} - g_{\psi\psi}\frac{\partial f}{\partial u^{\zeta}}\right) \\
&+ \frac{B^{\theta^*}}{JB^2\sqrt{g^{\theta^*\theta^*}}}\left(g_{\theta^*\zeta}\frac{\partial f}{\partial u^{\psi}} - g_{\theta^*\psi}\frac{\partial f}{\partial u^{\zeta}}\right) \\
&+ \frac{B^{\zeta}}{JB^2\sqrt{g^{\theta^*\theta^*}}}\left(g_{\zeta\zeta}\frac{\partial f}{\partial u^{\psi}} - g_{\zeta\psi}\frac{\partial f}{\partial u^{\zeta}}\right) \\
&\underset{\text{TK3X}}{=} -\frac{B^{\text{psi}}}{JB^2\sqrt{g_{i_\psi i_\psi}}\sqrt{g^{i_\theta i_\theta}}}\left(g_{i_\psi i_\psi}\frac{\partial f}{\partial u^{i_\varphi}}\right) \\
&- \frac{B^{\text{pol}}}{JB^2\sqrt{g_{i_\theta i_\theta}}\sqrt{g^{i_\theta i_\theta}}}\left(g_{i_\theta i_\psi}\frac{\partial f}{\partial u^{i_\varphi}}\right) \\
&+ \frac{B^{i_\varphi}}{JB^2\sqrt{g_{i_\varphi i_\varphi}}\sqrt{g^{i_\theta i_\theta}}}\left(g_{i_\varphi i_\varphi}\frac{\partial f}{\partial u^{i_\psi}}\right)
\end{aligned}
$$

$$
\begin{aligned}
u^{\zeta} &= \frac{B^{\psi}}{JB^2\sqrt{g^{\zeta\zeta}}}\left(g_{\psi\psi}\frac{\partial f}{\partial u^{\theta^*}} - g_{\psi\theta^*}\frac{\partial f}{\partial u^{\psi}}\right) \\
&+ \frac{B^{\theta^*}}{JB^2\sqrt{g^{\zeta\zeta}}}\left(g_{\theta^*\psi}\frac{\partial f}{\partial u^{\theta^*}} - g_{\theta^*\theta^*}\frac{\partial f}{\partial u^{\psi}}\right) \\
&+ \frac{B^{\zeta}}{JB^2\sqrt{g^{\zeta\zeta}}}\left(g_{\zeta\psi}\frac{\partial f}{\partial u^{\theta^*}} - g_{\zeta\theta^*}\frac{\partial f}{\partial u^{\psi}}\right) \\
&\underset{\text{TK3X}}{=} \frac{B^{\text{psi}}}{JB^2\sqrt{g_{i_\psi i_\psi}}\sqrt{g^{i_\varphi i_\varphi}}}\left(g_{i_\psi i_\psi}\frac{\partial f}{\partial u^{i_\theta}} - g_{i_\psi i_\theta}\frac{\partial f}{\partial u^{i_\psi}}\right) \\
&+ \frac{B^{\text{pol}}}{JB^2\sqrt{g_{i_\theta i_\theta}}\sqrt{g^{i_\varphi i_\varphi}}}\left(g_{i_\theta i_\psi}\frac{\partial f}{\partial u^{i_\theta}} - g_{i_\theta i_\theta}\frac{\partial f}{\partial u^{i_\psi}}\right)
\end{aligned}
$$